IPP-Report

MAX-PLANCK-INSTITUT
FÜR PLASMAPHYSIK

Gregor Birkenmeier

Structure formation at the edge of high temperature plasmas

IPP 2024-21
August 2024


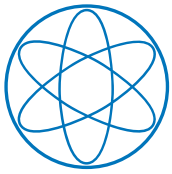


Structure formation at the edge of high temperature plasmas

Habilitation Thesis

in

Experimental Physics

at the

Technical University of Munich

written by

Gregor Birkenmeier

Corrected version (12th July 2024)
based on the version submitted in December 2022

Progress is possible and innocuous only when it is subject to the control of reason.
– Andrei D. Sacharow (1921 – 1989)

Zusammenfassung

Energiegewinnung durch Kernfusion ist emissionsfrei, grundlastfähig und erfordert aufgrund der hohen Energiedichte des Fusionsbrennstoffs einen vergleichsweise niedrigen Ressourceneinsatz, so dass Kernfusionskraftwerke in einem zukünftigen Energiesystem erneuerbare Energiequellen insbesondere in Regionen hoher Bevölkerungsdichte sinnvoll ergänzen könnten. Fusionsanlagen vom Typ Tokamak sind am weitesten fortgeschritten, um Fusionsbedingungen in einem Hochtemperaturplasma zu erreichen, das in einem ringförmigen Magnetfeld eingeschlossen ist. Am Rande des Plasmas, also im äussersten Bereich des eingeschlossenen Plasma, treten sehr hohe Dichte- und Temperaturgradienten auf, die über nicht-lineare Prozesse und aufgrund der Präsenz von geladenen und neutralen Teilchen sowie eines starken Magnetfelds eine äusserst komplexe und vielseitige Dynamik antreiben. Wie für andere dynamische Systeme dieser Komplexität typisch, tritt Selbstorganisation und Strukturbildung auf, die zu vielfältigen raum-zeitlichen Mustern und zu spontanen Phasenübergängen in neue dynamische Zustände führt. Diese Vielzahl an Mustern können eingeordnet werden in selbsterzeugte Strömungsstrukturen, selbsterzeugte Strukturen elektrischen Stroms, spontane Phasenübergänge in Regime hohen Einschlusses, Filamente und zeitliche Strukturen. Wie in dieser Arbeit gezeigt wird, sind diese Strukturen nicht nur ein interessantes physikalisches Studienobjekt, sondern das Verständnis und die Kontrolle einiger dieser Strukturen sind unabdingbar für einen zuverlässigen Betrieb eines zukünftigen Tokamakfusionsreaktors. Das bisherige physikalische Bild und aktuelle experimentelle Resultate werden für Filamente, spontane Phasenübergänge und Grenzzyklusoszillationen im Detail zusammengefasst und offene Punkte werden thematisiert. Wie gezeigt wird, sind für ein umfassendes Verständnis der vorgestellten Strukturen noch bessere Messungen am Plasmarand und aussagekräftigere theoretische Modelle notwendig. Bessere Messungen könnten mit Hilfe einer neu entwickelten Plasmaranddiagnostik, der bildgebenden Schwerionensonde, erzielt werden. Das Messprinzip und erste Signale dieser Diagnostik, die am Tokamak ASDEX Upgrade aufgebaut wurde, werden in dieser Arbeit vorgestellt.

Abstract

Energy generation through nuclear fusion is emission-free, base load capable and requires a relatively low amount of resources due to the high energy density of the fusion fuel, so that nuclear fusion power plants could complement renewable energy sources in a future energy system in particular in regions of high population density. Tokamaks are the most advanced devices to achieve fusion conditions in a high-temperature plasma, which is confined in a toroidal magnetic field. At the edge of the plasma, i.e. in the outermost region of the confined plasma, very high density and temperature gradients occur driving extremely complex and multifaceted dynamics due to non-linear processes and the presence of charged and neutral particles as well as strong magnetic fields. As typical for other dynamical systems, self-organization and structure formation occurs at the plasma edge generating spatio-temporal patterns and spontaneous phase transitions into new dynamic states. This variety of patterns can be classified into self-generated flow structures, self-generated structures of electric current, spontaneous phase transitions in regimes of high confinement, filaments and temporal structures. As shown in this thesis, these structures are not only an interesting physical object of study on its own, but the understanding and control of some of the structures is essential for the reliable operation of a future tokamak fusion reactor. The recent physical picture and current experimental results for filaments, spontaneous phase transitions and limit-cycle oscillations are summarized in detail and open points are addressed. It is shown, that improved measurement capabilities at the plasma edge and more meaningful theoretical models are necessary for a full understanding of the structures presented. Better measurements could potentially be achieved by means of a newly developed plasma edge diagnostics, the imaging heavy ion beam probe. The measurement principle and first signals of this diagnostic installed at the tokamak ASDEX Upgrade are presented in this work.

Contents

Chapter 1

Introduction

1.1 Controlled Nuclear Fusion

Energy is the basis of economic and cultural development for human civilization, and enhances the well-being of humans [1]. Plenty of reserves are available for energy production, but in order to cope with climate change, mankind is well-advised to keep the majority of fossil reserves untouched [2] in order to minimize greenhouse gas emissions and their harmful effects on civilization due to changes of atmospheric dynamics promoting extreme weather events, sea-level rise and desertification, among others [3]. Therefore, emission-free, reliable and scalable energy sources are needed for the transition to an energy system without greenhouse gas emissions. Apart from renewable energy sources and fission power plants, nuclear fusion power plants could potentially contribute to this transition in the course of the 21st century and, simultaneously, enables energy systems to be more independent from geographical and weather conditions. Due to the high energy density, fusion power would be most attractive to be employed in densely populated areas and highly industrialized regions, where land scarcity limits the use of renewable energy sources [4].

For energy production purposes, the deuterium-tritium (D-T) reaction

$$^{2}\mathrm{D} + {}^{3}\mathrm{T} \longrightarrow {}^{4}\mathrm{He}\ (3.52\ \ \mathrm{MeV}) + {}^{0}\mathrm{n}\ (14.06\ \ \mathrm{MeV}) \tag{1.1}$$

generating an alpha particle ^{4}He and a neutron ^{0}n is the most promising reaction, since the cross sections are largest of all known fusion reactions at comparably low temperature and, thus, easiest to be achieved on earth [5]. In order to start this thermonuclear reaction, very high temperatures in the order of 100 million Kelvin (K) corresponding to about 10 keV are necessary. At such high temperatures, the fusion fuel is in the plasma state, i.e. the

electrons are not bound anymore to the nuclei. Although electrically neutral on the macroscopic scale (the so called quasi-neutrality [6]), the free charges in the plasma can interact with electromagnetic fields inducing a broad variety of collective phenomena. Due to this, fusion research is intrinsically connected with high temperature plasma physics.

For energy production, a self-sustained fusion reaction is desirable, so that only the D-T fuel has to be refilled while the plasma is continuously maintaining the fusion conditions due to self-heating without the need of external heating. These burning plasma conditions are achieved, when the plasma heating due to the alpha particles produced in the fusion reaction according to equation 1.1 is greater than the energy losses of the plasma[1]. At fusion conditions, the main loss channel for a pure D-T plasma is the heat transport due to the collective behavior of the plasma, or more specifically, due to collisional and turbulent transport. The heat transport can be quantified by the energy confinement time,

$$\tau_{\mathrm{E}} = \frac{W}{P_{\mathrm{heat}}}, \tag{1.2}$$

with plasma energy content W and heating power P_{heat}. The greater the heat transport, the smaller the energy confinement time, i.e. for the given input power P_{heat} a smaller energy content W can be reached when the heat transport is large. τ_{E} is the time until the plasma has reached $1/e$ of the initial plasma content W after switching off the heating[2].

It is possible to quantify the balance between fusion-born alpha particle heating and transport losses resulting in a necessary condition for a burning plasma, the so called ignition condition [5]:

$$\overline{n}_0 \overline{T} \tau_{\mathrm{E}} > 3 \times 10^{24}\ \mathrm{eVs/m^3}. \tag{1.3}$$

The triple product, also called fusion product, consisting of the volume-averaged plasmas density $\overline{n}_0$, the volume-averaged plasmas temperature $\overline{T}$ and the energy confinement time τ_{E} is *the* figure of merit for fusion experiments to demonstrate, how close it is to burning plasmas conditions. The

[1] The neutrons do not play a role in this consideration since their interaction with the plasma quantified by its collisional cross section is negligible compared to the Coulomb collisions of the alpha particles with the charged particles. As shown below for magnetic confinement fusion, this effect is even more pronounced due to the fact that neutrons are not confined by the magnetic field in contrast to the alpha particles.

[2] The temperature of hot tea in a typical thermos flask would decrease to $1/e$ of the initial temperature at the filling within hours, thus, the energy confinement time of a thermos flask is a few hours. The confinement time of an uncovered cup of tea is much shorter, typically a few minutes, due to the lower thermal insulation i.e. worse confinement properties.

ignition condition was not yet achieved in nowadays fusion experiments, but the triple product was raised by more than three orders of magnitude in consecutively developed fusion devices over time [5] and is approaching the ignition condition in the next generation of fusion devices [7]. This condition is met e.g. for densities of $\overline{n}_0 = 2 \cdot 10^{19}$ m^{-3}, temperatures of $\overline{T} = 15$ keV and a confinement time of $\tau_\mathrm{E} = 3$ s.

The two most promising approaches to reach the ignition condition (equation 1.3) are inertial confinement fusion and magnetic confinement fusion [6]. For inertial confinement fusion, a small target (typically a solid capsule filled with D-T of a size of a few millimeters) is compressed by laser or particle beams to reach fusion conditions for a very small time span in order to burn the complete fuel inventory of the capsule. In this setup, the plasma density is high and the confinement time very short. Inertial confinement fusion research made tremendous progress in the last years and demonstrated plasma conditions close to net energy output [8].

Magnetic confinement fusion aims at plasma confinement with strong magnetic fields and large volumes to sustain a plasma over several hours in a reactor. In this approach, the plasma density is rather low but the confinement time relatively large. Magnetic confinement fusion likewise showed great progress in the last few years, and recent experiments at the JET tokamak in Culham, UK, generated 59 megajoules of fusion energy, i.e the largest amount of controlled fusion energy to date [9, 10].

In the remainder of this thesis, only magnetic confinement fusion is considered, since the phenomenology of structure formation is much richer and better diagnosed in magnetic confinement fusion than in inertial confinement fusion due to the presence of a strong magnetic field and the larger spatial and temporal scales involved.

1.2 Magnetic Confinement

In the course of the history of fusion research a variety of magnetic configurations have been explored [11]. Two classes of configurations have proven to perform best in terms of triple product: the stellarator [12] and the tokamak [5]. The magnetic field in a stellarator is exclusively generated by external coils providing the advantages of intrinsic steady state capabilities and low plasma currents, thus, avoiding undesired current-driven instabilities [13]. In addition, the three-dimensional nature of stellarators is connected with more degrees of freedom allowing for optimizations in many respects [14, 15]. However, without the numerical optimization of the stellarator magnetic field, the confinement is poor as it was the case in the first types of stellarators. This

is the reason, why stellarators are back on stage to be considered for fusion power plants only since a few years when sufficient computational power was available for confinement optimization. Consequently, the stellarator development is lacking behind the progress of tokamak research, which progressed steadily since the beginning of fusion research. Nevertheless, the latest stellarator experiment, Wendelstein 7-X, demonstrated exceptionally desirable properties [16], so that stellarators will be considered as serious alternative to tokamaks as a future fusion reactor configuration.

The tokamak configuration is axissymmetric and the coil geometry is simpler to build than the helical or non-planar coils in stellarator configurations. In contrast to stellarators, the magnetic field is not only given by external coils, but partially generated by a strong current, which is driven inductively in the plasma. This is shown in figure 1.1.

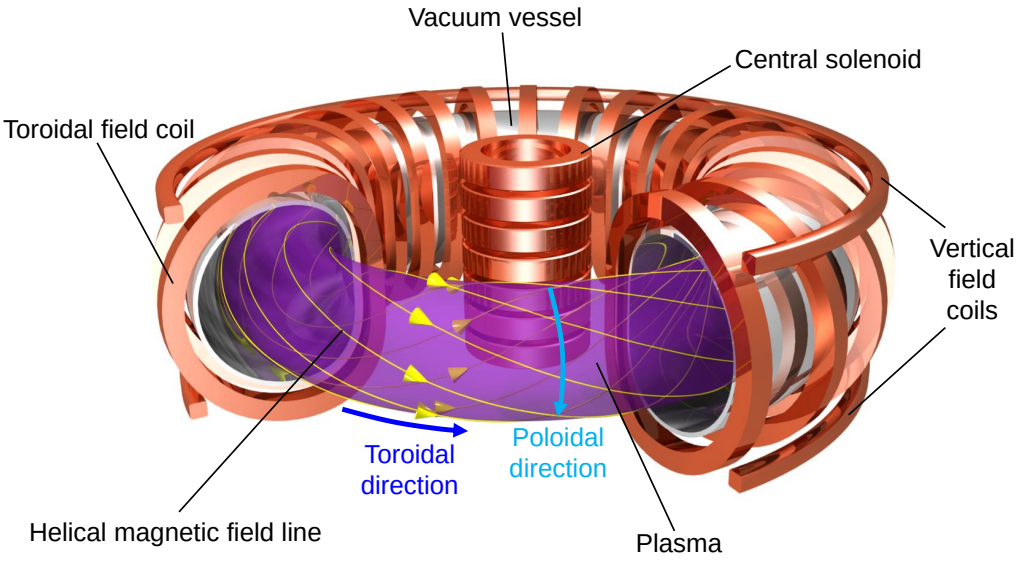

Figure 1.1: *Coil system and magnetic field structure of a tokamak. The helical magnetic field (yellow) results from a superposition of the magnetic field components in toroidal and poloidal direction. While the toroidal magnetic field component is produced by external toroidal field coils, the poloidal magnetic field component is generated by a toroidal current in the plasma. This current is inductively driven by a current ramp in the central solenoid. The vertical field coils are used for plasma shaping, plasma positioning and stabilization purposes. Rendering of tokamak by courtesy of C. Brandt, IPP.*

The central solenoid, i.e. a coil structure in the center of the tokamak around the torus axis, induces a plasma current in toroidal direction, i.e.

along the long circumference of the plasma. According to Ampère's law, this generates a magnetic field in poloidal direction, i.e. along the short circumference of the plasma. The total, helical field results then from a superposition of the inductively driven poloidal magnetic field and the toroidal magnetic field generated by external coils. The toroidal plasma current gives rise to ohmic heating in the plasma. This is one reason next to the simpler coil system and the confinement improving axissymmetry, why tokamaks became so successful [11], since they were comparably easy to heat to fusion relevant temperatures. The toroidal plasma current, however, is accompanied by current driven instabilities and can even fully disrupt within a fraction of a second, which induces strong forces in the structure material and can lead to undesired runaway electrons [17]. Such a disruption poses a major risk for large tokamaks and has to be fully avoided or mitigated for reactor-scale devices requiring further research [18]. Despite these challenges, the tokamak configuration is the most mature to show a positive net energy balance in the next few years. Therefore, the next generation of devices like ITER [7] or the various DEMO concepts [19] are of the tokamak type.

Although stellarator and tokamak plasmas are similarly prone to structure formation processes, this thesis focuses on tokamak plasmas due to their higher relevance for ITER and due to the fact that tokamak plasmas were much more investigated in respect of structure formation and self-organization than stellarator plasmas in recent years. Therefore, a few general aspects of tokamak plasmas are introduced in the following.

1.3 The Edge Plasma of a Tokamak

The presence of magnetic field lines in a tokamak does not allow the charged particles of the plasma to move freely in the vacuum chamber. Due to the Lorentz force[3]

$$\mathbf{F}_\mathrm{L} = q\,(\mathbf{E} + \mathbf{v} \times \mathbf{B}) \tag{1.4}$$

with q the charge of the particle, $\mathbf{v}$ the velocity of the particle, $\mathbf{E}$ the electric field and $\mathbf{B}$ the magnetic field, the particles are forced to orbit around the field line performing a gyration perpendicular to the magnetic field direction [6]. This way the particles, and hence the plasma, are bound to the magnetic field lines, which allows to form the plasma by means of shaping of the magnetic field configuration. Parallel to the magnetic field, however, the Lorentz force has no impact, so that the particles can almost freely move along the field lines.

[3]Bold symbols in equations etc. indicate vector quantities.

The magnetic field strength $B = |\mathbf{B}|$ is not constant inside the tokamak, but higher at the inner side of the torus, thus called high field side (HFS), and lower at the outer side, therefore called low field side (LFS). This means that the magnetic field is not homogeneous giving rise to drift motion (see Appendix A). This complicates the dynamics significantly, but is not further detailed for the sake of simplicity here.

A magnetic field line toroidally circulating around the torus axis performs a poloidal revolution, which is quantified by the safety factor q_s indicating the number of toroidal turns needed for one poloidal turn[4]. During several toroidal turns, the magnetic field line sweeps over a three-dimensional tube-shaped surface, the so-called flux surface. Magnetic field lines further outside sweep over tube-shaped surfaces with a larger inner diameter. Thus, the magnetic field structure in a tokamak consists of nested magnetic flux surfaces with the magnetic axis in the center. This is shown in figure 1.2.

The motion parallel to the field lines is very fast, so that parallel pressure gradients are balanced on time scales much faster than the motion perpendicular to the magnetic field lines, since the latter can only take place via drifts or collisions. Therefore, the pressure is constant on a single flux surface i.e. flux surfaces are isobars.

The pressure is typically highest on the magnetic axis and decreases towards the last closed flux surface (LCFS). The LCFS is called separatrix, when the plasma configuration possesses an X-point [5]. Outside the LCFS, the field lines are in contact with plasma-facing components (PFCs). Therefore, they cannot form closed flux surfaces, which changes the dynamics significantly, and charged particles and heat streaming towards PFCs are lost. This region of open magnetic field lines is the scrape-off layer (SOL) [20]. In order to keep the plasma clean, the plasma possesses an X-point as depicted in figure 1.2. In such a configuration, the open magnetic field lines are on purpose guided to the divertor, i.e. a region equipped with robust plates to withstand the strong heat fluxes there and good pumping capabilities to get rid of undesired impurities. The divertor concept is advantageous compared to limiter plasmas, in which the PFCs are much closer to the confined plasma [21].

The outermost part of the confined plasma, i.e. the outermost closed flux surfaces up to the LCFS, is the plasma edge indicated as blue shaded area in figure 1.2, right. This region is in the focus of interest for this theses, since there some of the most exciting dynamics takes place as described below.

[4]It turned out that a higher q_s makes the plasma less prone to a certain type of magneto-hydrodynamic (MHD) instability allowing for safer operation i.e. lower probability for disruptions.

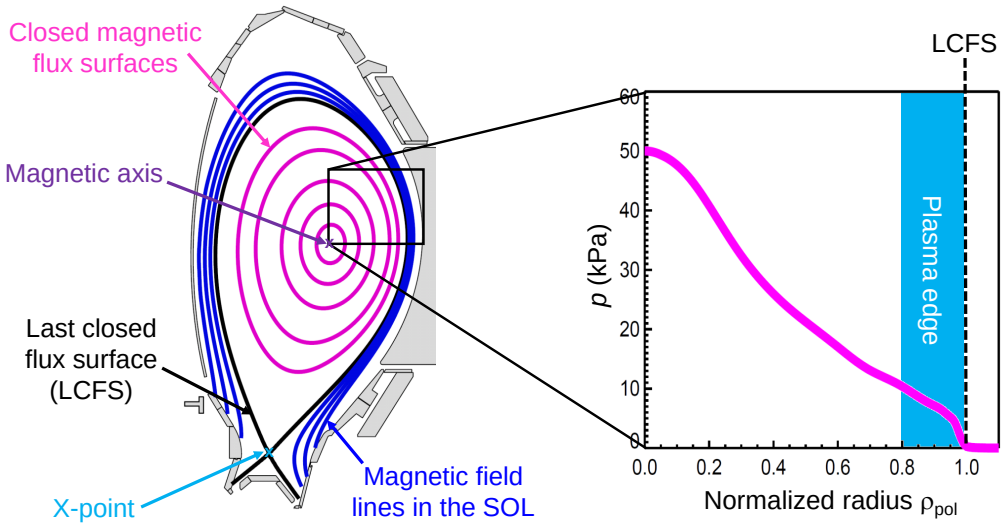

Figure 1.2: *Poloidal cross section (left) and typical radial pressure profile of a tokamak plasma (right). The pressure is constant on a single flux surface but decreases further out towards the last closed flux surface (LCFS). Outside the LCFS, the field lines do not form closed flux surfaces and are in contact with plasma-facing components. This region is the scrape-off layer (SOL). The light blue shaded area on the right indicates the plasma edge, which is in the focus of interest for this thesis.*

There is no exact definition of the plasma edge, but for this thesis we consider the outer 20 % of the minor radius as the plasma edge, i.e. the region from $\rho_{\mathrm{pol}} = 0.8$ to $\rho_{\mathrm{pol}} = 1.0$ with ρ_{pol} the normalized poloidal flux coordinate, which is by definition 0 on the magnetic axis and 1.0 at the LCFS [22].

Apart from generating a rich variety of plasma phenomena, which are interesting from a perspective of dynamical systems, the plasma edge is at the same time a region of crucial relevance for a tokamak fusion reactor: it represents the boundary condition defining the core performance due to profile stiffness [23], it hosts some of the most harmful instabilities for plasma operation [24], and it is the region where the heat flux challenge is met [25].

The plasma edge is special in many respects. It features the steepest pressure gradients in the fusion plasma, due to relatively low temperatures and the presence of neutrals different types of collisional processes take place, and the vicinity to the SOL with its own dynamics gives rise to a complicated interdependency of SOL and edge.

On the one hand, these complex conditions make it difficult to understand the physics in the edge, since successful strategies in other fields of plasma physics, e.g. to describe the dynamics in the plasma core, fail here. Consequently, several of the most important edge phenomena cannot be quantitatively explained by theoretical models or numerical simulations. This makes reliable predictions for reactor-scale fusion experiments impossible, and more experimental data and better theoretical models are needed for the success of fusion.

On the other hand, the complex conditions give rise to a large variety of multifaceted phenomena, structure formation and self-organization. In other words, the plasma edge is a fantastic playground for physicists to investigate, categorize and understand one of the most complex dynamical system far from thermodynamic equilibrium in the universe.

1.4 Structure Formation at the Plasma Edge

Laboratory plasmas necessarily require an energy input. Otherwise they would recombine to a neutral gas due to cooling by contact with wall material, which is on ambient temperature and thus far lower than the temperatures needed for ionization. In fusion plasmas, this situation is extreme as the center of the plasma has a temperature in the range of 10 keV, while the wall of the experiment is up to six orders of magnitudes colder. This requires a huge energy input and, as a result, strong pressure and temperature gradients are created. These are typical features of a system far from thermodynamic equilibrium. Although plasma physicists sometimes forget this non-equilibrium characteristics in their daily work, since they are concerned with methods of magneto-hydrodynamic (MHD) equilibrium or local thermodynamic equilibrium, the plasma is indeed a wonderful non-linear system exhibiting the same fascinating features as found in other fields of non-equilibrium dynamics: pattern formation [26], wave dynamics [27] and turbulence [28] as found in neutral fluids; zonal flow formation as in the earth's atmosphere [29], on planets [30] or in the ocean [31]; phase transitions as in many different physical systems [32]; limit-cycle oscillations as in biology [33] and economy [34]. Systems, which give rise to such phenomena, are sometimes also called dissipative systems or emergent systems and are classical examples of self-organization.

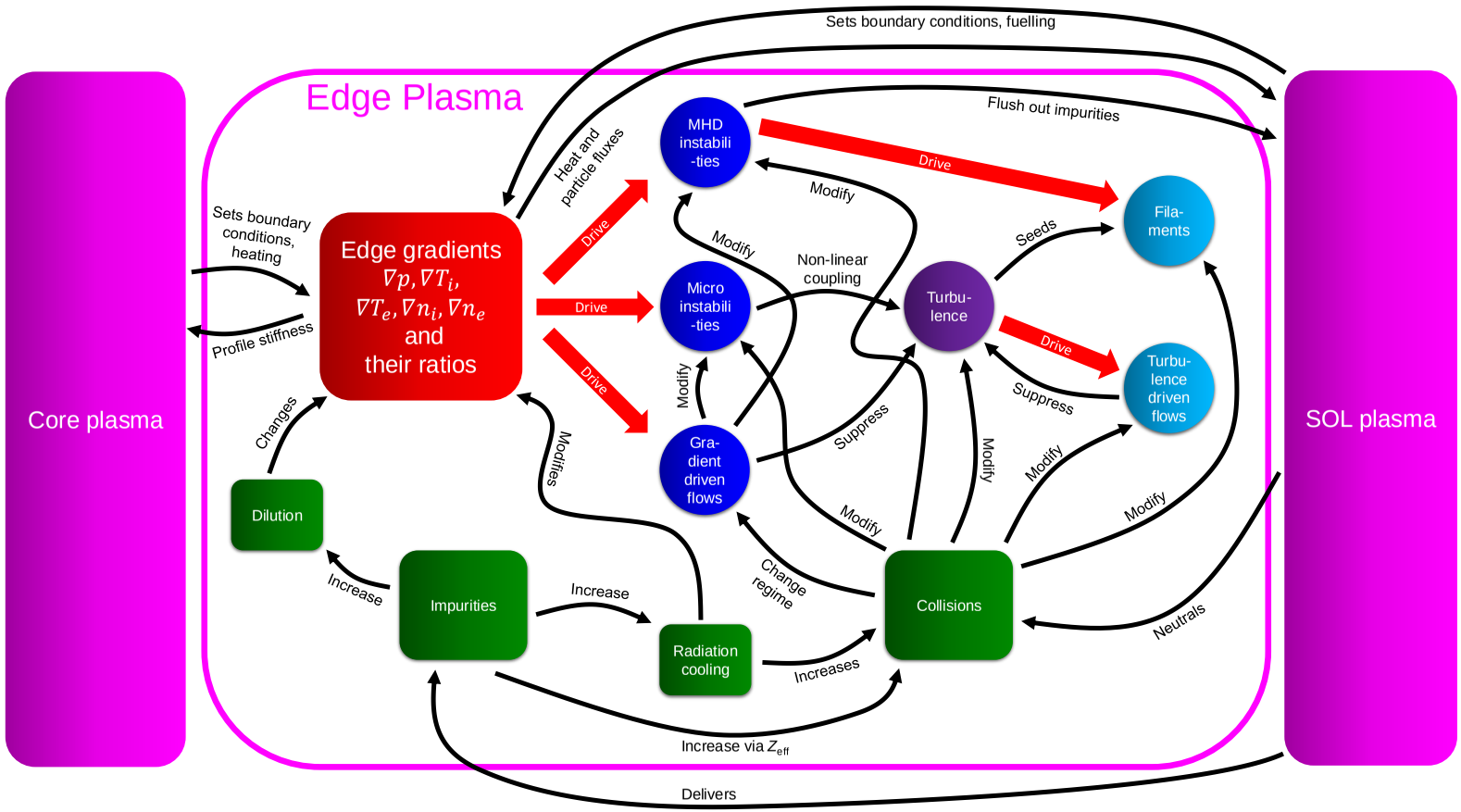

Figure 1.3: *Main players and interdependences at the plasma edge. A central role play the edge gradients and their respective ratios. They drive the main instabilities and flows at the edge, which generate the various edge phenomena. Non-linear effects, collisions and impurities determine, which of the manifold dynamics dominates. The heating in the core plasma on the one side and the fuelling as well as the impurity seeding from the SOL on the other side determine the properties at the edge plasma. But the plasma edge likewise can impact the dynamics in the core and SOL plasma.*

A central role play the strong gradients at the plasma edge. This is shown in figure 1.3. They provide the drive of macroscopic MHD instabilities [22], but likewise for micro instabilities [35]. Most of the plasma equations contain non-linearities[5], consequently, these non-linear processes lead to fully developed turbulence and to non-linear coupling of MHD modes, so that energy is transferred to a broader spectrum of modes. The same gradients, which drive the micro and MHD instabilities, can also generate self-organized flows (diamagnetic flows, see equation A.8 in Appendix A, and neoclassical flows [36, 37]), which can reduce the growth of MHD modes or turbulence. Flows generated by turbulent processes, likewise reduce growth rates and saturation levels of turbulence [38].

MHD instabilities and turbulence can drive and seed filaments [39] in the SOL. All the above mentioned processes are modified by the presence of impurities and collisions. The core plasma mainly provides the heat and particle fluxes from the inside impacting the gradients in the edge plasma, while the SOL delivers neutrals and impurities for the edge plasma. There are back reactions from the edge to the core e.g. via profile stiffness [23], and from the edge to the SOL via heat fluxes [25], impurity flush out due to transport or MHD instabilities [40].

Overall, it is clear from the schematic shown in figure 1.3, that the dynamics in the edge is complicated and multifaceted. However, despite these complicated interactions at the edge, the plasma arrives at a stationary, unique and reproducible state after the external control parameters were fixed and a transition phase has finished. In this stationary state, certain regular patterns can appear, which have a finite spatial extend and a typical temporal characteristic. Mostly these patterns can be experimentally detected as quite large perturbations relative to the background plasma or the surrounding. Since these resulting features sometimes are stationary in time and only consist of a single (e.g. radial) perturbation or excursion, we prefer to term them "structures", which is in our view the most appropriate umbrella term for the experimentally observable features connected to a specific phenomenon under discussion. Not all of the presented structures result from non-linear interactions or coupled dynamics in a strict sense as typical for other non-equilibrium dynamical systems. Nevertheless, all of them share that the structure formation takes place due to self-organization, i.e. without explicit external steering.

This thesis tries to categorize the various edge structures and its forma-

[5] In a fluid description of the plasma, the most prominent non-linear terms are contained in the convective derivatives of the continuity equation and of the equation of motion. Together with the usually low viscosity of the plasma and the strong drive due to the gradients, developed states of plasma turbulence are achieved.

tion conditions. The role of the structures in a future tokamak reactor is discussed and a comprehensive compilation of plasma edge phenomena regularly observed at several tokamak experiments worldwide is provided. This is done in the following pages in chapter 2. In addition, this thesis expands on some of the most relevant phenomena in more detail, for which the present state of research is presented. This part starts with chapter 3 about SOL filaments. Then, the present status of experiments and a heuristic picture of the transition into a self-organized plasma state of high confinement is presented in chapter 4, followed by an introduction into oscillatory structures at the plasma edge in chapter 5. Chapter 6 can be considered as a kind of outlook to a sophisticated edge plasma diagnostics, the so called imaging heavy ion beam probe, i-HIBP, which could potentially improve our understanding of several edge phenomena due to its great spatial and temporal resolution. In the last part, chapter 7, the main conclusions of this thesis are summarized.

Chapter 2

Structures at the Plasma Edge

As described above, the complicated interplay of various elements at the edge (see figure 1.3) generates a zoo of experimentally observed structures of different temporal and spatial scales. For the classification in categories, we would ideally sort them by the type of gradient drive or other main causing factors. This would allow to relate each specific phenomenon to a certain type of theory. However, in most of the cases it is impossible to identify the main causes of the observed structure, and only operational recipes of macroscopic control parameters exist in order to reproduce a certain phenomenon. Another approach would be to categorize the different edge structures in terms of the measurement quantity (e.g. density and its fluctuation), in which it appears predominantly. This is, however, likewise doomed to fail, since most of the fluctuations caused by a certain phenomenon can be measured in more than one, typically all available measurement quantities like density, temperature, magnetic field, and electrostatic potential.

Therefore, we choose a very rough approach focusing on the main measurable characteristic of the respective phenomenon exhibiting one or more structures at the edge, which could fall in one of the following category:

a) Self-generated flows, usually flows in the direction perpendicular to the magnetic field.

b) Self-generated electric currents.

c) Spontaneous phase transitions into improved confinement states.

d) Filaments, i.e. tube like density perturbations extended along magnetic field lines.

e) Temporal structures, i.e. regular oscillations or wobbling between two bi-stable states.

There are phenomena, which could be sorted into more than one of these categories, since they exhibit several types of structures. For example, the transition into the high confinement regime (H-mode, see section 2.3.1) is accompanied by a strong edge flow structure, the formation of a pedestal including a strong edge current density and the appearance of filaments, so called edge localized modes (ELMs)). Thus, it could fall in a), b) or d). But its main characteristic, which distinguishes it from other phenomena, is the spontaneous and fast transition into a state of reduced transport, so that c) is the most appropriate category for the transition into H-mode.

The structures discussed below are only a selection, and even more phenomena have been described in literature. But the following structures are observed at least at two different tokamaks, and can be considered as confirmed and thus reliably observed phenomena at the plasma edge. The main properties of the structures are marked in **bold** letters.

2.1 Self-Generated Flows

2.1.1 Equilibrium Flows

It can be shown by means of the two-fluid description of a plasma [41], that the flows in a plasma characterized by two fluid velocities, one for the ions $\mathbf{u}_\mathrm{i}$ and one for the electrons $\mathbf{u}_\mathrm{e}$, are related to the magnetic field $\mathbf{B}$ and electric field $\mathbf{E}$ according to the equation of motion

$$\rho_\mathrm{m}\left(\frac{\partial \mathbf{u}}{\partial t} + (\mathbf{u}\cdot\nabla)\mathbf{u}\right) = -\nabla p + \rho\mathbf{E} + \rho\mathbf{u}\times\mathbf{B} \tag{2.1}$$

with mass density $\rho_\mathrm{m} = mn$ and charge density $\rho = qn$, pressure p and number density n. Here, $\mathbf{u}$ is a placeholder for ion flow velocity $\mathbf{u}_\mathrm{i}$ and electron flow velocity $\mathbf{u}_\mathrm{e}$, respectively, and p is a placeholder for the ion pressure p_i and the electron pressure p_e, respectively. Thus, there are two equations of the form 2.1, one for electrons and one for ions.

We neglect the left-hand side of equation 2.1, since we are interested in stationary cases (first term vanishes) and small flow amplitudes (second term vanishes) only, yielding the stationary equation of motion

$$\mathbf{E} = -\mathbf{u}\times\mathbf{B} + \frac{1}{\rho}\nabla p. \tag{2.2}$$

Usually, there are neither stationary pressure gradients nor electric fields present *parallel* to the magnetic field, so that the only relevant dynamics

takes place in *perpendicular* direction [6], i.e.

$$\mathbf{u}_\perp = -\frac{\nabla p \times \mathbf{B}}{\rho B^2} + \frac{\mathbf{E} \times \mathbf{B}}{B^2} \tag{2.3}$$

with perpendicular flow velocity $\mathbf{u}_\perp$. Again, there are two equations of the form 2.3, one for electrons and one for ions. We recognize the fluid drifts as described in Appendix A. Thus, a pressure gradient and an electric field give rise to plasmas flows.

While the pressure gradient is naturally given in a tokamak plasma and can be manipulated by fuelling and heating of the plasma, the electric field is not that easy to manipulate. The radial component of equation 2.2, i.e. the relevant component for the perpendicular flows, reads

$$E_\mathrm{r} = \frac{\nabla_\mathrm{r} p}{\rho} - u_\theta B_\phi + u_\phi B_\theta \tag{2.4}$$

with the radial component of the electric field E_r, the pressure gradient in radial direction $\nabla_\mathrm{r} p$, poloidal and toroidal components of the velocity, u_θ and u_ϕ, and poloidal and toroidal components of the magnetic field, B_θ and B_ϕ, respectively.[1] For each species, i.e. for electrons, main ions as well as for impurities, a separate equation of the form 2.4 exists.

This equation is sometimes interpreted as a generation equation of the electric field. But this is not the case as can be demonstrated, when an ambipolarity condition is employed, i.e. a balance of radial flows [37], to clarify the causalities of electric field generation. It can be shown, that the inclusion of neutral friction and poloidal viscosity deliver analytical expressions for E_r. Thus, it is the ambipolarity condition together with the *radial* drift due to poloidal forces, which determine E_r, and as a consequence, the poloidal and toroidal flows arrange according to equation 2.4. The only remaining free parameter in this approach is then the parallel component of the flow, $u_{||}$, which is at the outboard midplane of a tokamak very similar (but not identical!) to the toroidal velocity u_ϕ and both velocities are typically relatively small at the edge, especially when multiplied with the comparably small component B_θ as in equation 2.4.

As a first approximation, which will be refined in the following sections, and assuming a negligible toroidal velocity, i.e. $u_{\phi,i} = u_{\phi,e} = 0$, we find that the following relations hold for a hydrogen plasma, i.e. $\rho_\mathrm{i} = +en$ and

[1] As introduced in figure 1.1, the poloidal direction indicated by the coordinate θ is pointing to the bottom at the outboard midplane. The toroidal direction indicated by the coordinate ϕ points into counter-clockwise direction when the torus is viewed from above.

$\rho_e = -en$ assuming the same densities for all species $n = n_i = n_e$, at the edge:

$$u_{\theta,i} = +\frac{\nabla_r p_i}{enB_\phi} - \frac{E_r}{B_\phi}, \tag{2.5}$$

$$u_{\theta,e} = -\frac{\nabla_r p_e}{enB_\phi} - \frac{E_r}{B_\phi}. \tag{2.6}$$

This means, that the plasma at the edge spins in poloidal direction with the (yet undetermined) $E \times B$ velocity, modified by the diamagnetic flow of the respective species. The difference between electron and ion velocity is $u_{\theta,i} - u_{\theta,e} = 2\frac{\nabla_r p_i}{enB_\phi}$, i.e. twice the diamagnetic flow of the ions (if $\nabla_r p_i = \nabla_r p_e$ is assumed).

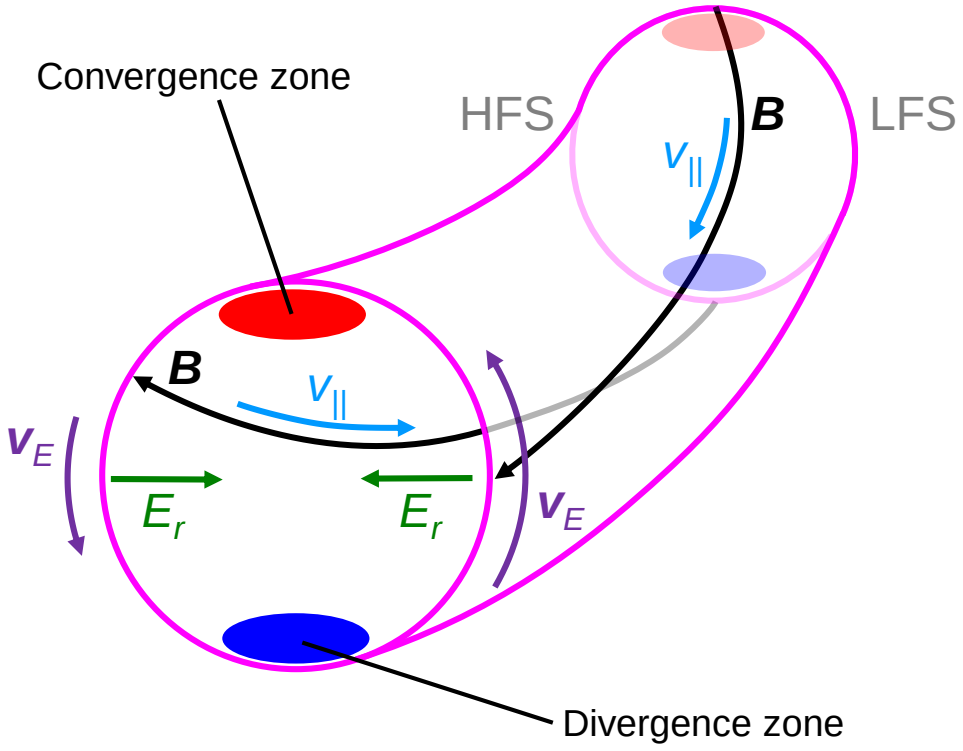

Figure 2.1: *Schematic picture of the equilibrium flows in a toroidal segment of a tokamak. The radial electric field according to equation 2.4 gives rise to a perpendicular mass flow due to the $E \times B$ drift $\mathbf{v}_E$. The magnitude of this drift is larger on the LFS than on the HFS due to its magnetic field dependence (see formula A.2). Therefore, the plasma flows converge at the top. This convergence is balanced by flows parallel to the magnetic field line, $v_{||}$, the so called Pfirsch-Schlüter flows.*

Due to the $E \times B$ drift (see equation A.2), the radial electric field (of yet undetermined origin) generates a **flow perpendicular to the magnetic field** lines, which shuffles mass poloidally from the LFS to the HFS. This perpendicular flow, however, is stronger on the LFS than on the HFS due to its inverse dependence on the magnetic field. In order to keep the flow divergence free, the convergence caused by the perpendicular flows is balanced by **parallel flows along the magnetic field lines, the so called Pfirsch-Schlüter flows**.

This equilibrium flow pattern of poloidal flows, balanced by parallel compensation flows, is the first kind of edge structure of interest. The poloidal and parallel flows are self-organized by the plasma and always present. For a few of the following phenomena, they play an essential role.

2.1.2 Neoclassical Flows

The radial electric field in the plasma is crucial for the edge flows, but up to now it was not discussed how it is determined. As mentioned above, neutral friction or any kind of poloidal viscosity would lead to radial forces, so that E_r is well defined due to ambipolarity apart from a relatively small contribution of the parallel velocity [37]. The most relevant effects, which determine the poloidal flows in equation 2.4, can be derived from neoclassical theory [36, 42]. Neoclassical effects can enter here via an effective poloidal viscosity [37], or the poloidal flow can directly be expressed as

$$u_{\theta,\mathrm{i}} = \frac{\alpha_\mathrm{neo}}{eB_\phi} \nabla_\mathrm{r} T_\mathrm{i}, \tag{2.7}$$

with a collisionality dependent prefactor α_neo, which has to be estimated by complicated but analytical formulas [36] or calculated with more complex numerical codes [43, 44]. With this neoclassical input the radial force balance 2.4 for the **neoclassical radial electric field** reads [45]

$$E_\mathrm{r,neo} = \frac{\nabla_\mathrm{r} p_\mathrm{i}}{e n_\mathrm{i}} - \frac{\alpha_\mathrm{neo}}{e} \nabla_\mathrm{r} T_\mathrm{i} + \frac{B B_\theta}{B_\phi} \left\langle u_{||,i} \right\rangle . \tag{2.8}$$

The last term in equation 2.4 reappears here in equation 2.8, but expressed in terms of the flux surface averaged parallel ion velocity $\left\langle u_{||,i} \right\rangle$. As before, this last term is small compared to the other terms, and in several studies at ASDEX Upgrade (AUG), it has been shown, that the first two terms on the right hand side of equation 2.8 are sufficient to describe the measured radial electric field sufficiently well close to confinement transitions (e.g. L-H transitions, see section 2.3.2) [46, 47]. For H-mode discharges or in dithering

phases (both plasma scenarios will be discussed below) at AUG, it was shown that even only the first term on the right hand side, the so called diamagnetic term,

$$E_{\mathrm{r,dia}} = \frac{\nabla_{\mathrm{r}} p_{\mathrm{i}}}{e n_{\mathrm{i}}}, \tag{2.9}$$

of the main ions is sufficient to describe the measured radial electric field [48, 49, 50, 51]. An example is shown in figure 2.2.

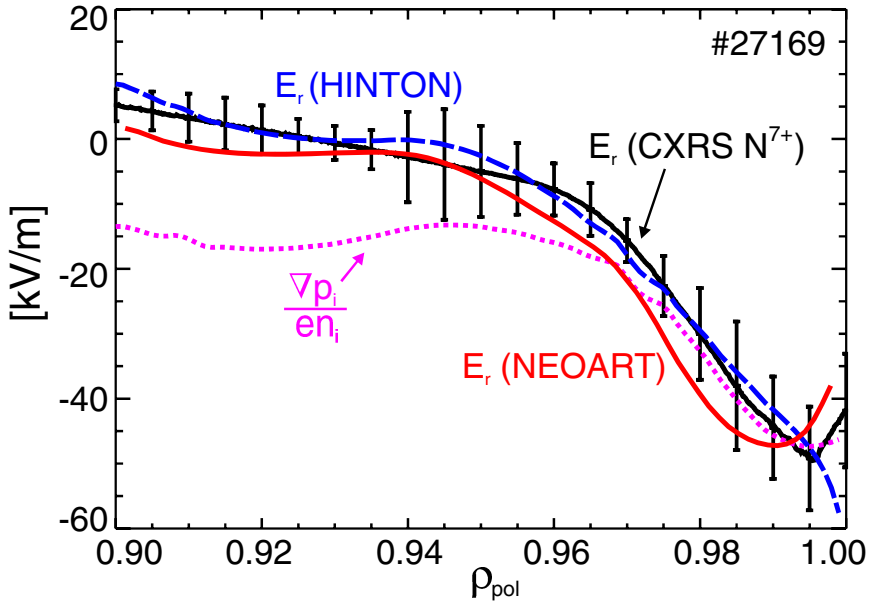

Figure 2.2: *Radial profile of the radial electric field at AUG (reprinted from [49]) in H-mode. The radial electric field measured with charge-exchange recombination spectroscopy (CXRS) on N^{7+} (black) agrees well with the neoclassical formula (blue) [36] and the output of the neoclassical code NEOART [43] (red). For the outermost region, the simple approximation $E_{\mathrm{r,dia}} = \frac{\nabla_{\mathrm{r}} p_{\mathrm{i}}}{e n_{\mathrm{i}}}$ applies.*

Consequently, the ions are approximately at rest, $u_{\theta,\mathrm{i}} \approx 0$, while the electrons spin poloidally with roughly twice the diamagnetic flow velocity $u_{\theta,\mathrm{e}} \approx -\frac{2\nabla_{\mathrm{r}} p_{\mathrm{e}}}{e n B_{\phi}}$ into electron diamagnetic direction according to equations 2.5 and 2.6, when equation 2.9 is inserted there. These conditions, i.e. ions at rest and electrons at twice the electron diamagnetic velocity, are the typical approximate conditions for the tokamak plasma edge. It was reported from other tokamaks that the diamagnetic term of the main ions is at least the dominant contribution to the radial magnetic field [52, 53], so that it can be assumed, that similar conditions as reported from AUG hold likewise for other tokamaks.

Although the toroidal rotation is small, as mentioned already, torque input by neutral beam injection (NBI) can change the radial electric field via the parallel velocity term (last term in equation 2.8) as the main effect [54]. This possibility of external control of E_r can be used to manipulate some of the below mentioned structure formations (see section 2.3.2).

2.1.3 Low Frequency Zonal Flows

The tokamak edge plasma is in practically all conditions in a turbulent state. This is illustrated in figure 2.3, which depicts the turbulent ion density and its fluctuations on the left resulting from the gyrokinetic turbulence code GENE-X [55]. It is not a question, whether the edge is turbulent or not, but a question of what type of turbulence dominates and how strong are the fluctuations. Turbulent transport is in the most cases undesired for fusion, since its increased levels of heat and particle transport leads to a degradation of confinement making it more difficult to achieve the ignition condition (see equation 1.3).

Inside the bath of rather randomly distributed turbulent fluctuations at the edge, which is always present, spontaneous order on larger scales can appear. More specifically, the turbulent fluctuations itself can drive a flow structure that is **poloidally and toroidally homogeneous**, but radially structured and varying on the spatial scale of tens of Larmor radii $\rho_{\mathrm{L,i}} = \sqrt{2m_\mathrm{i}T_\mathrm{i}}/(eB)$ [56] with ion mass m_i and ion temperature T_i. These types of flow patterns live on **time scales of a few 100 µs** and are called low frequency zonal flows or simply zonal flows (ZFs). These zonal structures are visible as ring-like patterns in the electrostatic potential fluctuations on the right of figure 2.3. Their radial gradient of the potential is related to a radial electric field via $\nabla_\mathrm{r}\phi = -\mathbf{E}_\mathrm{r}$ giving rise to perpendicular flows due to the $E \times B$ drift.

ZFs are an important component of the turbulent system [38], since they are able to absorb energy from other turbulent scales, and can saturate turbulence levels, especially in pure ion-temperature gradient turbulence [57, 58, 59]. This way, the undesired turbulent transport is relatively low and the confinement of the plasma improved, since part of the turbulent **energy is deposited in innocuous ZFs**, which cannot produce radial transport due to their toroidally and poloidally homogeneous structure corresponding to a toroidal mode number n = 0 and a poloidal mode number m = 0. The $E \times B$ flow components, and hence turbulent transport, cannot point into radial direction in such a case.

By means of a dimension analysis it can be shown, that turbulence in two-dimensional systems, as it is the case for a tokamak, tends to transfer

energy from small scales to large scales [60, 61] in a so called inverse cascade. The ZFs are the result of such an energy cascade representing the largest possible scale. As it was shown in dedicated experiments [62, 63], the energy transfer is non-local, i.e. it does not take place between adjacent scales, but comparably small scales transfer their energy to the largest scales in the system.

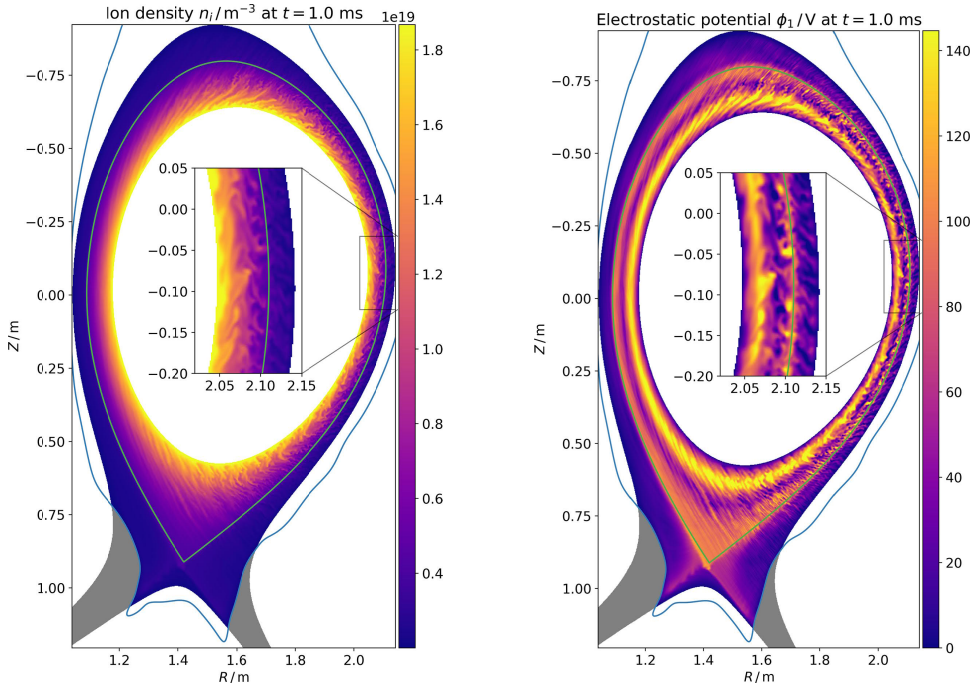

Figure 2.3: *Turbulent ion density fluctuations (left) and electrostatic potential fluctuations (right) at the edge of a divertered tokamak simulated with the gyrokinetic code GENE-X (reprinted from [55]). The electrostatic potential fluctuations exhibit radial stripes of poloidally symmetric structures, which are not visible in the ion density fluctuations. These are the low frequency zonal flows.*

Mathematically, it can be shown that in the simplest form the ZF interpreted as an average poloidal flow, $\langle u_\theta \rangle$, is driven by the Reynolds stress force i.e. by the radial derivative of the Reynolds stress (RS) $\langle \tilde{u}_\mathrm{r} \tilde{u}_\theta \rangle$ and damped by a (not furter specified) viscosity μ_V [64] according to

$$\frac{\partial}{\partial t} \langle u_\theta \rangle = -\frac{\partial}{\partial r} \langle \tilde{u}_\mathrm{r} \tilde{u}_\theta \rangle - \mu_\mathrm{V} \frac{\partial^2}{\partial r^2} \langle u_\theta \rangle \,. \tag{2.10}$$

They RS follows from a Reynolds decomposition [28] of the relevant quantities, which are split into a mean value indicated by the brackets $\langle . \rangle$ and a

fluctuating part indicated by a tilde above the symbol, and can be considered as a negative viscosity. Averaging is understood mathematically as an ensemble average, thus it can represent a time average or a spatial average e.g. along the toroidal coordinate (in this case it would represent a zonal average). In this formulation, we consider the radial and poloidal components of the velocity fluctuations $\tilde{u}_\mathrm{r}$ and $\tilde{u}_\theta$, which must correlate with each other in order to produce a finite RS. Similar driving forces exists likewise for other components of the flow field [65]. The RS force can be inserted into the radial force balance equation 2.4 [37] revealing that the RS is an additional source for the radial electric field.

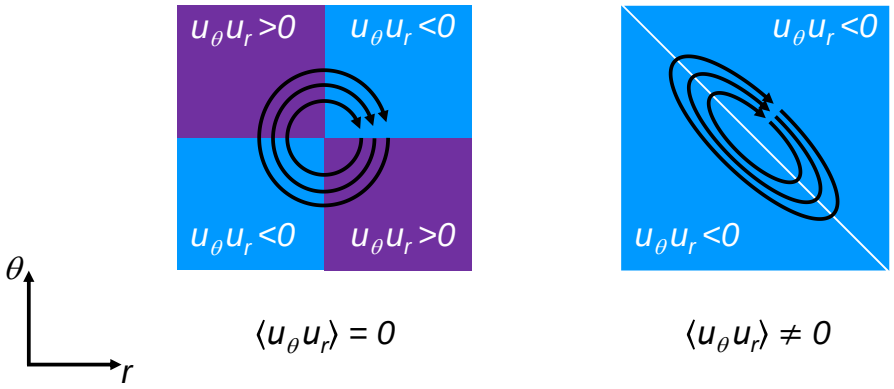

Figure 2.4: *Reynolds stress (RS) in a circular (left) and a tilted (right) eddy. The poloidal direction points to the top, thus, velocity components visualized as stream lines of the eddy (black) pointing to the bottom are counted negative. Likewise, velocity components pointing to the left are negative as well (all others positive). The products of velocity components in each quadrant of the circular eddy are finite, but cancel each other, so that the total RS is zero. A tilted eddy, however, has a finite value of RS, since the dominating velocity components on long edges deliver a negative RS.*

Although mathematically simple, it is not easy to understand the physical mechanism of how the **ZF is driven by the RS force**. A qualitative picture is given as follows. In a simplified picture, the RS quantifies the correlated appearance of radial and poloidal flows, as it appears in a turbulent eddy. As shown in figure 2.4, left, a circular eddy has a total RS equal to zero. The local RS according to the product of the local velocity components u_r and u_θ is finite in each quadrant, but cancel each other when all four quadrants are added up. When the eddy is tilted, however, a finite RS can be assigned to it as shown in figure 2.4, right. The upper right part of the velocity components as well as the lower left part of the eddy exhibit a negative product of the

velocity components, while the other components along the short edges are considered to be too small to compensate the RS at the long edges.

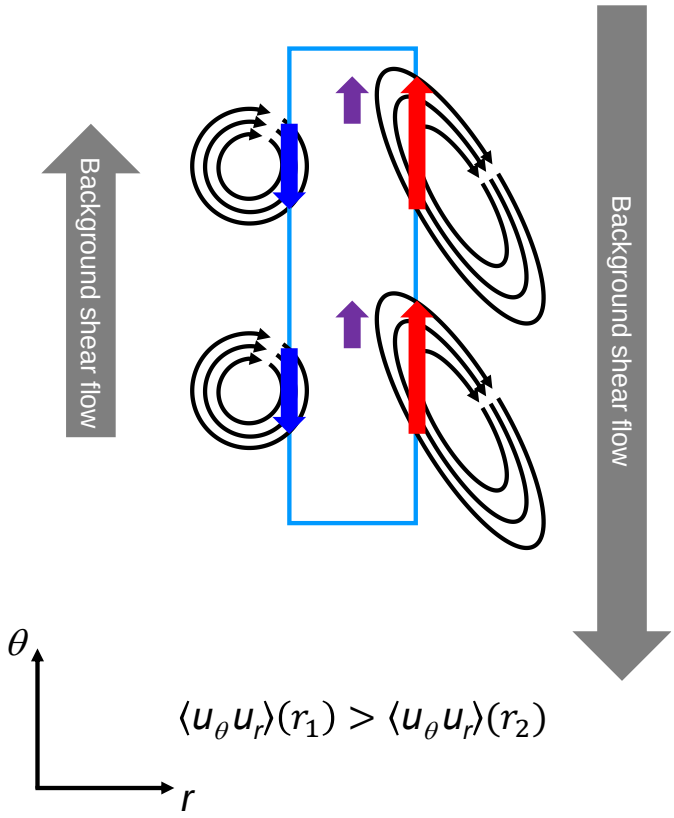

Figure 2.5: *Poloidal flow generation by the Reynolds stress force. A background shear flow (grey arrows) is stronger on the right hand side. Therefore, the eddies on the right hand side at r_2 (radially further outwards) are more tilted than the eddies on the left at r_1. For simplicity the eddies on the left are assumed to be circular, hence, their RS is zero. As discussed in figure 2.4, the RS of the tilted eddies is negative corresponding to a finite RS force pointing in poloidal direction (top) according to equation 2.10. This is reflected in a net velocity component (purple arrow), when all local velocity components in the volume between adjacent radial eddies (light blue box) are added up.*

If adjacent eddies exhibit different values of RS corresponding to a different tilt, a net flow appears at the interface layer between two eddies, when the local velocity components as depicted in 2.5 are considered. Thus, turbulent eddies can create a net flow in poloidal direction when the RS is not constant along the radius. The created net flow points into the same direction as the seed shear flow, hence amplifying the initial shear flow. This

flow amplification is accompanied by extraction of energy from the (relatively small) turbulent eddies to the background shear flow. The ZF amplification is either stopped when the energy of the turbulence is sufficiently depleted, or saturated by other damping mechanisms like the Kelvin-Helmholtz instability [66], collisions [67] or by the geodesic transfer effect [68, 69, 70] among others [38]. In the first case, predator-prey cycles can appear as it will be discussed in section 2.5.3. In the other cases, the flow will saturate on a more or less constant level.

The finite radial wavelength of ZFs is not unique, as can be shown due to its connection to pattern formation [71]. The same holds for the radial position of ZFs, which is determined randomly and changes on time scales much larger than turbulent time scales [38]. For fusion experiments, the life time of ZFs is in the order of hundreds of micro seconds, thus two orders of magnitude larger than typical turbulence time scales in the order of one micro second. Hence, they are called low frequency zonal flows. This way they are also distinguished from geodesic acoustic modes (see section 2.1.4), which oscillate with frequencies between turbulent and ZF time scales.

ZFs were studied experimentally on different tokamaks [72, 73, 74], but likewise appear in stellarators [75, 63, 62, 76, 77, 78], where its dependence on collisionality [79] and background flow shear was studied in detail [80]. They appear in the core and at the edge of the plasma. The experimental data, which is closest to the qualitative picture of ZFs as it is visible in turbulence simulation, is from JET [81]. Unfortunately, such clear experimental signatures were not confirmed at other tokamaks, and the detection and visualization of ZFs is still an active field of research in plasma physics.

ZFs are much clearer and easier to detect in other fields of physics: ZF-like structures appear on very large scales on planets [30], in the earth's atmosphere [29] and in the sea [31], and thus contribute to climate, ocean and weather conditions on planets. Laboratory experiments likewise contributed to the understanding of ZF generation by means of sophisticated setups [82].

2.1.4 Geodesic Acoustic Modes

The geodesic acoustic mode (GAM) is very similar to the low frequency ZFs as described above: it can be excited by the same mechanism as low frequency ZFs, its essential structure is likewise a poloidal flow and it interacts energetically with turbulence and flow shear as described above. However, the flow at the top of the plasma is too strong to be balanced by parallel flows as depicted in figure 2.1, so that compression takes place giving rise to a restoring force pushing the flow back to the midplane. Therefore, GAMs are not steady or wobbling with low frequency, but **oscillate with a very**

characteristic and coherent frequency, the so called GAM frequency [83, 84]

$$\omega_{\mathrm{GAM}}^2 = \frac{2c_{\mathrm{s,i}}^2}{R^2}\left(1 + \frac{1}{2q_{\mathrm{s}}^2}\right) \tag{2.11}$$

with major plasma radius R, safety factor q_{s}, and the ion sound speed $c_{\mathrm{s,i}} = \sqrt{\gamma\left(T_{\mathrm{e}} + T_{\mathrm{i}}\right)/m_{\mathrm{i}}}$ with the adiabatic index γ. Typical GAM frequencies are between 5 kHz and 20 kHz at the tokamak edge.

The generation mechanisma and spatial structure of the GAM is shown in figure 2.6. As for the low frequency ZF, the cycle starts with an **m = 0, n = 0 potential perturbation** giving rise to a perpendicular $E \times B$ flow, which is compressed at the top of the plasma due to the magnetic field dependence of $\mathbf{v}_{\mathrm{E}}$. In case of the GAM, the flow is so strong, that the parallel flows cannot balance the convergence, and, consequently, the top of the plasma is compressed. This leads to a positive pressure perturbation at the top and a depletion, i.e. a negative pressure perturbation at the bottom of the plasma. Hence, the GAM is characterized by an **m = 1, n = 0 pressure perturbation**. In this situation, diamagnetic currents (see formula in Appendix A) form around the pressure perturbations. These currents generate a pattern of **magnetic field perturbations, exhibiting a m = 2, n = 0** structure.

The compression at the top of the plasma gives rise to a restoring force $\mathbf{F}_{\mathrm{r}}$, which pushes the flow back to the midplane decreasing the pressure perturbation at the top. In this phase of the GAM cycle, all flows and currents invert the directions. When the former pressure perturbation is depleted, the cycle starts from the beginning (after a possible overshoot into the other direction).

The GAM is called "geodesic" since a finite geodesic curvature is intrinsically related to a divergence of flows [85]. This leads to a compression and, hence, a dynamics similar to acoustic waves. A purely acoustic wave or sound wave along the magnetic field line would follow the dispersion relation $\omega_{\mathrm{SW}} = c_{\mathrm{s,i}}/(qR)$, i.e. a wave with speed $c_{\mathrm{s,i}}$ and a parallel wavenumber $k_{||} = 2\pi/(2\pi qR)$ corresponding to a parallel length of the magnetic field line $2\pi qR$. The additional term in the GAM frequency in equation 2.11 indicates that the frequency of the GAM depends additionally on the geodesic curvature, which can be approximated with $1/R$.

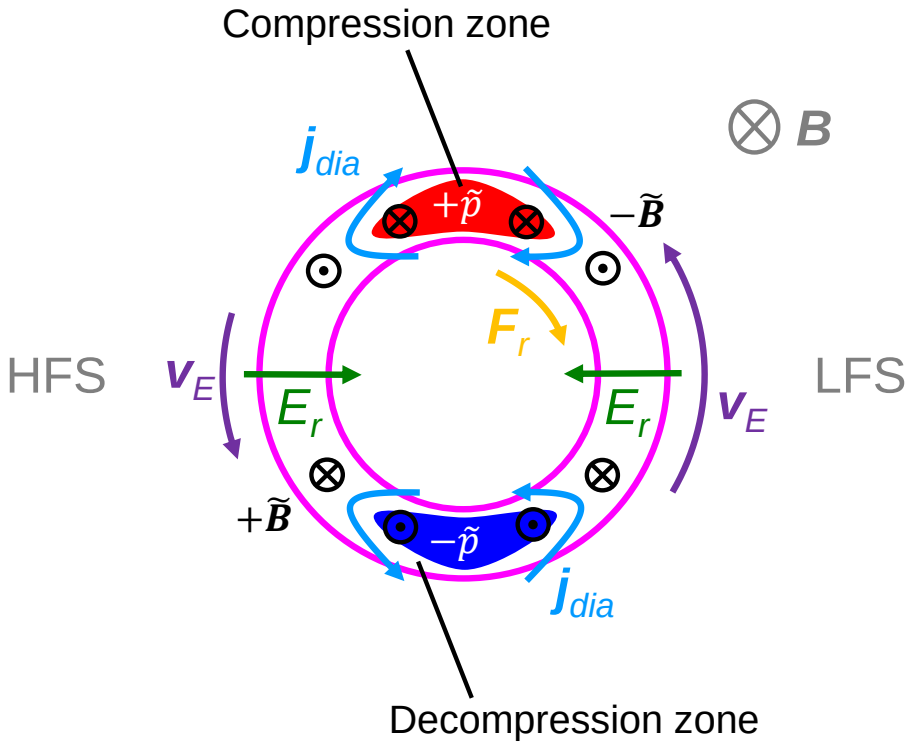

Figure 2.6: *Generation and spatial structure of a GAM. An $m = 0$, $n = 0$ potential perturbation creates a radial electric field E_r giving rise to an $E \times B$ drift $\mathbf{v}_E$. This drift is larger at the outboard side than at the inboard side due to lower magnetic field strength at the outboard side. Consequently the plasma is compressed at the top giving rise to a positive pressure perturbation $+\tilde{p}$. Simultaneously the plasma is decompressed at the bottom, so that an $m = 1$ pressure structure is formed. Due to this, diamagnetic currents $\mathbf{j}_{dia}$ are generated, and the resulting structure of the magnetic field perturbations $\tilde{\mathbf{B}}$ is $m = 2$. All quantities are toroidally symmetric, i.e. the toroidal mode number is $n = 0$. The compressibility of the plasma gives rise to a restoring force $\mathbf{F}_r$, pushing the flow back to the midplane, so that all arrows change directions signs in this schematic. When the initial conditions are reached, the oscillation cycle starts from the beginning.*

When quantiatively compared with experiments, the simple formula 2.11 has to be modified [83]. It depends on the plasma shape (elongation, Shafranov shift, triangularity, etc.) [86]. In addition, it shows dispersion, i.e. it can move radially [87, 88, 89]. Apart from the flow generation by the RS, GAMs can likewise be driven by energetic particles [90, 91]. In this case, they are called EGAMs. GAM oscillations are damped by continuum damping, phase-mixing, collisional damping, finite orbit width effects, Landau damping or toroidal resonance effects [83]. Turbulence driven GAMs (the "natural" ones) appear only at the edge, where the turbulence levels provide a large drive and the damping is low due to the high safety factor q_{s}. EGAMs can exist everywhere in the plasma, when the drive of energetic particles exceeds the damping.

2.1.5 Staircase

Next to the GAM, which can be considered as a kind of oscillating version of the low frequency ZF, the staircases are likewise a special type of ZF structures. They are ordinary low frequency ZFs, but appear in **groups of shear flows distributed along the full radius in a quite regular (i.e. almost equidistant) manner**. Due to this, the radial **pressure profile is flattened at several radial positions resembling a staircase**. This corrugation leads to comparably strong local temperature gradients. An example of a staircase in a flux driven gyrokinetic simulation is shown in figure 2.7.

Between the stairs, i.e. between two shear flow locations, the turbulent transport takes places as avalanches and is much higher than at the locations of the shear flow, where turbulence is partially reduced acting as a micro barrier. The step size between two corrugations is in the order of $10\rho_{\mathrm{L,i}}$. The locations of the shear flows moves slowly over time in radial direction and sometimes, a single shear flow barrier splits up into two new branches. But in general, the time scale is the same as for "normal" zonal flows (i.e. hundreds of microseconds).

The staircase was first found in gyrokinetic simulations [92, 93]. As a necessary condition for their appearance, the simulation has to be flux driven and only marginally stable, i.e. close to the linear threshold of the underlying instability. After the prediction and characterization of the staircases with numerical simulations, they were discovered in two different fusion devices [94, 95, 96]. This an exceptional situation, since normally plasma phenomena are first observed experimentally, and only afterwards explained by theory (if at all).

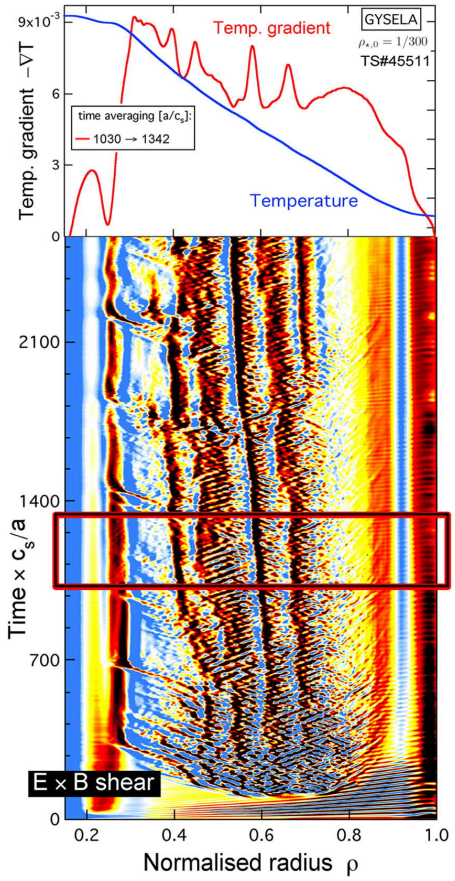

Figure 2.7: *Staircase in a flux driven simulation (reprinted from [93]). The $E \times B$ shear (bottom) exhibits clear vertical stripes of high shear, which act as transport barriers. Between the shear layers, avalanche-like transport takes places visible as comb-like structures between two shear layers in this spatio-temporal representation. As a consequence of the local shear suppression, the temperature gradient (top) is corrugated and highest in regions of high shear.*

2.2 Self-Generated Electric Currents

2.2.1 Neoclassical Edge Current Density

If no external current drive apart from the ohmically driven loop voltage is applied, the flux surface averaged parallel current density in a tokamak plasma is given by [97, 98]

$$\langle j \rangle = \sigma_{\text{neo}} \langle E_{||} \rangle - R\Big[\mathcal{L}_{31} p \partial_\psi \ln p + \mathcal{L}_{32} p_{\text{e}} \partial_\psi \ln T_{\text{e}} + \mathcal{L}_{34} \tilde{\alpha} p_{\text{i}} \partial_\psi \ln T_{\text{i}}\Big] \quad (2.12)$$

with σ_{neo} the neoclassical conductivity, $E_{||}$ the parallel electric field, R the major radius, p the total pressure, p_{e} the electron pressure, p_{i} the ion pressure, T_{e} the electron temperature, T_{i} the ion temperature, and ∂_{ψ} the derivative with respect to the normalized poloidal flux serving as a flux label, i.e. as a minor radius coordinate. The brackets $\langle . \rangle$ indicate a flux surface average. The prefactors $\mathcal{L}_{31}$, $\mathcal{L}_{32}$, $\mathcal{L}_{34}$, and $\tilde{\alpha}$ are complex integrals in phase space provided by neoclassial theory [97, 98]. They must be calculated with numerical kinetic codes or are sufficiently well determined by analytical expressions based on the output of full kinetic solvers [97, 98, 99]. For the relatively high collisionalities at the plasma edge, the recommended analytical expressions can be found in reference [100].

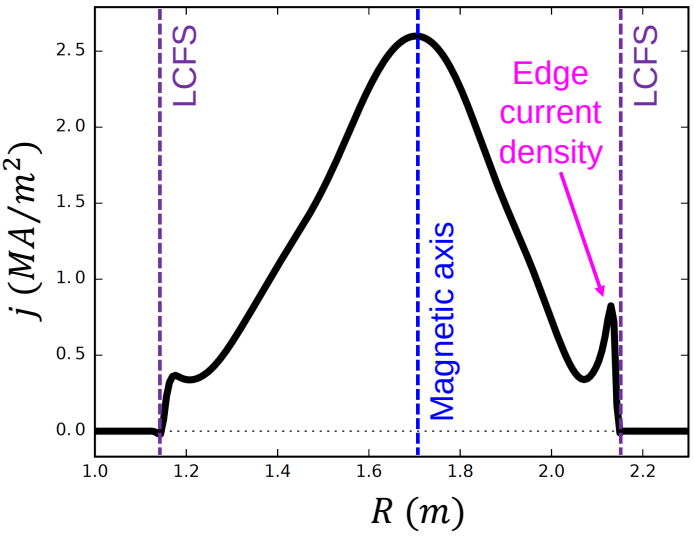

Figure 2.8: *Radial profile of the current density in type-I ELMy H-mode at AUG (#30701 at $t = 3.36$ s). The central peak around the magnetic axis is mainly due to the ohmic current driven by the transformer coil of the tokamak, while the edge current density peak is dominated by the bootstrap current driven by the steep edge gradients.*

The first term of equation 2.12 is the ohmic current inductively driven by the central solenoid. Due to the temperature and collisionality dependence of the conductivity σ_{neo}, it is maximum in the center of the plasma and decreases strongly towards the edge. The second term of equation 2.12 including the brackets is the so called **bootstrap current**. It is a very fascinating effect explained by neoclassical theory (see reference [101] for a nice introduction of the phenomenon): The magnetic field structure of the tokamak gives rise to magnetically trapped particles, which precess toroidally around the torus on

so called banana orbits. The ions precess into the opposite direction to the electrons, and the concomitant kinetic effects generate a net current on the flux surface, which depends on the gradients of the kinetic profiles. Since this self-generated **net current** is directed into the same direction as the (ohmic) plasma current, it is called bootstrap current, i.e. a current amplifying the inductively driven plasma current. For steady-state plasma operation of a tokamak, the bootstrap current is of extraordinary relevance [102].

Due to its **dependence on gradients** (most effectively on the density gradient), the Bootstrap current density is in H-mode typically the dominant current density at the plasma edge [103]. This is shown in figure 2.8 displaying the radial profile of the current density from the HFS to the LFS for an ELMy H-mode in AUG. The **pronounced peak at the LFS edge near the LCFS** is the edge current density. Except for the gradient drive and the magnetic curvature, the edge current density is the third important ingredient determining the MHD stability of the plasma edge. On the one hand, the edge current density can increase the (local) magnetic shear, which acts as a **stabilizing** term for most of the MHD modes and turbulent modes [22, 104, 105]. On the other hand, a high current density **can drive peeling modes** [24, 106]. The local shear, and thus edge current density, might also play a role for the L-H transition physics [107]. In any case, a precise experimental determination of the current density is of great importance for many fields of edge physics.

2.2.2 Pfirsch-Schlüter Currents

Analogously to the neutral equilibrium flows originating from the $E \times B$ drift as discussed in section 2.1.1 (see figure 2.1), a similar mechanism works likewise for the non-neutral diamagnetic flows, which involve perpendicular **diamagnetic currents $\mathbf{j}_{\mathrm{dia}}$** (see formula A.9). The magnetic field dependence of the diamagnetic currents and the fact, that the magnetic field strength in the tokamak is higher at the inboard side than at the outboard side, give rise to a charge accumulation at the top of the plasma. This is balanced by **parallel electric currents**, the Pfirsch-Schlüter currents. They generate (vertical) magnetic field components, $B_{\mathrm{z,PS}}$, being able to **modify the shape and position of magnetic flux surfaces** giving rise to the **Shafranov-shift** [5]. This shift moves inner flux surfaces and the magnetic axis towards the HFS and depends on the pressure-gradient, since steeper gradients drive stronger diamagnetic currents, thus, increasing the Pfirsch-Schlüter currents and, hence, the Shafranov shift. In contrast to the bootstrap currents (see above), the Pfirsch-Schlüter currents do not provide a net toroidal currents due to a **vanishing flux-surface average** of the Pfirsch-Schlüter currents.

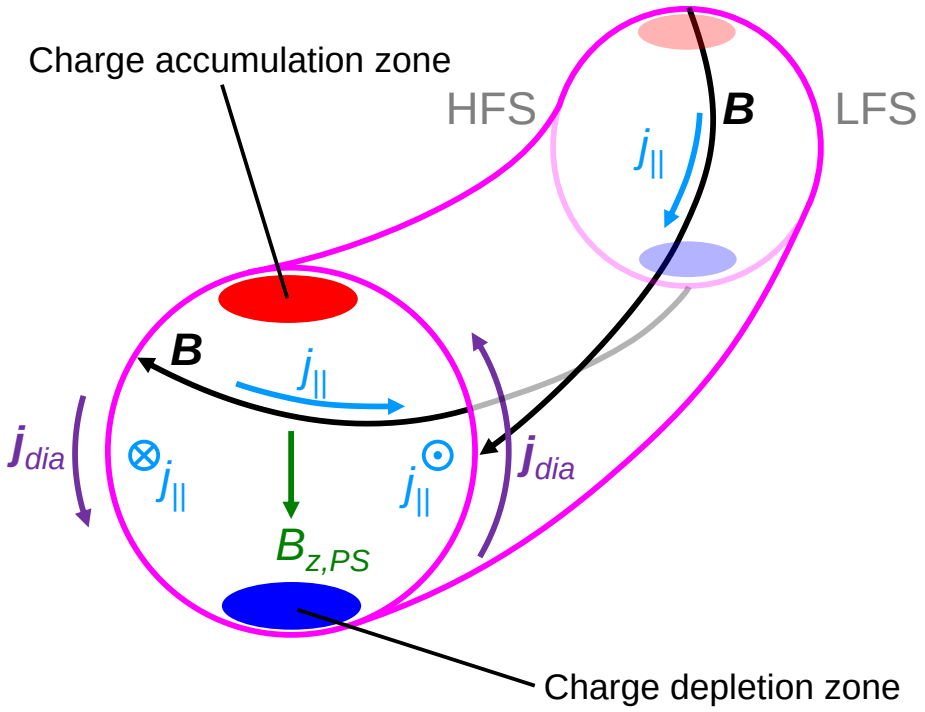

Figure 2.9: *Origin of the Pfirsch-Schlüter currents. Radial pressure gradients give rise to perpendicular diamagnetic currents* $\mathbf{j}_{\mathrm{dia}}$*, which are larger at the HFS than at the LFS due to the magnetic field dependence of the diamagnetic current (see formula A.9). This leads to a charge accumulation at the top of the plasma. The parallel currents,* $j_{||}$*, balancing the charge accumulation are the Pfirsch-Schlüter currents. They generate a z-component of the magnetic field,* $B_{\mathrm{z,PS}}$*, adding up to the existing tokamak magnetic field. This gives rise to the Shafranov-shift, i.e. a displacement of the magnetic axis and the inner flux surfaces to the LFS.*

2.3 Phase Transitions into Improved Confinement States

As other physical systems [32], the edge plasma can transition from one phase into the other, sometimes involving bifurcations, when certain control parameters are changed. The phase boundaries between the different confinement regimes are well defined and reproducible. Before some selected spontaneous transitions and their diagrams are discussed, the most relevant possible regimes are presented.

2.3.1 Confinement regimes

After creating the plasma during the startup phase, when the plasma current is stationary, the plasma does not arrive always in the same type of regime. Depending on the heating power, fuelling, magnetic field configuration, magnetic field strength, plasma current, heating method, wall conditioning, impurity content etc., different types of plasma regimes can be achieved. They differ in macroscopic properties, most notably in terms of confinement quality and ability to accumulate impurities, but all of them likewise show different and very fascinating structures at the edge, which in most of the cases play a central role for the macroscopic property of the regime. The most important regimes with its different confinement properties, are the following:

L-mode

The historically first and **natural tokamak regime**, which is achieved at low power and without any further requirements, is the L-mode. The "L" indicates "low confinement", since it has the lowest confinement compared to other regimes as discussed below. It is a **state of high turbulence without transients** or noteworthy coherent modes. But due to the high turbulence levels, especially at the edge, strong zonal flow activities can be present. Due to this, the neoclassical radial electric field according to equation 2.8 is sometimes not fulfilled possibly due to the influence of the ZFs. GAMs are likewise often visible, and the impurity concentrations are low due to high heat and particle transport levels. The equilibrium flows are always present, but comparably weak due to low power input and hence low gradients, which drive these flows.

H-mode

The H-mode was discovered 1982, when an L-mode in ASDEX plasma was heated with neutral beam injection (NBI) [108, 109, 110], and in later experiments it turned out, that a critical heating power threshold has to be exceeded in order to achieve the H-mode. It is a **regime of increased confinement time** τ_E (typically twice as high as in L-mode), which is why it is called high confinement regime or H-mode.

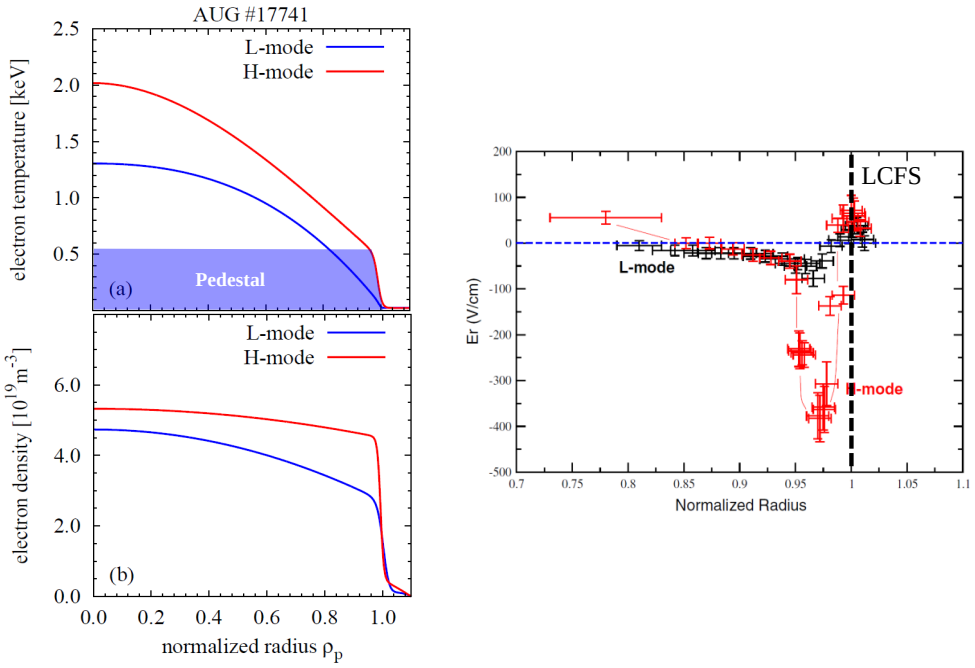

Figure 2.10: *Comparison of L-mode and H-mode. Left: The measured electron temperature (and thus pressure profiles) in H-mode (red) seem to be placed on a pedestal (blue shaded area), when compared with the L-mode profiles (blue). The edge transport barrier in H-mode causes steep gradients at the very edge (adapted from [111]). Right: The radial electric field profiles measured with Doppler reflectometry exhibit a deep E_r well in H mode (red) and reach much stronger flow shear than in L-mode (black) (adapted from [112]).*

The transition from L-mode to H-mode, called the L-H transition, takes place within less than 100 µs, and is therefore much faster than the confinement time in the order of hundreds of milliseconds. After the L-H transition, the heat and particle transport is much lower, so that the density and temperatures strongly rise. This way, **steep gradients** are created at the edge, indicative of an **edge transport barrier** (ETB). Interestingly, the gradients

of the profiles in the core plasma are very similar in H-mode compared to L-mode, and the major part of the pressure increase in H-mode comes from the edge. The H-mode profiles seem to be L-mode profiles, but put on a **pedestal** as depicted in figure 2.10, left. The H-mode is characterized by very **strong** $E \times B$ **shear flows** at the edge generated by the neoclassical electric field or simply by the ion pressure gradient as depicted in figure 2.2. The **fluctuation levels are much smaller** in H-mode than in L-mode, and it is suggested, although not the only possibility, that the strong flow shear in H-mode suppresses the turbulence giving rise to the ETB [113, 114] (see the detailed discussion about L-H transition models in section 2.3.2).

The H-mode is a regime of low turbulence levels and strong (neoclassical) flows and possesses a very good confinement. This makes the H-mode very desirable for a fusion power plant and most of the reactor studies assume that a tokamak reactor operates in H-mode [19]. But the good confinement comes at a price: the strong gradients in H-mode can drive MHD instabilities at the edge. These instabilities appear as strong bursts, which can eject heat, particles and impurities into the SOL. Since these bursts were localized at the edge, they are called **edge localized modes (ELMs)**, and they can appear as different types with different sizes and frequency dependencies on heating power [115, 24]. The ELMs are filament structures and discussed in more detail below (see section 2.4.2). The H-mode with large ELMs, the so called type-I ELMy H-modes, was the predominantly investigated plasma regime in the last decades. Unfortunately, it turned out within the last years, that it probably will not be compatible with a tokamak fusion reactor due to too large heat fluxes onto PFCs provided by ELMs [116].

I-mode

Since ELMs are probably not acceptable for a reactor, it would be desirable to combine the good properties of the L-modes, i.e. **absence of ELMs** and low impurity concentrations, with that of the H-mode, i.e. the good confinement. One possible regime, which fulfills these conditions, is the improved L-mode regime commonly referred to as I-mode nowadays. The I-mode[2] was discovered at AUG [117] and appears, when the access condition for the H-mode (details see below) are hampered [118]. This is normally achieved by choosing the so called unfavorable magnetic configuration, for which the ∇B drift of the ions points *away* from the active X-point. This is a regime rarely operated, since the divertor conditions are usually better in favorable

[2]The "I-mode", short for "improved L-mode", must not be confused with "I-phase", which stands for "intermediate phase". The I-phase exhibits characteristic limit-cycle oscillations and is part of the "normal" H-mode as will be discussed in section 2.5.3.

configuration, i.e. when the ion ∇B drift points *towards* the active X-point.

The I-mode exhibits a **temperature pedestal, but no density pedestal** as shown in figure 2.11, indicating that the heat transport is reduced, but the particle transport stays on L-mode level. In this sense, it is a hybrid confinement regime sharing properties of L-mode and H-mode at the same time. The deepness of the E_r well in I-mode is between the typical values of H-mode and L-mode [48].

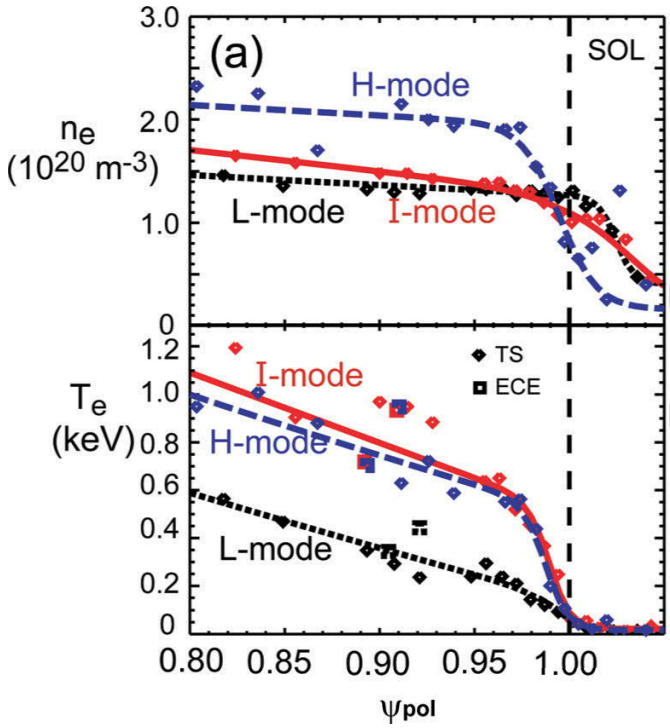

Figure 2.11: *Electron density and temperature profiles in L-mode (black), I-mode (red) and H-mode (blue) measured at Alcator C-mode (reprinted from [119]). The I-mode exhibits relatively low densities as in L-mode, but a temperature pedestal as in H-mode.*

The appearance of a **weakly coherent mode (WCM)** at the edge [119] seems to be strongly connected with the I-mode, so that the detection of the WCM is used as an indicator of the I-mode. The properties of the WCM are discussed in section 2.5.7. As mentioned, large type-I ELMs are absent in I-mode, but at higher heating powers pedestal relaxation events (PREs) can appear, which are burst-like events similarly to ELMs, but with different properties [120] (see section 2.4.3).

Enhanced D-Alpha H-mode

The enhanced D-alpha H-mode (EDA H-mode) [121, 122] is a special type of H-mode, i.e. a regime of improved confinement, but **without the appearance of ELMs**. It exhibits **high levels of D_α light emission** at the edge, which is a measure of particle transport at the edge, and a very strong and regular mode at the edge, the so called **quasi-coherent mode (QCM)**, is visible in fast density or temperature diagnostics in a frequency range between 15 kHz and 80 kHz at AUG and around 100 kHz at Alcator C-mod. They EDA H-mode is typically achieved by heating the plasma only marginally above the H-mode power threshold with wave heating i.e. electron cyclotron resonance heating (ECRH) or ion cyclotron resonance heating (ICRH). At higher powers or when heated with NBI, the plasma mostly transitions to type-I ELMy H-mode. For higher triangularity the power window for the EDA H-mode increases [122].

The QCM, which appears at the very edge slightly inside the separatrix [123, 124], is believed to provide an additional transport channel, lower than in L-mode to sustain the steep gradients, but large enough to keep the pedestal pressure (gradients) below the peeling-ballooning instability threshold [125], which is the underlying instability of type-I ELMs [126]. In this sense, the QCM possibly hampers the appearance of ELMs. Due to its possible central role, the origin of the QCM needs to be understood and investigations of the QCM is an active field of research. The main properties of the QCM will be presented in section 2.5.6.

Quasi-Continuous Exhaust Regime

The quasi-continuous exhaust (QCE) regime, is another special type of H-mode **without type-I ELMs** [104, 127, 128], which was also called an H-mode with small ELMs [129], type-II ELMs [115, 130, 131, 132] or grassy ELMs [133, 134] in the past. It appears at highest densities, is compatible with very high heating powers, and got its name from a **strong filamentary transport activity** at the separatrix [127]. It appears when the plasma is highly shaped, i.e. at high triangularity and high elongation and exhibits a very beneficial **broadening of the divertor power fall of length** [135]. The QCE regime is accompanied by a QCM, similar as the EDA H-modes, however the QCM is much less coherent in QCE than in the EDA H-mode.

Due to the shared appearance of the QCM and the (better) accessibility at highly shaped plasmas, it is under discussion, whether the QCE regime and the EDA H-mode are the same regime, but just differing in the amount of fuelling and, hence, separatrix densities.

Quiescent H-mode

The quiescent H-mode (QH-mode) is a plasma regime **without type-I ELMs**, which was originally achieved with strong **counter injection** of NBI, i.e. the injection of the heating particles is against the direction of the plasma current leading to drift orbits of the fast heating particles larger than the magnetic flux surfaces [136, 137]. As has been shown at DIII-D [138], QH-modes can likewise be achieved with co-injected NBI. But in all cases, very **deep** E_r **wells** [139] are achieved by means of NBI and this strong rotation seems to be a precondition to the generation of the **edge harmonic oscillation (EHO)** [140] and the **high frequency oscillation (HFO)** [141]. More details about the EHO and HFO are given in section 2.5.8 and 2.5.9.

Similar as for the other types of ELM-free regimes, it is believed that the edge modes (EHO and HFO) contribute to keep the pedestal below the peeling-ballooning stability boundary and provide the necessary impurity transport in order to avoid impurity accumulation [106]. Starting with a standard QH-mode and consecutively lowering the torque input to zero can lead to a wide pedestal in QH-mode and a very broadband EHO with excellent confinement properties [142]. It has to be shown in the future whether the QH-mode access conditions, especially the wide-pedestal QH-mode, are compatible with reactor plasma conditions (e.g. low torque input or even full absence of NBI heating systems and metallic wall conditions) [143].

Plasmas with Magnetic Perturbations

An external actuator to suppress type-I ELMs are magnetic perturbation (MP) fields in the order of magnitude of $\delta B/B \approx 10^{-4}$, which are created on purpose by means of an array of special magnetic field coils producing a **radial magnetic field perturbation with a certain toroidal and poloidal mode spectrum** [144]. Depending on the mode spectrum, the perturbations can locally resonate (or not) with the helical field line structure of the plasma mainly given by the safety factor q_s. Under certain conditions, an appropriate perturbation spectrum can lead to **ELM mitigation**, i.e. to more frequent and smaller ELMs [145, 146], or to **full ELM suppression**, i.e. absence of any kind of ELM, while keeping the good confinement of the H-mode [147, 148].

The interaction of the perturbation field with the plasma is complicated, since the plasma response, i.e. the ability of the plasma to shield external magnetic fields, has to be taken into account. This interaction leads to corrugations of magnetic surfaces and to lobes in the SOL [144]. Under some conditions, such plasmas show macroscopic effects like ELM suppression or

the **density pump out** [149, 150, 151]. But they likewise give rise to very interesting types of structure formation at the edge. One example for this, is a ballooning mode poloidally localized in valleys of the corrugations, where the local magnetic shear is lowest [152]. Another example is a similarly localized turbulent mode in a slightly different perturbation field scenario, which might be related to the density pump effect [153].

X-point Radiator Regime

Another ELM-free H-mode regime, which can be achieved with a specialized external actuator, is the regime of a strong X-point radiator (XPR). For this purpose, impurities, e.g. nitrogen or argon, are puffed in a controlled manner to sustain a **localized radiation zone close to the active X-point** at a desired vertical position [154, 155]. This way, the divertors are detached, i.e. the power (and particle) fluxes to the divertor plates are significantly reduced by means of a radiation induced pressure drop, so that the heat deposition on the PFCs is reduced to acceptable values even at highest heating power input.

Figure 2.12: *Camera image in the visible range of an X-point radiator plasma close to the L-H transition. A large fraction of power is radiated as line emission toroidally along the X-point due to the presence of nitrogen giving rise to the ring-like radiation structure. The divertor is detached in this situation. The usually visible D-alpha line radiation at the inner heat shield and in the outboard SOL does not appear due to very low temperatures in the SOL .*

As a side effect, the plasma **does not exhibit ELMs**, when the XPR is placed at a certain vertical position above the X-point. This regime provides a natural solution for the power exhaust challenge and comes without ELMs, both being prerequisites for a tokamak reactor.

This regime is fascinating due to many reasons: it is accompanied by a beautiful levitated annular structure of radiation (see figure 2.12), it can be combined with many other regimes due to its unpretentious requirements (it only needs controlled impurity seeding and a minimum power input), and its physics is close to be fully understood due to the availability of comprehensive numerical modeling [156] and simplified analytical models [157], which were quantitatively validated with experiments.

2.3.2 Transition to H-mode

The transition from L-mode to H-mode (L-H transition) was mainly investigated as a transition from L-mode into ELMy H-modes in the past. Since the ELMy H-mode is often the starting point to explore other types of H-mode regimes, the following discussion of the transition dynamics *qualitatively* applies likewise on transitions from L-mode into the EDA H-mode, the QCE regime, the XPR regime, the QH-mode and plasmas with MPs applied. However, the operating conditions of these different regimes involve boundary conditions, like the plasma shape and presence of impurities, which can *quantitatively* change the power threshold necessary to achieve the H-mode. These dependencies will be discussed in more detail in chapter 4. The transition into the I-mode is qualitatively different to the transition into H-mode, so that it will be discussed separately in the next section.

The L-H transition **takes place spontaneously** as it is shown in figure 2.13. At a certain heating power, the confinement of the plasma increases at a specific time point ($t = 15.76$ s). This confinement change is indicated by a significant **rise of the stored energy, a rise of the edge temperature, rise of the density and a sudden drop of the H_α light emission**, which can be interpreted as an indicator for edge transport.

This behavior of sudden spontaneous changes of parameters exhibiting a discontinuity (in this case it is a jump of the H_α light emission, but the turbulence amplitude [158] or the divertor currents [159] show similar jumps) resembles a first-order phase transition, e.g. from liquid to solid state exhibiting a discontinuity in the density. In the language of phase transitions, the **edge transport is the ordering parameter** for the edge plasma and this physical system, exhibits a **bifurcation** between a state of high turbulence and weak flows (L-mode), and a state of low turbulence and strong flows (H-mode). Therefore, models involving a bifurcation in (edge) transport or

radial electric field [160, 161, 162, 163, 164] were proposed to explain this sudden changes at the edge.

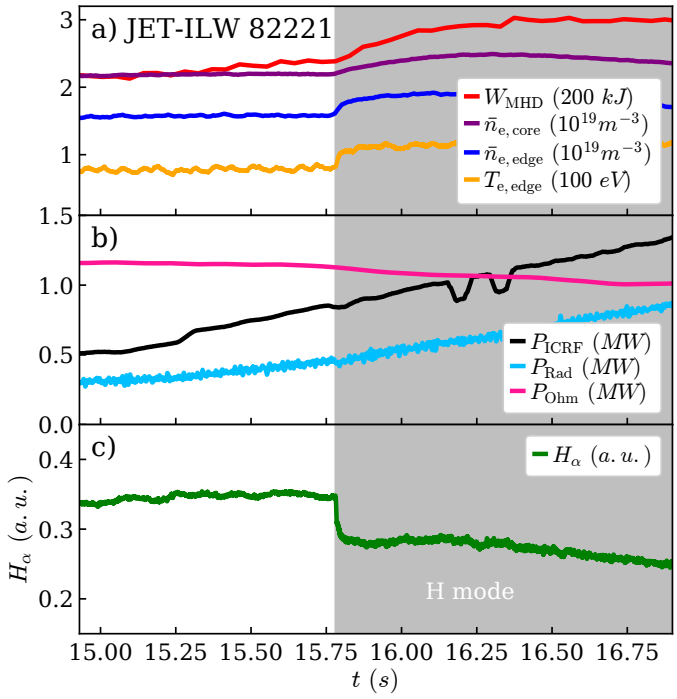

Figure 2.13: *L-H transition in a deuterium plasma at the JET tokamak. At a certain step of injected ICRH power (black line in b), the stored energy (red), the edge temperature (yellow) the densities in the core (purple) and edge (dark blue) spontaneously start to rise. This indicates a phase of better confinement and, hence, marks the L-H transition. At this time point, the H_α light emission (c) suddenly drops indicating that the edge transport is reduced.*

The decisive **external control parameter** to switch from L-mode to H-mode is the heating power of the plasma. It turned out that the L-H transition is achieved when the heating power exceeds the **L-H power threshold** P_{LH}. Similar as for other types of phase transitions, a phase diagram can be used to indicate under what conditions the plasma is in H-mode. Typically, the L-H power threshold P_{LH} is drawn against the line-averaged electron density of the plasma $\bar{n}_{\mathrm{e}}$. This parameter is chosen due to its good availability and due to the comparably strong dependence of P_{LH} on density.

A typical phase diagram in the P_{LH}-$\bar{n}_{\mathrm{e}}$ plane is shown in figure 2.14. The separation line, P_{LH}, between L-mode and H-mode is in most cases a U-shaped curve. For input powers above P_{LH}, the plasma is in H-mode, below

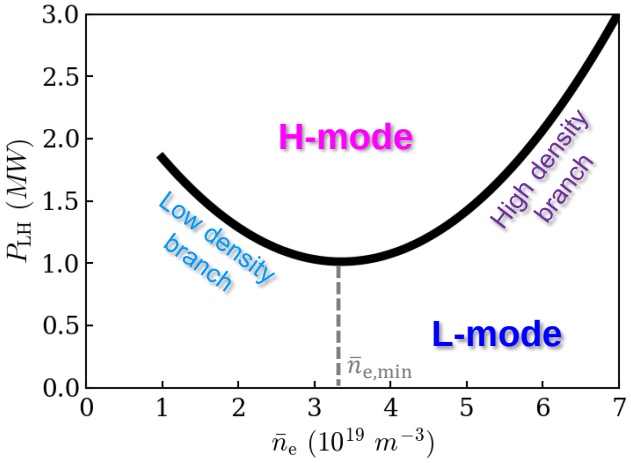

Figure 2.14: *Phase diagram of confinement regimes in a tokamak. Above the power threshold P_{LH} (black line), the plasma is in H-mode, below in L-mode. Typically, the power threshold curve exhibits a minimum when drawn against the line-averaged density $\bar{n}_e$. The density, where the minimum of P_{LH} is achieved, is referred to as $\bar{n}_{e,min}$. The branch on the left of $\bar{n}_{e,min}$ is called the low density branch, and on the right referred to as high density branch. Plasmas with lowest densities are very difficult to be achieved, but when successful, the plasma stays in L-mode even for very high input powers. The black line of P_{LH} is the fit curve for AUG data at a plasma current of 0.8 MA and a magenetic field of 2.5 T [47].*

the line in L-mode. The density, at which the minimum of P_{LH} is achieved, is referred to as $\bar{n}_{e,min}$. The P_{LH} on the right of $\bar{n}_{e,min}$ is the high density branch, on the left of $\bar{n}_{e,min}$ the low density branch. Very low densities are difficult to achieve in a tokamak. But data in this region indicate, that it is impossible to enter H-mode at such low density, at least when heated with electron heating [165].

The L-H transition is one of the most fascinating phenomena at the plasma edge due to its self-organizing nature, which impacts small scales, like turbulent fluctuations as well as macroscopic parameters and the overall confinement of the plasma. But it is also extremely important for the dimensioning of energy producing fusion reactors. First of all, P_{LH} defines the necessary minimum heating power for a reactor to fulfill the requirement to run in H-mode [19], and thus tells plant designers what heating power capabilities are needed for the reactor. Secondly, and this is even more important, P_{LH} has direct impact on the size of a tokamak reactor [166]. This is due to the need to *minimize* the heating power, in order to stay below the material limits to withstand the high heat fluxes in the divertor, and the

need to *maximize* the heating power in order to stay above P_{LH} allowing for H-mode operation. Therefore, the prediction of P_{LH} is essential for a decent reactor design. A good prediction of P_{LH} and its (known strong) isotope dependence is also needed to decide whether the non-nuclear phase of ITER can run in hydrogen, or whether a helium campaign has to be scheduled in addition [167].

Unfortunately, the power threshold P_{LH} depends on various more parameters and cannot be quantitatively predicted with existing models despite it was already discovered more than 40 years ago. Due to the lack of a sufficient model, only regressions of P_{LH} data from a multi-machine data base can be used in order to extrapolate P_{LH} to future devices. The most commonly used scaling is the ITPA scaling, P_{ITPA} (in MW) [168], which applies only for deuterium plasmas and for the high density branch of P_{LH}. It exhibits a dependence on line-averaged electron density $\bar{n}_{\mathrm{e}}$ in units of 10^{20} m^{-3}, toroidal magnetic field B_ϕ in T and the plasma surface S in m^2:

$$P_{\mathrm{ITPA}} = 0.0488 \bar{n}_{\mathrm{e}}^{0.72} B_\phi^{0.8} S^{0.94}. \tag{2.13}$$

The multi-machine data base, which was used to infer P_{ITPA}, contained the power threshold data of deuterium plasmas in different machines expressed in terms of the total power loss

$$P_{\mathrm{loss}} = P_{\mathrm{ohm}} + P_{\mathrm{aux}} - \frac{dW}{dt}, \tag{2.14}$$

which equals the sum of the whole input power from ohmic heating, P_{ohm}, and auxiliary power, P_{aux}, from other heating systems like NBI, ECRH or ICRH heating, and the rate of change of the energy content. P_{loss} is sometimes also called net heating power P_{net}.

In plasmas with high radiation fractions, as it is typical for JET, the power threshold is more reproducible, i.e. more coherent and systematic power threshold graphs can be achieved, when the radiated power inside the bulk plasma, i.e. inside the separatrix, P_{rad}, is subtracted from P_{loss}. This quantity corresponds to the net power reaching the separatrix by transport losses and reads

$$P_{\mathrm{sep}} = P_{\mathrm{ohm}} + P_{\mathrm{aux}} - \frac{dW}{dt} - P_{\mathrm{rad}} = P_{\mathrm{loss}} - P_{\mathrm{rad}}. \tag{2.15}$$

The scaling 2.13 agrees with measurements of P_{LH} in existing devices within a factor of about two at the high density branch, but many additional factors have been identified, which impact P_{LH}. These further parameter dependencies of P_{LH} and some selected models of the L-H transition will be discussed in more detail in section 4.

2.3.3 Transition to I-mode

Similar to the transition from L-mode to H-mode, the transition from L-mode to I-mode is accompanied by an increase of the temperature and, hence, an increase of the energy content of the plasma. But it **does not show a rise in density**. This is depicted in figure 2.15 for a an I-mode at AUG in unfavorable configuration. Due to this, only a pedestal in the temperature profile, but not in the density profile is created (see figure 2.11).

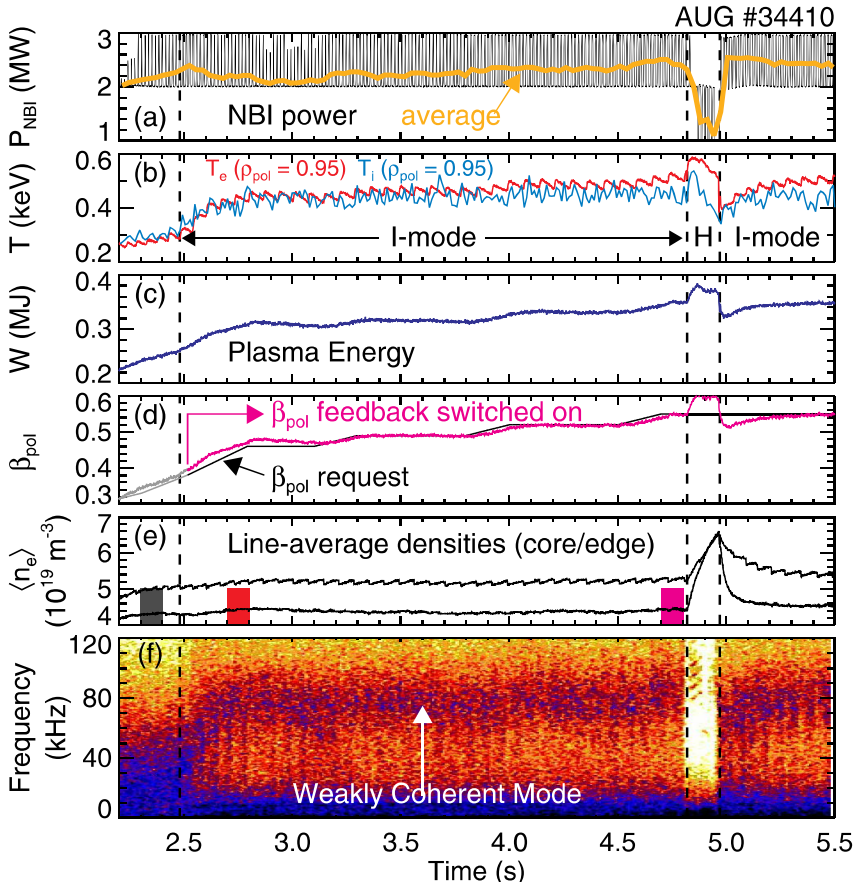

Figure 2.15: *Time traces of I-mode access at AUG (adapted from [169]). When the NBI power (a) rises, the plasma transitions from L-mode to I-mode at $T = 2.48$ s indicated by a rise in temperature (b), plasma energy content (c) and poloidal plasma beta (d). The density (e), however, stays on a constant level. Instead of a suppression of broadband turbulence as in H-mode, the I-mode is exhibiting a weakly-coherent mode (WCM) as visible in density diagnostics like the normal incidence reflectometers measuring at $\rho_{\mathrm{pol}} = 0.99$ (f).*

Instead of broadband turbulence as typical for L-mode (see figure 2.15f, prior to T = 2.48 s), the I-mode exhibits a relatively narrow band of turbulent fluctuations referred to as the weakly coherent mode (WCM). When the heating power is further increased during the I-mode, a second transition, from I-mode to H-mode, happens as shown in figure 2.15 at 4.82 s. Here, the density fluctuations (f) fully vanish at all measured frequencies, indicating that the edge turbulence is almost fully suppressed. Consequently, a stronger transport barrier has formed, which now impacts also the density, and the density and temperature rise strongly during this short, non-stationary H-mode phase. This clearly shows, that the confinement in H-mode is better than in I-mode, while the I-mode showed already a clear improvement of the thermal confinement with respect to the L-mode. The $E \times B$ flow in I-mode is likewise between L-mode and H-mode levels [48]. When the L-mode is specified as a state of strong broadband turbulence and low flow shear, and the H-mode as a state of low turbulence and strong flow shear, then the I-mode is a **state of narrow band turbulence and medium flow shear**.

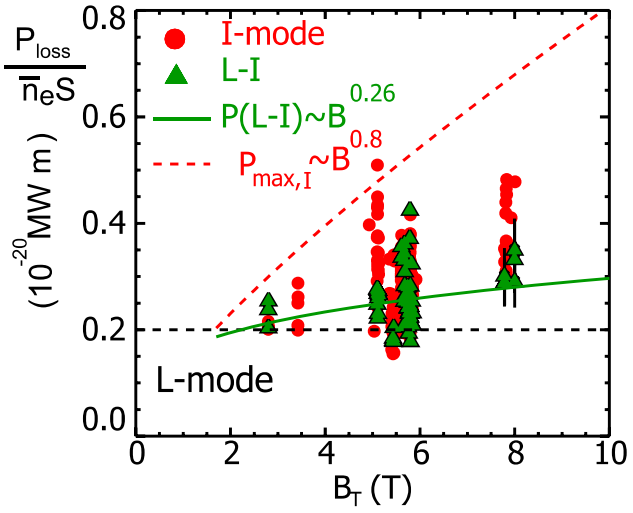

Figure 2.16: *Range of existence (phase diagram) of I-modes (circles) and L-I transitions (triangles) (reprinted from [170]). The y-axis indicates the heating power (P_{loss}) normalized to the density and surface of the plasma, and the x-axis the toroidal magnetic field. At higher magnetic fields, the I-mode can exist in a larger power window between the I-mode power threshold (green line) and the H-mode threshold according to the ITPA scaling 2.13 (red dashed line).*

In contrast to the power threshold of H-mode access, P_{LH}, according to the scaling 2.13, which is proportional to $B_\phi^{0.8}$, the power threshold for the I-mode access seems to scale as $B_\phi^{0.26}$ [170, 171]. This can explain, why

the power window for the I-mode at most of the operating devices, which operate mostly below 3 T, is so narrow. And it implies that a fusion device with larger magnetic field, as it was the case for Alcator C-mod [121] and as it will be the case for most of the power plant concepts [19], has a much wider power window for the existence of the I-mode. This is shown in figure 2.16. Consequently, one of the most ambitious high-field tokamak reactor concepts envisages the I-mode as ELM-free reactor regime [172].

2.4 Filaments

Filaments are **tube-like structures**, which are **extended along the magnetic field** line and appear most prominently in the **SOL**. They manifest as local and typically **large pressure perturbations with respect to the background** plasma being strongly anisotropic due to the fact that they extend several (tens of) meters into parallel direction, but only exhibit a size of a few centimeters in perpendicular direction. A filament is schematically shown in figure 2.17.

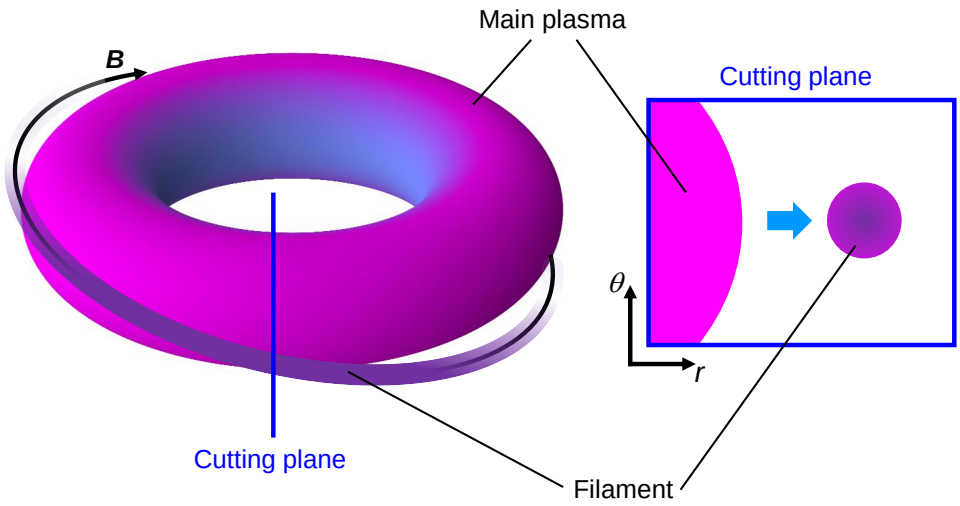

Figure 2.17: *Schematic of a filament. The filament (purple) detaches from the main plasma (magenta) and propagates radially outward. It is extended along the magnetic field line and, hence, much larger in parallel direction than perpendicular to the magnetic field line.*

2.4.1 Blobs

Blob filaments, or simply blobs [39, 173], appear in all plasma regimes in the SOL of a tokamak. They are **small in size** in perpendicular direction compared to other filaments (see below), typically several millimeters up to a few centimeters. Nevertheless, their associated pressure **perturbation is in the order of 100 %**, i.e. the background pressure is doubled during the lifetime of the blob, which is typically in the order of 10 µs to 100 µs. They appear quite frequently, in the order of 1000 blobs per second. They don't appear with a constant frequency, but **emerge randomly**, so that the distribution of the waiting time, i.e. the time between two blobs, is broad. The smaller the size the more frequent blobs appear, so that in most cases an exponential distribution function for the waiting time can be found [174, 175]. Blobs appear very clearly and with high frequency in L-mode, but they also appear in inter-ELM phases of the H-mode with slightly changed properties [176, 177, 127]. Compared to other filaments, blobs exhibit a finite but very **small magnetic signature** [178], thus, the dynamics of filaments is not dominated by electromagnetic effects for most of the relevant blob regimes. An example of a measured cross section of a blob emerging at the separatrix and moving radially outward is depicted in figure 2.18.

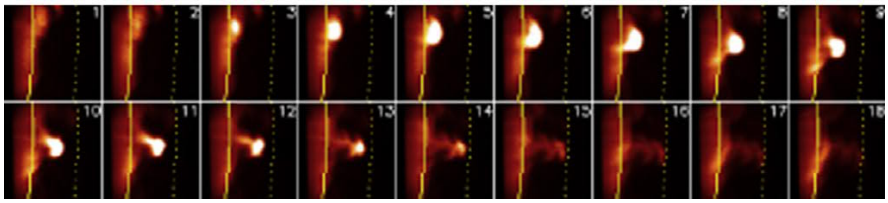

Figure 2.18: *Measured evolution of a single blob as it appears in the poloidal cross section at NSTX with gas puff imaging (adapted from [179]). This set of consecutive frames shows how the blob detaches from the separatrix (yellow line) and moves radially outwards towards the wall.*

Although considered for a long time as a nice but irrelevant side effect of edge turbulence, blobs are in fact very relevant for a fusion reactor for at least two reasons: First, the associated perpendicular convective transport due to blobs in the SOL is the dominant perpendicular loss channel, which contributes to reduce the heat load caused by parallel fluxes into the divertor by facilitation of divertor detachment and broadening of the power decay lengths. In this aspect, a high blob transport could be beneficial to support the heat exhaust solution in a tokamak reactor. Secondly, the blobs can provide a significant particle and heat flux to the first wall, especially at high densities [180, 181] giving rise to undesired erosion of PFCs [182]. It is

investigated [116, 183] whether it is possible to combine the favorable effect of heat flux reduction by blobs with a sufficient reduction of the undesired effect of erosion of the first wall in a future reactor, but is not certain whether a sufficient solution will be found.

Further properties of blobs like their role in the high density transition and the potential of eroding PFCs as well as simple analytical models for their size and propagation are discussed in detail in chapter 3.

2.4.2 Edge Localized Modes

Edge localized modes (ELMs) are **pronounced bursts** at the edge of the plasma appearing **exclusively in H-mode** and expelling significant amounts of heat, particles and impurities in one or several large filaments per bursts (see figure 2.20). They can occur with very regular and fixed frequency, but sometimes they also appear intermittently. ELMs exhibit a **strong magnetic signature**, so that they are clearly visible in magnetic pick-up coils. A typical time trace of ELMs after the L-H transition is shown in figure 2.19.

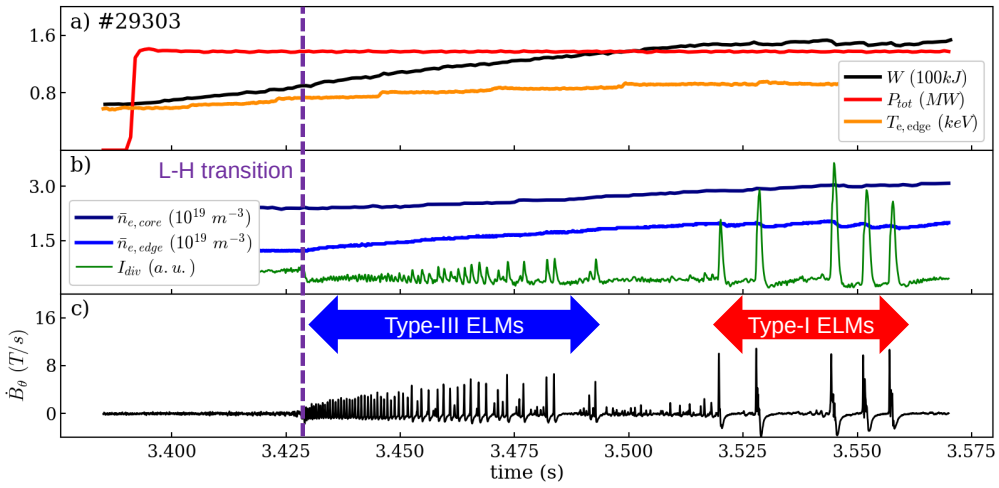

Figure 2.19: *Typical scenario of ELMs appearing after the L-H transition. Due to the increase in NBI heating power (red line), the energy content W (black line in a) and temperature at the edge (orange line) rise slowly. At a certain time ($t = 3.43$ s), the plasma enters H-mode indicated by the drop of the divertor shunt current (green line), and the density in the core (dark blue line) and edge (blue line) start to rise. The small bursts in the divertor shunt current I_{div} and the magnetic probe signal $\dot{B}_\theta$ (c) directly after the L-H transitions indicate type-III ELMs. After a short ELM-free phase, type-I ELMs appear.*

There are at least three types of ELMs, with different properties [184, 115]:

Type-I ELM: This is the largest type of ELM, expelling up to 15 % of the total plasma energy content within one burst [185] after the H-mode pedestal has fully developed after the L-H transition. It has two main characteristic features: the **occurrence frequency increases with increasing heating power**, and it **does not exhibit typical magnetic precursors** as other ELM types (although certain high frequency modes can exist prior to type-I ELMs [186, 187]). Large type one ELMs are a severe threat for a fusion reactor and regular type-I ELMs probably have to be avoided by any means for a stationary reactor plasma scenario [188, 116]. It is well accepted that type-I ELMs hit the **ideal peeling-ballooning limit** [24, 126] giving rise to an explosive burst of plasma at the edge.

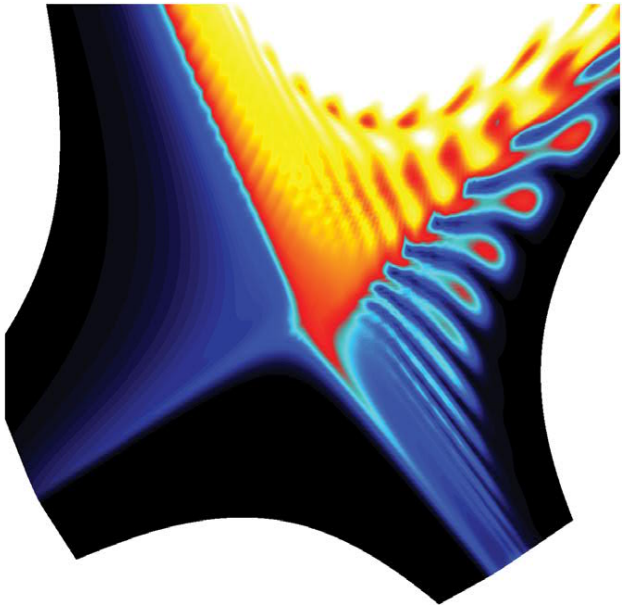

Figure 2.20: *Pressure fluctuation pattern around the X-point due to a type-I ELM triggered by the peeling-ballooning instability. This is a simulation output of the non-linear reduced MHD code JOREK (adapted from [189]). An ELM event manifests as ejection of rather a group of filaments instead of only a single filament.*

Type-II ELM: They are **much smaller in amplitude and much higher in frequency** than type-I ELMs and they appear only at **higher values of elongation or triangulation or closeness to double null**. Type-II ELMs don't possess clear main features (e.g. frequency dependence of heating power), which might have contributed to the fact that discharge phases with them are also called grassy ELMs [133, 134], small ELMs [129] or QCE scenario [104, 127].

Type-III ELM: Type-III ELMs appear typically directly after the L-H transition, sometimes during the pedestal build-up. They exhibit two clear features: the **frequency decreases with increasing heating power**, and each ELM burst is initiated by a characteristic **magnetic precursor**. More and more indications are found, that type-III ELMs are the same phenomenon as the limit-cycle oscillations (LCOs) after the L-H transition (see chapter 5) [159].

There are additional types of ELMs proposed [24], but they do not appear in all tokamaks, so that we do not consider them here.

Despite the undesired property of providing (too) high transient heat loads on PFCs in reactors, ELMs can be of use in present devices to keep the impurity concentration low by flushing-out impurities [190]. Pacing, i.e. triggering them, by means of pellets [191] or vertical kicks [192] of the plasma has become a robust and important method for controlling impurity concentrations in nowadays fusion experiments .

2.4.3 Pedestal Relaxation Events

The I-mode (see section 2.3.1) is considered as being ELM-free. However, it turned out, that the I-mode likewise exhibits ejections of heat and particles during **intermittent turbulent density bursts**, when the heating power is quite high, i.e. in I-mode scenarios **close to the transition from I-mode to H-mode** [193, 194]. These events are called pedestal relaxation events (PREs) [120] and seem to be related to the WCM (see section 2.5.7) [169].

They are much smaller than type-I ELMs and the relative energy loss of the pedestal due to PREs is only 1 % [194] compared to up to 30 % [149] for type-I ELMs. Consequently, the power load on the divertor due to PREs is comparably low, but still above the material limits for large PREs as they appear close to the I-H transition when extrapolated to reactor scale devices, if no further heat load reduction schemes are found [120]. They share some properties with type-III ELMs, e.g. a precursor activity and the amount of power loss. But in contrast to type-III ELMs, their frequency increases with

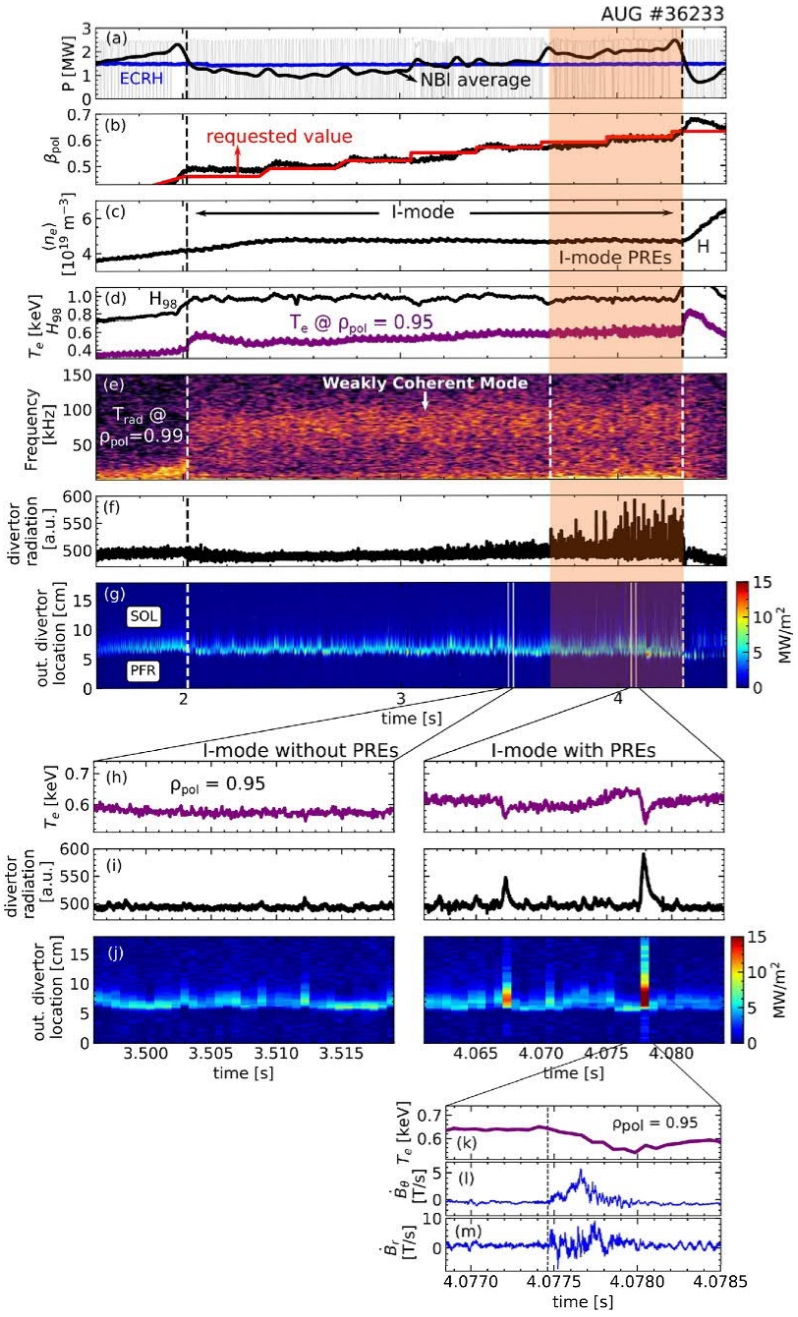

Figure 2.21: *Appearance of I-mode PREs in the typical AUG parameter range. (a) ECRH (blue) and NBI (black) power. (b) Requested β_{pol} (red) and measured value (black). (c) Line-averaged core electron density. (d) Electron temperature at $\rho_{\mathrm{pol}} = 0.95$ (purple) and H-factor (black). (e) Spectrogram of electron-cyclotron emission (ECE) radiation temperature measured at $\rho_{\mathrm{pol}} = 0.99$. (f) Radiation measured by a diode bolometer with line of sight in the upper divertor region. (g) Heat flux onto the upper outer divertor target. Panels (h), (i) and (j) show a magnification of the pedestal top electron temperature, divertor radiation and outer divertor heat flux, respectively, in two different time windows with and without PREs. Panels (k), (l) and (m) show a magnification of the pedestal top electron temperature, the $\dot{B}_\theta$ and $\dot{B}_\theta$ signal measured by magnetic pick-up coils during an I-mode PRE (reprinted from [194]).*

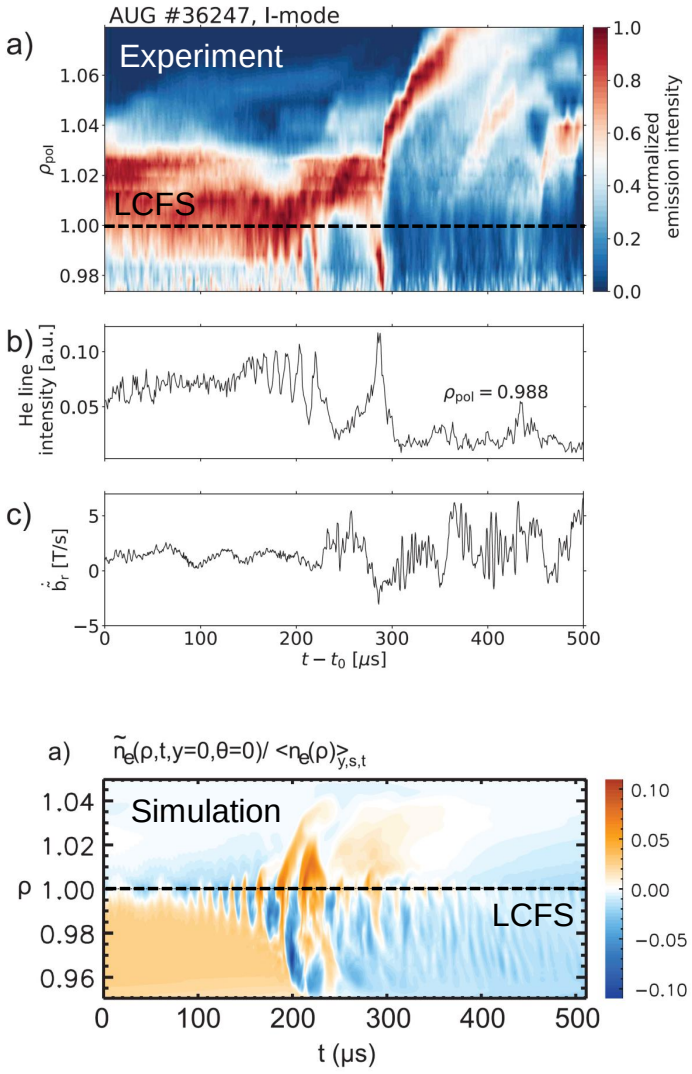

Figure 2.22: *Comparison of one PRE in the experiment (top three panels) and the GEMR simulation (bottom) as presented in reference [195]. The top panel shows the normalized intensity of a radial array of the thermal helium beam diagnostics. After the appearance of a precursor mode close to the LCFS (dashed line), which is better visible in the time trace of a single helium beam channel (second panel), stronger magnetic field activity is measured with a magnetic pick-up coil (third panel), and the PRE is expelled. The PRE propagates radially outwards as indicated in the first panel by the tilted stripe in the radius-time domain. The precursor activity close to the LCFS, the PRE burst and its outward propagation is also visible in the simulation (bottom panel) and takes place on a similar time scale.*

heating power. Nevertheless, PREs are not type-I ELMs, since they appear far below the peeling-ballooning stability limit [194]. A typical I-mode plasma with PREs is shown in figure 2.21.

The PREs were reproduced with the global gyrofluid turbulence code GEMR [195]. Although the simulations do not perfectly agree in all input parameters (e.g. the plasma beta is higher in the experiment), the similarity of experiment and simulations is remarkable. This is shown in figure 2.22. The following physical mechanism of the PRE is suggested: due to the high parallel conductivity at elevated electron temperatures, the electron and ion temperatures decouple and the electron temperature fluctuations are reduced. This gives rise to the (comparably coherent) WCM in the context of a weak ion temperature gradient drive as discussed in [196], and the WCM serves as a kind of precursor oscillation of the PREs. If the beta is sufficiently high, this precursor mode including its higher harmonics gives rise to magnetic fluctuations, and an accompanied change of the cross-phase from drift-wave-like to interchange-like boosts the transport leading to a strong burst. This is the PRE.

2.5 Temporal Structures

The structures presented above exhibit a characteristic order or pattern in space or phase space. The structures introduced in the following feature order or pattern formation in the time domain. They are more or less regular oscillations, mostly non-sinusoidal, and they appear at different locations of the edge plasma and within a very specific parameter range.

2.5.1 Fluctuation State in the Divertor

On the way **towards divertor detachment**, e.g. by rising the gas fuelling and, hence, density while keeping the heating power constant, pronounced **radiative fluctuations located close to the X-point** can appear [198]. This fluctuation state (FS) appears between the onset state of detachment (OS) and the complete detachment state (CDS). It is characterized by **broadband fluctuations in the low kilohertz range** (see figure 2.23) [197]. They can be detected with fast bolometer diodes, but are likewise visible in data of Langmuir probes at the divertor tiles [198] and in fast D_α light emission [199]. The frequency depends on the magnetic field direction and on the mass of the fuelling species. The latter was also found for an oscillation of a detachment state in a linear plasma [200], but it is not clear whether the physics there is the same as being active during the FS.

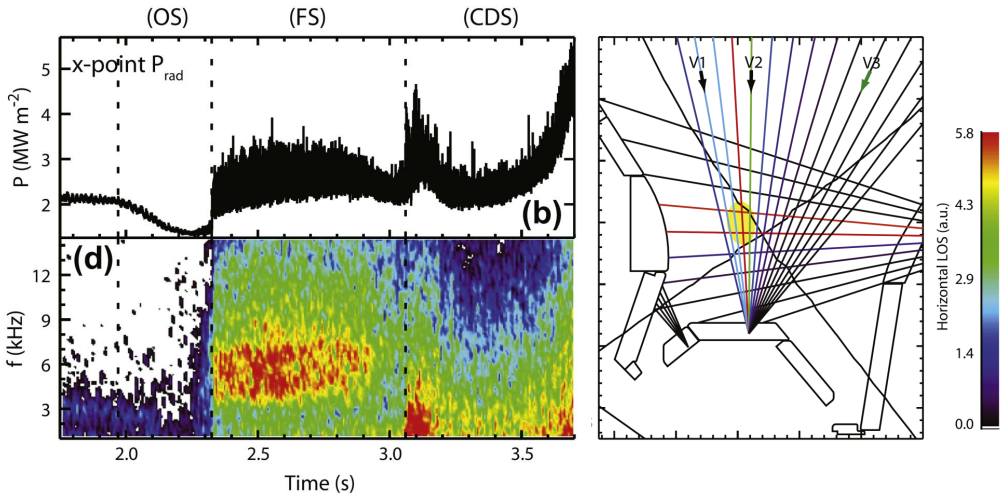

Figure 2.23: *Fluctuation state (FS) of the divertor (adapted from [197]). At a certain intermediate state of divertor detachment, fluctuations in the low kilohertz range (spectrogram at the bottom left panel) appear in signals of fast diode bolometers (time trace top left). The strongest intensity of the fluctuations appear in signals of the red lines of sight (LOS) of vertical and toroidal bolometer channels (left).*

A qualitative model suggests [201], that the FS is generated by the complex dynamics of the ionization front close to the X-point at the inner divertor. For increasing fuelling, the ionization front moves upstream. This proceeds up to a point, where the ionization cannot be supported by neutrals from the divertor region anymore, since the direct path from the recombination zone at the inner target is blocked by the inner divertor nose. Due to this, the ionization front quickly falls back downstream towards the inner target. Then it moves upstream again as before, and this repetitive dynamics produces the oscillatory behavior of the FS. This picture, however, was not yet quantitatively confirmed by simulations involving the complex atomic physics, so that the frequency of the fluctuations cannot be predicted yet.

Although the physics of the FS is not quantitatively understood, it is a useful and easily detectable indicator of a progressed detachment state (see next section 2.5.2).

2.5.2 Divertor Oscillations

Divertor oscillations (DO) are regular **alternations between two bi-stable states of divertor conditions**. In one state, the outer divertor is partially detached (low temperatures and low ion fluxes at the target), the main plasma density increases and the D_α light emission in the inner divertor is low. The divertor is in the fluctuation state (FS, see above). During the other state, the outer divertor is in the high-recycling regime, the main plasma density drops and the D_α light emission in the inner divertor is high. The whole divertor is considered to be in the onset state (OS) [201, 197]. The **outer and inner parts of the divertor show an opposite trend**, so that e.g. the D_α emission (or divertor shunt currents) in the outer divertor is increased when it is decreased in the inner divertor and vice versa. Time series of two DO cycles are shown in figure 2.24.

DOs appear only above a certain power threshold, but are still below and typically close to the L-H transition power threshold in the high density branch (see section 2.3.2) [199]. Under certain conditions, they can also appear in H-mode [202]. The frequencies at AUG are between 7 Hz and 70 Hz and at JET around 10 Hz in L-mode and 100 Hz in H-mode. At JET, there are indications that the L-H transition to a sustained H-mode only happens, when the outer divertor is in the high-recycling regime, never when it is detached. This could be related to the radial electric field in the SOL, which is larger for higher target temperatures and might indicate that the outer shear layer of the E_r well contributes to the turbulence suppression in H-mode (see chapter 4). The DOs were predicted by theory [203, 204] and are related to a bifurcation, which can be derived from the plasma and atomic physics present in the divertor [205]. A conclusive mechanism is proposed in [201] and works as follows: The cycle starts in the OS, i.e. the outer divertor is in the high recycling regime and the inner divertor is (close to be) detached. When the fuelling is increased (or the heating power decreased), the ionization front at the inner target moves upstream i.e. upwards along the magnetic field lines at the HFS. When the ionization front has moved above the X-point, the private flux region (PFR) becomes transparent for neutrals, since there is not enough hot plasma in the inner target, which would hinder them. Therefore, the neutrals reach the outer target and increase the density and reduce the temperature there. The outer target leaves the high-recycling regime when the temperatures fall below about 10 eV and the outer divertor starts to partially detach. In the meantime, the FS takes place at the inner target as explained above (see section 2.5.1). In this state, due to the lower temperature in the divertor region, the neutrals reach the confined plasma better and the density of the main plasma rises. This reduces the neutral

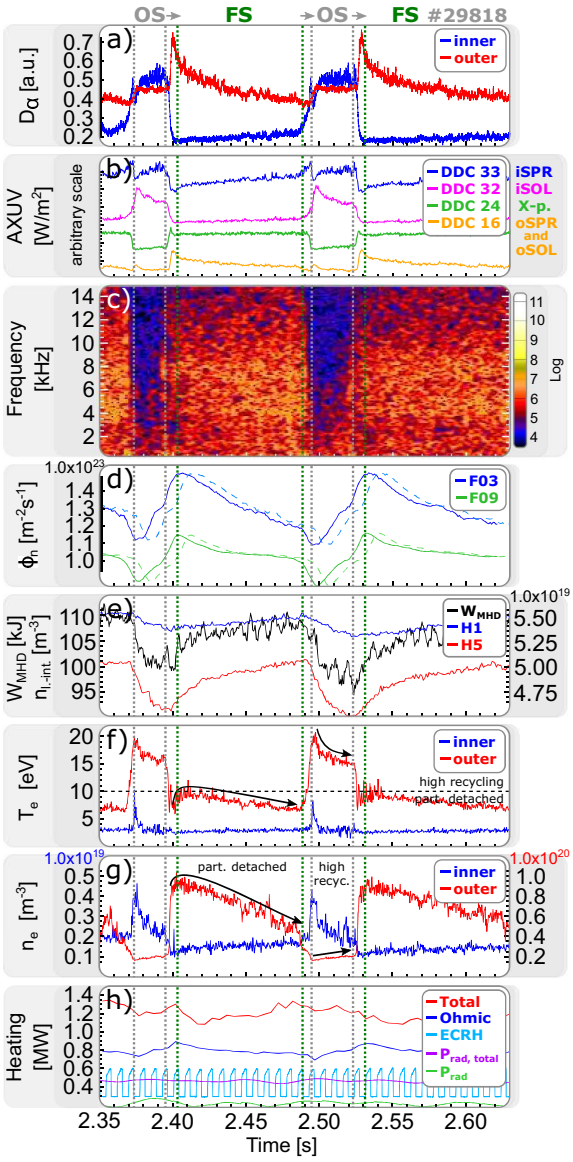

Figure 2.24: *Typical time traces of divertor oscillations at AUG. The time traces show the D_α radiation (a), diode bolometer signals from different LOS (b), the spectrogram of the X-point radiation (c), neutral flux (d), plasma stored energy W, central and edge line-averaged density (labeled as H1 and H5) (e), electron temperature (f) and density (g) measured by Langmuir probes closest to the strike line in the divertor, and the heating power (h). Reproduced from [201].*

content in the PFR (the plasma absorbs more neutrals then provided by the sources) and, in addition, the lower temperature in the outer target reduce the $E \times B$ drifts, which shuffled ions from the outer to the inner target. At a certain point, there are not enough ion flux and neutrals available, so that the ionization front above the inner target moves downstream towards the target. Once it is below the X-point, the PFR becomes opaque for neutrals, and, hence, the outer target is not sufficiently supplied by neutrals anymore. Therefore, the detachment process at the outer target ceases and the high-recycling regime is recovered there. In this situation, the divertor is in the OS again, and the cycle can start from the beginning.

2.5.3 Limit-Cycle Oscillations after the L-H Transition

Directly ***after* the plasma has accessed the H-mode**, limit-cycle oscillations (LCOs) with typical frequencies in the **low kilohertz range** can occur. They are visible in signals of the D_α radiation, the divertor shunt currents, the poloidal magnetic field perturbations $\dot{B}_\theta$, the toroidal loop voltage, the edge density and temperatures, but most prominently they were discussed as **oscillations of the turbulence amplitude and the radial electric field** (equivalent to flows) [206, 207, 208]. Due to the **non-sinusoidal** shape of the signals in time series and the fact, that the measured quantities, e.g. the turbulence amplitude vs. $E \times B$ flow, form circles in an appropriate phase space due to a **phase delay** between the quantities, the term limit-cycle oscillations prevailed. An example is shown in figure 2.25.

Due to the similarities known from population dynamics, the LCOs were called predator-prey cycles initially interpreting the turbulent energy as prey and the Reynolds-stress-driven zonal flow as predator [209]. This dynamics predicts a clockwise evolution in phase space corresponding to the type-Y cycles (see figure 2.25). However, experimentally also type-J cycles, i.e. counter-clockwise dynamics were found. The latter points to a central role of the background pressure gradient and was then described with extended predator-prey models successfully showing type-Y or type-J cycles similar as in the experiments [210, 211]. Both types of LCOs appear also in fluid simulations of the L-H transition, which coexist at different radial positions [212]. The RS driven zonal flow is not a stringently required ingredient to produce a LCO dynamics as many models without turbulence-driven ZFs demonstrate [213, 161, 214, 215].

When the heating power is chosen properly, i.e. marginally above the L-H power threshold, the plasma can steadily stay in this state of LCOs. Therefore, this plasma regime has been labeled with dedicated names: I-phase at AUG emphasizing the *intermediate* character between L-mode and

H-mode [216] similar to the IM-mode at DIII-D [217, 218], M-mode at JET highlighting the *magnetic* activity [219], and LCOs as a general name at other devices [220, 221]. At HL-2A and EAST, the term I-phase was borrowed [222, 223, 224, 225]. Direct comparisons with the same methods by the same person have clearly demonstrated, that the I-phase at AUG and the M-mode at JET is the same phenomenon [226].

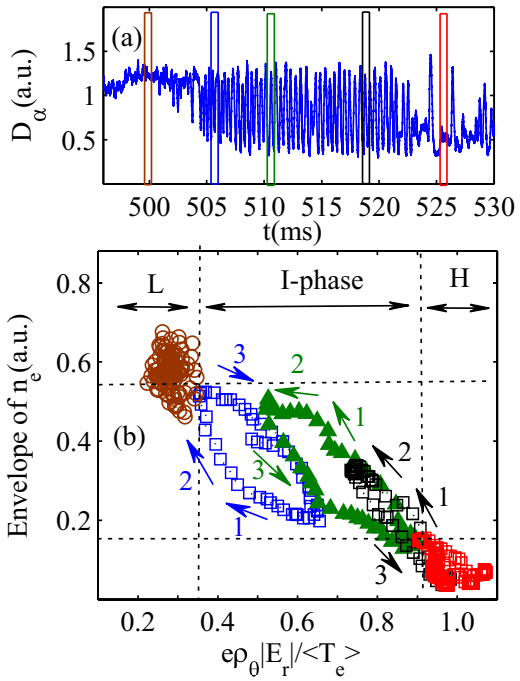

Figure 2.25: *Limit-cycle oscillations (LCOs) at HL-2A (adapted from [223]). The D_α signal (top) indicates the transition from L-mode (before 505 ms) to the LCO phase (505 ms to 525 ms) and finally to fully established H-mode (from 525 ms). The colored frames at the top indicate the time windows, for which LCOs in the phase space are shown in the same color at the bottom. The phase space is spanned by the turbulence amplitude (measured as the Hilbert envelope of the density signal) and the radial electric field. Both quantities are measured with a Langmuir-probe array. The early cycles rotate clockwise called type-Y cycles, while the counter-clockwise cycles are dubbed type-J.*

The LCOs can also appear at high heating power, when the major part of the power is cooled away by radiation, so that the remaining power reaching the separatrix is close to the power threshold [227]. Thus, proximity to the L-H power threshold is a necessary condition for the appearance of LCOs. Although the LCOs were considered to exist *prior to* the L-H transition (as

reflected in the titel of reference [206]), most of the studies nowadays consider the LCOs as a part of the H-mode, since the confinement improvement and the (transient) formation of a pedestal is clearly visible after the LCOs have emerged. Under some conditions, however, less coherent LCOs with smaller amplitudes can be present prior to the H-mode. These will be discussed in section 2.5.5. More details about the experimental appearance of LCOs at AUG and the possible role of ZFs are given in chapter 5. Additionally, experimental results will be presented suggesting that type-III ELMs and LCOs are the same phenomenon.

2.5.4 Dithering Transitions

The dithering transitions give rise to an oscillatory **alternation between L-mode and the I-phase** (see section 2.5.3), and only appears at the **high-density branch** (see section 2.3.2), when the heating power is marginally above the L-H power threshold. Since the I-phase is part of the H-mode, indicated by the drop of the D_α signal (or divertor shunt current), dithering transitions labeled as L-I-L [51, 225] or L-H-L transitions[3] [228], can easily be detected by oscillations in D_α, with a simultaneous oscillation of density and temperature at the edge. An example of a dithering transition at JET is shown in figure 2.26.

The density and temperature is high in the state of low D_α (I-phase), and in this state, likewise LCOs can be usually detected (typically only a few spikes). The frequency of dithering transitions is in the range between 2 Hz and 200 Hz. Hence, it is in a similar frequency range as the DOs (see chapter 2.5.2), although the frequencies of DOs are typically lower for the same plasma conditions, and it is sometimes not easy to discriminate them, since both phenomena appear at the high density branch of the L-H power threshold. But the following differences exist: Dithering transitions are clearly visible in the edge temperature signals due to the improved confinement in I-phase compared to L-mode phases. This is not that clear in the case of DOs. The density oscillates in both cases similarly. Another difference takes place in divertor signals, e.g. the D_α signal at the inner and outer target: the dithering transitions modulate the D_α signals rather *in phase* (the confinement improvement due to the I-phase affects both divertor sides similarly), while during DOs they are mostly *in anti-phase* due the physics explained above. This is also reflected in signals of the ion-saturation current of Langmuir probes at the target, which are usually more symmetric in the case of

[3]The dithering and L-H-L transitions discussed in references [213, 161] are in fact LCOs as it is known today.

dithering transitions than during DOs. However, the safest discrimination is possible by comparing the fluctuation signals: dithering transitions show the typical spikes of the LCOs burst in different signals during the I-phase, which are absent in all phases of DOs [229], and on the other hand, DOs exhibit the broadband modes at the X-point related to the fluctuation state (see section 2.5.1), which are absent in dithering transitions.

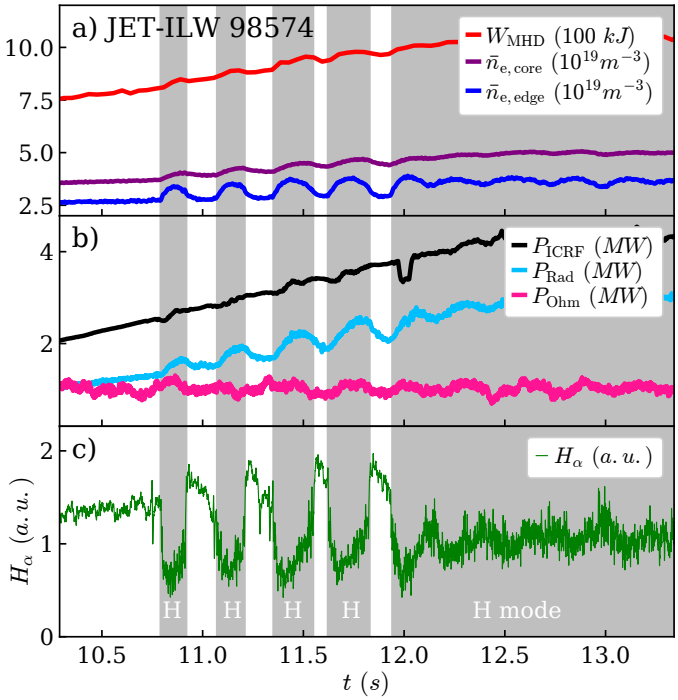

Figure 2.26: *Typical dithering transitions at JET. In this pure tritium discharge, the ICRF heating power is continuously ramped up (black line). Due to this, the L-mode enters the first time the H-mode at $t = 10.79$ s indicated by a drop of the H_α emission (green), a rise in densities (dark blue and purple), energy content (red), ohmic power (magenta), and radiated power (light blue). After 130 ms, the plasma falls back into L-mode and three further dithers appear, before a sustained H-mode is reached. The broadband fluctuations visible in the H_α signal during the H-phases are the LCOs bursts, since these are actually I-phases.*

The reason for dithering cycles is the following: during the heating ramp, the plasma enters the H-mode when the heating power, or more precisely P_{sep}, exceeds the (density dependent) power threshold $P_{\mathrm{LH}}(n)$ (see figure 2.27). Due to this, the confinement improves and, thus, the density rises. If the heating ramp is sufficiently slow, this rise in density, dn/dt, can let the

plasma drop out of H-mode if

$$\frac{dP_{\mathrm{sep}}}{dt} < \frac{dP_{\mathrm{LH}}}{dn} \cdot \frac{dn}{dt}. \tag{2.16}$$

This means that the operational point of the plasma moves to the right in the P_{LH}-density plane in figure 2.27 and falls back into L-mode again. This dropping out of H-mode is facilitated by two further contributions: First, the dW/dt term in P_{sep} is typically rising after the L-H transition, hence, lowering P_{sep}, and, secondly, the improved confinement typically leads to higher impurity concentration and, hence, higher radiation, P_{rad}, which likewise lowers P_{sep}. At some point, e.g. when the rise in density saturates while the heating ramp continues, P_{sep} exceeds again P_{LH} and the plasma enters H-mode again. The L-H-L cycle starts from the beginning.

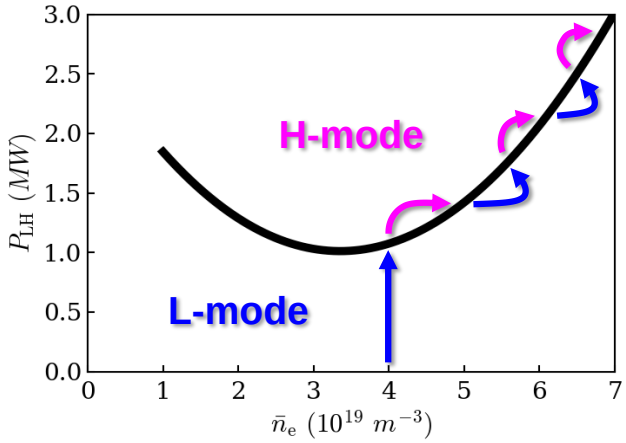

Figure 2.27: *Qualitative mechanism of the dithering transitions. A heating power ramp started in L-mode at relatively high density (blue vertical arrow) let the plasma transition to H-mode, when the power through the separatrix, P_{sep}, exceeds the L-H power threshold, P_{LH} (black line). Due to the confinement improvement in H-mode, the density rises and the operational point moves to the right (magenta arrow), so that the plasma falls back in L-mode. The rise in power and drop of density due to worse confinement in L-mode (blue curved arrow), let the operational point cross again the P_{LH}-curve and the next H-mode is achieved. This dithering between L-mode and H-mode continues until the heating power ramp has finished or the plasma disrupts due to reaching the L-mode density-limit in one of the L-mode phases.*

2.5.5 Small Amplitude Limit-Cycle Oscillations

The small amplitude limit-cycle oscillations (SAOs) appear **prior to the L-H transition** [225, 230, 231] in the low kilohertz range and are oscillations of the same quantities as the LCOs, i.e. D_α signal, divertor shunt currents, edge radial electric field, fluctuation levels etc., but have a much **smaller amplitude** in the D_α signal of typically a few percent in SAOs compared to up to 80 % in LCOs. In addition, SAOs are much **less coherent**, i.e. with a larger noise contribution and a more irregular oscillation, and very importantly, there is **no confinement improvement** involved during the SAO phase. They were described as a phenomenon different from LCOs the first time in reference [232] based on data in the EAST tokamak, but indications for SAOs were already visible in the data of other experiments [233, 234]. Due to its detailed investigations at EAST [225, 230], the name SAO was established in order to separate it from the LCOs after the L-H transitions as described in section 2.5.3, which are much more regular and possess larger amplitudes although the frequency is the same.

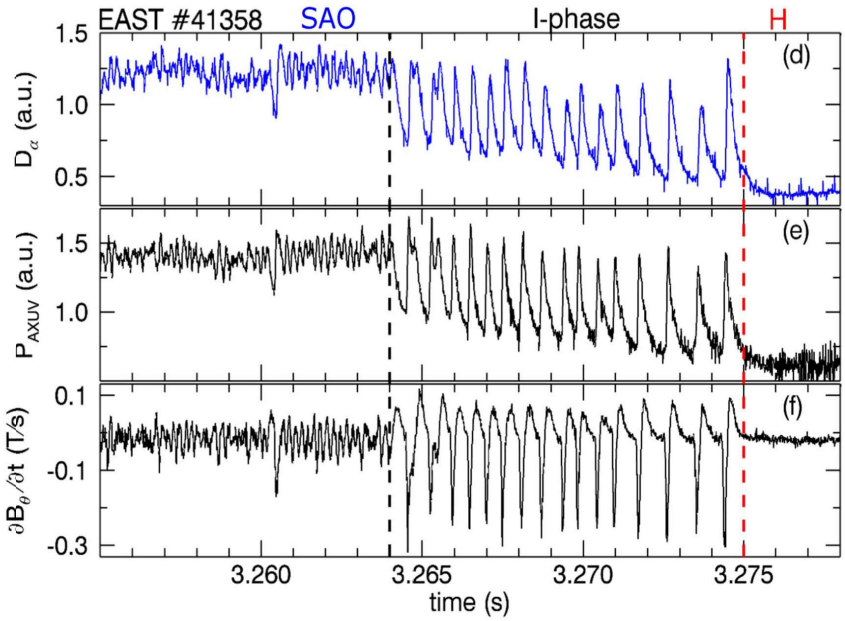

Figure 2.28: *Small amplitude limit-cycle oscillations (SAOs) at EAST (reprinted from [230]) compared to I-phase and H-mode. The SAOs are visible in the D_α signal in the outer divertor (top), the radiated power of an AXUV diode (middle) and a magnetic pick-up coil (bottom). Compared to the I-phase bursts, they are much smaller in amplitude and no confinement improvement is associated with the presence of SAOs.*

As discussed below (see chapter 5), more and more indications are found that the I-phase might not be dominated by the ZF-turbulence interaction as suggested in reference [209]. But more and more evidence is gained, that this ZF-turbulence interaction might be causing the dynamics of the SAOs.

2.5.6 Quasi-Coherent Modes

Quasi-coherent modes appear typically in **ELM-free H-modes**, either in the transient phase between the type-III ELMs and the type-I ELMs of the H-mode establishment [235, 236] or stationary in ELM-free regimes like the EDA H-mode (see section 2.3.1) [121, 122] or the QCE regime (see 2.3.1) [104, 127]. Most prominently, they are visible as **large amplitude density fluctuations** in a range between **20 kHz and 150 kHz** with a weak or no magnetic signature. The QCM is thought **to provide an additional loss channel** [124] for particles and impurities, so that the H-mode does not suffer in impurity accumulation, and the edge profiles are kept below the peeling-ballooning limit to avoid ELMs. Thus, it plays a decisive role for the attractive EDA H-mode regime.

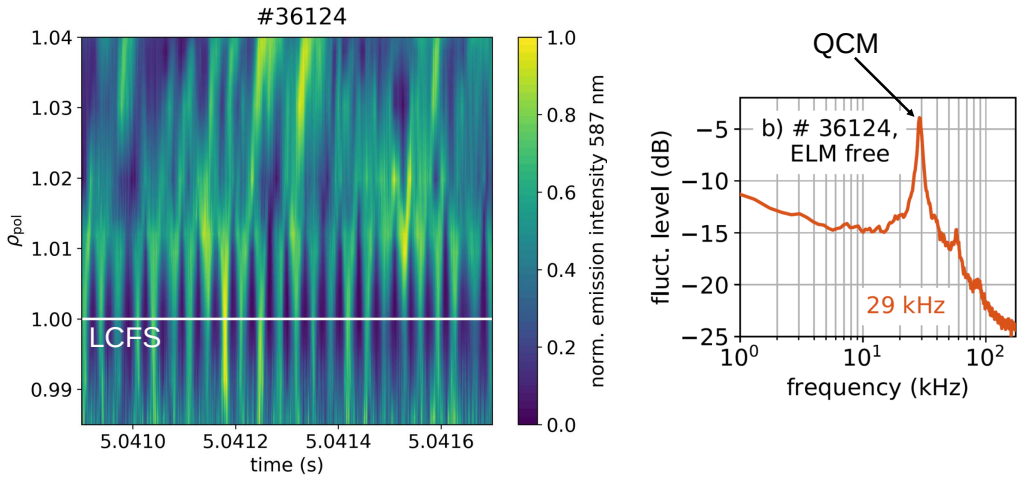

Figure 2.29: *Quasi-coherent mode (QCM) in EDA H-mode at AUG measured with the thermal helium beam diagnostic (adapted from [127]). As shown on the left, the QCM appears as a comb-like structure in the radius-time domain around the LCFS. The structures further outward are blob filaments. A Fourier spectrum of the 587 nm line intensity measured at the LCFS (right) shows a very coherent peak at 29 kHz indicating the QCM.*

As shown in figure 2.29 on the left, the QCM can be very coherent, i.e. the width of the QCM peak in the Fourier spectrum amounts to only a few kilohertz. But also very broadband versions of the QCM exist, e.g. in the QCE regime [127].

The QCM has a normalized poloidal wavenumber of about $k_\theta \rho_\mathrm{s} \approx 0.06$ with the poloidal wavenumber k_θ and the drift scale $\rho_\mathrm{s} = \sqrt{m_\mathrm{i} T_\mathrm{e}}/(eB)$ with electron temperature T_e [124]. Its maximum amplitude is located slightly inside the LCFS, but the mode can be detected in a broader radial region [127, 124, 123]. GYRO simulations indicate that the QCM could be a dissipative trapped electron mode [236], but also resistive ballooning X-point modes are a candidate [237] as well as a pressure-driven surface wave [238] and a turbulent saturated state consisting of a poloidally arrayed train of blobs [239].

2.5.7 Weakly Coherent Modes

Similarly to the QCM, the weakly coherent mode (WCM) is visible in **density fluctuations in the range of 80 kHz to 300 kHz**, but much more broadband than the QCM (see figure 2.30) and with lower amplitude [119]. The WCM plays a decisive role to **keep the plasma ELM-free and on low impurity concentrations** and is strongly connected to the I-mode regime (see figure 2.15 in section 2.3.1) or generally speaking to all regimes, which exhibit an "unusual" high L-H power threshold [118]. This is normally achieved by choosing the unfavorable configuration i.e. with the ion-∇B-drift pointing away from the active X-point, but also special plasma shapes in favorable configuration (ion-∇B-drift pointing towards the active X-point) open an access window to the I-mode due to the high L-H power threshold [119]. There are some indications that the WCM also exists in L-mode phases [169].

Simultaneously to the emergence of the WCM, a GAM (see section 2.1.4) is visible in appropriate diagnostics (at Alcator C-mode the GAM is even exclusively visible in I-mode) and both modes are coupled to each other as bispectral analyses suggest [240, 241]. In this picture, the GAM is responsible for the broadening of the WCM by modulation with the GAM frequency.

Fluid simulations with good agreement of experimental findings suggest that the WCM is a drift-Alfvén wave driven by parallel pressure gradients [242, 243] and that the WCM gives rise to a significant particle transport despite the strong radial electric field shear flow and low potential fluctuations due to a phase relation of $\pi/2$ between potential and density fluctuations [244]. Gyro-fluid simulations with parameters similar to AUG plasmas interpret the WCM as the remaining part of the turbulent fluctuation spectrum,

when the large scales are reduced due to phase randomization by magnetic field line stochastization while the small scales are subject to finite-Larmor-radius effects [196]. As described in section 2.4.3, the WCM serves as a precursor mode for PREs, when the plasma beta is sufficiently high, so that magnetic fluctuations and an accompanied increase of the interchange drive gives rise to a large transport event manifesting as the PRE.

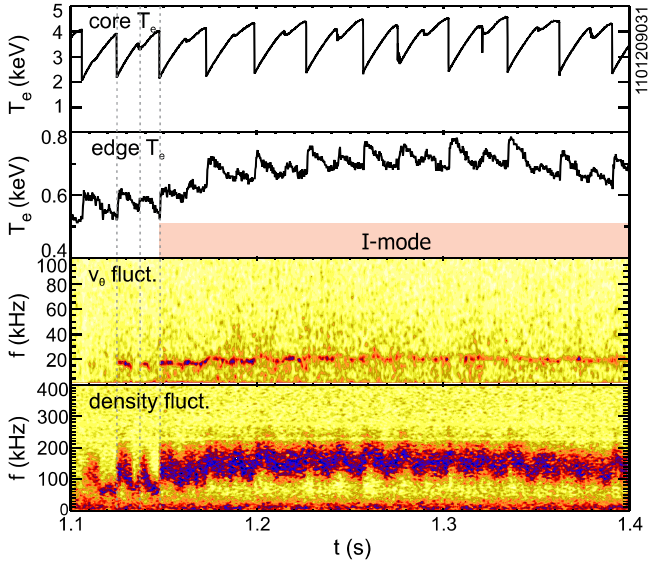

Figure 2.30: *Core (first panel) and edge (second panel) electron temperature from the ECE diagnostics as well as spectrograms of the poloidal velocity fluctuations (third panel) and density fluctuations (bottom panel) measured with gas puff imaging (GPI) at Alcator C-mod (reprinted from [240]). The appearance of the GAM as visible in the velocity fluctuations is strongly linked to the WCM manifesting as a broadband feature in the density fluctuations.*

2.5.8 Edge Harmonic Oscillation

A third type of mode at the edge, which prevents the H-mode plasma from type-I ELMs and impurity accumulation similar as the QCM and WCM, is the edge harmonic oscillation (EHO). It **appears in the quiescent H-mode** (see section 2.3.1) [140, 141] or in other regimes of high rotational shear (e.g. hot ion H-mode at JET were it is called the outer mode [245, 246]). As the name suggests, the EHO manifests in spectrograms of magnetic probe signals as **a set of pronounced coherent modes with harmonic toroidal mode numbers n = 1, 2, 3, 4, etc** localized in a radial region between $\rho_{\mathrm{pol}} = 0.95$ and $\rho_{\mathrm{pol}} = 1.0$ with a relative peak amplitude of up to 40 % [248] at about $\rho_{\mathrm{pol}} = 0.97$ [141, 137]. The lowest mode number has

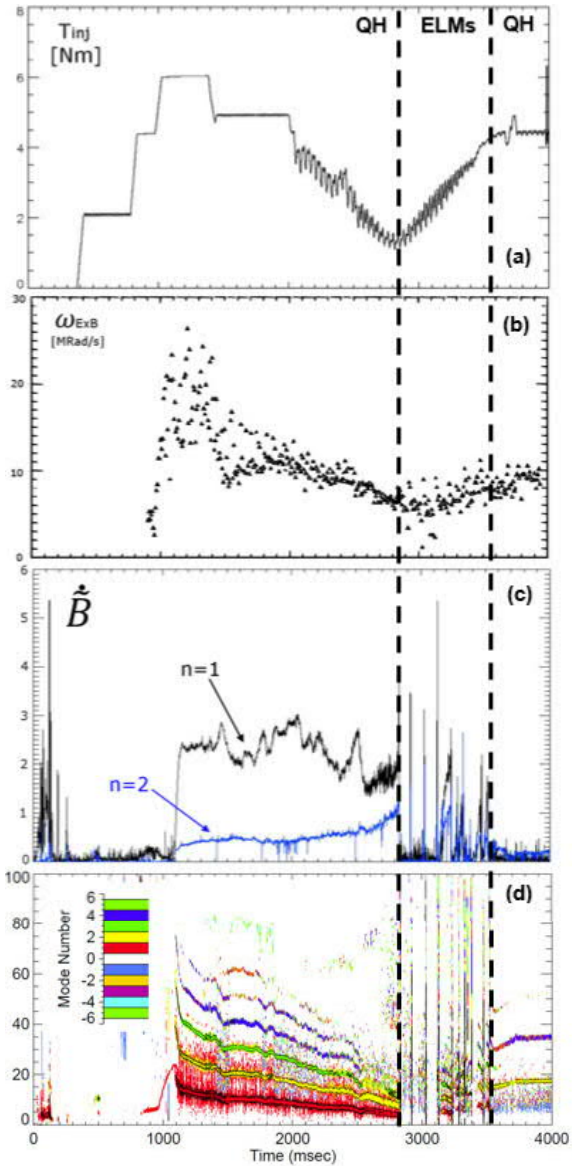

Figure 2.31: *Time traces from DIII-D shot #163466 for (a) external counter torque injection, (b) maximum Hahm-Burrell shearing rate in the outer shear layer of the E_r well in the edge pedestal, (c) RMS amplitude of magnetic signal from the Mirnov coils for $n = 1$ and $n = 2$ dominant modes, and (d) magnetic spectrogram from the Mirnov coils (reprinted from [247]). The higher harmonics in the spectrogram indicate the edge harmonic oscillations (EHO), which vanish below a certain shearing rate.*

a typical **frequency of around 10 kHz** and the highest harmonics are observed up to n = 15 [246]. Poloidal mode numbers of the lowest harmonics are typically low, i.e. m = 3, 4 or 5 depending on the local safety factor q_s [249, 140].

As shown in figure 2.31, the frequency of the EHO depends on the $E \times B$ velocity and decreases with decreasing torque input. Below a certain value of the $E \times B$ shear, the EHO vanishes and a type-I ELMy H-mode is achieved. Under certain conditions, the standard QH-mode with a classical EHO can transition to a wide-pedestal QH-mode with a broadband EHO, when the torque is decreased to zero [143, 142]. The EHO is thought to be a low-n saturated edge-current-driven kink-peeling mode, additionally destabilized by rotational shear [106, 138, 250, 251]. It seems to need a certain minimum rotational shear to excite the lower harmonics [142] in agreement with the measurements.

2.5.9 High Frequency Oscillation

The high frequency oscillation (HFO) appears simultaneously to the EHO and **exists only in QH-mode**. Its frequency is much higher than the frequency of the EHO and typically in the range between **300 kHz and 500 kHz**. Due to its high frequency, the HFO is not easy to measure and is mostly visible in Mirnov coils measuring the radial component of the magnetic field, $\dot{B}_r$. The envelope of the amplitude of the HFO is modulated with the EHO frequency as shown in figure 2.32, left.

The D_α emission from the outer divertor shows a similar modulation indicating, that the transport is largest at large HFO amplitudes. This is even better visible in figure 2.32, right, which shows a super-modulation on top of the modulation with the EHO frequency, i.e. an additional modulation of the HFO amplitude by about 1 kHz. The D_α emission follows mainly the super-modulation on the time scale of about 1 kHz, which is correlated to the HFO envelope. The modulation with the EHO frequency of about 10 kHz is still visible as small amplitude oscillations, but not the dominant modulation.

The high frequency coherent edge fluctuations seen at DIII-D [252] seem to be different from the HFO observed at AUG due to its missing signature in magnetic probes.

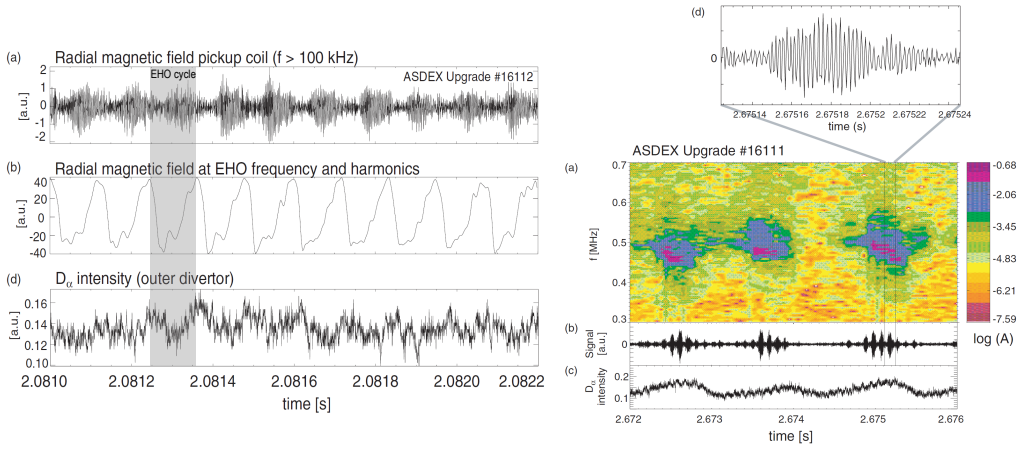

Figure 2.32: *The high frequency oscillation (HFO) and its relation to the EHO in QH-mode. Left: Signals of a high-pass filtered magnetic pick-up coil measuring $\dot{B}_\mathrm{r}$ at the outer midplane (top), magnetic signal filtered around the EHO frequency and its harmonics (middle), and D_α emission from the outer divertor (c) (bottom) (adapted from [137]). The envelope of the HFO amplitude is modulated by the EHO, and the D_α light indicating transport, is likewise modulated with the EHO frequency. Right: Spectrogram (second panel) and zoom (first panel) of the magnetic pick-up coil signal (third panel), and D_α emission from the outer divertor (bottom panel) (adapted from [141]). In addition to the modulation of the HFO with EHO frequency, a super-modulation at frequencies lower than the EHO can appear.*

2.5.10 Inter-ELM Modes

Between type-I ELMs in a developed H-mode, strong mode activity can be observed in magnetic probes measuring $\dot{B}_\mathrm{r}$, fast ECE-channels or reflectometer signals [253]. The mode activity seems to be related to different phases of the inter-ELM period, so that the presence of modes can be correlated to the strength of density and temperature gradients after an ELM crash.

The most prominent modes appear at **high frequencies**, i.e. between **200 kHz and 500 kHz** [186, 187, 254]. The toroidal mode number of the modes is in the range between $\mathbf{n = -10}$ **and** $\mathbf{n = -12}$ (the negative sign indicates propagation into counter-current direction in the lab frame) and the normalized poloidal wavenumber was determined to be $k_\theta \rho_\mathrm{s} \approx 0.04$. The modes **appear in the last phase of the inter-ELM period**, when the temperature and density gradients are clamped until the next ELM crash appears.

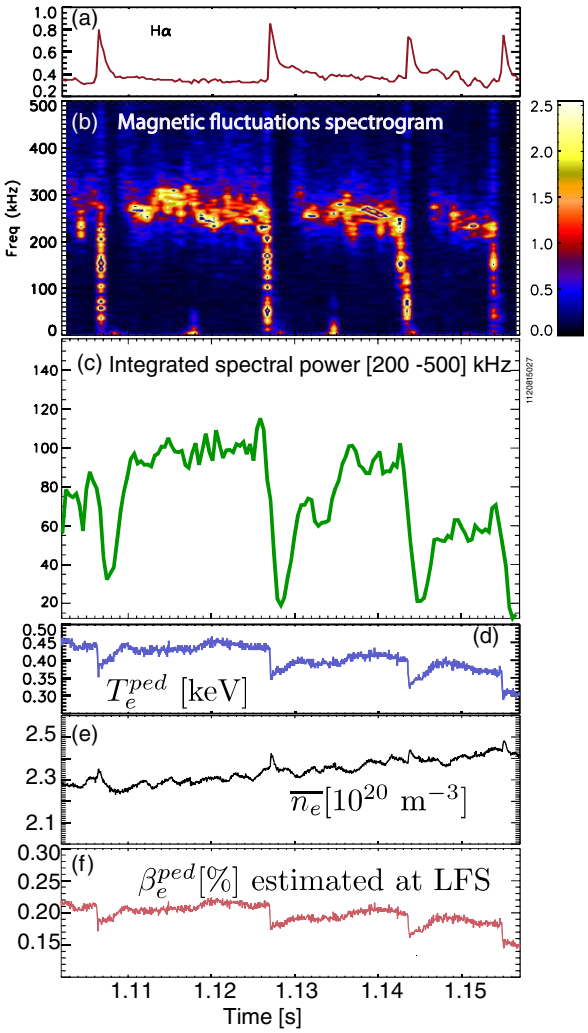

Figure 2.33: *Example of high-frequency inter-ELM modes at DIII-D (reproduced from [186]). (a) H_α signal indicating the ELMs. (b) Magnetic fluctuation spectrogram displaying the inter-ELM fluctuations. (c) Integrated spectral amplitude obtained from integrating the above spectrogram between 200 kHz and 500 kHz. (d) Edge temperature evolution measured using the ECE. (e) Line-averaged density evolution. (f) Estimate of the pedestal electron β_e evolution.*

In addition to these high frequency modes, there are two other categories of inter-ELM modes, which appear at lower frequencies, during other phases of the inter-ELM period and are localized at different radial positions [253, 255]. In contrast to the high frequency modes, the other modes are typically not detectable on the HFS of the tokamak.

2.6 Table of Phenomena

The following table 2.1 shows a summary of properties of the presented filament structures, flow structures, temporal structures and current structures. The phase transitions as described in section 2.3 are not listed here, since they are associated with more than one of the structures presented here.

Type	Name	Plasma regime	Time scale	δn/n (%)	δϕ (V)	δB (mT)	Theory available?
Filaments	Blobs	All	10-100 μs	10-100	10-50	-	Yes
	ELMs	H-mode	1-5 ms	100	100-500	10-100	Yes
	PREs	I-mode	0.1-1 ms	10	?	0.05	Yes
Currents	Edge current density	H-mode	10 ms-∞	-	-	20	Yes
	PS currents	All	10 ms-∞	-	-	100	Yes
Flow structures	Neoclassical flows	All	10 ms-∞	-	500	-	Yes
	Zonal flows	All	1 ms	-	50	-	Yes
	GAMs	L-mode	100 μs	25	50	0.02	Yes
	Staircases	L-mode	1 ms	20	50	-	Yes
Temporal structures	Fluctuation state	Towards detachment	0.1-1 ms	?	?	-	No
	Divertor oscillations	Close to L-H transition	10-100 ms	500	?	-	No
	LCOs	After L-H transition	0.1-1 ms	40	250	5	No
	L-H dithering	Close to L-H transition	10-100 ms	100	500	20	No
	SAOs	Before L-H transition	0.1-1 ms	10	10	2	No
	QCM	EDA H-mode	10-100 μs	40	?	1	Yes
	WCM	I-mode	10 μs	1	?	-	Yes
	EHO	Quiescent H-mode	100 μs	40	?	1	Yes
	HFO	Quiescent H-mode	2 μs	?	?	?	No
	Inter-ELM modes	H-mode	5 μs	?	?	1	No

Table 2.1: *Plasma edge phenomena and their properties. They appear in different plasma regimes, and they differ in terms of typical time scales, the magnitude of the (relative) perturbation amplitude of the density, $\delta n/n$, electrostatic potential, $\delta\phi$, and magnetic field, δB. The latter is the magnetic field at the measurement position (e.g. the Mirnov coil outside the plasma), which can differ from the magnetic field at the location, where the respective phenomenon actually takes place. The last column indicates, whether there is a* ***quantitative*** *description from theory available, which goes beyond basic ideas or a qualitative understanding. Light blue fields indicate, where experimental data is missing and numbers given there are from theoretical models.*

Chapter 3

Size, Dynamics and Erosion Properties of Blob Filaments

Blob filaments (see section 2.4.1) appear in all plasma regimes and are the dominant perpendicular transport channel in the SOL. They can support desired divertor detachment but could potentially lead to undesired erosion and heat loads on PFCs at the first wall. The transport originating from blobs depends on the heat and particle content of a single blob, its velocity and the occurrence frequency of blobs. The latter is difficult to predict, since it is related to turbulent processes determined by conditions in the confined plasma inside the LCFS. However, the size and velocity of a single blob is comparably well understood and depends mainly on local parameters of the SOL. Therefore, after an introduction into the physical processes determining the size and velocity of blobs and the resulting analytical scaling laws, measurements of blob sizes and velocities are presented. Based on these basic concept, a possible explanation for the density shoulder formation in the SOL is given, and the role of blobs for the erosion of first wall components is discussed. The presented measurements of blob properties and the erosion estimation described in this chapter are taken from references [256] and [182].

3.1 What Determines the Velocity of a Blob Filament?

The velocity of the blob in the SOL is primarily determined by the polarization of the blob, i.e. the charge-separation due to the magnetic field inhomogeneity at the outboard midplane (LFS) of the tokamak giving rise to $E \times B$ convection. A qualitative picture of the causality chain of blob motion is given in figure 3.1.

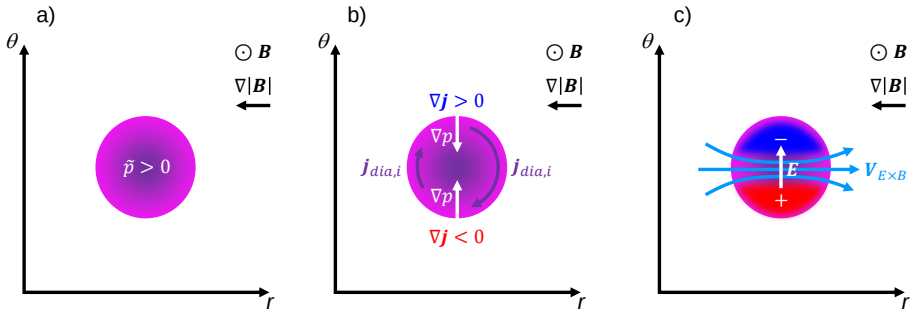

Figure 3.1: *Origin of the radial motion of a blob at the outboard midplane of a tokamak. A blob is a positive monopolar pressure perturbation, $\tilde{p}$, in the plane perpendicular to the magnetic field (a). The gradient of the magnetic field strength, ∇B, points to the left towards smaller radii and the magnetic field vector* $\mathbf{B}$ *out of the plane. The pressure is highest in the center of the blob, so that the pressure gradient, ∇p, points to the center and the corresponding diamagnetic current of the ions,* $\mathbf{j}_{\mathrm{dia,i}}$ *(see formula A.9 in Appendix A), rotates clockwise around the center of the blob (b). Due to its magnetic field dependence, the diamagnetic current is higher on the right hand side than on the left hand side corresponding to a finite divergence, $\nabla \mathbf{j}$, at the bottom and top of the blob. Thus, positive charges accumulate at the bottom and negative charges at the top of the blob (c). This gives rise to an electric field,* $\mathbf{E}$*, and, hence, an $E \times B$ flow,* $\mathbf{v}_{\mathbf{E}\times\mathbf{B}}$*, moving the blob radially outward.*

The positive pressure perturbation and the associated pressure gradients of the blob give rise to diamagnetic currents, $\mathbf{j}_{\mathrm{dia,i}}$ (see formula A.9 in Appendix A). The circular currents along the isobars are not equal on the right and left of the blob: The current on the right hand side is larger than on the left hand side, due to the magnetic field dependence of the diamagnetic current $|\mathbf{j}_{\mathrm{dia,i}}| \propto 1/B$ and the fact, that the tokamak field decreases for larger radii (see figure 3.1b). This leads to a finite divergence of the currents at the bottom and the top of the blob, or in other words, positive charges accumulate at the bottom and negative charges at the top in this magnetic field configuration (see figure 3.1c). The associated electrostatic potential structure is a dipole and this mechanism of creating a charge separation is called *polarization* in this context. The charge accumulation generates an electric field, which in turn gives rise to an $E \times B$ convection radially outwards. The $E \times B$ convection moves the blob and its particle content to the outer regions of the SOL.

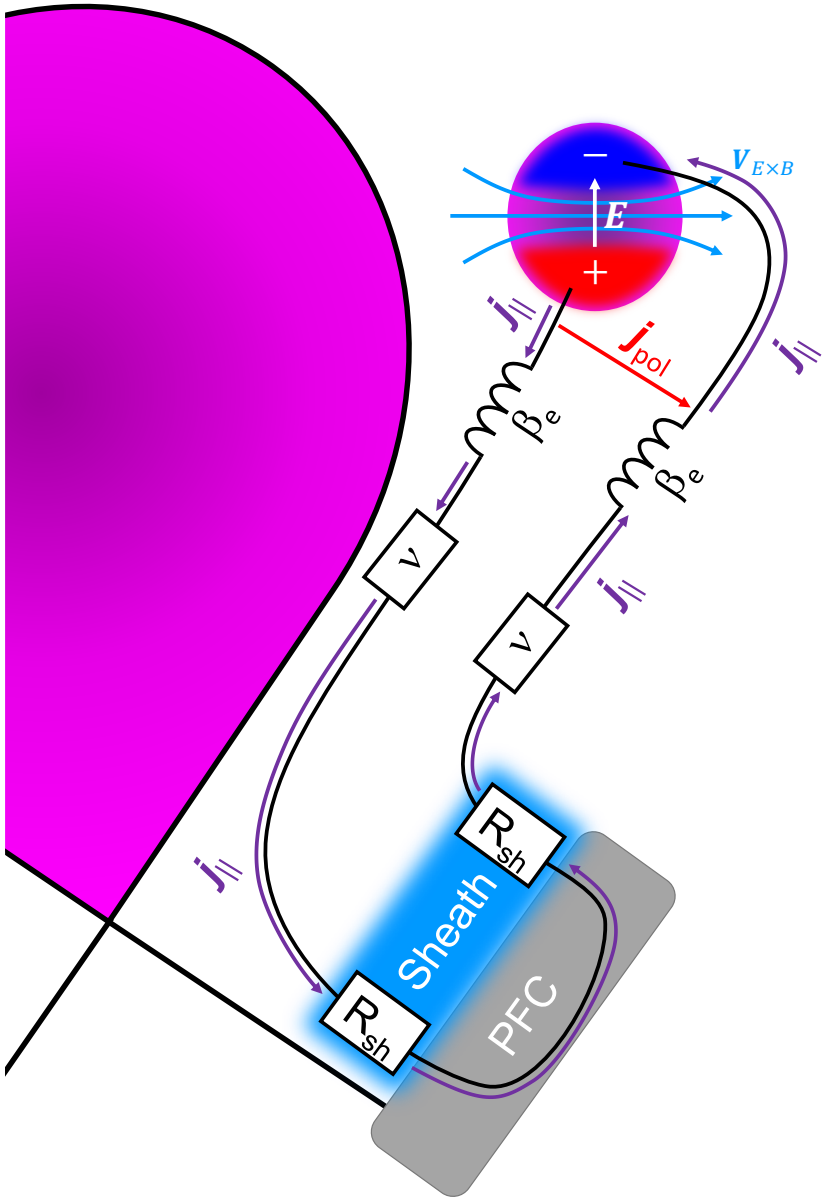

Figure 3.2: *Equivalent circuit diagram of a blob. The charge accumulation generated by the interchange drive is balanced by parallel currents,* $\mathbf{j}_{||}$*, and by the polarization current,* $\mathbf{j}_{\mathrm{pol}}$*. These currents reduce the dipolar electrostatic potential, and thus the blob velocity. The plasma sheath in front of plasma facing components (PFCs), described as a resistor* R_{sh}*, and collisions quantified by a collision frequency* ν *act as electric resistances, and reduce the parallel current. A finite electron beta,* β_{e}*, gives rise to parallel induction, which retards the parallel currents, hence it is described as an inductivity in the circuit.*

The discussed origin of blob motion can likewise be described by means of single particle drifts (see Appendix A) with the same result. In that case, the magnetic field curvature drift (or the associated ∇B-drift) can play a similar role as the the magnetic field dependent diamagnetic drift. Therefore, the radial blob motion is said to be attributed to the *curvature drive* and the related instability is the *interchange instability* [22, 257], which is the Rayleigh-Taylor instability for magnetized plasmas. This instability only occurs in "bad" curvature regions, i.e. in regions, where the pressure gradient of the main plasma, ∇p, and the curvature vector $\boldsymbol{\kappa}$ of the magnetic field line (or ∇B) are parallel, $\nabla p \cdot \boldsymbol{\kappa} > 0$. Regions of "good" curvature ($\nabla p \cdot \boldsymbol{\kappa} > 0$) are located on the HFS (= inboard side) of the tokamak. Since the outboard side of the tokamak is always a bad curvature region, it is natural that the blobs most prominently emerge there.

The interchange drive is always present and represents the only drive of blob motion (unless other subdominant effects as neutral wind [258] or the conducting wall instability [259] contribute). But the blob velocity is typically smaller than expected from the pure polarization without any loss of charges as discussed above. The reason is the following: The charge accumulation generated by the diamagnetic currents is reduced by means of perpendicular and parallel currents. This is depicted in figure 3.2, which schematically shows the possible paths of the currents reducing the blob polariztion. The interchange drive inside the blob at the midplane can be considered as a current source (battery), which drives currents parallel along the magnetic field lines, $\mathbf{j}_{||}$, and perpendicular to the field lines via the polarization current, $\mathbf{j}_{\mathrm{pol}}$. Different effects in certain regions of the plasma can modify the parallel currents, and can be considered as circuit components of an electric equivalent circuit [260]. The main control parameters for the reduction of the dipolar electrostatic blob potential, and thus the essential elements of the blob equivalent circuit, are:

1. **Polarization drift**

   In perpendicular direction, the polarization drift (see formular A.7 in Appendix A) of the ions giving rise to a polarization current, $\mathbf{j}_{\mathrm{pol}}$, provide a possibility to reduce the charge accumulation perpendicular to the magnetic field. This is most effective for small blobs, for which the ions have to drift only small distances to effectively compensate the dipolar potential structure. Since the polarization drift is the dominant contribution to the "inertial term" of the vorticity equation (see below), the effect of the polarization drift is sometimes summarized as the "effect of inertia" [261].

2. **Sheath resistivity**

   Under certain conditions, the magnetic field lines connect the drive region of the blob at the midplane with PFCs in the divertor or main chamber wall, so that a parallel current along the magnetic field lines, $\mathbf{j}_{||}$, can reduce the charge accumulation inside the blob. This parallel current is, in this case, limited by the resistance in the plasma sheath (also called electrostatic sheath or Debye sheath [20, 6]), which is the interface layer between PFCs and the plasma. Therefore, the sheath resistance R_{sh} determines eventually, how strong the polarization of the blob can be sustained and, thus, impacts its radial velocity [262].

3. **Collisions**

   Collisions of the current carrying species (typically electrons) with other plasma species (electrons, ions, impurities) or neutrals along the magnetic field lines act as a resistance for the parallel current $\mathbf{j}_{||}$. The collisions are represented by a (not further specified) collision frequency ν. The higher the collision frequency, the higher the resistivity, and, hence, the highest blob velocities. At very high resistivity, the parallel currents are so weak, that the blob electrically disconnects from the sheath at PFCs and inertial effects dominate [263, 264].

4. **Induction**

   At higher (electron) plasma beta, β_{e}, the parallel currents driven by parallel pressure gradients inside the blob are so strong, that magnetic induction plays a role. According to Lenz's rule, the magnetic field associated with the strong parallel currents induces an electric field antiparallel to the initial parallel current. This reduces the parallel currents and is represented by an inductance in the circuit [265]. Finite beta effects are also called "electromagnetic effects" in this context. Overall, induction controlled by β_{e} tends to increase the blob velocity. But the processes at higher beta are complex due to the involvement of emitted Alfvén waves, field line bending and mutual current attraction [39, 260, 265].

5. **Warm ions**

   A very important parameter, which cannot be represented in the equivalent circuit, is the ion temperature, T_{i}. In early versions of blob models, the ion temperature was neglected [262, 261]. However, the ion temperature in the SOL is finite and usually larger than the electron temperature [266, 267]. The influence of the ion temperature is at least

threefold [268, 241]: First, it provides an additional kinetic pressure contribution relevant for the interchange drive. Thus, a blob with a fixed electron temperature and with warm ions exhibits a larger charge accumulation than the same blob with cold ions, and, hence, the warm ion blob moves faster than the cold ion blob. Secondly, the warm ions give rise to a monopole potential structure, which is in phase with the initial pressure perturbation of the blob [269]. This leads to an internal rotation (spin) of the blob keeping it more coherent for longer distances and to a small poloidal propagation velocity component. Thirdly, warm ions modify the Bohm criterion and thus the sheath resistivity R_{sh}. In all three cases, higher ion temperatures lead to higher blob velocities.

The discussed effects are the main factors determining the blob dynamics, but further factors like neutrals [258], wall properties [259], the effect of magnetic geometry [263, 264] or 3D effects [270] are possible. They are, however, considered to be of minor importance for most of the plasma conditions in a tokamak.

3.2 Analytical Velocity Scaling Laws

The effects qualitatively introduced above can be quantified by means of simple analytical scaling laws for the blob propagation velocity v_{b}. They reveal the main parameter dependencies of v_{b} and typically contain a dependence on the blob size δ_{b}, which is the spatial extend of the blob in vertical (poloidal) direction. The following derivations are simplified approaches to derive the main dependencies of the blob velocity scalings. A more detailed and comprehensive overview of scaling laws including existence boundaries and scaling expressions combining several effects are given in [268].

Starting point of the derivation of scaling laws is the charge conservation being a prerequisite of the quasi-neutrality of a plasma. According to this, the divergence of parallel currents has to be balanced by the divergence of perpendicular currents

$$-\nabla \cdot \mathbf{j}_{\perp} = \nabla_{||} j_{||}. \tag{3.1}$$

For the perpendicular currents, $\mathbf{j}_{\perp}$, we consider the currents due to the generalized polarization drift [271] and the diamagnetic currents of electrons and ions (see equation A.9), so that equation 3.1 can be written as

$$\nabla \cdot \left(\frac{\partial}{\partial t} \left\{ \frac{n m_{\mathrm{i}}}{B^2} \nabla_{\perp} \phi + \frac{m_{\mathrm{i}}}{e B^2} \nabla_{\perp} p_{\mathrm{i}} \right\} + \frac{\nabla p_{\mathrm{e}} \times \mathbf{B}}{B^2} + \frac{\nabla p_{\mathrm{i}} \times \mathbf{B}}{B^2} \right) = \nabla_{||} j_{||}, \tag{3.2}$$

which can be derived from different types of plasma fluid equations or gyrofluid equations [270, 261, 268]. The identical equation can likewise by derived starting from the equation of motion and taking the curl of it [261, 272] and is referred to as vorticity equation [260] or polarization equation [268]. This equation describes the temporal evolution of the generalized vorticity $\tilde{\Omega} = 1/B^2 \nabla_\perp^2 \left(\phi + p_\mathrm{i}\right)$.

The divergence of the diamagnetic current can be related to the magnetic curvature (only perpendicular components are considered, since there is no diamagnetic current possible parallel to the magnetic field):

$$\nabla_\perp \cdot \mathbf{j}_\mathrm{dia} = \nabla_\perp \cdot \left(\frac{\mathbf{B} \times \nabla p}{B^2} \right) \tag{3.3}$$

$$= \left(\nabla \times \frac{\mathbf{B}}{B^2} \right)_\perp \cdot \nabla_\perp p \tag{3.4}$$

$$= \frac{2}{B} \mathbf{b} \times \boldsymbol{\kappa} \cdot \nabla_\perp p \tag{3.5}$$

with magnetic curvature vector $\boldsymbol{\kappa}$ and the unit vector in magnetic field direction $\mathbf{b} = \mathbf{B}/B$. The first equality is just the definition of the diamagnetic current (see equation A.9 in Appendix A), the second one made use of a vector identity, and in the last step (this is the difficult one, which is typically omitted in literature) makes use of the fact, that a vector $\boldsymbol{\eta}_\perp$ perpendicular to the magnetic field can be constructed from an arbitrary vector $\boldsymbol{\eta}$ by means of $\boldsymbol{\eta}_\perp = -\mathbf{b} \times (\mathbf{b} \times \boldsymbol{\eta}) = (\mathbf{b} \cdot \boldsymbol{\eta})\, \mathbf{b} - \boldsymbol{\eta}$. Using this, the identity $\left(\nabla \times \frac{\mathbf{B}}{B^2}\right)_\perp = -\mathbf{b} \times \left(\mathbf{b} \times \left[\nabla \times \frac{\mathbf{B}}{B^2}\right]\right)$ holds, which can be simplified by the application of many vector identities to $\mathbf{b} \times \boldsymbol{\kappa}/B + \mathbf{b} \times \nabla B/B^2$. At low beta, the identity $\nabla B/B = \boldsymbol{\kappa}$ can be employed to further simplify the latter as done in equation 3.5.

The relation 3.5 is very important, since it connects the local properties of the magnetic field configuration to the dynamics of the plasma fluid. Via this term, the fascinating but complex impact of the three-dimensional magnetic field geometry is introduced as used for plasma turbulence investigations [273, 274, 270]. It also should be mentioned, that the last term in equation 3.5 is proportional to the geodesic curvature $\kappa_\mathrm{g} = \boldsymbol{\kappa} \cdot (\mathbf{b} \times \nabla p/p)$ and thus responsible for the Pfirsch-Schlüter flows and currents (see section 2.1.1) as well as for the GAMs (see section 2.1.4).

The curvature vector $\boldsymbol{\kappa}$ in a tokamak can be simply expressed in terms of the curvature radius vector $\boldsymbol{\kappa} = -\mathbf{R}_\kappa / R_\kappa^2$ and the magnitude of the curvature radius is approximately the major radius R. Therefore, in this simplified geometry applicable to the outboard midplane in a tokamak (curvature vector

points radially inward), the vorticity equation 3.2 can be written as

$$\frac{\partial}{\partial t}\left\{\frac{n_0 m_\mathrm{i}}{B^2}\nabla_\perp^2\phi + \frac{m_\mathrm{i}}{eB^2}\nabla_\perp^2 p_\mathrm{i}\right\} = -\frac{2}{BR}\left(\nabla_\perp p_\mathrm{e} + \nabla_\perp p_\mathrm{i}\right) + \nabla_{||} j_{||}. \tag{3.6}$$

For this last step, it is assumed that the density n_0 interpreted as a background density and the magnetic field strength B do not vary much spatially, as typically assumed for blob scaling laws (referred to as Boussinesque approximation, see discussion in [260]). In contrast to the density n_0, which is considered as the background density, the pressure in this equation is interpreted as the perturbation amplitude of the blob.

As a next step, we use the blob correspondence principle [275, 39], which assumes, that spatial derivatives in equation 3.6 are related the perpendicular and parallel spatial extensions of the blob, δ_b and $\delta_{||}$, respectively and the time derivative is governed by the typical time scale of a blob, τ_b, interpreted as the lifetime or autocorrelation time of a blob (in fact it is the transit time of a blob to move a distance δ_b with a velocity of v_b), which can be expressed in terms of the blob velocity v_b and perpendicular blob size δ_b as $\tau_\mathrm{b} = \delta_\mathrm{b}/v_\mathrm{b}$. The magnitude of the electrostatic potential is related to the $E \times B$ velocity via $|\nabla_\perp\phi| = |\mathbf{E}| = |\mathbf{v}_\mathrm{E}|B$, so that the potential can be replaced by blob quantities according to the correspondence principle. We take into account relative phases by means of the imaginary unit i, so that the replacements according to the blob correspondence principle read:

$$\frac{\partial}{\partial t} \to \frac{i v_\mathrm{b}}{\delta_\mathrm{b}}, \quad \nabla_\perp \to \frac{i}{\delta_\mathrm{b}}, \quad \nabla_{||} \to \frac{i}{\delta_{||}}, \quad \nabla_\perp\phi = -v_\mathrm{b}B. \tag{3.7}$$

With these relations and expressing the ion pressure by means of the ion temperature to electron temperature ratio $\tau_\mathrm{i} = T_\mathrm{i}/T_\mathrm{e}$ as $p_\mathrm{i} = \tau_\mathrm{i} p_\mathrm{e}$, equation 3.6 can be written as

$$\frac{i v_\mathrm{b}}{\delta_\mathrm{b}}\left\{\frac{n_0 m_\mathrm{i}}{B^2}\frac{(-i)}{\delta_\mathrm{b}}v_\mathrm{b}B - \frac{m_\mathrm{i}}{eB^2}\frac{1}{\delta_\mathrm{b}^2}\tau_\mathrm{i}p_\mathrm{e}\right\} = -\frac{2i}{BR}\left(\frac{1}{\delta_\mathrm{b}}p_\mathrm{e} + \frac{1}{\delta_\mathrm{b}}\tau_\mathrm{i}p_\mathrm{e}\right) + \frac{i}{\delta_{||}}j_{||} \tag{3.8}$$

or after some rearrangements as

$$v_\mathrm{b}^2\frac{n_0 m_\mathrm{i}}{B\delta_\mathrm{b}} - i v_\mathrm{b}\frac{m_\mathrm{i}}{eB^2\delta_\mathrm{b}^2}\tau_\mathrm{i}p_\mathrm{e} = -i\frac{2}{BR}\left(1+\tau_\mathrm{i}\right)p_\mathrm{e} + i\frac{\delta_\mathrm{b}}{\delta_{||}}j_{||}. \tag{3.9}$$

This equation is the starting point for the derivations of different blob regimes below.

3.2.1 Inertial Regime

The inertial regime assumes that the blob dynamics is governed by "inertia", i.e. all mass dependent terms of equation 3.9, which result from the generalized polarization drift on the left hand side of the equation. Thus, the term with parallel currents vanish, and equation 3.9 reads in this case

$$v_\mathrm{b}^2 \frac{n_0 m_\mathrm{i}}{B\delta_\mathrm{b}} - i v_\mathrm{b} \frac{m_\mathrm{i}}{eB^2\delta_\mathrm{b}^2} \tau_\mathrm{i} p_\mathrm{e} = -i \frac{2}{BR} \left(1 + \tau_\mathrm{i}\right) p_\mathrm{e}. \tag{3.10}$$

For low ion temperatures, all terms with τ_i can be neglected and solving for v_b yields the cold ion inertial scaling as introduced in reference [261] with the typical square-root dependence on the blob size

$$|v_\mathrm{b}| = \sqrt{\frac{2\delta_\mathrm{b}}{nRm_\mathrm{i}} p_\mathrm{e}} = c_\mathrm{s} \sqrt{\frac{2\delta_\mathrm{b}}{R} n/n_0} \tag{3.11}$$

with sound velocity $c_\mathrm{s} = \sqrt{T_\mathrm{e}/m_\mathrm{i}}$ and the relative perturbation amplitude of the blob density n/n_0. As discussed in section 3.1, the curvature is the drive of the radial motion, and for small blob sizes the polarization drift is most effective to compensate the charge accumulation, so that smallest velocities are achieved for smallest blob sizes.

If the ions a very hot and/or the blob amplitudes very large, i.e. τ_i so large, that the first term in equation 3.10 is negligible, then the so called ion pressure dominated resistive ballooning regime is achieved [268]

$$|v_\mathrm{b}| = \frac{2eB\delta_\mathrm{b}^2}{m_\mathrm{i} R} \left(\frac{1 + \tau_\mathrm{i}}{\tau_\mathrm{i}}\right) = \frac{2\sqrt{2} c_\mathrm{s} \delta_\mathrm{b}^2}{\rho_\mathrm{s} R} \left(\frac{1 + \tau_\mathrm{i}}{\tau_\mathrm{i}}\right). \tag{3.12}$$

This is most relevant for small blob sizes, i.e. $\delta_\mathrm{b} < 10\rho_\mathrm{s}$ for typical parameters at the tokamak edge.

For larger blob sizes, the potential term (first term in equation 3.10) cannot be neglected and then the hot ion version of the classical inertial regime is achieved. This is called the conventional resistive ballooning regime [268]

$$|v_\mathrm{b}| = \sqrt{\frac{2\delta_\mathrm{b}}{n_0 R m_\mathrm{i}} \left(1 + \tau_\mathrm{i}\right) p_\mathrm{e}} = c_\mathrm{s} \sqrt{\frac{2\delta_\mathrm{b}}{R} \left(1 + \tau_\mathrm{i}\right) n/n_0}. \tag{3.13}$$

It is the warm ion version of equation 3.11.

3.2.2 Sheath-Limited Regime

In case that the plasma of the blob is attached to the sheath at the PFCs, and ion inertia terms are small, e.g. for large blob sizes, the dynamics of the blobs is governed by the sheath resistance R_{sh} as depicted in figure 3.2. This is called the sheath-limited or the sheath-connected regime, and the remaining terms of equation 3.9 for this case are

$$\frac{2}{BR}\left(1+\tau_{\mathrm{i}}\right)p_{\mathrm{e}} = \frac{\delta_{\mathrm{b}}}{\delta_{||}} j_{||}. \tag{3.14}$$

The parallel current $j_{||}$ is in this case determined by the current through the sheath for a given blob potential ϕ_{b} and can be described by the Langmuir-probe characteristics [20]

$$j_{||} \approx \frac{1}{2} e n_0 c_{\mathrm{s}} \left(1 - \exp\left(-\frac{e\phi_{\mathrm{b}}}{T_{\mathrm{e}}}\right)\right) \approx \frac{1}{2} e^2 n_0 c_{\mathrm{s}} \frac{\phi_{\mathrm{b}}}{T_{\mathrm{e}}}. \tag{3.15}$$

In the last approximation we assumed small potentials relative to the electron temperature $\phi_{\mathrm{b}}/T_{\mathrm{e}} \ll 1$.

With this, equation 3.14 can be written as a balance of the curvature drive and the sheath currents

$$\frac{2}{BR}\left(1+\tau_{\mathrm{i}}\right)p_{\mathrm{e}} = \frac{\delta_{\mathrm{b}}}{\delta_{||}} \frac{1}{2} e^2 n_0 c_{\mathrm{s}} \frac{\phi_{\mathrm{b}}}{T_{\mathrm{e}}}. \tag{3.16}$$

As before, the blob velocity is obtained from the potential according to the blob correspondence principle and the blob extension in parallel direction, $\delta_{||}$, is replaced by the parallel connection lengths of the field line, $L_{||}$, since the blob is assumed to be extended along the full length of the field line. This results in the sheath-connected scaling [262] for warm ions [268]

$$|v_{\mathrm{b}}| = \frac{\phi_{\mathrm{b}}}{\delta_{\mathrm{b}} B} = \frac{4 T_{\mathrm{e}} L_{||} \left(1+\tau_{\mathrm{i}}\right) p_{\mathrm{e}}}{n_0 e^2 B^2 R c_{\mathrm{s}} \delta_{\mathrm{b}}^2} = 4 c_{\mathrm{s}} \frac{L_{||}}{R} \left(\frac{\rho_{\mathrm{s}}}{\delta_{\mathrm{b}}}\right)^2 \left(1+\tau_{\mathrm{i}}\right) \frac{n}{n_0}. \tag{3.17}$$

In this scaling, the highest velocities are achieved for smallest blob sizes, and largest parallel connection lengths.

3.2.3 Role of Collisions

The effect of collisions on the blob velocity enters via the parallel currents in equation 3.9. A relation between currents and collisions is provided by the parallel Ohm's law [20]

$$-\nabla_{||}\phi = -\frac{1}{e n_0} \nabla_{||} p_{\mathrm{e}} + \frac{j_{||}}{\sigma_{||}} \tag{3.18}$$

with the parallel conductivity $\sigma_{||} = e^2 n_0/(m_\mathrm{e}\nu_\mathrm{ei})$, electron mass m_e and the electron-ion collision frequency

$$\nu_\mathrm{ei} = \frac{0.51 e^4 \ln\Lambda Z_\mathrm{i} n_\mathrm{e}}{3\sqrt{m_\mathrm{e}}\epsilon_0^2 (2\pi T_\mathrm{e})^{3/2}} \approx 0.795 \cdot 10^{-15} Z_\mathrm{i} n_\mathrm{e}/T_e^{3/2} \tag{3.19}$$

with ion charge number Z_i, Coulomb logarithm $\ln\Lambda$ [6], vacuum permittivity ϵ_0. For the approximated formula, $\ln\Lambda = 17$ is assumed and T_e has to be inserted in units of keV [20].

Solving equation 3.18 for $j_{||}$ and inserting the result in equation 3.9 yields

$$\frac{2}{BR}(1+\tau_\mathrm{i})\, p_\mathrm{e} = \frac{\delta_\mathrm{b}}{\delta_{||}}\sigma_{||}\frac{1}{\delta_{||}}\left(\frac{p_\mathrm{e}}{e n_0} - i v_\mathrm{b} B \delta_\mathrm{b}\right). \tag{3.20}$$

For this, all inertial terms were neglected and the blob correspondence principle was applied. The curvature drive is balanced by the parallel currents, which are limited by collisions through ν_ei. Equation 3.20 can be solved for v_b resulting in

$$v_\mathrm{b} = \frac{\frac{2}{B^2 R}(1+\tau_\mathrm{i})\, p_\mathrm{e} - \frac{p_\mathrm{e}}{e n_0 B \delta_\mathrm{b}}\frac{\delta_\mathrm{b}^2}{\delta_{||}^2}\sigma_{||}}{\frac{\delta_\mathrm{b}^2}{i\delta_{||}^2}\sigma_{||}} \approx \frac{\frac{2}{B^2 R}(1+\tau_\mathrm{i})\, p_\mathrm{e}}{\frac{\delta_\mathrm{b}^2}{i\delta_{||}^2}\sigma_{||}}. \tag{3.21}$$

The approximation is justified, since $\delta_\mathrm{b}^2/\delta_{||}^2$ is a very small number and the conductivity in this collisional regime is assumed to be low. Thus, the blob speed in the collisional regime is [268]

$$|v_\mathrm{b}| = \frac{2}{B^2 R}(1+\tau_\mathrm{i})\, p_\mathrm{e}\frac{\delta_{||}^2}{\delta_\mathrm{b}^2}\frac{m_\mathrm{e}\nu_\mathrm{ei}}{e^2 n_0} = 2 c_\mathrm{s}\frac{\delta_{||}^2}{R L_{||}}\left(\frac{\rho_\mathrm{s}}{\delta_\mathrm{b}}\right)^2 (1+\tau_\mathrm{i})\frac{n}{n_0}\Lambda_\mathrm{ei}. \tag{3.22}$$

The blob speed scales inversely with the blob size δ_b and is large for larger collision frequencies. As argued in reference [263, 180], this scaling only applies when $\Lambda_\mathrm{ei} = L_{||}\sqrt{m_\mathrm{e}}/\lambda_\mathrm{ei}\sqrt{m_\mathrm{i}} = \nu_\mathrm{ei} L_{||} m_\mathrm{e}/(m_\mathrm{i} c_\mathrm{s}) > 1$, i.e. when the mass ratio normalized mean free path due to electron-ion collisions λ_ei is shorter than the parallel connection length of the magnetic field line. The collisional scaling 3.22 is very similar to the sheath-limited scaling 3.17 if $\delta_{||} = L_{||}$ is assumed and differs then only by a factor of $\Lambda_\mathrm{ei}/2$.

3.3 What Determines the Size of Blob Filaments?

The *size of a blob*, as it is understood in the following, is the spatial extend of the blob in the plane perpendicular to the magnetic field line (e.g. the circular cross section of the filament shown in figure 2.17). It is sometimes also called *blob width* in order to discriminate it from the *blob amplitude*, i.e. the density or temperature perturbation associated with the blob.

In a first step, the size of a blob depends on the initial pressure perturbation close to the LCFS providing a seed for the blob generation. The initial pressure perturbation can be considered as a result of a (linearly) growing instability or, more realistically, as a large turbulent fluctuation from the typical edge turbulence. This initial pressure perturbation starts to move radially outward through the SOL towards the first wall due to the mechanism described above (see figure 3.1). In a second step, the initial size of the blob is modified by *secondary instabilities*. The two most important secondary instabilities are the Kelvin-Helmholtz instability, which fragments the blob filament due to strong local velocity components into smaller parts, or the interchange instability, which splits up the filament into Rayleigh-Taylor fingers due to the bad curvature at the outboard side at the tokamak [276]. While the Kelvin-Helmholtz instability can fully fragment small blobs to undetectable amplitudes by distributing the initial perturbation over a wider area (see figure 3.3, bottom), the interchange drive acts most severely on large blobs (see figure 3.3, top). Only blobs on intermediate scales, which are too small to be severely affected by the interchange instability, but sufficiently large to withstand the Kelvin-Helmholtz instability, can propagate significantly far radially outwards as a singular structure (figure 3.3, middle row). At high dissipation levels determined by viscosity and diffusion, the blob is very coherent since it is less prone to the Kelvin-Helmholtz instability and smaller gradients lead to likewise smaller interchange drive [276].

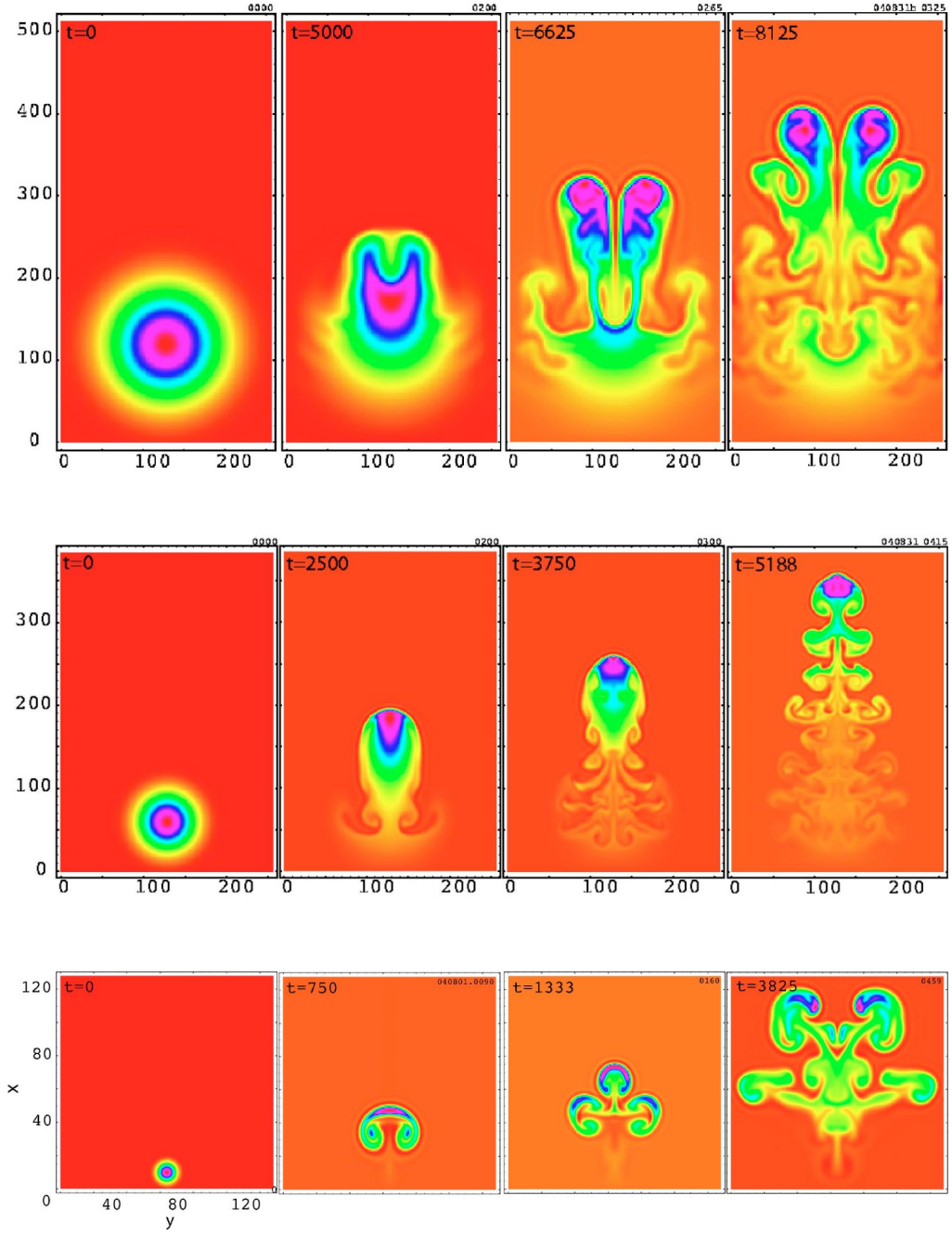

Figure 3.3: *Blob size and secondary instabilities in a seeded blob simulation (adapted from [276]). Large blobs (top row) are subject to the interchange instability and split up into Rayleigh-Taylor fingers. Small blobs (bottom row) are fragmented quickly by the Kelvin-Helmholtz instability. Blobs of a particular intermediate size (middle row) are too small for strong Rayleigh-Taylor effects and sufficiently large to withstand the Kelvin-Helmholtz instability, so that they can propagate as a singular structure for longer distances than in the other cases.*

3.4 Analytical size scalings

Analytical expressions for the size of blobs can be obtained similarly as done for the velocity scalings derived from the vorticity equation 3.9. Let's assume for the sake of simplicity, that the parallel terms are given by the sheath connected physics as in equation 3.16, and that the ion diamagnetic contribution to the polarization term (second term in equation 3.9) is small. In this case the simplified vorticity equation reads

$$v_\mathrm{b}^2 \frac{n_0 m_\mathrm{i}}{B\delta_\mathrm{b}} = -i\frac{2}{BR}\left(1+\tau_\mathrm{i}\right)p_\mathrm{e} + \frac{\delta_\mathrm{b}}{\delta_{||}}\frac{1}{2}e^2 n_0 c_\mathrm{s}\frac{v_\mathrm{b} B\delta_\mathrm{b}}{T_\mathrm{e}}. \tag{3.23}$$

For very large blobs with $\delta_\mathrm{b} \to \infty$, the polarization term (first term in equation 3.23) is of minor importance, and the dynamics is given by the sheath-limited scaling. In this case the blobs are very slow (see equation 3.17), thus, the Kelvin-Helmholtz instability does not play a role, but the large size and the slow velocity gives rise to interchange fingers as seen in simulations [276] (see figure 3.3). For very small blobs $\delta_\mathrm{b} \to 0$, the sheath dissipation term (last term in equation 3.23) can be neglected and the blobs are in the inertial regime. In this regime with low dissipation, the blobs form mushroom-like propagation fronts as seen in simulations [261, 276] or even neutral fluids [277]. Thus, they are strongly affected by the Kelvin-Helmholtz instability. Only at an intermediate scale δ_*, for which both affects are minimized, the blobs can sustain longer as a coherent singular structure. Formally, the scale δ_* can be derived by equating the sheath dissipation term with the polarization term, i.e.

$$v_\mathrm{b}^2 \frac{n_0 m_\mathrm{i}}{B\delta_\mathrm{b}} = \frac{\delta_\mathrm{b}}{\delta_{||}}\frac{1}{2}e^2 n_0 c_\mathrm{s}\frac{v_\mathrm{b} B\delta_\mathrm{b}}{T_\mathrm{e}}. \tag{3.24}$$

One v_b cancels on each side of the equation, and the remaining v_b can be replaced by the sheath-limited scaling (equation 3.17), since it is believed that the scaling is still valid at the boundary between the two regimes. Solving for δ_b yields

$$\delta_* = \delta_\mathrm{b} = \sqrt[5]{8\left(1+\tau_\mathrm{i}\right)\frac{n}{n_0}\frac{L_{||}^2}{R\rho_\mathrm{s}}}. \tag{3.25}$$

Although δ_* was derived from simple analytical scaling laws, it was confirmed in more complex numerical simulations, that it describes acceptably well the size of blobs in the respective regime [260], when the diffusion and viscosity is sufficiently high [276]. Similar expressions for δ_* can be derived for other blob regimes. The most complete set of characteristic blob sizes given by certain regime boundaries are presented in reference [268].

3.5 Measured Blob Sizes and Velocities

The theoretical scaling laws for size and velocity of blobs presented above can be tested experimentally. For this purpose, beam emission spectroscopy based on a neutral lithium beam (Li-BES) at AUG is used to determine the relevant blob parameters. After introducing the diagnostic principle, blob parameters like amplitudes, frequency, size and velocities are presented. In a last step, they are compared to the relevant scaling laws. This section reproduces in large parts results from reference [256].

3.5.1 Blob Detection with Li-BES

The lithium beam emission spectroscopy (Li-BES) system at AUG injects a neutral beam of lithium atoms at typically around 50 kV radially into the plasma. Due to the interaction with the plasma (mainly by electron impact excitation) the lithium atoms are excited and radiate electromagnetic line emission, which is detected with a spectrometer or by filter-photo multipliers [278, 279, 280, 281]. The neutral lithium beam is ionized further inside the plasma, so that the relevant neutral line emission decreases after reaching a maximum intensity slightly inside the LCFS. Thus, the Li-BES signals are highest in the region of interest to measure blobs, i.e. slightly inside the LCFS and in the SOL.

It turned out, that it is sufficient to detect the 670.8 nm line of the neutral lithium atom (Li_{2p-2s} transition) in order to reconstruct the electron density profile at the plasma edge from the measured line emission [282]. Therefore, the Li-BES diagnostic is a routine diagnostic to measure electron density profiles at the plasma edge with high precision and a comparably high time resolution (typically one profile per millisecond).

For blob studies, the side optics ("new optical head" as described in [281]) with a toroidal view approximately along the magnetic field lines is used. It detects the light from volumes covering a radial region from about $\rho_{\mathrm{pol}} = 0.90$ to $\rho_{\mathrm{pol}} = 1.05$ given by the crossing points of the 26 lines of sight (LOS) with the lithium beam. Due to the acquisition frequency of 200 kHz of the rawsignal and a moderate but appropriate signal-to-noise ratio, the Li-BES diagnostic at AUG is well suited to detect blobs.

3.5.2 Experimentally Determined Blob Parameters

In order to study the magnetic field and the plasma current dependence of certain blob parameters, Li-BES signals were measured in a set of L-mode discharges with different parameters listed in table 3.1.

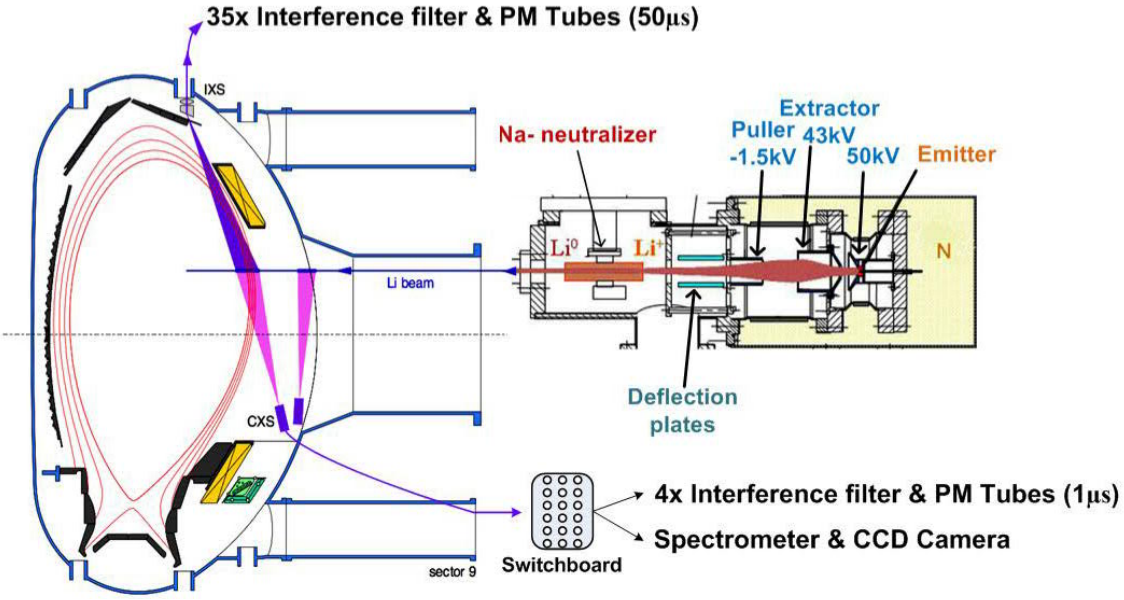

Figure 3.4: *Setup of the lithium beam emission spectroscopy (Li-BES) system at AUG (adapted from [280]). Lithium ions are extracted thermoionically from an β-eukryptite emitter and accelerated towards the plasma. In a sodium vapor cell, the ion beam is neutralized and the neutral lithium beam is injected about 32 cm above the midplane. The light is most intense in the SOL and around the LCFS and is detected by 35 filter-photo multipliers from the top and by further 26 channels parallel to the magnetic field lines in toroidal direction (not shown).*

B_t (T)	I_p (MA)	q_{95}	$L_{\|\|}$ (m)	$f_G W$	discharge	time interval (s)	
-2.5	0.6	6.85	14.99	0.35	#29302	[2.9,3.3]	$I_p \approx$ const
-1.8	0.6	4.96	10.80	0.35	#29303	[2.9,3.3]	
-1.4	0.6	3.85	9.00	0.37	#29306	[2.9,3.3]	
-1.4	0.6	3.85	9.00	0.35	#29307	[2.9,3.3]	
-3.2	0.6	8.72	18.90	0.35	#29308	[2.9,3.3]	
-2.5	0.83	4.90	10.90	0.25	#29309	[2.9,3.3]	$q_{95} \approx$ const
-1.4	0.47	5.00	11.50	0.45	#29310	[2.9,3.3]	
-1.8	0.6	4.94	10.90	0.35	#29311	[2.9,3.3]	
-1.8	0.6	4.96	11.10	0.36	#29312	[2.9,3.3]	
-3.2	1.07	4.96	10.80	0.22	#29315	[2.6,3.0]	

Table 3.1: *Toroidal magnetic field B_t, plasma current I_p, edge safety factor q_{95}, parallel connection length $L_{||}$ at $\rho_{pol} = 1.044$ from magnetic field line tracing, Greenwald fraction f_{GW}, discharge number and considered time interval of the analyzed discharges.*

The varied main parameters are the toroidal magnetic field B_t, plasma current I_p and, as a consequence, the edge safety factor q_{95} and likewise the connection length at the radial position of ρ_{pol}= 1.044 calculated by a magnetic field line tracing code. The density was kept the same, i.e. the edge electron density profiles were identical within errors for the analyzed time ranges in all plasmas [256]. However, due to different plasmas currents, the Greenwald fraction $f_{GW} = \bar{n}/n_{GW}$ defined as the ratio between the central line-averaged density $\bar{n}$ measured with a laser interferometer [283] and the Greenwald density $n_{GW} = I_p/(\pi a^2)$ [284] with minor plasma radius a. Nevertheless, the Greenwald fractions are low, hence the plasmas were operated far away from the L-mode density limit.

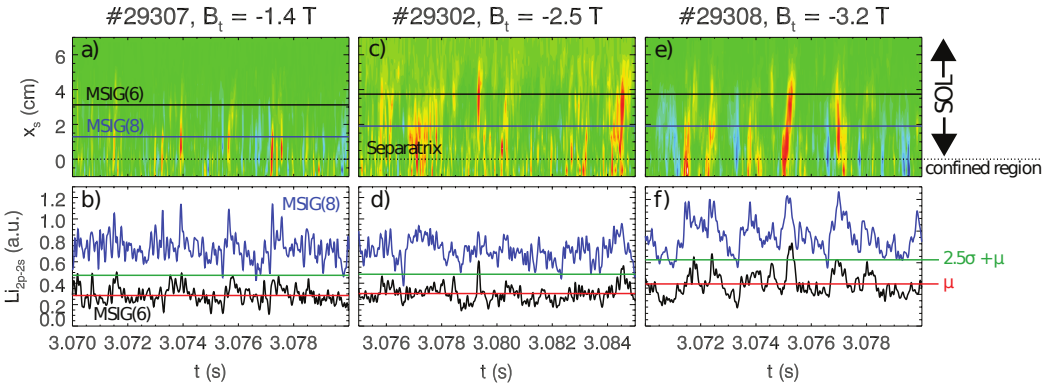

Figure 3.5: *Time traces of the Li-BES intensity signals for different magnetic fields (repdoduced from [256]). The upper row shows the intensity of the Li-BES signal (mean subtracted) for different radial distance to the separatrix x_s in the SOL (red color corresponds to higher intensity) versus time. Solid lines in the upper row indicate the radial positions of two selected signals MSIG(6) (black) and MSIG(8) (blue) shown in the lower row. The red line indicates the temporal mean μ and the green line the 2.5σ threshold value for conditional averaging of the lower time series (adapted from [256]).*

Some example time traces of Li-BES signals with blobs for plasmas at different magnetic fields are shown in figure 3.5. The upper row shows the color coded the intensity (blue are low, red are high values) of the Li-BES signal at different radial positions in a distance x_s from the LCFS versus time. $x_s > 0$ indicates the SOL outside the LCFS (referred to as separatrix in the figures), and $x_s < 0$ are positions inside the LCFS. The temporal mean value μ was subtracted from the time traces and the signals were filtered with a low-pass Butterworth filter with a cutoff frequency of 20 kHz for the color coded panels. The lower row shows two selected filtered time traces without

background subtraction, MSIG(8)[1] close to the LCFS in the near SOL, i.e. in a distance of about one power-fall of length from the LCFS, and MSIG(6) further out in the far SOL, i.e. more than one power-fall of length away from the LCFS. For the lower time trace, the temporal average μ and the level of 2.5 standard deviations σ is indicated by vertical lines. It is an arbitrary, but common tradition in blob analysis, to consider events with a transient amplitude larger than 2.5σ as a blob [39]. Therefore, the same condition is also used in the analysis presented here. Especially for the data at higher magnetic field, for which the blobs seem to be larger in amplitude, the large events exceeding the 2.5σ-condition in MSIG(6) are indeed likewise visible in the color coded panels and appear there as red elongated structures. They are sometimes tilted, typically to the right, in the $x_\mathrm{s} - t$ plane indicating that they are propagating outward away from the LCFS towards the wall with a speed of about 100 m/s.

The individual blobs visible in the raw data slightly differ in amplitude, frequency, velocity and duration. In order to extract *typical* parameters of the blobs, i.e. an average amplitude, frequency, velocity and duration, which can then be compared to typical quantities predicted by the blob scaling laws, a statistical evaluation of the blobs is required. Due to the low signal-to-noise ratio of the Li-BES data, a determination of distribution functions of blob parameters based on the evaluation of single blobs is not possible. Thus, the conditional average technique [285, 286] is the best choice for this type of signals. For this purpose, first, individual blobs are detected by the 2.5σ-condition in the MSIG(6) signal, which serves in this case as the reference channel. The signals of a time window of 100 µs before and 100 µs after reaching the 2.5σ-condition is stored for each detected blob. Time traces for the same time windows are likewise stored for MSIG-channels from other radial positions. In a second step, the stored time windows from each MSIG-channel are averaged separately, and as a result a single characteristic conditional averaged spatio-temporal intensity pattern $I(x_\mathrm{s}, \Delta t)$ with a window length of $\Delta t = 200$ μs is obtained. This procedure implicitly assumes, that all individual blobs are sufficiently similar, so that the conditionally averaged result represents the typical properties, which all blobs exceeding the 2.5σ-condition share.

An example of the intensity pattern $I(x_\mathrm{s}, \Delta t)$ resulting from conditional averaging of the data in discharge #29302 is shown in figure 3.6a. Similar as in the raw signal in figure 3.5c, a tilted positive intensity pattern is found.

[1] MSIG is just a meaningless signal name for the Li-BES signals and the number is the channel number

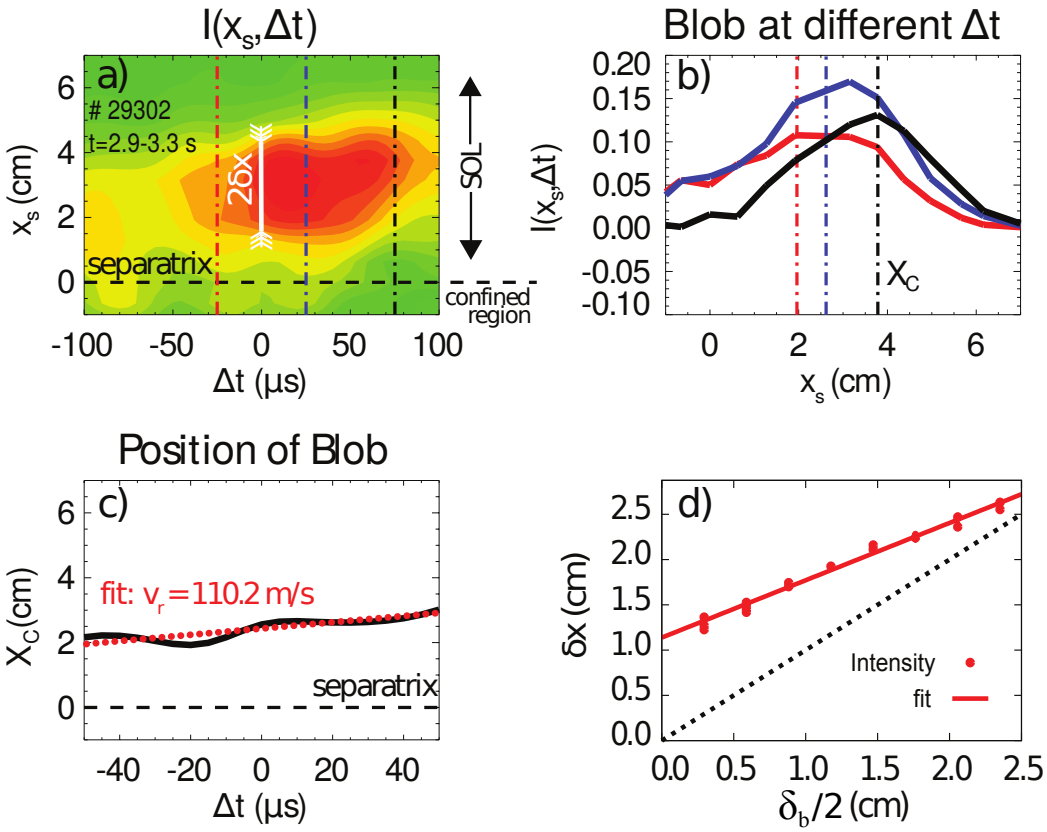

Figure 3.6: *(a) Color coded representation of the radial-temporal data $I(x_s, \Delta t)$ resulting from conditional averaging (red color corresponds to high intensity). (b) Radial profiles of the intensity response at different Δt and the corresponding center-of-mass position X_C (dashed lines). The different colors indicate different Δt shown as dashed lines in (a). (c) Temporal evolution of the center-of-mass position (solid) and linear fit for velocity estimation (dotted). (d) Relation between measured intensity width δx and model predicted density blob width δ_b. The solid line indicates a linear fit of the simulation data (circles) and exceeds the one-to-one relation $\delta x = \delta_b/2$ (dashed). Adapted from [256].*

From this pattern the most relevant quantities like blob amplitude, radial extension of the blob and blob velocity can be extracted. The first quantity, which can be obtained from $I(x_s, \Delta t)$, is the apparent radial blob width δx. It is determined as the half-width at the half maximum (HWHM) of the intensity peak at $\Delta t = 0$, i.e. of $I(x_s, 0)$ (see figure 3.6a). Unfortunately, the width of the actual density perturbation of a blob is not the same as the width determined from the intensity of the detected Li-BES signals as simulations with a forward model of Li-BES including a collisional-radiative

model show [281]. The reason is the finite lifetime of the Li_{2p-2s} state, so that the line emission associated with a density perturbation is distributed over a finite length along the neutral beam path after its excitation. As a result, the blobs appear to be larger in the Li-BES intensity, quantified by δx, than they actually are in terms of the width of the density perturbation δ_b. By means of the radiative collisional model, however, it is possible to translate the apparent blob width δx into the actual blob width δ_b (or blob radius, $\delta_b/2$). The result of such a simulation is shown in figure 3.6d.

The blob velocity can be extracted from the conditionally averaged data in the following way. First, a center of mass coordinate is defined as

$$X_c = \frac{1}{Q}\int x_s I(x_s, \Delta t) dx_s \quad \text{with} \tag{3.26}$$

$$Q = \int I(x_s, \Delta t) dx_s. \tag{3.27}$$

It represents the weighted average of the blob perturbation along the spatial coordinate x_s and is well defined for each time step Δt separately as shown in figure 3.6b. Second, the temporal derivative of the center-of-mass trajectory $X_c(t)$ provides the instantaneous blob velocity, from which a maximum velocity

$$v_{r,max} = \max\left\{\frac{dX_C(\Delta t)}{d\Delta t}\right\}, \tag{3.28}$$

can be determined. As shown in figure 3.6c, a linear fit of the blob trajectory in the X_c-Δt-plane provides the average velocity $v_{r,mean}$. The two definitions of the radial velocity, $v_{r,max}$ and $v_{r,mean}$, provide an upper and lower limit of the measured the velocities.

The measured relative intensity perturbation $\delta I/I$ is determined as the ratio of the maximum of $I(x_s, \Delta t)$ divided by the temporal average of $I(x_s, \Delta t)$ at the location of the reference channel. Similar as for the blob width, this apparent relative amplitude has to be translated into the corresponding relative density perturbation amplitude $\delta n/n$ by means of the collisional-radiative model [281].

The lifetime of the blob or more specifally the transit time of the blob at the Li-BES channel, τ_b, is determined similarly as δx from $I(x_s, \Delta t)$. It is determined as the full-width at the half maximum (FWHM) of $I(x_s, \Delta t)$ of the reference probe along the time axis.

The blob frequency given as the number of blobs per second, is simply the number of time points, for which the 2.5σ-condition (at a rising edge and after an idle time of 500 µs after the previous conditional time point) is fulfilled.

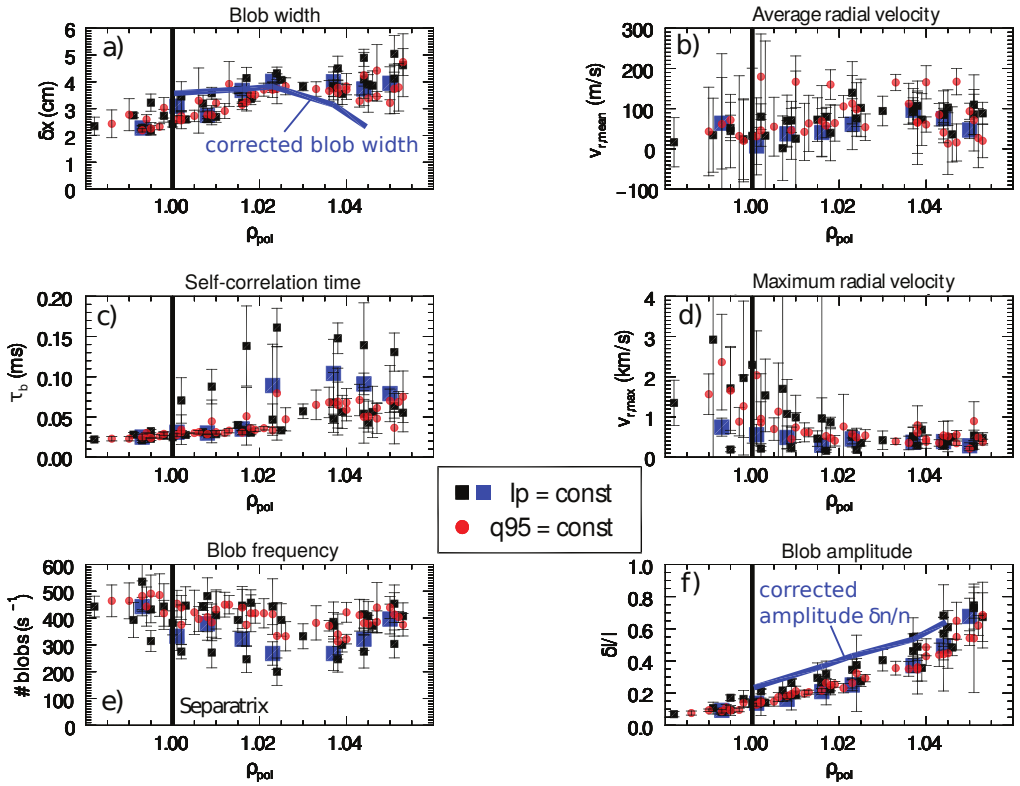

Figure 3.7: *Radial width of the blobs in the emission profile δx (a), average radial blob velocity $v_{\mathrm{r,mean}}$ (b), self-correlation time τ_{b} (c), maximum radial blob velocity $v_{\mathrm{r,max}}$ (d), blob frequency (e), and relative intensity $\delta I/I$ (f) from conditional averaging depending on the radial position of the reference channel for discharges with constant I_{p} (boxes) and q_{95} (circles). The blue lines in (a) and (f) indicate the translated values $\delta x \rightarrow \delta_{\mathrm{b}}/2$ and $\delta I/I \rightarrow \delta n/n$ for selected data points in discharge #29302 (blue boxes). Adapted from [256].*

In total, the conditional average technique provides the radial blob extension δx or translated the blob width δ_b, the average velocity $v_\mathrm{r,mean}$, the blob transit time τ_b, the maximum velocity $v_\mathrm{r,max}$, blob frequency, and the relative blob amplitude $\delta n/n$ at the location of the reference channel (in this example it was MSIG(6)). Choosing different reference channels allows to obtain the different blob parameters at different radial position, so that it is possible to determine radial profiles of blob parameters. This is shown in figure 3.7, which depicts radial profiles of blob quantities for the set of discharges given in table 3.1. Despite the magnetic field and the plasma current were varied in this set of plasmas, the blob parameters remain roughly the same for the whole set. The strongest variation is found in the blob frequency and the blob transit time. The blob transit time τ_b scales with q_{95} and is highest in the plasma with highest edge safety factor. On the contrary, the blob frequency decreases with q_{95} and is lowest for the highest q_{95} [256]. All other blob parameters do not show any clear dependence on plasma parameters. Since the connection length of the magnetic field is related to the edge safety factor as $L_{||} \sim q_{95}R$, the found dependencies of the lifetime might be related to processes parallel to the magnetic field lines.

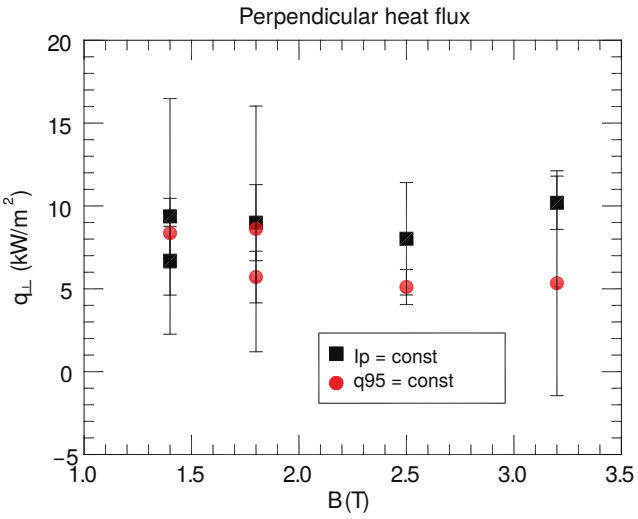

Figure 3.8: *Peak ion heat flux of a single blob depending on toroidal magnetic field B_t (adapted from [256]).*

The peak ion heat flux carried by a single blob estimated as $q_{\perp,i} = T_\mathrm{i}\delta n v_r$ likewise shows no strong dependence on the magnetic field as shown in figure 3.8. $q_{\perp,i}$ is calculated assuming an ion temperature of $T_\mathrm{i} = 100$ eV as mea-

sured in filaments with a retarding field analyzer in L-mode [266]. The radial velocity is set to $v_r = v_{\mathrm{r,max}}$ as an upper limit, and the measured δn are in the range of $\delta n \approx 0.6$ to $2.0 \cdot 10^{18}$ m^{-3}. Therefore, the peak ion heat flux of a blob amounts to several kW/m^2 and is therefore orders of magnitudes smaller than the parallel heat flux which is in the range of several MW/m^2 as measured with thermography on divertor target plates in the considered discharges. This demonstrates that the perpendicular transport of blobs in these low density discharges is negligible and the blobs are not able to produce relevant heat loads on PFCs. Further details to the measurement procedure and more results of these study can be found in reference [256].

3.5.3 Blob Size and Velocities

The measured blob quantities presented above can now be compared to the blob scaling laws introduced in section 3.2 and 3.4. For this purpose, the blob velocities are normalized to the sound velocity $c_\mathrm{s} = \sqrt{(T_\mathrm{e} + T_\mathrm{i})/m_\mathrm{i}}$, for which the electron temperature $T_\mathrm{e} = 15$ eV measured at a radial position $\rho_\mathrm{pol} = 1.044$ with the Thomson scattering diagnostic [287] was used and an electron-to-ion temperature ratio $\tau_\mathrm{i} = 3$ was assumed as measured with a retarding field analyzer in comparable discharges [266].

First, the blob sizes δ_b measured at a radial position $\rho_\mathrm{pol} = 1.044$ are compared with the size scaling formula δ_* of equation 3.25. This is shown in figure 3.9a assuming a circular cross section of the blobs, i.e. that the radial and poloidal diameter of the blobs are the same. The measured blob sizes δ_b do not agree very well with δ_*, when cold ions, i.e. $\tau_\mathrm{i} = 0$, are assumed (blue symbols). The agreement improves, when warm ion effects are included via $\tau_\mathrm{i} = 3$. This indicates, that warm ion effects could play a role determining the blob size. Similar results were obtained with a gas-puff imaging diagnostic at AUG [176].

Secondly, the measured radial maximum velocities, $v_{\mathrm{r,max}}$ are normalized to c_s and then drawn against the measured blob size normalized to the (mixed) Larmor radius ρ_s (black circles in figure 3.9b). Inserting the measured δ_b, $\delta n/n$, and the radial detection position $R = 2.155$ m into the inertial scaling law equation 3.13, we obtain velocities in the range of $v_r/c_s \approx 0.1$ which is more than an order of magnitude larger than the measured velocities (for cold ions as well as warm ions). Together with the fact that the measured velocities rather decrease with increasing blob size in contrast to the scaling, we exclude a blob dynamics dominated by inertial effects for the considered data set. This is supported by the measured blob sizes which tend to be larger than the size boundary between sheath-connected and inertial regime, δ_*, resulting in a minor contribution of inertial effects [288, 276].

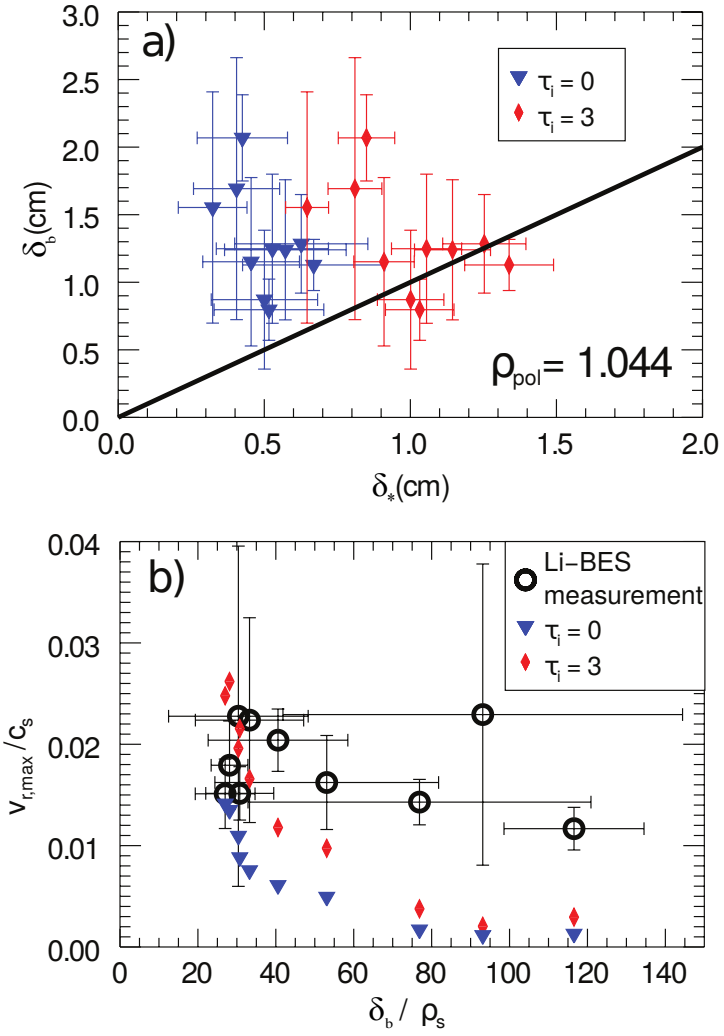

Figure 3.9: *Measured blob sizes δ_b compared with the size scaling δ_* according to equation 3.25 (a), and measured normalized radial blob velocities v_r/c_s (black symbols) versus normalized blob size δ_b/ρ_s (b). The measured blob sizes agree better with the size scaling, when a finite ion temperature with $\tau_i = 3$ (red symbols) is assumed instead of the cold ion approximation $\tau_i = 0$ (blue symbols). Similarly, the measured normalized velocities agree better with the warm ion sheath-connected scaling assuming $\tau_i = 3$ than with the cold ion scaling assuming $\tau_i = 0$ (adapted from [182]).*

The agreement between measurements and scaling law improves a lot, when the sheath-connected scaling equation 3.17 is compared with the data. The order of magnitude of the scaling agrees with the measurements and the warm ion version of the scaling with $\tau_\mathrm{i} = 3$ agrees better with the measurements than the cold ion version ($\tau_\mathrm{i} = 0$). The velocities in both the scalings as well as the measurements tend to be lower for larger normalized blob sizes, which can be interpreted as a further indication, that the velocity as well as the size is dominated by sheath-limited effects.

For the considered data set, which was taken at low density for which collisional effects should not play a role, and electromagnetic effects are likewise negligible due to the low beta of the SOL, a reasonable agreement of measured blob sizes and velocities with the respective formulas of the sheath-limited regime was found. In agreement with measurements of the ion temperature in the SOL [266], the data agrees better with the warm ion version of the scalings choosing $\tau_\mathrm{i} = 3$ indicating that warm ion effects are important for the blobs dynamics in the SOL.

3.6 Blobs and Density Shoulder Formation

As shown above on the basis of a low density data set, the blob parameters do not change much with macroscopic parameters like the magnetic field or the plasma current. But they change drastically when the density is risen above a certain threshold. This is shown in figure 3.10 for a data set presented in reference [180].

For low densities below $f_\mathrm{GW} = 0.45$ expressed in terms of the Greenwald fraction $f_\mathrm{GW} = \bar{n}/n_\mathrm{GW}$, the considered blob parameters transit time τ_b, blob frequency f_blob, blob amplitude δn, radial maximum velocity $v_\mathrm{r} = v_\mathrm{r,max}$ and the blob transport estimated as

$$\Gamma_\mathrm{blob} = \tau_\mathrm{b} f_\mathrm{blob} v_\mathrm{r} \delta n \tag{3.29}$$

do not change much with density. But above $f_\mathrm{GW} = 0.45$ most of the parameters increase by almost an order of magnitude. Above this critical density of $f_\mathrm{GW} = 0.45$ the local value of the background profile at $\rho_\mathrm{pol} = 1.02$ likewise rises.

The reason for this drastic change in blob properties is shown to be related to the parallel collisionality parameter Λ_ei [180, 289]. For low collisionality, i.e. for $\Lambda_\mathrm{ei} < 1$ as it is the case for the low density data set presented in section 3.5.2, the blobs are in the sheath-limited regime (equation 3.17) and comparably slow. The reason for the jump in blob properties could be related to a feedback loop: If the density is increased above a certain value,

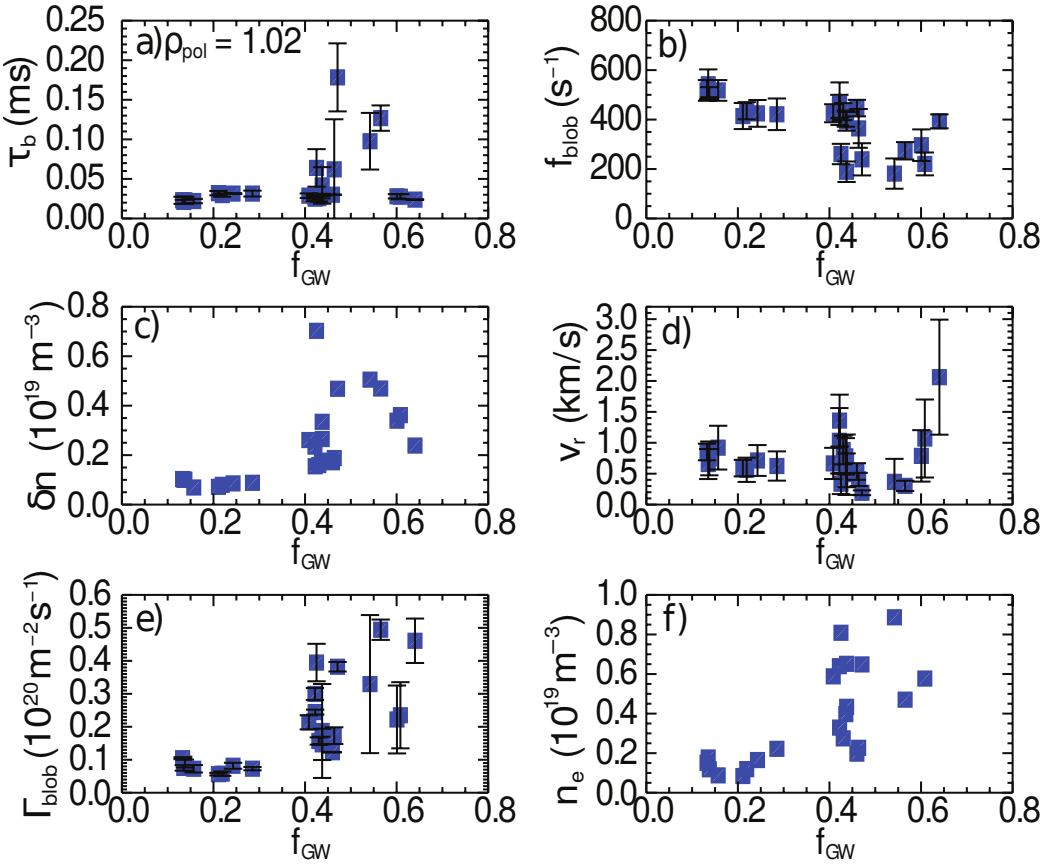

Figure 3.10: *With rising density (expressed as Greenwald fraction $f_{\mathrm{GW}} = \bar{n}/n_{\mathrm{GW}}$), the blobs transition from a sheath-connected regime into a regime of enhanced convective transport associated with larger transit time (a), lower blob frequency (b), larger amplitude (c), higher radial maximum velocity (d), and increased blob transport (e). The local background density at $\rho_{\mathrm{pol}} = 1.02$ (f) is likewise increased (adapted from [182]).*

so that $\Lambda_{ei} > 1$, the blob dynamics enters the collisional regime and the scaling equation 3.22 applies, which introduces an additional temperature and density dependence to the scaling $\Lambda_{ei} \propto n_e T_e^{-2}$. Due to the higher blob velocity under these conditions, the blob transport increases according to equation 3.29 and thus cools down the SOL plasma at the considered location due to increased perpendicular heat transport caused by (convective) blob transport. This decreases the temperature there, and hence non-linearly increases Λ_{ei}, which leads to even more blob transport and further cooling of the SOL. Finally, a relatively cool SOL and a state of faster and larger blobs inducing more perpendicular transport is achieved.

Under such conditions, a shoulder of the SOL electron density profile is observed as it is shown in figure 3.11 for two tokamaks, AUG (left) and JET (right). The shoulder appears for a Greenwald fraction above $f_{GW} = 0.45$, i.e. for the same values for which the blob transport is strongly increased (see figure 3.10). This correlation of a density shoulder in the SOL and a change of blob properties suggests that the blobs are causing the shoulder due to their involved enhanced perpendicular transport. Since the Li-BES profiles shown in figure 3.11 are profiles averaged over 1 ms, i.e. a time scale much larger than the blob time scale, they can be considered as a temporal average of many blobs propagating along the radial array of LOS of the Li-BES diagnostic. In other words, the density shoulder is largely just the temporal average of a bunch of trains of blobs. The regime of high blob transport and a shoulder formation in the SOL was called "Main chamber recycling regime" [290, 291] at Alactor C-mod. It was shown with a theoretical model, the shoulder formation of the ensemble-averaged profile can be attributed to synergistic effects of blob transport and recycling [292]: the increased perpendicular blob transport leads to more recycling at the main chamber wall, which increases the ionization in the SOL, and hence increases the blob transport (equation 3.29) via Λ_{ei} in equation 3.22.

The shoulder formation in the SOL can be related to divertor detachment, i.e. divertor detachment appears close to the collisionality, for which the enhanced blob transport and the shoulder formation is observed [180, 289, 293, 181]. However, the shoulder formation, especially in H-mode, seems to be not only related to divertor conditions, but the neutral gas inventory at the midplane can play a role [294]. In any case, the shoulder formation can lead to increased perpendicular particle fluxes to the main chamber wall and an increased electron heat transport as quantitative measurements at AUG have shown [295]. A potential role of the shoulder formation and whether it appears in next step fusion experiments is discussed in reference [296].

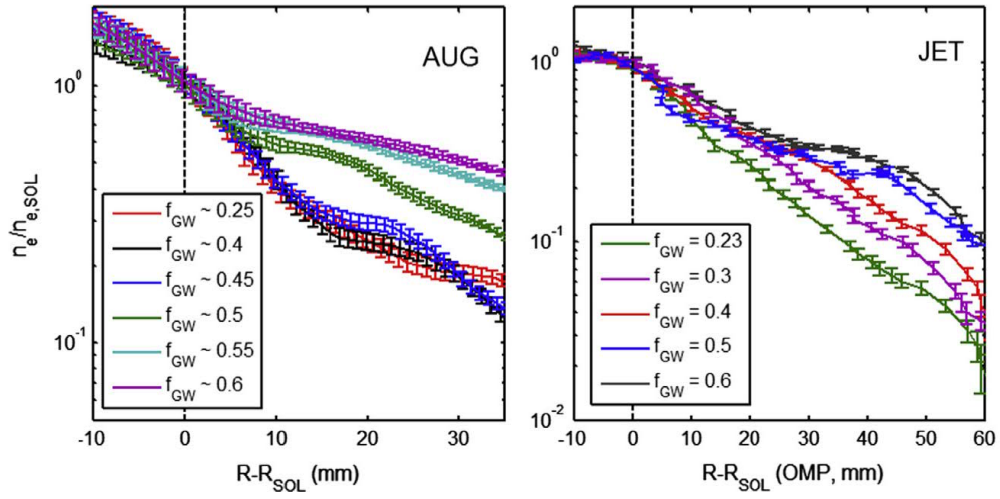

Figure 3.11: *With rising Greenwald fraction f_{GW}, the electron density profiles measured with Li-BES in the SOL at AUG (left) and JET (right) start to develop a shoulder, i.e. a flat region with relatively high density covering the whole SOL (adapted from [293]). The profiles are normalized to their value at the LCFS $n_{\mathrm{e,SOL}}$, and the radial coordinate $R - R_{\mathrm{SOL}}$ indicates the distance to the LCFS.*

3.7 Influence of Blobs on First Wall Erosion

As shown above, blobs can contribute to perpendicular particle transport and carry typically up to 20 % of the perpendicular heat transport in the SOL [295]. This is in general not considered to be a danger for the main chamber wall, which is expected to withstand these heat fluxes due to the large area involved and the use of tungsten as first wall material [297]. But strong particle transport, even when the related temporally averaged heat flux is low, can lead to high erosion rates of PFCs, especially, when high ion temperatures, as it is the case in blobs, are present. The transient, but high, temperature peaks could potentially lead to much larger erosion rates than expected from temporally averaged background profiles due to the non-linear dependence of the sputter yield on temperature [298]. The experimental quantification of the influence of blobs on first wall erosion as shown in the following reproduces the results of reference [182].

In order to estimate the expected erosion rates due to blobs in the SOL on PFCs of the main chamber wall, the blob parameters measured at AUG are used to extrapolate erosion levels and rates in a reactor assuming that the blob properties in a reactor are the same as in AUG. The erosion due to

the background plasma with density n_i is estimated as [20]

$$E_\mathrm{back} = \frac{1}{2} c_\mathrm{s} n_\mathrm{i} Y \cdot 2.26 \cdot \Delta t \cdot \sin\beta / n_{PFC}. \tag{3.30}$$

E_back is given in units of a length and represents the thickness of eroded PFC material of density n_PFC, which is exposed to the background plasma for a time span of Δt. Y is the effective sputtering yield for normal incidence, i.e. the number of expelled PFC atoms per incident plasma ion hitting the PFC perpendicular to its surface. It is a non-linear function of T_i and T_e. This yield needs to be corrected by the influence of non-perpendicular incident angles. We define α as the angle between the velocity vector of the incident ion and the surface normal vector of the PFC at the impact position. For D^+ and C^{4+} it was shown that the impact angle must be chosen as $\alpha \approx 60^o$ [299]. For this impact angle, the effective sputtering yield is multiplied by a factor of 2.26 according to the Yamamura formula [300, 301, 302], which takes the angle dependence of the sputtering process into account. As a last factor, the angle β between the magnetic field and the PFC surface is taken into account, in order to quantify the effective particle flux impinging on the PFC. This angle is chosen to be $\beta = 2^o$.

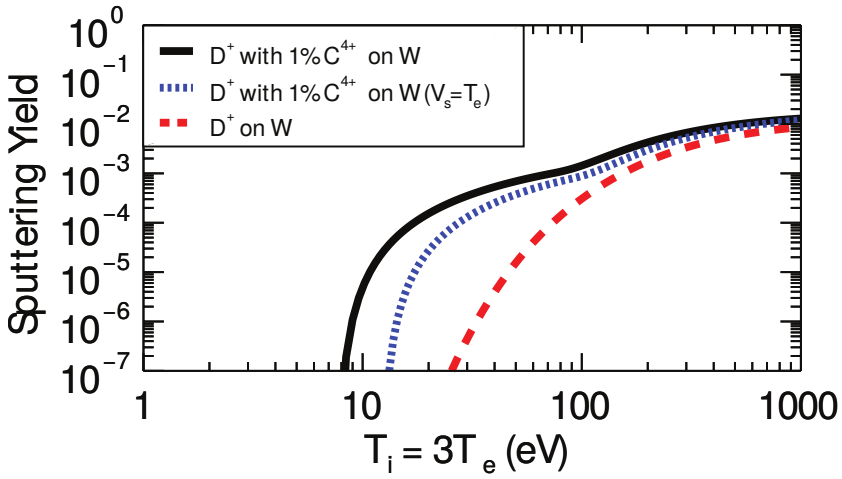

Figure 3.12: *Effective sputtering yield Y for normal incidence of a tungsten surface in contact with a deuterium plasma without impurities (dashed line), with 1 % of C^{4+} impurity concentration (solid line), and with impurities but reduced sheath potential drop (dotted line) for different ion temperatures $T_\mathrm{i} = 3 \cdot T_\mathrm{e}$ (adapted from [182]).*

The effective sputtering yield of a tungsten surface in contact with a pure deuterium plasma is shown in figure 3.12 (dashed line). For this calculation,

the ions are assumed to be Maxwellian distributed having an energy of [20]

$$E_\mathrm{i} = 2T_\mathrm{i} - ZeV_\mathrm{s}. \tag{3.31}$$

The first term is the approximate thermal energy of the ions at the sheath edge and the second term represents the energy of an ion with charge state Z gained in the sheath potential drop V_s. The latter is typically negative for floating conditions and given in units of T_e by

$$\frac{eV_\mathrm{s}}{T_\mathrm{e}} = 0.5 \ln \left[\left(2\pi \frac{m_\mathrm{e}}{m_\mathrm{i}} \right) \left(1 + \frac{T_\mathrm{i}}{T_\mathrm{e}} \right) (1 - \delta_\mathrm{se})^{-2} \right] \tag{3.32}$$

with secondary electron coefficient δ_se. We set $\delta_\mathrm{se} = 0$ (see discussion below) and, in agreement with measurements in the SOL of ASDEX Upgrade at a Greenwald fraction of $f_{GW} = 0.44$ [266], the ion temperature is assumed to be three times higher than the electron temperature ($\tau_\mathrm{i} = 3$) resulting in an effective sheath potential drop of $V_s \approx 2.5 T_\mathrm{e}/e$. The sputtering yield for a pure deuterium plasma ($Z = 1$) strongly rises above $T_\mathrm{i} > 30\,\mathrm{eV}$, but is negligible below (see figure 3.12, dashed line).

For the estimation of the erosion of blobs, we consider the following situation. From the measurements we know that a blob of density δn stays for the time span of the residence time τ_b within our Li-BES observation volume of a single LOS (purple region in figure 3.13). Since the blob is connected parallel to the magnetic field with a PFC, it passes during the same time span the contact region (orange) on the PFC close to the divertor. A single blob therefore induces an erosion of

$$E_\mathrm{blob} = \frac{1}{2} c_\mathrm{s,blob} \delta n Y_\mathrm{blob} \cdot 2.26 \cdot \tau_\mathrm{blob} \sin\beta / n_{PFC}. \tag{3.33}$$

For this estimation, the sound velocity $c_\mathrm{s,blob}$ inside the blob is used, i.e the electron temperature of the blob has to be inserted. The same holds for the sputtering yield Y_blob, for which the blob parameters have to be inserted.

3.7.1 Erosion by a Pure Deuterium Plasma

For the background plasma (pure deuterium) we now assume $T_\mathrm{i} = 18\,\mathrm{eV}$ and $T_\mathrm{e} = 7\,\mathrm{eV}$, and for the blobs $T_\mathrm{i,blob} = 100\,\mathrm{eV}$ and $T_\mathrm{e,blob} = 30\,\mathrm{eV}$ as it was measured with an RFA in comparable discharges at fixed $f_{GW} = 0.44$ [266]. Furthermore, we assume $\Delta t = 31.5 \cdot 10^6\,\mathrm{s}$ corresponding to a full year of plasma operation (burn year) in order to relate our results to the operating conditions in a fusion power plant in terms of pulse duration. For the blobs,

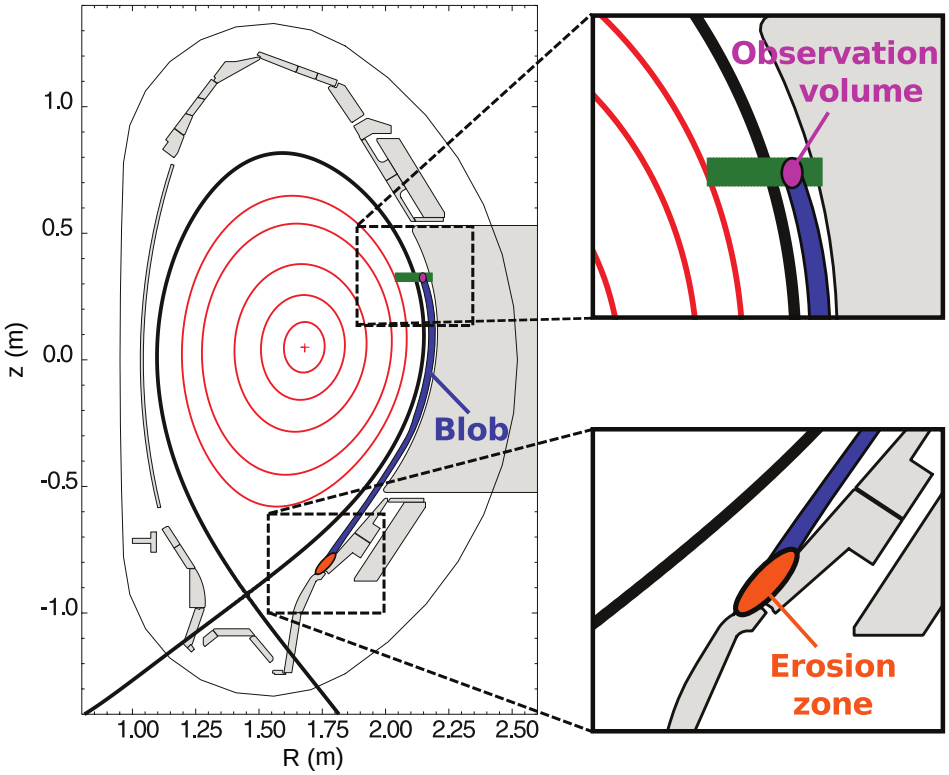

Figure 3.13: *Schematic of blob induced erosion: A blob (blue) in the SOL passes the observation volume (purple) of the Li-BES diagnostic during a residence time of τ_b. For the same time span τ_b, the blob is connected along the field line to a contact region (orange) on a PFC close to the divertor. The plasma parameters of the blob determine the erosion properties in the contact region. (reproduced from [182]).*

we have to multiply Δt by a weighting factor of $w = \tau_\mathrm{b} f_\mathrm{blob}$ due to the fact that the blobs exist only for a short fraction of time (typically $w \approx 2\,\%$ of a time trace consist of 2.5σ-blobs). For tungsten we set $n_\mathrm{PFC} = 6.3 \cdot 10^{28}\,\mathrm{m}^{-3}$, and all other parameters are used as measured and shown in figure 3.10. The result of this estimation according to equations 3.30 and 3.33 for different densities of a pure deuterium plasma is shown in figure 3.14. The erosion E_back induced by the background plasma only (open triangles) is typically one order of magnitude smaller than the total erosion $E_\mathrm{tot} = E_\mathrm{blob} + E_\mathrm{back}$ (filled triangles) which accounts for both blob and background induced erosion. This is a striking result since the blobs are only a fraction of time ($w \sim 1/50$ of a second) in contact with the PFC while the background plasma continuously sputters the contact region. But the higher plasma density δn and the substantially higher ion temperature T_i in combination with the non-linear dependence of Y on T_i overcompensate the shorter contact time.

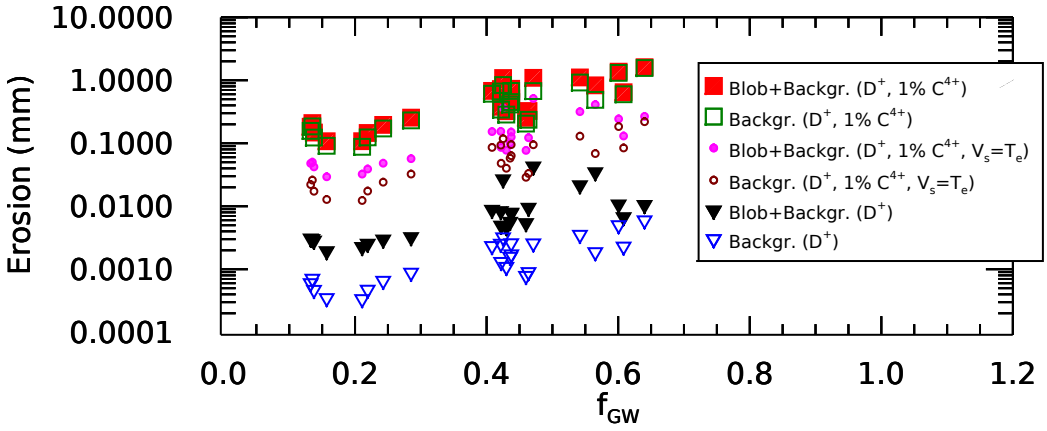

Figure 3.14: *Gross erosion (i.e. erosion without redeposition) at the contact region for one burn year (365 d, 24 h/d) for ASDEX Upgrade L-mode conditions (logarithmic scale) for different impurity concentrations and sheath potentials in dependence of the Greenwald fraction (adapted from [182]).*

With increasing density both the background induced erosion E_back and the total erosion E_tot including blobs increase due to the density dependence of equations 3.30 and 3.33. While the absolute values of the erosion of the background plasma of maximum $E_\mathrm{back} \approx 0.006\,\mathrm{mm}$ are very low, the total erosion achieved including blobs reaches much higher values up to $E_\mathrm{tot} \approx 0.4\,\mathrm{mm}$. Such low values are not a concern for the first wall material in future reactor designs, despite breeding requirements in the blankets and safety reasons call for a small thickness of the tungsten layer on PFCs.

3.7.2 Erosion with 1 % Impurity Concentration

As has been shown in previous investigations of sputtering of tungsten PFCs in ASDEX Upgrade [298, 303, 304], even low fractions of impurity concentrations can substantially increase the sputtering yield due to the higher ion mass and charge state Z of impurity ions (compare also equation 3.31). The measured erosion levels could only be explained by erosion models which take into account a few percent of C^{4+} as a placeholder for all low-Z impurities typically present in ASDEX Upgrade. As shown in figure 3.12 (solid line), the effective sputtering yield of a deuterium plasma containing 1 % of C^{4+} impurity ions is between 8 eV and 80 eV several orders of magnitude greater than a pure deuterium plasma and significant sputtering sets in already at comparatively low temperatures.

If this effect is taken into account for the comparison of background and blob induced erosion, the relevance of the higher ion temperatures in blobs decreases. The total erosion including blobs (figure 3.14, filled squares) is maximum 37 % higher than the background erosion only (open squares). Due to the higher charge number $Z = 4$ for impurity ions, the sheath acceleration gains in importance. Therefore, the high ion temperatures in blobs play only a minor role for the effective sputtering yield. Due to the same effect, the sputtering curve is flatter at lower temperatures resulting in small differences of the sputtering yields for background and blob plasma parameters. This is in contrast to the pure deuterium case, where the differences between background and blob sputtering yields could even balance the less frequent occurrence of blobs.

The absolute values of erosion of almost 2 mm is quite significant, given the fact, that the PFCs in a reactor will only have a tungsten layer of a thickness of a few mm. Therefore, such erosion estimations and their parameter dependences are crucial to be estimated for all kind of plasma scenarios envisaged for a reactor.

3.7.3 Erosion with 1 % Impurity Concentration and Reduced Sheath Potential

So far, we used the approximation $V_s \approx 2.5 T_e/e$ assuming $\delta_{se} = 0$ in equation 3.32 for the calculation of the sputtering yields. For finite secondary electron emission $\delta_{se} \neq 0$, however, the sheath potential can be reduced significantly as indicated by measurements in different tokamaks [305, 306, 307]. This reduction of the sheath potential decreases the acceleration of ions in the sheath and therefore reduces the impact of impurities for the erosion process (see figure 3.12, dotted line). In order to account for this effect,

we determined the erosion for background plasma parameters (open circles) and the total erosion including blobs (filled circles) as an example assuming $V_\mathrm{s} = 1\ T_\mathrm{e}/e$ corresponding to $\delta_\mathrm{se} = 0.775$ as shown in figure 3.14. In this case, the absolute erosion levels are reduced by an order of magnitude relative to the case with impurities and $V_\mathrm{s} \approx 2.5 T_\mathrm{e}/e$, but still much higher than the erosion levels without impurities at all. For finite δ_se, the erosion levels with blobs are a factor of two larger than the background erosion only. This reveals again the complementarity of the sheath effect and the influence of blobs on erosion: weak impact of the sheath acceleration involves strong blob contribution and vice versa.

We have to state clearly that equations 3.30 and 3.33 are only rough estimates for the evaluation of *gross* erosion. It does not account for redeposition or for the fact that parallel density and temperature gradients along the magnetic field line could exist. Furthermore, we assumed the same temperatures and temperature ratio $\tau_\mathrm{i} = 3$ for the whole density range. However, as it was shown in reference [308], τ_i depends on the density and can range from 2 to 8 changing the erosion due to the sheath potential (see equation 3.32). The very high erosion of up to 2 mm in the case with impurity ions at high Greenwald fraction (figure 3.14, filled squares) might therefore be an upper limit of a worst case scenario.

On the other hand, the estimations are done for L-mode parameters. In H-mode plasmas, however, significantly higher densities in filaments of edge localized modes (ELMs) [309] (even in scenarios with small ELMs [310]), and hence higher erosion could be achieved. This is possibly of relevance for ITER which will operate in H-mode and at much higher temperatures [7]. Together with the fact that sputtering of Beryllium sets in already at much lower ion temperatures than it is the case for tungsten, this is unfavorable for the first wall in ITER. Another issue, which has not been taken into account in our estimation, is self-sputtering of tungsten which also can increase erosion. Averaged over a whole campaign (6300 s of plasma operation) at ASDEX Upgrade, a net erosion of maximum 100 nm corresponding to a net erosion rate of $1.59 \cdot 10^{-11}$ m/s was measured by means of Rutherford backscattering on baffle tiles [311]. This is only a factor of four lower than the gross erosion rate of about $6.34 \cdot 10^{-11}$ m/s (~ 2 mm in one burn year) as derived from our blob erosion model including impurities described above. In this sense, our estimation is not far from reality.

Chapter 4

Parameter Dependence and Physical Mechanism of the L-H Transition

In addition to the main parameter dependencies of the L-H power threshold P_{LH} as obtained from the multi-machine data base according to equation 2.13, many more engineering and plasma parameters have been found to impact P_{LH}. The most common parameter dependencies will be shown in the following. In addition to the parameter dependence of P_{LH}, a few further observations around the L-H transition have been made, which have a potentially strong impact on the theoretical description of the L-H transition. They point to a crucial role of the edge ion heat flux and to a critical $E \times B$ velocity at the edge. These two elements have predictive or at least an explanatory power and are related to the shear suppression paradigm of the L-H transition. The main experimental findings and their relations to a selection of L-H transition models are discussed at the end of this chapter.

4.1 Experimental Parameter Dependence of the L-H Power Threshold

4.1.1 Isotope Dependence of the L-H Transition

At AUG it was found that the L-H power threshold, P_{LH}, is about a factor of two higher in hydrogen (H) compared to deuterium (D) [47, 312], see figure 4.1. This indicates, that the power threshold might scale as

$$P_{\mathrm{LH}} \propto 1/A_{\mathrm{eff}} \tag{4.1}$$

with the effective isotope mass

$$A_{\mathrm{eff}} = \frac{n_{\mathrm{H}} + 2n_{\mathrm{D}} + 3n_{\mathrm{T}}}{n_{\mathrm{H}} + n_{\mathrm{D}} + n_{\mathrm{T}}}, \tag{4.2}$$

depending on the H density n_{H}, D density n_{D} and tritium (T) density n_{T}. As a few examples, $A_{\mathrm{eff}} = 1$ for H, $A_{\mathrm{eff}} = 2$ for D, and $A_{\mathrm{eff}} = 2.5$ for a deuterium-tritium (D-T) mixture with 50 % D and 50 % T. Very similar observations were made at other tokamaks [313, 314], although slight deviations from equation 4.1 were found, especially in plasmas with mixed ion species [315, 316].

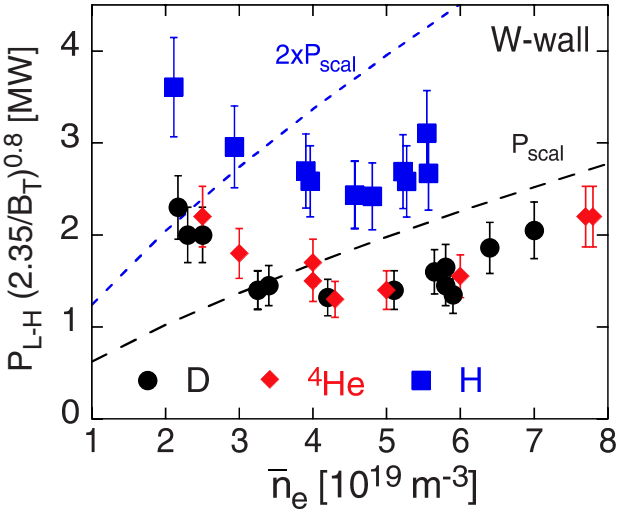

Figure 4.1: *Power threshold of the L-H transition, P_{loss}, measured at AUG in plasmas of different main ion isotope (adapted from [47]). The dashed lines indicate the scaling of P_{LH} according to equation 2.13.*

Helium (He) plasmas apparently have the same L-H power threshold as D in AUG (see figure 4.1), but this is not confirmed at other tokamaks, which typically find a higher power threshold in He compared to D [314, 313, 317, 318]. The additional charge of the He ions or the specific effects of He pumping, which differ in the considered tokamaks, might impact the power threshold in a more complicated way.

The JET tokamak is the only experiment with T plasma operation capability, at which systematic studies of the L-H power threshold in T plasmas or D-T mixtures were undertaken. Results of first investigations in T and D-T plasmas in the carbon wall era, i.e. at a time when the first wall in JET was made of graphite tiles, confirmed the mass scaling (equation 4.1) even for mixed ion species as it is shown in figure 4.2. For the estimation of P_{LH}

the quantity P_{sep} (see equation 2.15) was used in order to correct the power levels from too high radiation levels as they are typical in JET. A similar result is found, when P_{loss} is used in this study [319], hence, radiation does not change the conclusion about the isotope scaling of P_{LH}.

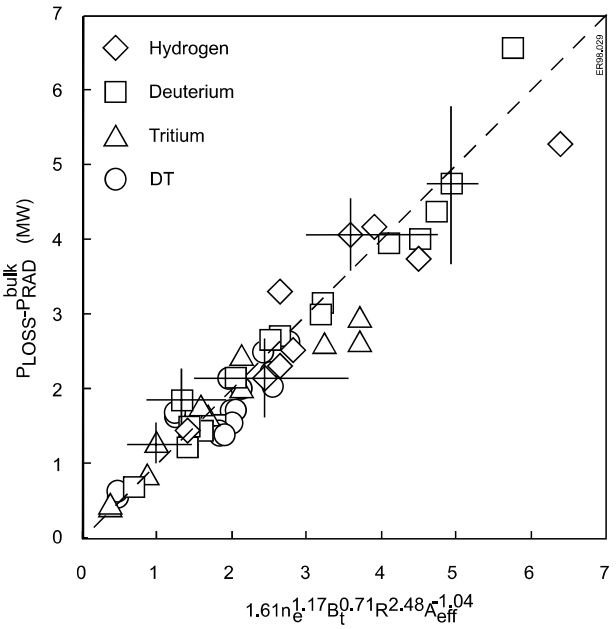

Figure 4.2: *Scaling of the L-H transition power P_{LH} estimated as P_{sep}=P_{loss}-P_{rad} at the JET tokamak, when it was equipped with a carbon wall (reproduced from [319]). A mass scaling $P_{\mathrm{LH}} \sim 1/A_{\mathrm{eff}}$ was found.*

Based on the experimental results in H and D plasmas from smaller tokamaks and the T data of JET shown in figure 4.2, we can construct an isotope dependent ITPA scaling

$$P_{\mathrm{scal}} = 0.0488 \bar{n}_{\mathrm{e}}^{0.72} B_{\phi}^{0.8} S^{0.94} \cdot 2A_{\mathrm{eff}}^{-1}. \tag{4.3}$$

by just extending equation 2.13 by an inverse dependence on the effective isotope mass. The factor of 2 is due to the fact, that the ITPA scaling (equation 2.13) was derived from a regression of D plasmas only. Equation 4.3 can be considered as a natural isotope mass dependent power threshold scaling as derived from a multi-machine data base consisting mainly of P_{LH}-data from carbon wall machines [168].

In early 2011, the JET tokamak was fully equipped with a metallic wall, i.e. a tungsten (W) divertor and a main chamber first wall made of beryllium

(Be) [320], since a carbon wall is considered to be not suitable for a future fusion reactor due to too high tritium retention and unfavorable erosion levels [321, 322]. The materials of PFCs of JET, i.e. a Be main chamber and a W divertor, are the same as in the next step fusion experiment ITER [7], which is planned to demonstrate positive net energy production from fusion, so that JET with its ITER-like wall (ILW) can provide valuable support to ITER to study reactor-relevant plasma scenarios and safety issues in metallic wall conditions.

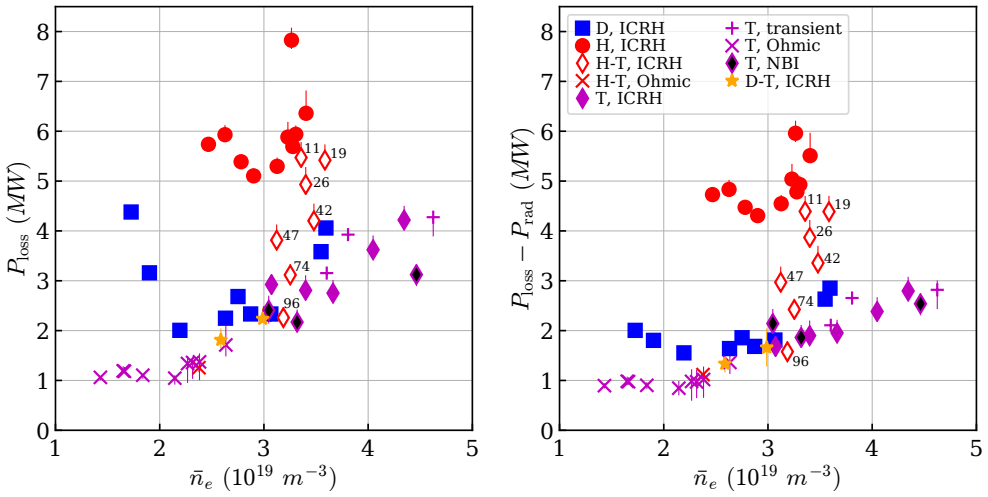

Figure 4.3: *L-H power threshold in JET with ILW estimated as P_{loss} (left) and P_{sep} (right) against line-averaged core density $\bar{n}_{\mathrm{e}}$ for different main ion plasma isotopes and isotope mixtures heated with different heating schemes. The data points labelled as "transient" are dithering L-H transitions and were heated with ICRH. The numbers next to the symbols of the H-T mixtures indicate the tritium content of these plasmas (reproduced from [323]).*

In a more recent investigation of the L-H power threshold in JET plasmas with ILW at a magnetic field of $B_\phi = 1.8$ T [324, 323], pure T plasmas and plasmas of tritium-containing mixtures like hydrogen-tritium (H-T) and the reactor-relevant fuel mixture D-T were studied. The typical L-H power threshold curves depending on density differ quite significantly for the different isotope mixtures as shown in figure 4.3. Among the pure plasmas, H plasmas exhibit the highest power thresholds, while D plasmas are more than a factor of two lower in terms of P_{loss} (figure 4.3, left). The power thresholds in T plasmas tend to be even lower than in D plasmas, at least in the high

density branch and at lowest densities. At medium densities, there is hardly any difference between D and T. The overall lowest power thresholds were found in ohmically heated T plasmas at lowest densities. For the H-T mixed plasmas, P_{loss} decreases with increasing T concentration, i.e. with increasing isotope mass A_{eff}. Two D-T data points are between the D and the pure T data, which don't differ much at medium densities.

When the radiation is subtracted, the data set looks very similar (see figure 4.3, right). The slight differences between plasmas heated with ICRH and NBI as visible in the T data of P_{loss}, have vanished for P_{sep}. This means that the actual L-H power threshold represented by P_{sep} is the same in ICRH and NBI heated plasmas, but ICRH heated plasmas suffer from higher radiation levels probably due to ICRH induced sputtering of Be in the SOL due to rectified RF fields [325]. The higher Be concentrations in the SOL lead to sputtering of W, so that increased W concentrations in the confined plasma raise the radiation levels there. Since sputtering yields depend on the isotope mass [326], this effect is most severe in T plasmas. Consequently, P_{loss} in ICRH heated T plasmas can be comparably high and can hamper H-mode access, so that only dithering transitions but no sustained H-modes are achieved [324].

In contrast to H and D plasmas, the T data does not exhibit a clear minimum, so that $\bar{n}_{\mathrm{e,min}}$ cannot easily be determined from this data. However, a rise of density in ohmic phases of T plasmas lets the plasma enter into H-mode (corresponding to the $\times$-symbols in figure 4.3) and a further rise in density lets the plasma fall back into L-mode [324]. This dynamics points clearly to a typical transition in the low-density branch, so that the ohmic data points of the T plasmas can be considered as the low-density branch.

The curves of P_{loss} and P_{sep} shown in figure 4.3 qualitatively confirm, that the L-H power threshold scales inversely with the effective isotope mass A_{eff}, since heavier isotopes exhibit lower power thresholds in pure plasmas and higher T concentrations in H-T mixed plasmas continuously lowered P_{LH}. But how is the data related to the ITPA isotope scaling (equation 4.3), which is the reference for carbon wall machines? In order to validate the isotope-dependent ITPA scaling, the P_{LH} data shown in figure 4.3 is divided by equation 4.3 and drawn against the effective isotope mass A_{eff}. This is shown in figure 4.4.

The data of the pure isotope plasmas and the D-T data points cluster around the respective effective isotope masses (H around $A_{\mathrm{eff}} = 1$, D around $A_{\mathrm{eff}} = 2$, T around $A_{\mathrm{eff}} = 3$ and D-T around $A_{\mathrm{eff}} = 2.5$), while the H-T mixed plasmas covers the full range from $A_{\mathrm{eff}} = 1$ to $A_{\mathrm{eff}} = 3$. Similar as in figure 4.3, the data for P_{sep} (right) exhibits less scatter than the data for P_{loss} (left), since the scatter introduced by P_{rad} is removed for P_{sep}. Despite this

improvement, the P_{sep} data is still scattered in y-direction, which could be due to the measured density dependence of the P_{LH}-curve, which is not fully compensated by the density dependence of the scaling. Thus, the scaling formula (equation 4.3) does not reflect the correct density dependence although only data from the high-density branch is used in this investigation, or other missing parameters, which did not enter the scaling, are relevant for P_{LH}.

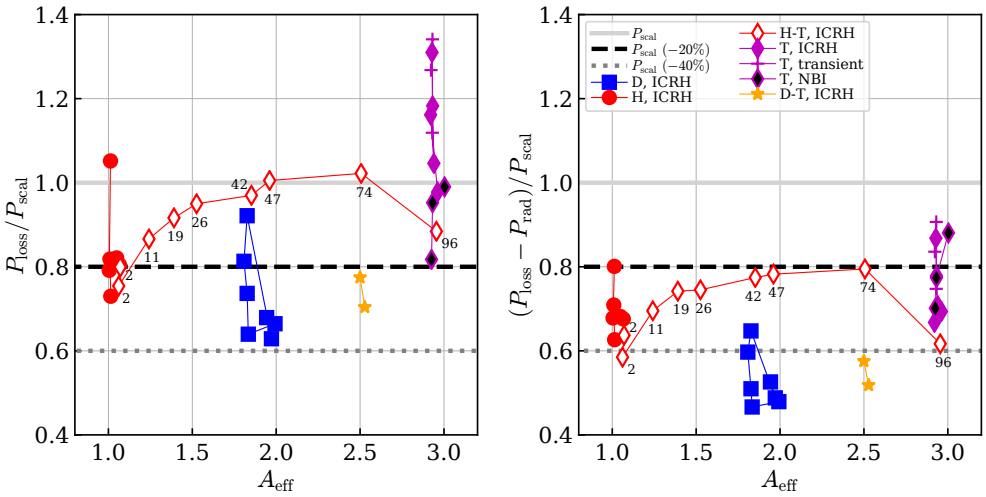

Figure 4.4: *P_{loss} (left) and P_{sep} (right) normalized to the scaling P_{scal} (equation 4.3) against effective isotope mass, A_{eff}. Only data from the high density branch are shown. The power threshold can vary significantly for the same A_{eff} indicating that the isotope effect of P_{LH} is not well described by the effective isotope mass (reproduced from [323]).*

In general, the measured values of P_{loss} are about 20 % lower than the scaling for H, D and D-T plasmas, and P_{sep} about 40 % lower than the scaling. This is a well known effect of the metallic wall, which was studied in detail at JET [327] and AUG [47, 45] (as a reminder: the ITPA scaling was derived from a data set consisting mainly of data from carbon wall devices). For T plasmas and some of the H-T mixtures this effect seems to be absent in P_{loss} possible due to the high radiation especially in ICRH heated plasmas, but P_{sep} is still 20 % to 30 % lower than the scaling, so that the metallic wall effect also might play a role for T containing plasmas, albeit to a minor extend.

The most intriguing outcome of this representation of the data is the fact, that the L-H power threshold can differ significantly in plasmas of the same

isotope mass. More specifically, the isotope mass of D is the same as for the H-T mixture with about 50 % T (both have $A_{\mathrm{eff}} = 2$), but the power threshold e.g. in terms of P_{sep} is 65 % lower in D than in the corresponding H-T mixed plasma at the same density. Similarly, P_{sep} of the D-T plasma is much lower than P_{sep} of the corresponding H-T plasma with 74 % T concentration, although both plasmas have $A_{\mathrm{eff}} \approx 2.5$. Obviously, it is not (only) the isotope mass, which matters for P_{LH}, but rather the isotope *composition*. This means, that a description of isotope effects of the L-H power threshold only with A_{eff} will fail, and models or scalings, which do not take into account the isotope composition, will not be able to correctly predict the isotope dependence of P_{LH} in future machines. As an example, fluid models, which try to predict the L-H power threshold [212, 328] should model each isotope species as a separate fluid instead of using a single fluid representing a mixture of ions with an effective isotope mass A_{eff}.

While A_{eff} might be an appropriate parameter to roughly parameterize the isotope effect of the L-H power threshold for plasmas with pure isotopes, this approach fails for mixed plasmas. As it will be shown below in section 4.2.2, it is the L-mode transport of the respective isotope composition which determines the L-H power threshold [323].

4.1.2 Current Dependence

The L-H power threshold depends on the plasma current I_{p} as shown in figure 4.5 for AUG. Since the Greenwald density limit [284] depends on the plasma current as well, only relatively low densities can be achieved in L-H transition experiments at lower currents. Thus, it is not clear whether the high-density branch likewise possesses a current dependence or not at AUG. At JET, however, a current dependence on the full range of densities was found [329] and a general current scaling of $P_{\mathrm{LH}} \sim I_{\mathrm{p}}^{0.2}$ was suggested [327]. At DIII-D the current dependence on P_{LH} was found to be stronger at high density than at low density [330]. In general, the observations point all to an increase of P_{LH} with plasma current I_{p}.

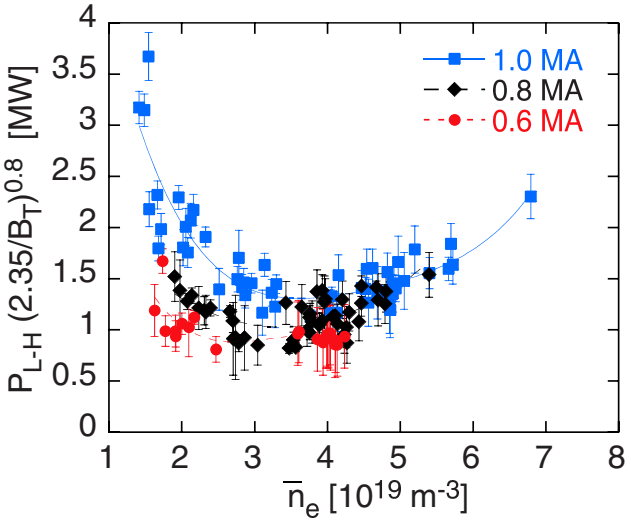

Figure 4.5: *L-H power threshold for AUG in deuterium plasmas (reproduced from [47]). In the low-density branch, the power threshold depends on the plasma current* I_p.

4.1.3 Plasma Shape Dependence

Investigations at JET have shown that a higher triangularity of the plasma can change the slope of the density dependence of P_{LH} [331]. As a consequence, P_{LH} is lower for higher triangularity in the high-density branch. It turned out, that the lower triangularity is decisive for the change in P_{LH}, and that the length of the divertor leg can impact the transition as also found in DIII-D [313, 332] and in Alcator C-mod [333]. Strikingly, a longer outer divertor leg corresponding to a higher X-point position increased the L-H power threshold in DIII-D, while it reduced P_{LH} in C-mod.

At JET, similar observations were made [327, 334, 335], and it is not clear whether the change of neutral content in the divertor or the effective charge number Z_{eff} is the decisive quantity determining the L-H transition power, since both quantities are proportionally increased with P_{LH}, when the shape was changed. Not only the leg lengths can change P_{LH}, but similarly the location, where the outer leg is placed, can impact P_{LH} as shown in figure 4.6. Placing the outer leg on the vertical target (VT) can increase P_{LH} by up to a factor of two compared to the horizontal target (HT) configuration [336]. It is discussed, whether the paths of the neutrals in the private flux region, i.e. the region below the X-point and between the two divertor legs, are impacting the temperatures on the outer target and thus changing the outer shear of the radial electric field profile facilitating the L-H transition in HT configuration [337].

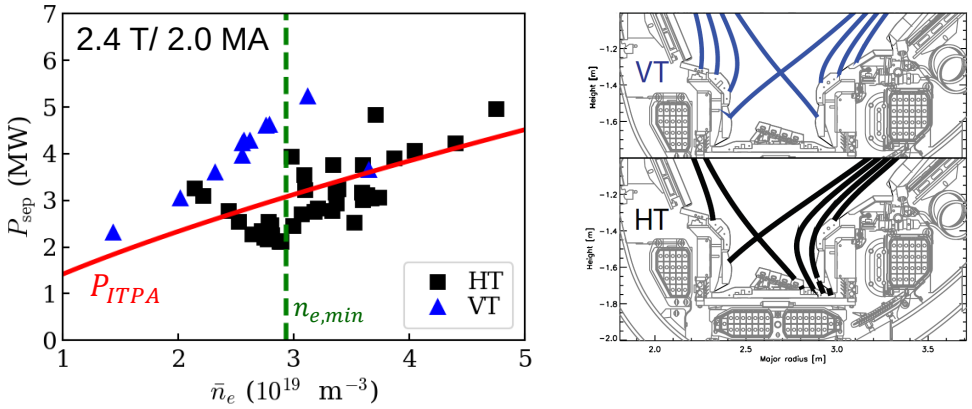

Figure 4.6: *L-H power threshold depending on the divertor geometry at JET. When the outer divertor leg is placed on the horizontal target (HT), the power threshold (black symbols) is lower and exhibits a clear minimum at* $\bar{n}_{\mathrm{e,min}}$*. In this case, the data agrees quite well with the ITPA scaling (equation 2.13). If the outer leg is placed on the vertical target plate (VT), the power threshold (blue symbols) is up to a factor of two higher and does not exhibit a minimum.*

The magnetic configuration, i.e. the direction of the ion ∇B-drift with respect to the active X-point[1]. X-point location, has a strong influence on P_{LH} [338, 118, 339]. In favorable[2] configuration, for which the ∇B-drift of the ions is pointing to the active X-point, the L-H power threshold is typically a factor of two (or more) lower than in unfavorable configuration, in which the ion ∇B-drift points away from the active X-point. This effect is not well understood, but opens a window to high power L-modes, which show improved confinement. This are called improved L-modes or I-modes and were discussed in section 2.3.1.

[1]In this case *active X-point* describes the primary X-point, which is defining the main separatrix being in direct contact to the confined plasma. The secondary X-point is typically far in the SOL (unless a double null configuration is chosen) and has no strong impact on processes in the confined plasma.

[2]This configuration was dubbed favorable, since in this configuration, the impurity ions are believed to drift due to the ∇B-drift towards the actively pumped divertor, which leads to cleaner plasmas.

4.1.4 Dependence on Wall Material and Divertor Geometry

As shown in JET [327], but also investigated in AUG [47], the L-H power threshold is lower in a metallic wall compared to the same conditions (same divertor geometry and plasma shape) with a carbon wall. At AUG it was shown [45], that the density profile is steeper in a metallic wall than in a carbon wall, so that the diamagnetic contribution to the radial electric field (see equation 2.8) is stronger, thus, facilitating the L-H transition due to higher E_r-shear. This change in density might be related to higher neutral reflection coefficients for W PFCs compared to C PFCs [45].

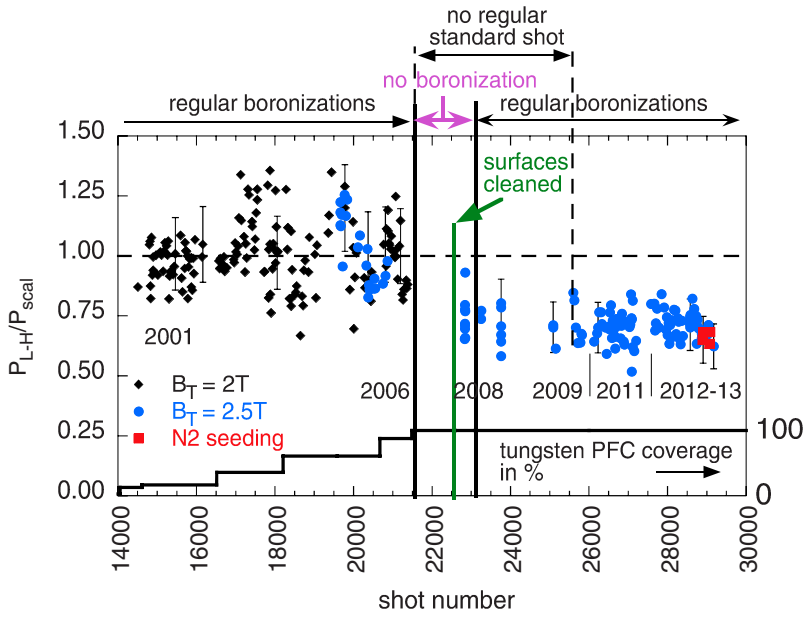

Figure 4.7: *L-H power threshold normalized to the scaling in standard H-mode discharges with similar parameters in AUG during the course of time indicated by the plasma pulse number (shot number). The L-H power threshold decreased by about 20 % after the PFCs were fully covered with tungsten (reproduced from [47]).*

Not only the material of the PFCs has an impact on P_{LH}, but also the geometry of PFC components especially in the divertor can modify P_{LH}. As shown in several studies at JET, the presence of a dome (or septum) between the divertor legs or changes of single components in the divertor cassette can change the L-H power threshold by 25 % [327, 329, 334].

4.1.5 Torque Dependence

The DIII-D tokamak allows for changing the torque in a plasma largely independent of the heating power due to the use of two neutral beam injectors systems, which are launching their heating beams in opposite direction. This enabled L-H transition studies depending on the torque input [332]. The result is shown in figure 4.8: A higher torque input in co-current direction (i.e. into the same toroidal direction as the plasma current) increases the power threshold. Similar results were also found at AUG [165] and JET (most prominently in H plasmas [336]).

As will be discussed in more detail below (see section 4.3.2), the torque input changes the toroidal velocity in the radial force balance (see equation 2.4) impacting the radial electric field in a way that the E_r-shear is large for negative torque (with respect to the plasma current direction) facilitating the L-H transition. Thus, the torque input is a powerful external actuator to change the L-H power threshold.

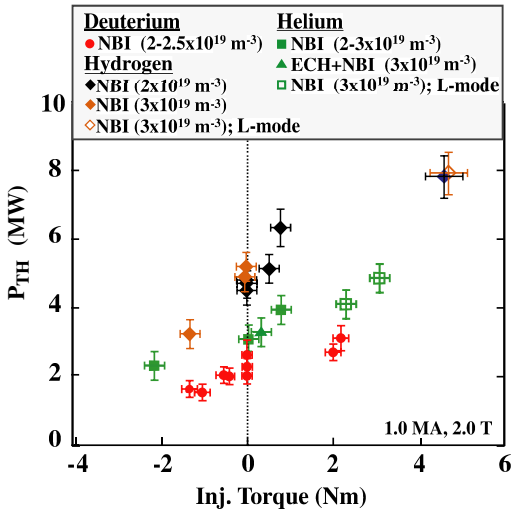

Figure 4.8: *L-H power threshold (here called P_{TH} being equivalent to P_{loss}) depending on NBI input torque in DIII-D for different isotopes (reproduced from [332]). Positive torque points in co-current direction, i.e. in the same toroidal direction as the plasma current, and negative values of the torque indicate counter-current injection.*

4.1.6 Impurities and Seeding

The presence of impurities increasing the effective charge Z_{eff} increases P_{LH} [340, 327, 341]. But since this correlates with other parameters (e.g. changes in shape, density and neutral density in the divertor) it is not clear, whether Z_{eff} is really causing higher P_{LH}. However, seeding of low-Z impurities for cooling the SOL in order to facilitate divertor detachment, clearly increases P_{loss}. This is shown in figure 4.9.

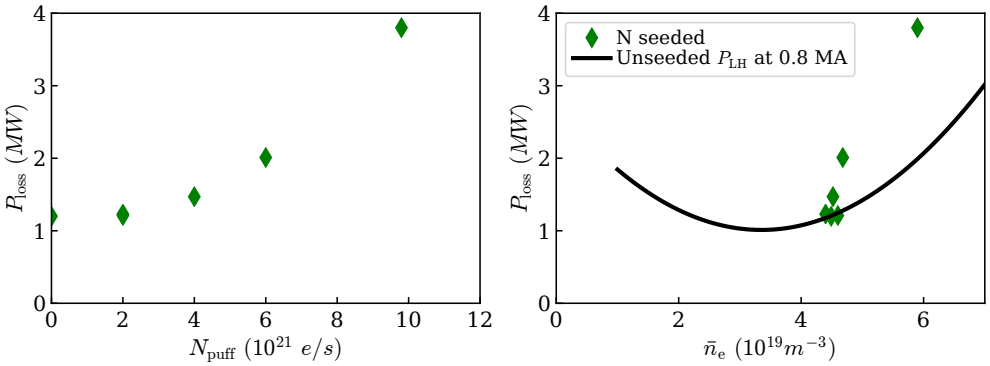

Figure 4.9: *L-H power threshold at AUG in plasmas with nitrogen seeding.* P_{loss} *increases monotonically with nitrogen seeding rate,* N_{puff} *(left). Compared to the unseeded case (black line) at the same line-averaged density* $\bar{n}_{\mathrm{e}}$*, the power threshold in terms of* P_{loss} *with nitrogen seeding increases up to a factor of two (right). The unseeded* P_{LH} *is the fit curve of data at* $I_{\mathrm{p}} = 0.8$ *MA from [47].*

The L-H power threshold in terms of P_{loss} increased almost a factor of four at the highest nitrogen seeding rate of $N_{\mathrm{puff}} = 9.8 \cdot 10^{21}$ (e/s) (4.9, left). For high seeding rates, the density in the plasma rises, so that the increased P_{loss} must be compared with the respective L-H power threshold at the same density. As shown in figure 4.9, right, P_{loss} at the highest seeding rates is still a factor of two higher than in the unseeded case at otherwise identical parameters. It is not fully clear yet, why seeding increases P_{loss}, although radiation might play a key role. But for reactor-scale fusion devices, for which detachment by impurity seeding might be mandatory in all phases of operation, this could imply that they suffer from comparably high L-H power thresholds under these conditions. As shown in JET [227], high power plasmas with impurity seeding feature edge plasma dynamics as typical for operational points close to the L-H power threshold confirming this hypothesis.

4.1.7 Further Dependencies

In addition to the parameters presented above, there are a few further parameters or actuators, which are able to change the L-H power threshold:

- Magnetic perturbation fields as they are used for ELM suppression (see chapter 2) likewise increase P_{LH}. The necessary perturbation field amplitude for ELM suppression is lower than the threshold, above which P_{LH} increases significantly due to perturbation fields, so that an ELM-suppressed regime in H-mode can be achieved in AUG without increasing P_{LH} [342]. For DIII-D data, however, this is not that obvious [313], and for future devices like ITER it is still open, whether the H-mode and ELM-suppression in H-mode is possible to achieve during the non-nuclear phase at the beginning of its operation with already elevated P_{LH} due to the use of hydrogen as the main species and limited heating power.

- Pfirsch-Schlüter flows (see section 2.1.1) might impact P_{LH} and could explain, why P_{LH} is higher in unfavorable configuration [343].

- The presence and distribution of neutral density certainly plays a role for the L-H transition [344, 327] and different gas puff locations can change the access condition to H-mode [345]. It is argued that a gas puff from the HFS is more beneficial to access H-mode than any other puffing location, since then the toroidal flows are less damped at the LFS due to low neutral density at the outboard midplane leading to stronger radial electric fields and, hence, facilitate the L-H transition.

4.2 Experimental Observations Around the L-H Transition

4.2.1 Similar Edge Electron Temperatures

The P_{LH} data set obtained in plasmas at JET with ILW at $B_\phi = 1.8$ T presented above in the context of the isotope dependence of the L-H power threshold (see section 4.1.1), is unique, since it covers the full range of hydrogenic isotope masses from $A_{\mathrm{eff}} = 1$ to $A_{\mathrm{eff}} = 3$ and a wide range of power thresholds from $P_{\mathrm{sep}} \approx 1$ MW in ohmic T plasmas to $P_{\mathrm{sep}} \approx 6$ MW in H plasmas for otherwise identical parameter (magnetic field, plasmas current, plasma shape, etc.).

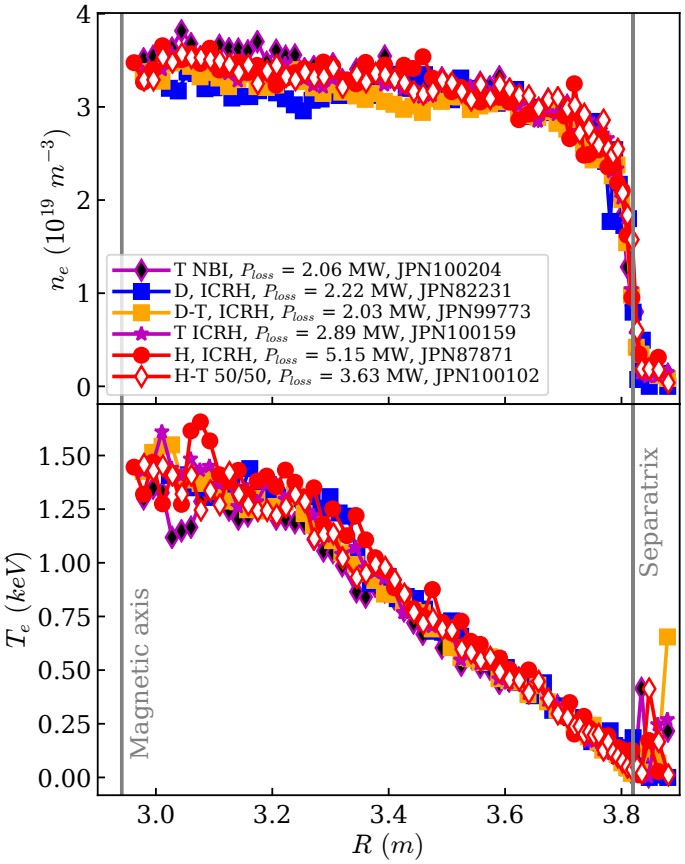

Figure 4.10: *Electron density profiles (top) and electron temperature profiles (bottom) averaged over 200 ms in the L-mode phase prior to the L-H transition measured with the high resolution Thomson scattering diagnostic in plasmas at JET with ILW at $B_\phi = 1.8$ T for similar densities and different isotope mixtures (reproduced from [323]).*

Despite these large differences in isotope mass and threshold power, the radial profiles of electron temperature and density measured by the high resolution Thomson scattering diagnostic [346] prior to the L-H transitions in plasmas with similar line-averaged densities in the range between $\bar{n}_e = 3.0 \cdot 10^{19}$ m^{-3} and $\bar{n}_e = 3.2 \cdot 10^{19}$ m^{-3} are very similar. The density profiles (see figure 4.10, top) are quite similar, and the small differences are due to the fact, that the densities were not perfectly matched. The agreement between the electron temperature profiles of the different isotopes is even better (see figure 4.10, between). They show reasonable agreement in the core plasma and perfectly agree in the outer half of the radius within errors. The finding of similar kinetic profiles at the L-H transition for different isotopes and isotope mixtures is not new and was already described before for JET [347, 336] and also for edge temperatures at AUG [312, 348]. But it is impressive to see that this effect is also present in T containing plasmas and over a now extended range of P_{LH} and A_{eff}.

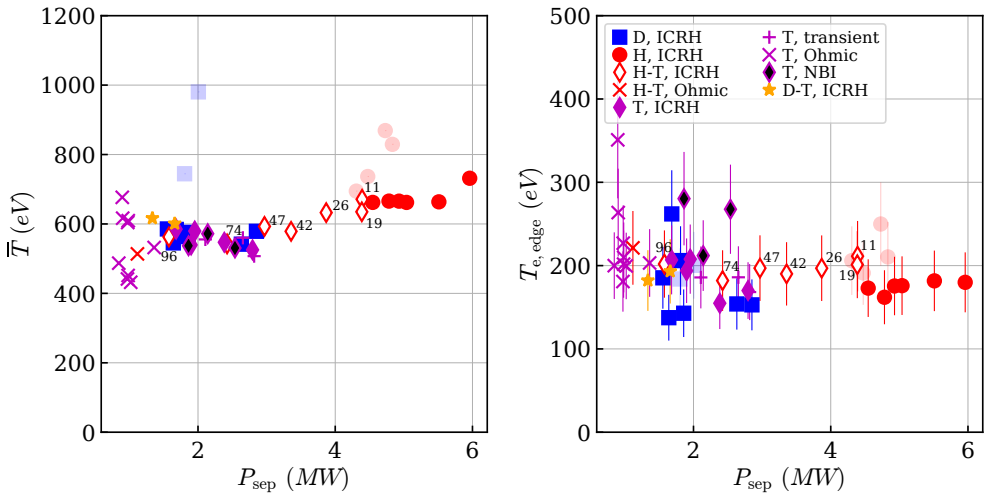

Figure 4.11: *Average temperature, $\overline{T} = W/(3\bar{n}_e V)$ (left), and edge electron temperature measured with the ECE diagnostic, $T_{e,edge}$ (right), taken 9.95 cm inside the LCFS. The semi-transparent symbols indicate data from the low density branch. Numbers next to symbols indicate the tritium concentration of H-T mixtures (reproduced from [323]).*

For different line-averaged densities, the electron density profiles naturally cannot agree as the ones shown in figure 4.10, top. But the electron temperature profiles agree quite well for all isotopes and all considered line-

averaged densities. This is represented in two different ways in figure 4.11. The panel on the left shows the volume-averaged temperature estimated as $\overline{T} = W/(3\bar{n}_e V)$ with energy content W and plasma volume V. Despite the variation of the L-H transition power P_{sep} of a factor of 6 and a variation in line-averaged density between $\bar{n}_e = 1.5 \cdot 10^{19}$ m^{-3} and $\bar{n}_e = 4.7 \cdot 10^{19}$ m^{-3}, the averaged temperature of most of the data points ranges between 500 eV and 700 eV with a small upward trend for higher P_{sep}. Only the points from the low-density branches in D and H plasmas (semi-transparent symbols) deviate from the main line of data. This could be related to finite ICRH-induced fast ion contributions to W at low densities or a mismatch of electron and ion temperatures, so that $\overline{T}$ is not a meaningful quantity to draw conclusions about thermal temperature profiles. But for data of the high-density branch, $\overline{T}$ is very well aligned for all isotope masses and over a wide range of densities.

A similar conclusion can be drawn from the edge electron temperature $T_{e,edge}$ measured with ECE [349] 9.95 cm inside the LCFS corresponding to a normalized poloidal flux coordinate of $\rho_{pol} \approx 0.90$. The data is quite scattered, but the main part of the data clusters around 200 eV despite the large variation of heating power. In this case, the data of the low-density branch (semi-transparent symbols) is within the errors of the other data points indicating that the temperatures of the thermal plasma are very similar for the whole density and power range.

Constant edge electron temperatures at the L-H transition in a wide range of densities for otherwise fixed parameters were already found earlier at JET [334, 331, 327, 350] and at other experiments [351, 352, 353]. Nevertheless, it is intriguing to see that the same is found in the presented data set, since it exceeds previous studies in terms of covered density range and heating power range.

4.2.2 Power Threshold and L-mode Transport

As shown above (see figure 4.4), the different isotope compositions with the same effective isotope masses exhibited different L-H power thresholds. This raises the question, what hidden parameter could be the reason for this difference in P_{LH}? A possible answer is given in figure 4.12. It shows how P_{sep} is related to the one fluid heat diffusivity

$$\chi_{eff} = \frac{aVP_{sep}}{WS} \tag{4.4}$$

with minor plasma radius a and plasma surface area S of the LCFS. χ_{eff} can be considered as an average heat diffusivity assuming that the electron

and ion temperatures are the same, $T = T_\mathrm{i} = T_\mathrm{e}$, which is usually a good approximation for the confined plasma at JET, and that the temperature gradient is constant along the radial coordinate, which is likewise not far from reality (see figure 4.10). A further approximation, which enters equation 4.4, is the fact that P_sep instead of the full net power is used for the estimation of the confinement time

$$\frac{P_\mathrm{sep}}{W_\mathrm{p}} \approx \frac{1}{\tau_\mathrm{E}} = \frac{S}{V}\frac{\chi_\mathrm{eff}\nabla T}{\overline{T}} \approx \frac{S}{V}\frac{\chi_\mathrm{eff}}{a}. \tag{4.5}$$

In this sense, the confinement time is radiation-corrected for our purposes.

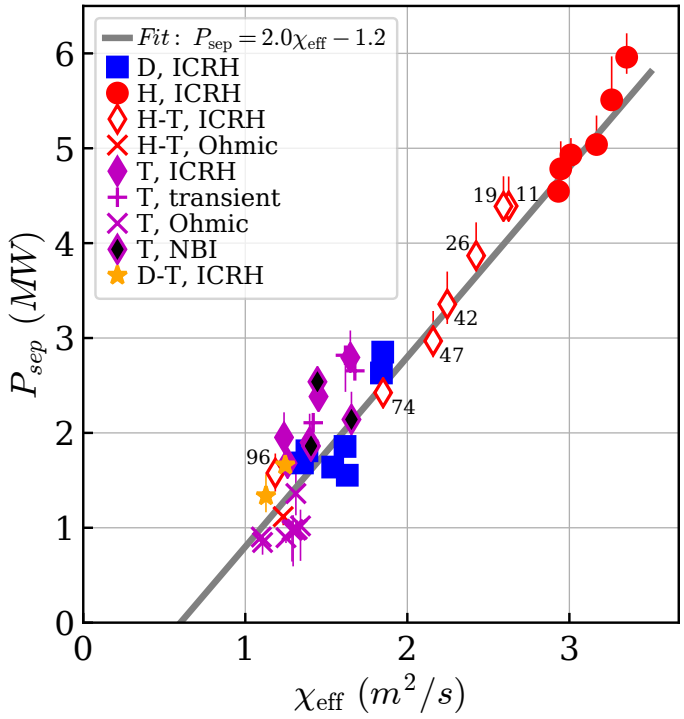

Figure 4.12: *Relation between L-H power threshold estimated as P_sep and the effective one fluid heat diffusivity $\chi_\mathrm{eff} = (aVP_\mathrm{sep})/(WS)$. The offset linear relation suggests that the L-H power threshold is determined by the transport in L-mode prior to the transition. Semi-transparent symbols indicate data from the low-density branch and the numbers indicate the tritium concentration in H-T mixtures (reproduced from [323]).*

The offset linear relation between χ_{eff} given in (m^2/s) and P_{sep} given in MW following approximately a fit curve of

$$P_{\text{sep}} = 2.0\chi_{\text{eff}} - 1.2 \tag{4.6}$$

reveals that the L-mode heat transport estimated by χ_{eff} is responsible for the amount of heating, manifesting as P_{sep}, which is necessary to reach the critical temperature profiles in order to access the H-mode. For high transport, as it is the case for H plasmas, P_{sep} is highest, and for lowest transport levels as typical for T plasmas, P_{sep} is lowest. This way, the L-H transition physics is connected to the physics of the L-mode isotope effect of transport [347, 354, 355].

The linear offset relation between P_{sep} and χ_{eff} explains why the L-H power threshold for the pure deuterium plasma is lower than in the corresponding H-T mixture with 47 % T content (both have $A_{\text{eff}} \approx 2.0$): The transport in the pure deuterium plasma ($\chi_{\text{eff}} = 1.38$ m^2/s) is lower than the transport in the H-T mixture ($\chi_{\text{eff}} = 2.16$ m^2/s), and thus P_{sep} is lower. The same relation holds for the comparison between the D-T plasma ($\chi_{\text{eff}} = 1.245$ m^2/s) and the H-T mixture with 74 % T content ($\chi_{\text{eff}} = 1.85$ m^2/s), which both have $A_{\text{eff}} \approx 2.5$. This data clearly demonstrates, that the heat transport quantified by χ_{eff} can be very different for the same effective isotope mass A_{eff}, and, consequently, the L-H power threshold is very different. This implies that A_{eff} is not a good parameter to describe the isotope effect of transport consistently, similarly as concluded for the isotope effect of P_{LH}.

It should be emphasized that the offset linear relation manifesting in equation 4.6 is only valid for the chosen magnetic field, plasma current, plasma shape and divertor material and geometry present for the data at hand. Other magnetic fields, currents and plasma shapes were shown to be related to other critical edge temperatures [356, 335]. But since likewise constant edge temperatures were found in other scenarios [334, 331, 327], it is reasonable to assume that a similar kind of offset linear relation between P_{sep} and χ_{eff} exists likewise for other conditions.

4.2.3 Key Role of Edge Ion Heat Flux

L-H transition studies at AUG [165, 312] and Alcator C-mod [357] using torque-free heating systems, i.e. ECRH for AUG and ICRH for Alcator C-mod, revealed a crucial role of the edge ion heat flow

$$Q_{\text{i,edge}} = q_{\text{i,edge}} S = -n_{\text{i}} \chi_{\text{i}} \nabla T_{\text{i}} S. \tag{4.7}$$

$q_{\text{i,edge}}$ is the edge ion heat flux and χ_{i} the local ion heat diffusivity.

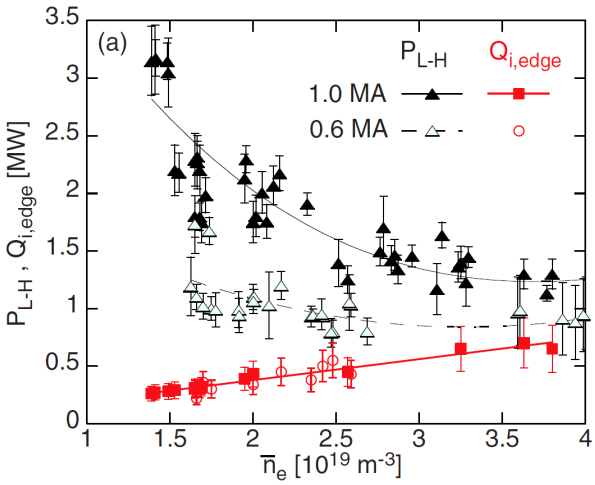

Figure 4.13: *L-H power threshold (black) and edge ion heat flow (red) for two different plasma currents in ECRH heated plasmas at AUG (adapted from [165]). Despite the different P_{LH} for the two plasma currents, the edge ion heat flow shows in both cases the same linear dependence on the line-averaged density.*

As it is shown in figure 4.13, the edge ion heat flow $Q_{\mathrm{i,edge}}$ exhibits an accurate linear dependence in the line-averaged density $\bar{n}_{\mathrm{e}}$, despite the fact that the power threshold, P_{LH}, varies non-monotonically. In addition, the identical linear relation between the edge ion heat flow

$$Q_{\mathrm{i,edge}} = 1.8\bar{n}_{\mathrm{e}} \tag{4.8}$$

in MW and line-averaged core density $\bar{n}_{\mathrm{e}}$ in units of 10^{20} m^{-3} holds for two different plasma currents (1 MA and 0.6 MA), although P_{LH} in these two cases are up to a factor of two different.

A data base combining data from AUG and Alcator C-mod revealed an additional magnetic field and surface dependence, and indicated that the L-H transition in low torque conditions are associated with a critical edge ion heat flow with the parameter dependence

$$Q^{\mathrm{crit}}_{\mathrm{i,edge}} = 0.0029\bar{n}_{\mathrm{e}}^{1.05} B_{\phi}^{0.68} S^{0.93} \tag{4.9}$$

with the $Q^{\mathrm{crit}}_{\mathrm{i,edge}}$ in MW, line-averaged core density $\bar{n}_{\mathrm{e}}$ in units of 10^{19} m^{-3}, toroidal magnetic field B_{ϕ} in T, surface area S of the LCFS in m^2. It is noteworthy, that the main parameters for the critical edge ion heat flow, namely $\bar{n}_{\mathrm{e}}$, B_{ϕ} and S, are the same one as in the ITPA scaling of P_{LH} (equation 2.13). At AUG it was shown [312], that the critical edge ion heat flow in H plasmas is about two times higher than in D plasmas suggesting an isotope scaling of

the critical edge ion heat flow inversely proportional to the effective isotope mass, $Q_{\mathrm{i,edge}}^{\mathrm{crit}} \propto 1/A_{\mathrm{eff}}$, so that equation 4.9 should be extended by an isotope dependent factor to be applicable to other isotopes [358, 324].

The advantage of a critical edge ion heat flow, as it was found in torque-free heating scenarios, over the ITPA scaling is, that it also applies to the low-density branch, which is not the case for the ITPA scaling. As it will be shown below, the critical edge ion heat flow condition (equation 4.9) can be used to derive a power threshold formula for the whole density range [358].

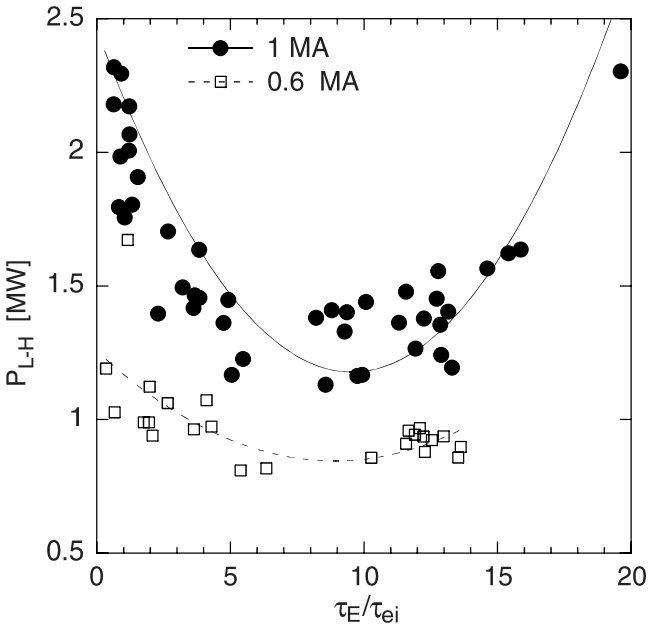

Figure 4.14: *L-H power threshold at AUG against the ratio between energy confinement time and electron-ion energy transfer time (reproduced from [165]). For both data sets at different currents, the minimum of P_{LH} is reached, when the energy confinement time is about nine times larger than the electron-ion energy transfer time to allow for equipartition of electrons and ions.*

The possibility to predict P_{LH} by means of the edge ion heat flux condition is possible due to the (experimentally validated) hypothesis, that the collisional electron-ion energy exchange becomes less effective for low densities explaining the increase of P_{LH} with decreasing density. According to this idea, it is very inefficient to reach the required critical edge ion heat flux at lowest densities due to the temperature and density dependence of the electron-ion energy transfer time $\tau_{\mathrm{ei}} \propto T_{\mathrm{e}}^{3/2}/n$, when only electron heating is used, so that a relatively high amount of heating is needed to access the H-mode. The minimum of P_{LH} is achieved for the lowest density, $\bar{n}_{\mathrm{e,min}}$, for

which equipartition, i.e. a balance between ion heating and electron heating, is achieved. Above this density, electron and ion temperatures typically agree over a wide range of the radius.

As shown in figure 4.14, it was experimentally found at AUG [165] that equipartition takes place, i.e. $\bar{n}_{\mathrm{e,min}}$ is achieved, when the energy confinement time τ_{E} exceeds the electron-ion energy transfer time τ_{ei} by a factor of 9. Under this conditions, the plasma has sufficient time to balance the electron and ion temperatures by means of collisions.

4.2.4 Critical Velocity

Measurements of kinetic profiles at AUG indicated already over a longer period of time, that the edge pressure gradients in ECRH heated plasmas at the L-H transition are constant for a given magnetic field, i.e. the gradients exhibited the same values despite different densities and thus power thresholds [359, 46, 47]. The same trend was also found at JET [327].

This indicated that the radial electric field at the L-H transition might be constant, i.e. the same for different densities or heating powers, due to the relation between the (normalized) ion pressure gradient and the radial electric field (see equation 2.8) [47, 49]. Measurements with charge-exchange recombination spectroscopy (CXRS) [51, 229] and Doppler reflectometry confirmed this and found a critical $E \times B$ velocity at the L-H transition of about 6.7 km/s as shown in figure 4.15.

The critical velocity is estimated as the maximum velocity inside E_{r} well prior to the L-H transition. Since the $E \times B$ velocity is related to the magnetic field of the plasma as $v_{E\times B} = E_{\mathrm{r}}/B$, different magnetic fields are associated with different critical values for E_{r}. But apart from this magnetic field dependence, E_{r} seems to be remarkable unaffected by any other plasma parameters, and is even the same in H and D plasmas despite the different values of P_{LH} of about a factor of two.

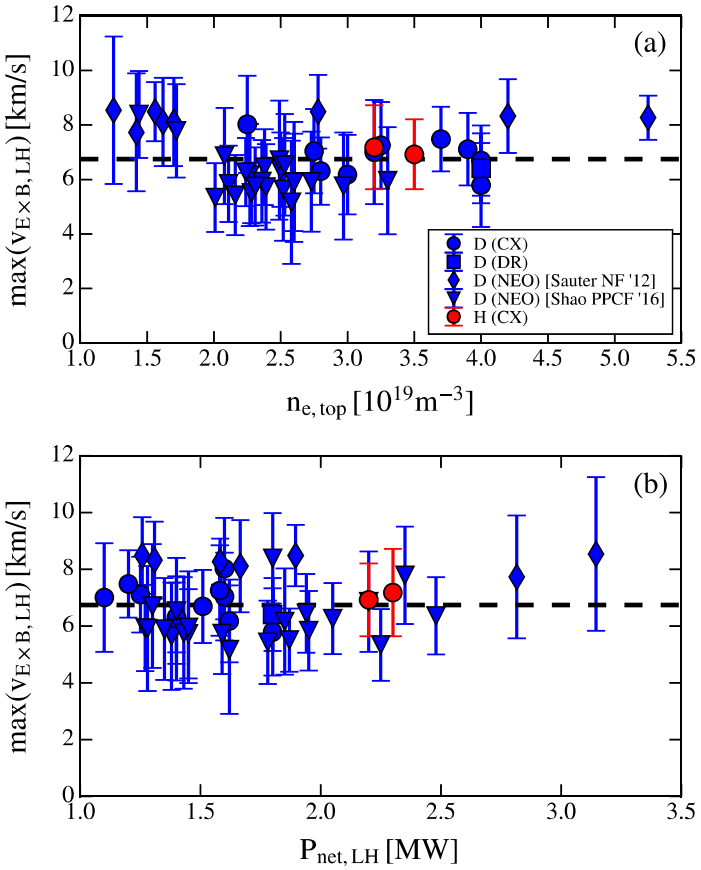

Figure 4.15: *The maximum $E \times B$ velocity in the E_r-minimum is approximately the same at the L-H transition at AUG for a large range of densities (top) and heating power (bottom), and is even valid for different isotopes despite large differences in P_{LH} (reproduced from [229]).*

4.3 A Heuristic Picture of the L-H Transition

The main observations around the L-H transition presented above are

(O1) a critical edge temperature for a wide range of densities and isotope masses (for constant field, current and shape),

(O2) an offset linear relation between L-mode transport (quantified by χ_{eff}) and the L-H power threshold (see equation 4.6),

(O3) a critical edge ion heat flow proportional to the line-averaged density, the toroidal magnetic field, the plasma surface and the isotope mass

$$Q_{\mathrm{i,edge}}^{\mathrm{crit}} = 0.0058 \bar{n}_{\mathrm{e}}^{1.05} B_{\phi}^{0.68} S^{0.93} A_{\mathrm{eff}}^{-1}, \tag{4.10}$$

(O4) and a critical value of the maximum $E \times B$ velocity in the E_{r} well for a wide range of densities, magnetic fields and isotope masses.

Although these findings are subject to measurement errors and are valid mostly at AUG, and only partially confirmed at JET and Alcator C-mod due to missing diagnostic capabilities, we assume in the following that these findings are applicable to the L-H transition physics in general. Based on this assumption, we evaluate the possibility to predict the power threshold of the L-H transition, P_{LH}, taking into account these main observations. As it will be shown below, observation (O4) implies the other observations. This approach of postulating a critical $E \times B$ velocity as essential condition for the L-H transition is what we consider as the heuristic picture of the L-H transition developed in the last years based on data from AUG, Alcator C-mod and JET.

4.3.1 The Predictive Power of a Critical Ion Heat Flux

First, we mainly use observation (O3), i.e. we assume that equation 4.9 is valid including a possible additional isotope dependence $Q_{\mathrm{i,edge}}^{\mathrm{crit}} \propto Z_{\mathrm{eff}}/A_{\mathrm{eff}}$ as written explicitly in equation 4.10, and we implicitly consider observation (O2) by assuming that the L-mode transport (and thus L-mode confinement) is determining the dynamics at the L-H transition. Based on this, we try to deduce analytical formulas for $\bar{n}_{\mathrm{e,min}}$ and the L-H power threshold P_{LH}.

The first predictive formula related to the key role of the edge ion heat flux is the explanation of the existence of a minimum of P_{LH}, and, thus, a formula providing a scaling expression for $\bar{n}_{\mathrm{e,min}}$. As shown above (see section 4.2.3), equipartition is assumed to be achieved for the line-averaged density $\bar{n}_{\mathrm{e}} = \bar{n}_{\mathrm{e,min}}$, and this condition is equivalent to the situation, when

$\tau_{\mathrm{E}} = 9\tau_{\mathrm{ei}}$ holds in the plasma. For this purpose, the confinement time scaling for L-mode plasmas in units of seconds [360]

$$\tau_{\mathrm{E,L-mode}} = 0.023 B_{\phi}^{0.03} I_{\mathrm{p}}^{0.96} A_{\mathrm{eff}}^{0.2} P_{\mathrm{in}}^{-0.73} R^{1.83} \kappa_{\mathrm{e}}^{0.64} n^{0.4} (R/a)^{0.06} \tag{4.11}$$

with given B_{ϕ} in T, I_{p} in MA, input heating power P_{in} in MW, density n in 10^{19} m^{-3}, minor and major radius a and R, respectively, given in m is used. The plasma elongation κ_{e} and the effective mass, A_{eff} are normalized quantities without associated units. With this and the definitions of the electron-ion energy transfer time (e.g. from [41]), an expression for the density, where the P_{LH} minimum occurs, can be derived as [165] (neglecting the dependence on elongation)

$$n_{\mathrm{e,min}}^{\mathrm{scal}} \approx 0.7 B_{\phi}^{0.62} I_{\mathrm{p}}^{0.34} a^{-0.95} (R/a)^{0.4}. \tag{4.12}$$

This formula together with the condition for equipartition and the ITPA scaling were the main approach to predict the L-H power threshold for ITER in the non-nuclear phase [167]. Equation 4.12 is an important ingredient to predict the lower validity limit of the ITPA scaling, which only applies to the high-density branch.

The same ingredients, i.e. observation (O3) providing the formular for the critical edge ion heat flow (equation 4.9) and the L-mode scaling (equation 4.11), can be used to derive an analytical formula for P_{LH} [358]. The difficulty in this approach is to introduce the effect of the electron-to-ion energy transfer sufficiently well in order to infer P_{LH} from equation 4.9. A possible path to describe these effects is the trick to split up the energy confinement time into an ion part

$$\tau_{\mathrm{E,i}} = \frac{3}{2} \frac{\overline{n}_{\mathrm{i}} \overline{T}_{\mathrm{i}} V}{P_{\mathrm{heat,i}} + P_{\mathrm{eq}}} \tag{4.13}$$

depending on the volume-averaged ion density $\overline{n}_{\mathrm{i}}$, volume-averaged ion temperature $\overline{T}_{\mathrm{i}}$, heating of the ions provided by the (external) heating system $P_{\mathrm{heat,i}}$ and the collisional energy transfer from electrons to ions

$$P_{\mathrm{eq}} = \frac{3}{2} \left\langle \frac{n_{\mathrm{e}} (T_{\mathrm{e}} - T_{\mathrm{i}})}{\tau_{\mathrm{ei}}} \right\rangle_V \cdot V \tag{4.14}$$

with volume average $\langle . \rangle_V$, and into an electron part

$$\tau_{\mathrm{E,e}} = \frac{3}{2} \frac{\bar{n}_{\mathrm{e}} \overline{T}_{\mathrm{e}} V}{P_{\mathrm{heat,e}} - P_{\mathrm{eq}}} \tag{4.15}$$

with analogous definitions.

Based on this, and reordering the terms to explicitly obtain $\tau_{\mathrm{ei}}/\tau_{\mathrm{E}}$, an analytical formula for P_{LH} can be derived being applicable to the full density range. Using the L-mode confinement time scaling (equation 4.11) for the energy confinement time and using the critical ion heat flow condition (equation 4.9), the analytical formula for the L-H power threshold according to Bilato *et al.* reads

$$P_{\mathrm{LH}}^{\mathrm{Bil}} = \frac{\left(1 + \frac{\tau_{\mathrm{E,i}}}{\tau_{\mathrm{E,e}}}\right)}{1 - \frac{\mathcal{GT}}{\bar{n}_{\mathrm{e}}^{2.3}} Q_{\mathrm{i,edge}}^{\mathrm{crit}}} Q_{\mathrm{i,edge}}^{\mathrm{crit}}. \tag{4.16}$$

According to this formular, the L-H power threshold P_{LH} is proportional to the critical ion heat flow $Q_{\mathrm{i,edge}}^{\mathrm{crit}}$ modified by a prefactor consisting of a large fraction. The enumerator contains the ratio of the ion and electron confinement times, and the denominator dependes again on the critical ion heat flow, the line-averaged density, and two more complex expressions $\mathcal{G}$ and $\mathcal{T}$. The first, contains the physics of the electron-ion heat exchange

$$\mathcal{G} = \alpha_{\mathrm{B}} \beta_{\mathrm{B}} \frac{\tau_{\mathrm{E}}}{\tau_{\mathrm{E,e}}} \frac{P_{\mathrm{eq}}}{P_{\mathrm{loss,i}} + P_{\mathrm{eq}}} \tag{4.17}$$

with two scalar parameters, $\alpha_{\mathrm{B}} > 1$, which is related to the temperature difference between electrons and ions, and $\beta_{\mathrm{B}} > 0$, which takes into account the differences between line-averages as used in scaling laws and volume-averages as used for the derivation of equation 4.16 (see reference [358] for exact definitions).

The second expression[3]

$$\mathcal{T} = 2 \cdot 10^{-6} \frac{A_{\mathrm{i}}}{Z_{\mathrm{i}}} \left(\frac{1}{3}\right)^{3/2} \left(\frac{10^6}{1.6022}\right)^{3/2} \frac{P_{\mathrm{in}}^{0.73}}{\bar{n}_{\mathrm{e}}^{0.4} V^{3/2}} \tau_{\mathrm{E,L-mode}}^{1/2} \tag{4.18}$$

contains the L-mode confinement time scaling (see equation 4.11), the mass number of the ions, A_{i}, and ion charge number Z_{i} (these are remnants of the electron-to-ion energy transfer time). The factor in front of the L-mode confinement time contains the input power and density in a form, so that it cancels the power and density dependence of the L-mode confinement time scaling. This way, the right hand side of equation 4.16 does not depend on the heating power, but a density dependence $\bar{n}_{\mathrm{e}}^{-2.3}$ still remains (in addition to the density dependence present in $Q_{\mathrm{i,edge}}^{\mathrm{crit}}$).

[3]Equation 4.18 is the correct expression to be inserted into equation (11) and (12) of [358]. The definition of $\mathcal{T}$ given there in equation (10) is misleading.

In order to make the parameter dependencies clearer, equation 4.16 can be rewritten with explicit dependencies as

$$P_{\mathrm{LH}}^{\mathrm{Bil}} = \frac{\left(1+\frac{\tau_{\mathrm{E,i}}}{\tau_{\mathrm{E,e}}}\right) Q_{\mathrm{i,edge}}^{\mathrm{crit}}}{1-\mathcal{G}\cdot 28.78 A_{\mathrm{i}} Z_{\mathrm{i}}^{-1} V^{-3/2} I_{\mathrm{p}}^{0.48} B_{\phi}^{0.015} \kappa_{\mathrm{e}}^{0.32} R^{0.915} \left(\frac{R}{a}\right)^{0.03} A_{\mathrm{eff}}^{0.1} \bar{n}_{\mathrm{e}}^{-2.3} Q_{\mathrm{i,edge}}^{\mathrm{crit}}}. \tag{4.19}$$

The main properties of this equation are the following:

- For very high densities, the denominator on the right hand side is approximately equal to one, so that the L-H power threshold is proportional to the ion heat flow $Q_{\mathrm{i,edge}}^{\mathrm{crit}}$, i.e. $P_{\mathrm{LH}} \propto \bar{n}_{\mathrm{e}}^{1.05} B_{\phi}^{0.68} S^{0.93}$ according to the parameter dependence of equation 4.9. This approximately reproduces the parameter dependencies of the ITPA scaling (equation 2.13), which is valid for the high density branch.

- For pure ion heating, the electron-to-ion energy transfer term is negative, $P_{\mathrm{eq}} < 0$, hence, $\mathcal{G} < 0$. In this case, the denominator is positive, and the main fraction on the right hand side is positive as well, so that no minimum in P_{LH} as a function of the density is possible as experimentally found in AUG for dominantly ion-heated plasmas [165].

- For pure electron heating, $\mathcal{G} > 0$, the main fraction on the right hand side produces a minimum due to the fact that a decreasing density decreases the denominator, hence, increasing P_{LH}. This reproduces the typical U-shaped curves for P_{LH} despite the linear dependence of $Q_{\mathrm{i,edge}}^{\mathrm{crit}}$ on density as achieved for electron heated plasmas in AUG. Determining the maximum of the denominator of equation 4.19 delivers a formula for $\bar{n}_{\mathrm{e,min}}$ very similar to equation 4.12. Equation 4.19 quantitatively agrees well with measured data for H, D, and He plasmas at AUG. $\mathcal{G}$ and the confinement time ratio $\tau_{\mathrm{E,i}}/\tau_{\mathrm{E,e}}$, which can be considered as free fitting parameter, since they are difficult to predict, have then typical values of $\mathcal{G} \approx 4.5$ and $\tau_{\mathrm{E,i}}/\tau_{\mathrm{E,e}} \approx 0.1$ [358].

- This formula contains a natural current dependence due to the inclusion of the L-mode confinement properties. A higher current decreases P_{LH} by lowering the denominator. This effect is most significant in the low-density branch and affects likewise $\bar{n}_{\mathrm{e,min}}$.

- The isotope dependence via A_{eff} (and more hypothetically via Z_{eff}) and the magnetic field dependence via B_{ϕ} enters through the respective

dependences of $Q_{\mathrm{i,edge}}^{\mathrm{crit}}$ into equation 4.19. The dependence on Z_{i} is a remnant of the electron-ion energy transfer time $\tau_{\mathrm{E,i}}$. As mentioned above, equation 4.19 correctly predicts the power threshold for H, D and He at AUG [358], when $Q_{\mathrm{i,edge}}^{\mathrm{crit}} \propto Z_{\mathrm{eff}}/A_{\mathrm{eff}}$ is assumed.

A comparison of equation 4.16 with JET data [361], for which transport simulations provided the correct input parameters for $\mathcal{G}$ and $\tau_{\mathrm{E,i}}/\tau_{\mathrm{E,e}}$ showed excellent agreement, when the actual ion heat flux instead of the ion heat flow scaling (equation 4.9) is used. This indicates that the explanation of the minimum of P_{LH} at a certain density $\bar{n}_{\mathrm{e,min}}$ by the physics of the electron-to-ion energy transfer is well confirmed by experimental data. However, it also showed, that equation 4.16 can only be used in low-torque conditions, for which the ion heat flow scaling (equation 4.9) is valid. For high-torque applications, the analytical formula for P_{LH} has to be modified.

4.3.2 The Explanatory Power of a Critical Velocity

As shown above, the analytical formula for the L-H power threshold (equation 4.19) can explain the main empirical parameter dependencies of the L-H power threshold, namely the dependence on I_{p}, B_ϕ, A_{eff}, κ_{e}, V, S, R, a, and Z_{i}, and it explains the minimum of P_{LH} by the effect of the energy transfer between electrons and ions. However, it fails to predict the effect of input torque by neutral beam heating, and it makes use of the critical ion heat flow, but cannot explain, why it exists. In the following, we try to address the last two points, and discuss a few further aspects by putting the observation of a critical $E \times B$ velocity (observation (O4)) into the focus.

We start our consideration with the definition of the L-H power threshold P_{LH} and the associated power balance

$$P_{\mathrm{LH}} = P_{\mathrm{loss}} = P_{\mathrm{ohm}} + P_{\mathrm{aux}} - \frac{dW}{dt} - P_{\mathrm{rad}} \tag{4.20}$$

$$= Q_{\mathrm{i}} + Q_{\mathrm{e}} \tag{4.21}$$

$$= -n_{\mathrm{i}}\chi_{\mathrm{i}}\nabla T_{\mathrm{i}} S - n_{\mathrm{e}}\chi_{\mathrm{e}}\nabla T_{\mathrm{e}} S. \tag{4.22}$$

The first part (equation 4.20) is P_{sep} as defined in equation 2.15 and represents the total power input minus the temporal evolution of the energy content of the plasma and radiation losses. This is balanced by the transport losses[4], i.e. the ion heat flow Q_{i} and the electron heat flow Q_{e} (equation 4.21), which can be expressed in terms of the respective densities, heat diffusivities, χ_{i} and χ_{e}, respectively, and the gradients of the temperatures (equation 4.22).

[4]This is the reason, why P_{loss} is called the loss power.

Convective transport is neglected for this considerations. S is the surface of the plasma. This power balance equation is fulfilled at all times and not specific to the L-H transition, but at the time of the L-H transition, we can set it equal to P_{LH}. If it is assumed that all heating sources deposit the power in the core of the plasma inside a certain radial position $r = r_0$ (and radiation losses and changes in W likewise take place inside r_0), this power balance equation is valid locally at all points outside r_0.

Next, the conditions at the L-H transition are inserted into the power balance equation 4.22. For this purpose, we assume as a first condition, that the radial electric field at the L-H transition is determined by neoclassics (see equation 2.8)

$$E_{\mathrm{r,neo}} = \frac{\nabla p_{\mathrm{i}}}{e n_{\mathrm{i}}} - \frac{\alpha_{\mathrm{neo}}}{e}\nabla T_{\mathrm{i}} + \frac{B B_\theta}{B_\phi}\left\langle u_{||,i}\right\rangle . \tag{4.23}$$

$$= \frac{1}{e}\nabla T_{\mathrm{i}} + \frac{T_{\mathrm{i}}}{e}\frac{\nabla n_{\mathrm{i}}}{n_{\mathrm{i}}} - \frac{\alpha_{\mathrm{neo}}}{e}\nabla T_{\mathrm{i}} + \frac{B B_\theta}{B_\phi}\left\langle u_{||,i}\right\rangle . \tag{4.24}$$

For the second step we used the product role to split the pressure gradient into a temperature gradient term and a density gradient term. As next step, equation 4.24 is solved for the ion temperature gradient

$$\nabla T_{\mathrm{i}} = \frac{e}{1-\alpha_{\mathrm{neo}}}\left(E_{\mathrm{r,neo}} - \frac{T_{\mathrm{i}}}{e}\frac{\nabla n_{\mathrm{i}}}{n_{\mathrm{i}}} - \frac{B B_\theta}{B_\phi}\left\langle u_{||,i}\right\rangle\right). \tag{4.25}$$

Inserting this into equation 4.22 yields

$$\begin{aligned} P_{\mathrm{LH}} = &- n_{\mathrm{i}}\chi_{\mathrm{i}}\left(\frac{e}{1-\alpha_{\mathrm{neo}}}\left(E_{\mathrm{r,neo}} - \frac{T_{\mathrm{i}}}{e}\frac{\nabla n_{\mathrm{i}}}{n_{\mathrm{i}}} - \frac{B B_\theta}{B_\phi}\left\langle u_{||,i}\right\rangle\right)\right) S \\ &- n_{\mathrm{e}}\chi_{\mathrm{e}}\nabla T_{\mathrm{e}} S. \end{aligned} \tag{4.26}$$

The density gradient at the location r can be replaced by an integral of the radially dependent density source S_{n} (typically electron impact ionization) from the plasma center up to position r. This can be derived from the stationary continuity equation assuming a diffusive particle flux $\Gamma = -D_{\mathrm{p}}\nabla n$ with particle diffusion coefficient D_{p} and we obtain

$$\begin{aligned} P_{\mathrm{LH}} = &- n_{\mathrm{i}}\chi_{\mathrm{i}}\left(\frac{e}{1-\alpha_{\mathrm{neo}}}\left(E_{\mathrm{r,neo}} + \frac{T_{\mathrm{i}}}{e}\frac{\int_0^r S_{\mathrm{n}}(r)dr}{D_{\mathrm{p}} n_{\mathrm{i}}} - \frac{B B_\theta}{B_\phi}\left\langle u_{||,i}\right\rangle\right)\right) S \\ &- n_{\mathrm{e}}\chi_{\mathrm{e}}\nabla T_{\mathrm{e}} S. \end{aligned} \tag{4.27}$$

Due to this replacement, we implicitly assume very slow changes of the density prior to the L-H transition and we neglect convective contributions to the particle flux.

The next step is decisive: We replace the radial electric field by the critical velocity $v_{\mathrm{crit}} = 6.7$ km/s into electron diamagnetic direction as it was found at AUG (observation (O4))

$$E_{\mathrm{r,neo}} = -|v_{\mathrm{crit}}|B. \tag{4.28}$$

Inserting this into equation 4.27 delivers an expression for the L-H power threshold based on the assumption that the plasma enters H-mode, when the critical $E \times B$ velocity is reached:

$$\begin{aligned} P_{\mathrm{LH}} = &- n_{\mathrm{i}}\chi_{\mathrm{i}} \left(\frac{e}{1-\alpha_{\mathrm{neo}}} \left(-|v_{\mathrm{crit}}|B + \frac{T_{\mathrm{i}}}{e} \frac{\int_0^r S_{\mathrm{n}}(r)dr}{D_{\mathrm{p}} n_{\mathrm{i}}} - \frac{BB_\theta}{B_\phi} \left\langle u_{||,i} \right\rangle \right) \right) S \\ &- n_{\mathrm{e}}\chi_{\mathrm{e}} \nabla T_{\mathrm{e}} S. \end{aligned} \tag{4.29}$$

This equation has to be evaluated at the position r, where the critical velocity is reached, i.e. inside the E_{r} well, where the velocity is maximum.

Equation 4.29 is somewhat unhandy, but can explain several main parameter dependences of P_{LH} including effects not covered by equation 4.19 as shown in the following.

Explanation of Parameter Dependence of ITPA scaling

The ITPA scaling (see equation 2.13) is valid only for the high-density branch, thus, we can assume equipartition, so that T_{i} and T_{e} have sufficiently equilibrated. Under this conditions $\nabla T_{\mathrm{e}} = \nabla T_{\mathrm{i}}$ holds, and equation 4.22 reads

$$P_{\mathrm{LH}} = -n_{\mathrm{i}}\chi_{\mathrm{i}}\nabla T_{\mathrm{i}} S - n_{\mathrm{e}}\chi_{\mathrm{e}}\nabla T_{\mathrm{e}} S = -n_{\mathrm{i}}\chi_{\mathrm{tot}}\nabla T_{\mathrm{i}} S \tag{4.30}$$

with total heat diffusivity $\chi_{\mathrm{tot}} = \chi_{\mathrm{i}} + \chi_{\mathrm{e}}$. We assumed furthermore $n_{\mathrm{i}} = n_{\mathrm{e}}$.

Replacing the ion temperature gradient by equation 4.25 and assuming that the density gradient term contributes equally to the radial electric field as the ion temperature gradient term, i.e. $eE_{\mathrm{r,neo}} = \nabla p_{\mathrm{i}}/n_{\mathrm{i}} = \nabla T_{\mathrm{i}} + T_{\mathrm{i}}\nabla n_{\mathrm{i}}/n_{\mathrm{i}} \approx 2\nabla T_{\mathrm{i}}$, as well as neglecting the parallel ion velocity term and assuming $\alpha_{\mathrm{neo}} = 0$, we obtain

$$P_{\mathrm{LH}} = e n_{\mathrm{i}}\chi_{\mathrm{tot}} \frac{1}{2} |v_{\mathrm{crit}}| BS. \tag{4.31}$$

Inserting $v_{\mathrm{crit}} = 6.7$ km/s and an order of magnitude estimation of the total heat diffusivity $\chi_{\mathrm{tot}} = 1$ m^2/s yields

$$P_{\mathrm{LH}} \approx 0.05 n_{\mathrm{i}} BS \tag{4.32}$$

with P_{LH} in MW, n_{i} in 10^{20} m^{-3}, B in T, and S in m^2. The density is here the local ion density instead of the line-averaged density as used in the ITPA scaling. But apart from this detail, the agreement between this simple formula 4.32 and the ITPA scaling (see equation 2.13) is remarkable. Thus, the critical velocity condition together with the assumption of a neoclassical field naturally explains the main parameter dependences of the ITPA scaling, i.e. the dependence of P_{LH} on density, magnetic field and plasma surface.

Explanation of Isotope Effect of P_{LH}

The simple formula 4.31 is proportional to the total heat diffusivity χ_{tot}, and the critical velocity is likewise valid for other isotopes than D as shown in AUG plasmas [229]. Thus, any isotope dependence of transport, e.g. $\chi_{\mathrm{tot}} \propto Z_{\mathrm{i}}/A_{\mathrm{eff}}$, directly introduces an isotope dependence of P_{LH}.

This is also true for the general expression 4.29, since it likewise depends on the heat diffusivities of ions and electrons.

Explanation of Torque Dependence of P_{LH}

The torque dependence of P_{LH} enters equation 4.29 via the flux-surface averaged parallel ion velocity $\langle u_{||,i} \rangle$. Torque contributions, which increase this velocity, increase P_{LH}, and torque components anti-parallel to $\langle u_{||,i} \rangle$ decrease the L-H power threshold. This is a result of the fact that the parallel velocity component supports (or weakens) the radial electric field in the radial force balance (see equation 2.4), so that the critical velocity is reached easier (or more difficult) compared to the case without torque input.

Explanation of Wall Effect and Fuelling on P_{LH}

As shown above in section 4.1, metallic wall devices exhibit lower L-H power thresholds than carbon wall devices. As shown in AUG [45], the different wall material mainly affected the density profile due to different fuelling properties, which might be related to particle reflection coefficients of the wall material. The term containing the integral over the particle source S_{n} in equation 4.29 can take into account such effects. More specifically, neutrals reflected from a tungsten wall penetrate deeper and in higher amounts into the plasma than in a carbon wall, so that the (integral of the) source profile is higher in the tungsten case [45]. According to equation 4.29, a higher fuelling decreases the L-H power threshold.

In general, a better fuelling deep inside the confined plasma increases the source term and, hence, the normalized density gradient, so that a lower L-H power threshold can be expected.

Fuelling and the presence of neutrals in different regions of the plasma can impact the intrinsic rotation of the plasma [345]. Thus, effects of neutrals can also potentially enter equation 4.29 via the parallel velocity term.

Explanation of Plasma Shape Dependence on P_{LH}

The plasma shape and its parameters do not directly enter equation 4.29, but the shape, especially the divertor geometry and the X-point position, can change the distribution of neutrals and the fuelling properties of the plasma. As explained above, fuelling conditions enter the term containing the particle source S_{n} and could change the intrinsic rotation, consequently, modifying P_{LH}.

Changes in plasma shape could potentially also change the transport coefficients χ_{e}, χ_{i} and D due to modification of the linear stability conditions or non-linear effects of microturbulence [362, 363]. These are, however, difficult to predict.

Explanation of Constant Edge Temperature

If we assume $\nabla T_{\mathrm{i}} + T_{\mathrm{i}} \nabla n_{\mathrm{i}}/n_{\mathrm{i}} \approx 2\nabla T_{\mathrm{i}}$, i.e. equal contributions of the temperature gradient term and the density gradient term to the diamagnetic part of E_{r} as done for the derivation of equation 4.32, the critical velocity condition implies

$$-e|v_{\mathrm{crit}}|B = eE_{\mathrm{r,neo}} = (2 - \alpha_{\mathrm{B}})\,\nabla T_{\mathrm{i}} - \frac{BB_{\theta}}{B_{\phi}}\left\langle u_{||,i}\right\rangle \tag{4.33}$$

For low torque conditions as it is the case for the JET data presented above, e.g. in figure 4.10, and neglecting the neoclassical contribution by setting $\alpha_{\mathrm{B}} = 0$, the ion temperature gradient is simply

$$\nabla T_{\mathrm{i}} = -e\frac{1}{2}|v_{\mathrm{crit}}|B. \tag{4.34}$$

Thus, a critical velocity implies a constant ion temperature gradient for a given magnetic field B. At high collisionality, for which we can assume $T_{\mathrm{i}} = T_{\mathrm{e}}$ the same expression holds for the electron temperature gradient. As shown at AUG, the critical velocity seems to be independent from the isotope [229], explaining why the temperature profiles at the edge are so similar for different isotopes as found for JET [81, 323] and AUG [312]. In this sense, observation (O4) (critical edge $E \times B$ velocity) explains observation (O1) (critical edge temperature).

Explanation of Linear Relation between P_{LH} and Transport

Solving equation 4.33 for the ion temperature gradient and inserting the result into the power balance equation 4.22 while $T_{\mathrm{i}} = T_{\mathrm{e}}$ is assumed (same approach as done for equation 4.31) yields

$$P_{\mathrm{LH}} = -n_{\mathrm{i}}\chi_{\mathrm{tot}}\nabla T_{\mathrm{i}}S = \frac{-en_{\mathrm{i}}\chi_{\mathrm{tot}}}{2-\alpha_{\mathrm{neo}}}\left(-|v_{\mathrm{crit}}|B - \frac{BB_\theta}{B_\phi}\left\langle u_{||,i}\right\rangle\right)S \tag{4.35}$$

This equation can be further simplified by neglecting neoclassical effects ($\alpha_{\mathrm{B}} = 0$) to

$$P_{\mathrm{LH}} = \frac{en_{\mathrm{i}}|v_{\mathrm{crit}}|BS}{2}\chi_{\mathrm{tot}} + \frac{en_{\mathrm{i}}\chi_{\mathrm{tot}}}{2}\frac{BB_\theta}{B_\phi}\left\langle u_{||,i}\right\rangle S. \tag{4.36}$$

The first term is linear in χ_{tot} for a constant magnetic field B, constant density n_{i} and plasma surface S, while the second term is more complex, since the parallel velocity component $\left\langle u_{||,i}\right\rangle$ is difficult to be parameterized. But since this term is in general rather small, it is not difficult to imagine that equation 4.36 has a similar formal composition as the fit curve 4.6, which revealed a linear relation between P_{sep} and the effective heat diffusivity χ_{eff} for a set of plasmas with different effective isotope masses in a limited density range (figure 4.12). This indicates, that observation (O2) as described by equation 4.6 follows directly from the critical velocity condition (observation (O4)).

Explanation of Critical Ion Heat Flux

Solving equation 4.33 for the ion temperature gradient and inserting the result into the ion heat flow yields

$$Q_{\mathrm{i}} = -n_{\mathrm{i}}\chi_{\mathrm{i}}\nabla T_{\mathrm{i}}S = \frac{-en_{\mathrm{i}}\chi_{\mathrm{i}}}{2-\alpha_{\mathrm{neo}}}\left(-|v_{\mathrm{crit}}|B - \frac{BB_\theta}{B_\phi}\left\langle u_{||,i}\right\rangle\right)S \tag{4.37}$$

Again, neglecting neoclassical effects ($\alpha_{\mathrm{B}} = 0$) and neglecting the parallel velocity term yields a simple expression

$$Q_{\mathrm{i}} = \frac{en_{\mathrm{i}}\chi_{\mathrm{i}}}{2}|v_{\mathrm{crit}}|BS. \tag{4.38}$$

Choosing $\chi_{\mathrm{i}} = 0.5\chi_{\mathrm{tot}}$ and a critical velocity of 6.7 km/s delivers an expression very similar to the simplified formula for P_{LH} in equation 4.32:

$$Q_{\mathrm{i}} = 0.025n_{\mathrm{i}}BS \tag{4.39}$$

for a heat flow given in MW, density given in 10^{20} m^{-3}, B in T, and S in m^2. The similarities with the Schmidtmayer-Ryter scaling [357] (equation 4.9) is remarkable. As an example, inserting $B = 2.35$ T and $S = 40$ m^2 as typical parameters at AUG into equation 4.39 yields $Q_\mathrm{i} = 0.235 n_\mathrm{i}$. This is very close to the formula (2) given in reference [165]. As in the case for the simplified P_LH scaling, the difference here is that the multi-machine scaling of Schmidtmayer-Ryter contains the line-averaged density, while equation 4.39 contains the ion density at the edge and slighty different exponents for density, magnetic field and plasma surface. Despite these limitations, our considerations clearly show that the critical ion heat flux condition is just a consequence of the critical velocity condition, i.e. observation (O3) follows from observation (04).

In cases with finite torque, i.e. a finite parallel ion fluid velocity $\langle u_{||,i} \rangle$, the ion heat flux does not follow a simple dependence on n_i, B, and S anymore and the more complex expression equation 4.37 holds. The input torque by NBI modifies $\langle u_{||,i} \rangle$ in a complex way depending on specific NBI beam parameters. But as a general rule, the effect of NBI torque on $\langle u_{||,i} \rangle$, and hence on P_LH, is higher at low densities [165] and for higher heating powers [336]. In this sense, the strongest deviations of Q_i from a linear dependence on density are expected at low densities as found at JET [361].

4.3.3 Evaluation of the Heuristic Picture

We have shown that a critical maximum $E \times B$ velocity at the plasma edge as a condition correlating with the L-H transition (observation (O4)) is the key postulation of the heuristic picture of the L-H transition presented here. This condition implies all other key observations (constant edge temperatures (O1), linear relation between P_LH and heat transport (O2), and critical edge ion heat flux (O3)) including only weak additional assumptions. By means of this condition, the two central equations for P_LH, equation 4.19 and equation 4.29, were derived. Equation 4.19 shows the most important parameter dependencies of P_LH explicitly and includes a parameterization of the electron-to-ion energy transfer, which is relevant at low densities. But it does not contain the effect of torque, which is, however, well explained by equation 4.29. In total, practically all parameter dependencies and main observations can *qualitatively* be explained by these two formulas.

For one fusion device, e.g. AUG, these formulas allow for quantitative comparisons with experimental data. As an example: once the critical $E \times B$ velocity is measured or a good fit to one of the data points is found, it is possible to apply equation 4.19 and equation 4.29 successfully to plasmas sufficiently similar to the reference plasma [358]. However, a quantitative

prediction of P_{LH} for future devices remains difficult for two main reasons: First, the critical $E \times B$ velocity is not known (it is even not known whether this would exist in a future device), and, second, the (turbulent) transport models are not reliable yet to make good predictions of the transport coefficients $\chi_{\mathrm{e}}, \chi_{\mathrm{i}}$ and D, which are essential.

Whether a critical $E \times B$ velocity is present in all conditions at the L-H transition, is not clear. Despite there is a wealth of data supporting a critical $E \times B$ velocity at AUG [46, 45, 229] and at JET [327, 350], recent measurements with Doppler reflectometry at JET [364, 365] and CXRS at AUG [348] have shown that there is no critical velocity or that its value depends on the plasma configuration and density under certain conditions. Thus, a predictive model for P_{LH} must contain a predictive description of the critical $E \times B$ velocity in addition to the anyhow required transport coefficients.

4.3.4 Relation to Shear Suppression Model

The leading model for the suppression of turbulence and the consequential transition to H-mode is the model of turbulence suppression by $E \times B$ shear [366, 162, 367]. The basic idea is that turbulence is suppressed, when the $E \times B$ shearing rate (here in its simplest form) [107]

$$\omega_{E\times B} = r\frac{\partial}{\partial r}\left(\frac{E_{\mathrm{r}}}{rB}\right) \tag{4.40}$$

exceeds the linear growthrate γ_{t} of the most unstable turbulent mode, i.e.

$$\omega_{E\times B} > \gamma_{\mathrm{t}}. \tag{4.41}$$

In this picture, the growing instability cannot extend into radial direction, since it is decorrelated due to the strong shear field. The inverse relation

$$\tau_{E\times B} < \tau_{\mathrm{t}}, \tag{4.42}$$

which relates the shearing time $\tau_{E\times B}$ to the autocorrelation time or eddy turn-over time of turbulence τ_{t}, is an equivalent representation of the suppression condition. In this picture, the shear field has decorrelated, i.e. torn apart, the turbulent eddy already, before the eddy can perform one turn, which corresponds to its natural life time. A third equivalent suppression condition is

$$L_{E\times B} < L_{\mathrm{t}}, \tag{4.43}$$

with shear lengths $L_{E\times B} = \tau_{E\times B} v_{E\times B}$, which is the length scale of the shear field depending on the $E \times B$ velocity of the shear field, and the turbulent correlation length $L_\mathrm{t} = \tau_\mathrm{t} v_\mathrm{turb}$, which can be interpreted as the average size of the eddy spinning with a typical turbulent velocity v_turb.

In a graphical representation, the $E \times B$ shear field first tilts, then stretches and finally strains the turbulent eddies. This way, their perpendicular size L_t (the extension perpendicular to the shear flow) is reduced (see figure 4.16). Consequently, the random walk diffusion coefficient [6, 5], i.e. the transport coefficient of turbulence for this case

$$D_\mathrm{RW} = \frac{L_\mathrm{t}^2}{2\tau_\mathrm{t}} \tag{4.44}$$

is reduced.

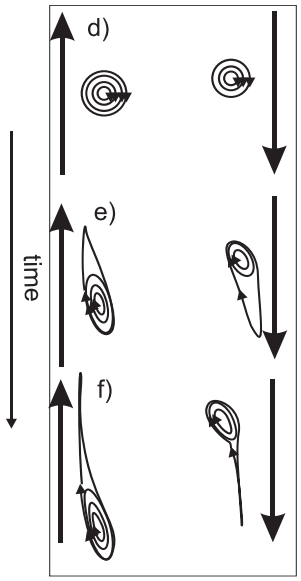

Figure 4.16: *Shearing of turbulent eddies in an $E \times B$ velocity shear field (adapted from [63]). The background shear is sufficiently strong to tilt, stretch and strain the smaller eddies. This way, energy is transferred from small to large scales and the turbulent transport suppressed or at least reduced due to smaller radial widths of the eddies.*

The conditions shown above can also be formulated as an energetic equivalent [368], and measurements in laboratory experiments have shown [63], that the energy transfer from turbulence to the background shear field is non-local in wave-number space, i.e. relatively small eddies interact with the largest flow scales.

The idea of the critical $E \times B$ velocity as discussed above, can be related to the shear suppression paradigm. For this, we assume that the $E \times B$ shearing rate (equation 4.40) inside the E_r well can be written as

$$\omega_{E\times B} = r\frac{\partial}{\partial r}\left(\frac{E_\mathrm{r}}{rB}\right) \approx \frac{1}{\Delta r}\frac{E_\mathrm{r,min}}{B} = \frac{v_\mathrm{crit}}{\Delta r} \tag{4.45}$$

with the value of the minimum of the radial electric field profile $E_\mathrm{r,min}$ and the radial width Δr of the slope of E_r. Hence, Δr is about half the width of the E_r well. Since the critical velocity as introduced above is interpreted as the $E \times B$ velocity of the neoclassical radial electric field, this condition implies that the shear rate is exclusively given by the *background* flow profile. Inserting this into the shear suppression condition equation 4.41 indicates, that

$$v_\mathrm{crit} = \gamma_\mathrm{t}\Delta r \tag{4.46}$$

holds at the transition. There is some evidence from AUG and DIII-D, that the pedestal width in real space is approximately constant for a large range of parameters [369]. Thus, Δr interpreted as the pedestal width, which does not change much in different plasma conditions, implies that the turbulent growth rate is proportional to the critical $E \times B$ velocity. In other words, the property of v_crit of being constant for a large range of densities, magnetic fields and for different isotopes must hold likewise for γ_t in this picture. There are some indications, that the turbulent growthrate γ_t depends only weakly on the ion mass [370], but it is not certain, that this applies in other conditions, and more dedicated edge simulations at higher collisionality found a rather strong isotope dependence of the turbulent growthrate [354] making it more difficult to explain a critical $E \times B$ velocity being largely independent of the isotope mass. It is also possible, that the condition 4.46 is too simple and the energy balance between turbulence and flows [368] has to be employed, as successfully done for a large data set at AUG. Most likely, a quantitative comparison between experiment and theory requires non-linear turbulence simulations at the edge [55, 371] in order to take the complex turbulent dynamics and its parameter dependencies correctly into account.

In summary, the heuristic picture of the L-H transition based on a critical $E \times B$ velocity is consistent with the shear suppression mechanism of the L-H transition, and basic properties of the turbulence and its parameter dependences can explain the heat flow scaling as argued in reference [358]. But the postulate of a critical $E \times B$ velocity does not require the shear suppression mechanism as explanation, and could be independent from it from a logical point of view.

4.4 Alternative Models

The shear suppression mechanism by the (neoclassically driven) background shear can be connected to the critical velocity condition as shown above, but this mechanism is not the only suggested concept explaining the L-H transition. In fact there is a plethora of alternative models [353]. Therefore, a few selected alternative concepts are presented, which are either important, since often discussed in the scientific community, or which contain intrinsically a condition similar to the critical velocity condition introduced above.

4.4.1 Zonal Flows as a Trigger

Directly connected to the shear suppression mechanism as introduced above is the shear suppression by low-frequency zonal flows [162, 372, 74, 373, 374, 375] or GAMs [216]. It is the same mechanism based on the same suppression conditions (equations 4.41, 4.42 and 4.43), but here the shear provided by ZFs or GAMs instead of the shear provided by the (stationary or neoclassical) background flow is interpreted as being causal for triggering the L-H transition. Despite there is some evidence, that the Reynolds-stress driven flows are triggering the L-H transition [162, 372, 74, 373, 374, 216], it is not confirmed in all experiments [51, 221, 376]. In addition, the majority of the investigations conclude that the background shear flow is essential to *sustain* the H-mode even in cases, in which ZFs or GAMs trigger the L-H transition. Thus, the access to a long-lasting H-mode operation scenario needs in any case the presence of a background shear flow. Despite there are some approaches to qualitatively explain specific features of the L-H power threshold like the existence of a minimum in P_{LH} for a certain density [377], the predictive capability of models involving Reynolds-stress driven flows are very limited. First global full-f simulations show a possible beneficial role of Reynolds-stress driven flows [378]. But they are to expensive yet for parameter scans, which would be necessary to elucidate the parameter dependences of P_{LH} and to reveal the key physical ingredients for the L-H transition.

4.4.2 Separatrix Operational Space

A very successful approach, which is able to correctly separate operational points of H-mode and L-mode phases collected in large data bases, is the characterization of plasmas in terms of a set of separatrix plasma parameters [352, 379, 368]. These parameters are analytical formulas for stability boundaries of MHD or turbulence driven instabilities and were first introduced by

Rogers, Drake and Zeiler [380]. Based on this set of separatrix operation space parameters, a condition for the L-H transition can be derived [368], which is essentially an energetic version of the shear suppression model introduced above, and some specific assumption about turbulent drive of electrons and ions. It is the only model based on shear suppression, which includes simple formulas to be evaluated at the separatrix and providing quantitative predictions including all desired parameter dependencies of P_{LH}. Thus, it is certainly worth to test this formalism at more tokamaks than only Alcator C-mod and AUG, in order to evaluate its predictive capabilities.

4.4.3 Transition from Diamagnetic to Paramagnetic Filaments

As shown in plasma physics textbooks [22], the linear pinch plasma is paramagnetic for low plasma beta, and becomes diamagnetic for higher beta. Based on this principle, a theory for the L-H transition was developed [381] associating the L-H transition as a magnetic phase transition, at which diamagnetic filaments are attracted by the main plasma, thus, forming a pedestal and the H-mode profiles. This theory provides a testable condition, and postulates the L-H transition, when the poloidal current density j_θ reverses its sign, i.e. a state boundary with $j_\theta = 0$ should exist. Since the poloidal current density is related to a poloidal velocity v_θ, this model intrinsically contains a critical velocity, which might translate to a critical $E \times B$ velocity under some further weak assumption.

Despite its simplicity and apparent compatibility with a critical velocity, the model based on the magnetic phase transition in the present state does not allow predictions of parameter dependences of P_{LH}.

4.5 Do We Understand the L-H Transition?

A future tokamak reactor cannot be reliably designed without the exact knowledge of P_{LH} [166] and, therefore, a better prediction than just the ITPA scaling (equation 2.13) is needed. Great progress has been made since the discovery of H-mode in 1982 [108] and many of the measured parameter dependences as presented above can be explained by existing models. But none of the models can quantitatively predict P_{LH} for a future reactor. The main lack in understanding of the L-H transition is not due to missing data, but due to a missing understanding of the L-H transition from first principle models. More than 35 analytical models for the L-H transition have been proposed already twenty years ago [353] and the number of further L-H transition mod-

els continuously increased since then. Most of these models have directly or indirectly two unknowns included: transport coefficients mimicking or representing heat transport and a criterion for a critical value of a certain edge parameter (e.g. temperature or $E \times B$ flow or more complex quantities provided by theory). Unfortunately, these parameters cannot be quantitatively predicted yet, since turbulent transport processes and turbulence suppression conditions are involved, for which reliable quantitative models applicable at the plasma edge do not exist yet. In other words, the prediction of P_{LH} will not be possible until an edge turbulence code is available, which can correctly handle steep gradients, a large range of collisionalities, large fluctuation amplitudes, complex magnetic topologies including X-point, neoclassical effects, effects of intrinsic rotation and neutral physics including atomic processes as it is attempted in recent code developments [378, 371, 55].

Chapter 5

Dynamics of Limit-Cycle Oscillations at ASDEX Upgrade

The first phase of the H-mode plasma after the L-H transition exhibits under certain conditions limit-cycle oscillations (LCOs) as introduced in section 2.5.3. In this chapter, we focus on the classical LCOs *after* the L-H transitions also called I-phase or M-mode, i.e. we will not discuss SAOs and other temporal structures. The main purpose of this chapter is to show experimental signatures of LCOs in detail as they were measured at AUG as presented in reference [159]. In a second step, a comparison of main experimental features with selected models of LCOs is presented.

5.1 Experimental Features of Limit-Cycle Oscillations at ASDEX Upgrade

5.1.1 General Observations

The regular or irregular pulsing of LCOs in the low kilohertz range can be measured in practically all plasma edge diagnostics provided that the diagnostic has a sufficient time resolution in order to resolve the single LCO bursts. Figure 5.1 shows an example of LCOs of an NBI heated plasma at AUG. Directly after switching on the NBI heating, the temperatures (figure 5.1c) start to rise continuously. The density (figure 5.1b) first stays on the same level as before the heating was switched on, but at about 50 ms after the NBI step, the density rises suddenly. At the same time the divertor shunt current I_{div} (figure 5.1d) drops significantly indicating that less particles and heat reach the divertor plates, and, hence, the confinement has improved. This is the time point of the L-H transition or, since the LCO phase is also

called the I-phase, the L-I transition. The LCOs, i.e. the I-phase bursts, are not visible in the time traces in the left panels of figure 5.1 due to too low time resolution of this representation.

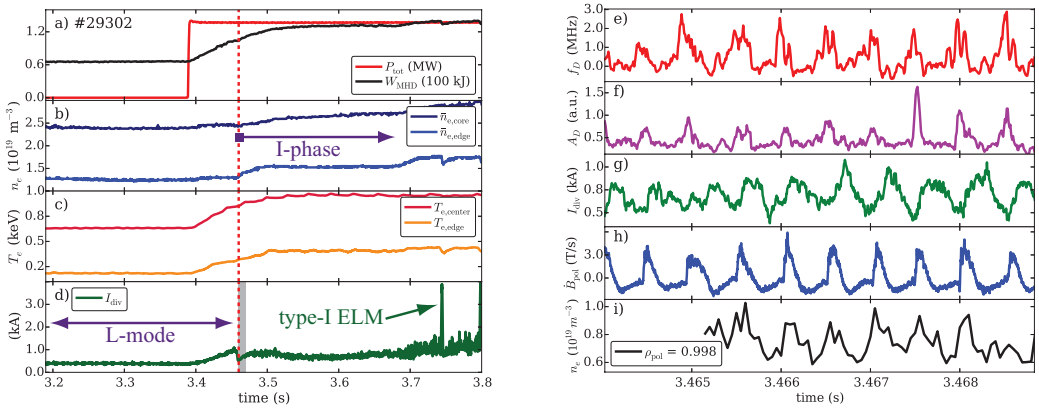

Figure 5.1: *Typical L-H transition at low density in AUG (reproduced from [159]): after switching on the auxiliary heating (red line in a), the plasma energy content (black line in a) and the temperatures in the center and at the edge (c) rise. The rise in line-averaged density (b) starts with a delay of about 50 ms and coincides with a drop in the divertor shunt current (d) and the start of the LCOs (dashed line). The time traces (e)–(i) show a short segment of the LCOs and correspond to the shaded area in (d). The LCOs are visible in the Doppler shift f_D (e) and the backscattered amplitude A_D of the Doppler reflectometry signal, as well as in the divertor current (g), magnetic probe signal below the divertor (h), and the local density slightly inside the LCFS (i).*

A zoom into a short time interval (grey bar in figure 5.1d) after the L-I transition is displayed in the right column of figure 5.1. It shows time traces of two signals obtained from Doppler backscattering [382, 72] in figure 5.1e and f. The first one is the Doppler shift f_D, which is proportional to the perpendicular plasma flow velocity $u_\perp = u_{E\times B} + u_{ph} \approx u_{E\times B}$, which can be assumed to be approximately equal to the $E \times B$ flow of the plasma $u_{E\times B}$, since the phase velocity u_{ph} of the turbulent structures, which give rise to the backscattering, is assumed to be small. The second signal is the amplitude of the backscattered Doppler signal A_D, which is proportional to the power of the density fluctuations, $\tilde{n}^2$, of the turbulence at the probing scale ($k_\perp \approx 9$ cm^{-1}). The microwave frequency was 68.5 GHz corresponding to a radial position of $\rho_{pol} = 0.995$.

The local measurements of $f_D \propto u_{E\times B}$ and $A_D \propto \tilde{n}^2$ indicate that the LCO bursts are associated with a flow modulation and an (almost) simulta-

neous rise in density fluctuations. The same oscillations, but slightly time shifted, are visible in the signal of the divertor shunt current (figure 5.1g) and in a magnetic pick-up coil below the divertor (figure 5.1h) measuring the time derivative of the poloidal magnetic field, $\dot{B}_{\mathrm{pol}}$. The local value of the edge electron density at ρ_{pol}= 0.998 (figure 5.1i) measured with the Li-BES diagnostic [281] likewise oscillates like the other quantities.

In this example, the LCOs are very regular, i.e. the waiting time between two bursts is constant. Although the frequency is so constant in this case, the signals do not look like sinusoidal oscillations, but are rather spiky with a steep rising edge and a slightly shallower falling edge.

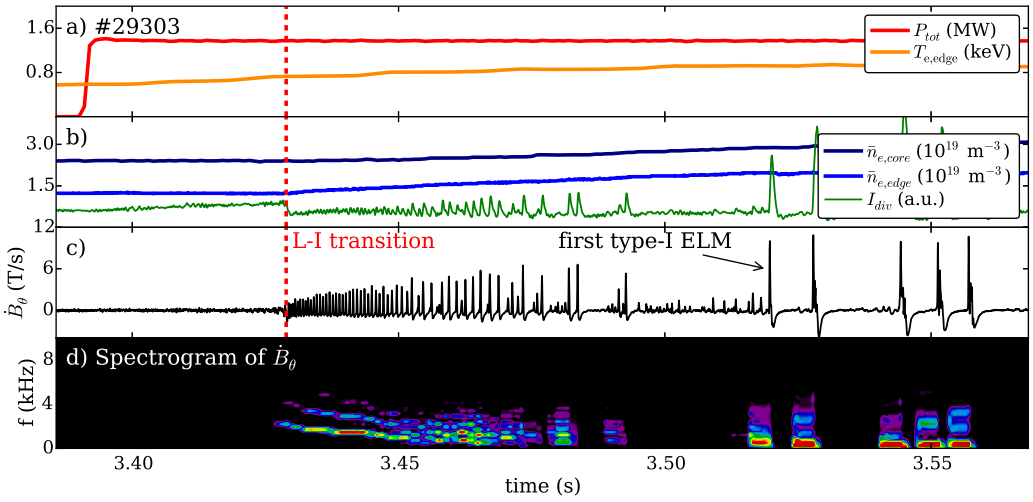

Figure 5.2: *(a) Heating power (red) and edge electron temperature (orange), (b) line-averaged density (dark blue: core, light blue: edge) and divertor shunt current (green) for a neutral beam heated L-H transition. The LCOs are clearly visible in the signal of the poloidal magnetic field pick-up coil below the divertor (c). Its spectrogram (d) exhibits higher harmonics at the beginning which vanish due to increasing degree of intermittency of the LCOs in the later phase (reproduced from [159]).*

The LCO bursts can smoothly transit from a very regular phase into a more intermittent, i.e. irregular phase as shown in figure 5.2. As visible in the divertor shunt current (figure 5.2b) and the magnetic pick-up coil signal (figure 5.2c), the bursts are regular and relatively small at the beginning, but they increase in amplitude and, simultaneously, they do not appear very regularly anymore, but arise intermittently until the first type-I ELM appears. The can even be observed between two type-I ELMs, i.e. they can coexist with type-I ELMs. Due to the non-sinusoidal shape of the oscillations, the

LCOs produce higher harmonics above the base frequency of a few kilohertz in spectrograms of the magnetic pick-up coil signal (figure 5.2d). This way, the LCOs can be very easily detected, at least as long as the pulsation is regular.

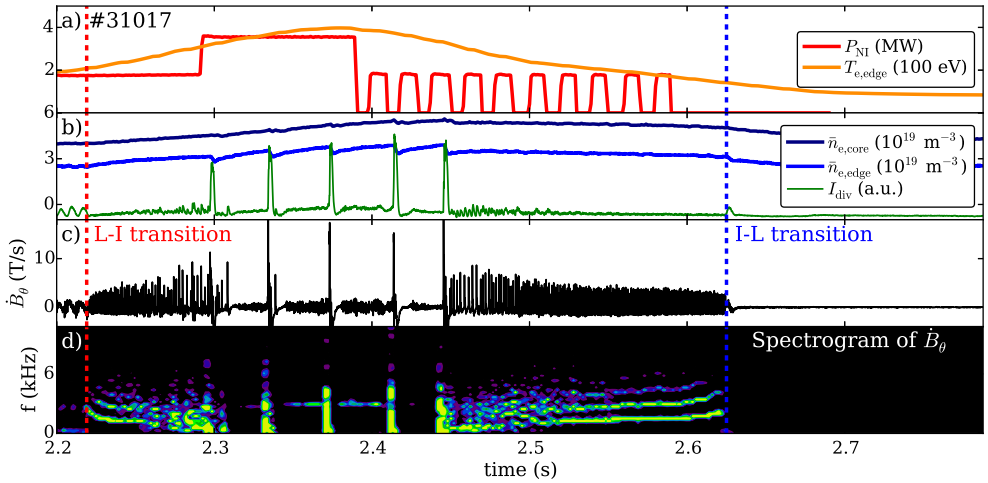

Figure 5.3: *Example of an L- to H-transition (red dashed line) induced by injection of neutral beam power and back transition (blue dashed line) to L-mode after a short H-mode phase in the same representation as figure 5.2. LCOs appear at the L-H transition as well as at the back transition to L-mode as recognizable by the higher harmonics in the spectrogram of the magnetic signal (reproduced from [159]).*

A similar example is shown in figure 5.3. The LCOs appear after the L-I transition and are clearly visible in the spectrogram of the magnetic signal with higher harmonics and a decreasing frequency. Then a fully developed H-mode phase with five type-I ELMs and without LCOs is established, but at a certain point, when the heating power is ramped down, the LCOs appear again. This time the frequency rises in time until the LCOs are suddenly stopped by the backtransition to L-mode at the I-L transition. This means, that the LCOs are not restricted to appear only during the pedestal build-up after the L-H transition, but they can appear in the same way close to the H-L transition. The dynamics after the L-I transition (increase in burst amplitude, decrease in frequency, increase of intermittency) is mirrored close to the I-L transition (decrease in burst amplitude, increase in frequency, increase of regularity). For a properly chosen heating power marginally above the L-H power threshold, the I-phase can kept constant arbitrarily long as was demonstrated in AUG plasmas.

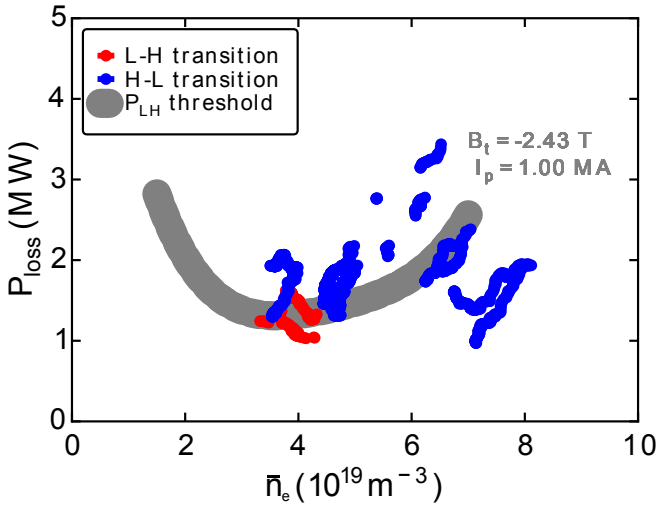

Figure 5.4: *Existence of LCOs depending on loss power, P_{loss}, and line-averaged core density $\bar{n}_{\mathrm{e}}$ for a set of comparable discharges with $B_{\mathrm{t}} = -2.43$ T and $I_{\mathrm{p}} = 1$ MA. LCOs at the transition from H- to L-mode (blue) are found at higher densities relative to the LCOs at the L- to H-transition (red). The grey bar indicates the L-H power threshold as presented in [47] (adapted from [159]).*

The I-phase at the L-H transition is considered to be the first part of H-mode, since the LCO phase is associated with a lower level of broadband turbulence and the kinetic profiles already exhibit a pedestal. In addition, global parameters like the energy content W or the energy confinement time τ_{E} are close to H-mode levels. Consequently, the I-phase at the L-H transition appears very close to the corresponding reference L-H power threshold (fit curve of P_{LH} data from figure 3 of reference [47]) as shown in figure 5.4 (red symbols). Similarly, the operational points of I-phases close to the H-L transition (blue symbols) are likewise close to P_{LH}. Parts of the I-phase operational points are below the reference power threshold. At the L-H transition, this is mainly due to the dW/dt-term in the definition of P_{loss}, since W rises quite strongly especially at the beginning of the I-phase, which decreases P_{loss}. For the data close to the H-L transition, two further factors come into play. First, the H-mode exhibits typically relatively high radiation levels due to improved impurity confinement, which can increase the operational points above the reference P_{LH}. Second, the I-phase can prolong the H-mode phase by several tens of milliseconds after the total heating power has fallen below the nominal L-H power threshold due to the good confinement properties of the I-phase sustaining the pedestal and the associated radial electric field

profile. In such a case, the operational point of the I-phase can be far below P_{LH}.

The I-phases at the L-H transition have typically lower density and higher temperatures than the I-phases at the H-L transition. This is due to the fact, that the density is relatively low in the first phase of H-mode, but the temperature can be already high provided by the external heating. In contrast, the I-phases at the H-L transition exhibit still quite high densities as typical for H-mode, but in cases, in which the heating was already switched off, the temperatures can be relatively low. Thus, I-phases and their accompanied LCOs are not restricted to low densities.

5.1.2 Radial Propagation

The I-phase bursts as shown in figure 5.1 on the right appear in many diagnostics, but the maximum of the bursts are sometimes shifted in time with respect to each other. Typically, signals further inside the plasma reach first its maximum and signals further outside or in the divertor reach the maximum later. Such a causality indicates that particles and energy are transported outward of the plasma. An example for such a radial propagation is shown in figure 5.5. It shows the normalized cross-correlation function

$$C_{\mathrm{i}}(\Delta t) = \frac{\langle x_{\mathrm{ref}}(t) x_{\mathrm{i}}(t+\Delta t)\rangle}{\sigma_{\mathrm{ref}}\sigma_{\mathrm{i}}} \tag{5.1}$$

with time delay Δt and the standard deviations σ_{ref} and σ_{i} of the reference signal and the signal of channel i under consideration, respectively. $\langle\cdot\rangle$ represents a temporal average (in the considered case from $t = 3.465$ to 3.475 s). The reference signal is the f_{D}-time trace of the Doppler backscattering measuring at $\rho_{\mathrm{pol}} \approx 0.995$. The different cross-correlation functions of this signal and the respective Li-BES channels are placed to the radial position of the line of sight of the considered Li-BES channel i given in terms of the normalized poloidal flux coordinate ρ_{pol}. The cross-correlation technique is very similar to the conditional averaging technique [285, 286] as introduced in chapter 3 and delivers similarly an averaged spatio-temporal picture of the respective phenomenon.

The spatio-temporal pattern of the cross-correlation function shown in figure 5.5 shows two main features: First, the I-phase bursts are clearly visible inside a wide radial range from $\rho_{\mathrm{pol}} = 0.98$ to $\rho_{\mathrm{pol}} = 1.7$. It might exist even further inside, but the Li-BES diagnostic is not sensitive there anymore [281]. The temporal periodicity is very clearly visible in the correlation. Second, the local maxima (one ribbon) of correlation is not perfectly vertically aligned,

but slightly tilted. This indicates, that a certain radial propagation of the density pattern takes place. A radial propagation velocity of about 100 m/s to 300 m/s can be obtained from the tilt. This demonstrates, that a radial transport of particles (and probably heat) is associated with the LCO bursts.

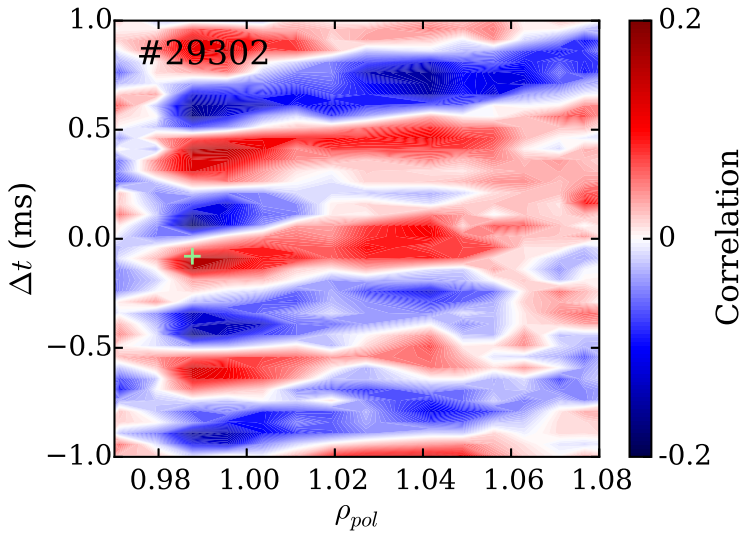

Figure 5.5: *Cross-correlation of the f_D-signal of the Doppler reflectometer with several radial channels of the Li-BES system during the I-phase of discharge #29302. The local maximum of the cross-correlation starts slightly inside the separatrix and propagates outward. The green cross indicates the maximum correlation (reproduced from [159]).*

5.1.3 Magnetic Structure

The LCOs are most clearly visible in a magnetic pick-up coil below the divertor as shown in figure 5.1h. This is, however, not the only coil, in which the pulsing can be detected. AUG possesses a full poloidal array of pick-up coils measuring $\dot{B}_{\mathrm{pol}}$. This array consists of 32 coils (see figure 5.6, right) and an example of their raw signals in I-phase is shown in figure 5.6, left. The amplitudes of the rawsignal are highest in coils 22 to 25, which are located below the divertor. This might be related to the fact that the transport associated with the LCO bursts induce currents in the active X-point region of the plasma generating measurable magnetic fields.

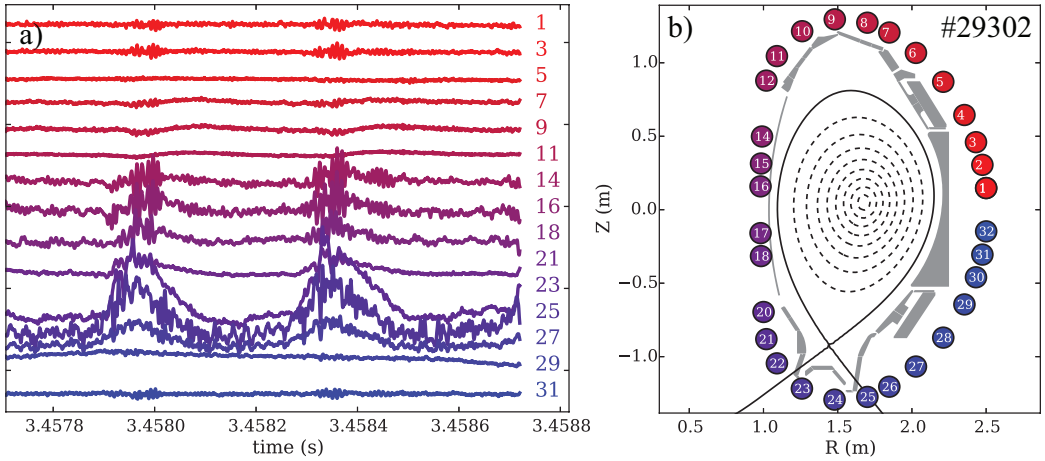

Figure 5.6: *Selected signals (a) of magnetic pick-up coils measuring $\dot{B}_{\mathrm{pol}}$ from a poloidal probe array (b) for discharge #29302 during the I-phase. The strongest pulsation is found in probes 22 to 25 below the divertor (reproduced from [159]).*

Besides the relatively large LCO bursts in the low kilohertz range, the raw signals exhibit a high frequency component in the range of about 100 kHz, which seems to be correlated to the appearance of the LCO bursts. As will discussed below, these high frequency oscillations might be related to precursor modes. The same features were found in M-modes at JET [226], which was one of the key features proving that the M-mode at JET is the same phenomenon as the I-phase at AUG.

Similar as done for the radial propagation of the Li-BES data as shown in figure 5.5, a cross-correlation analysis can likewise be applied to the magnetic pick-up coil data in order to study the poloidal propagation of the bursts. For this purposes, coil 25 was chosen as a reference signal. The result of the correlation analysis is again a spatio-temporal pattern shown in figure 5.7a. The poloidal angle θ is 0 at the outboard midplane, $\theta \approx \pi/2$ at the top of the plasma and $\theta \approx -\pi/2$ at the bottom of the plasma. The global maximum is indicated with a green cross, which likewise marks the position of the reference coil 25. It is obvious from figure 5.7a, that a high positive correlation at the bottom of the plasma (red areas) is accompanied by a very high anti-correlation (blue area) at the top of the plasma. Thus, the I-phase bursts induce an up-down asymmetry in the magnetic probe signals. This can also be described in terms of the poloidal mode number as an m = 1 perturbation.

This is even better visible in figure 5.7b, which shows color-coded the value of the cross-correlation function $C_{\mathrm{i}}(\Delta t = 0)$ at the respective coil num-

ber i for the time delay $\Delta t = 0$. The low correlation levels at the outboard midplane might be due to a comparably large distance between plasma and pick-up coils as well as a few in-vessel components shielding the magnetic signals.

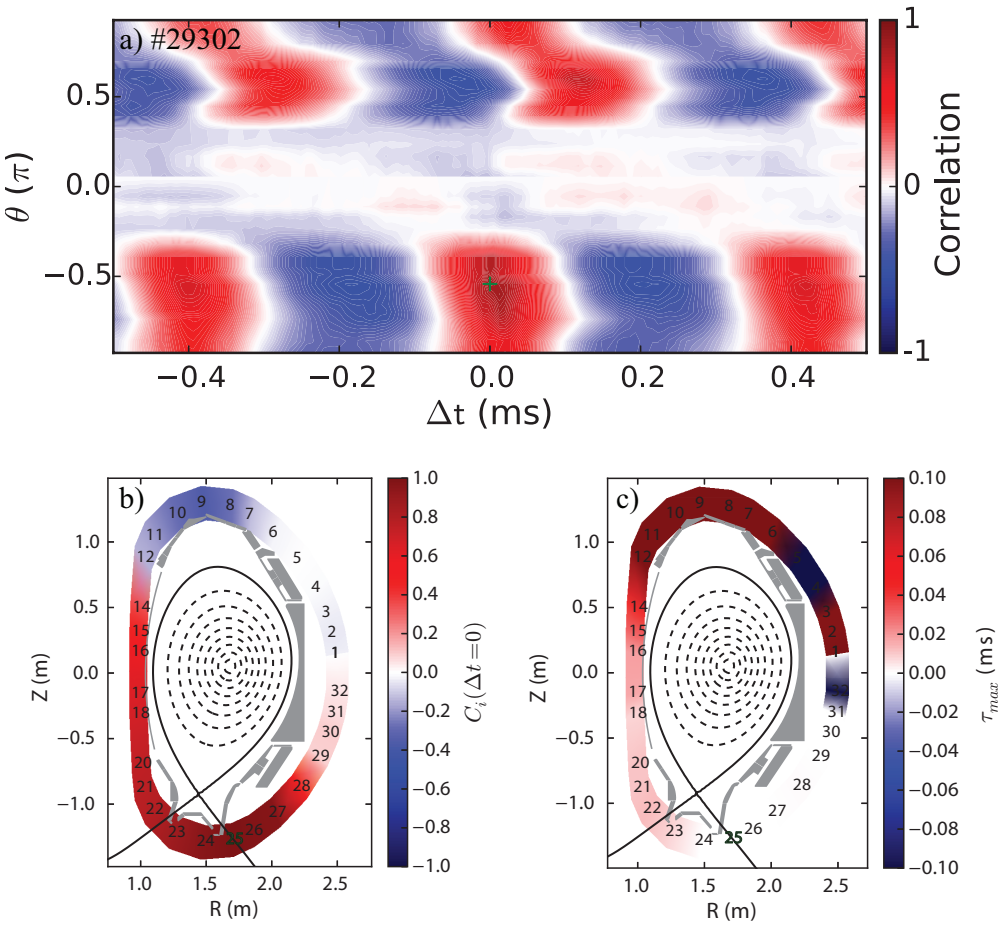

Figure 5.7: *Poloidal mode structure of $\dot{B}_{\mathrm{pol}}$-signals from a cross-correlation analysis (a) with reference probe 25 (green). The correlation at time delay $\Delta t = 0$ (b) reveals the up-down asymmetry of the LCO pulsation. The pulsation starts at the reference probe and propagates upwards along the HFS resulting in increasing time delays τ_{max} (c) (reproduced from [159]).*

The cross-correlation analysis provides in addition a time delay τ_{max} between the maximum of the reference coil signal and the respective maximum of the other coils. This way, the temporal evolution of the burst maximum is

revealed. For chosen reference coil 25, the time delays $\tau_{\max}$ are very small in the vicinity of coil 25 as indicated by the white color of the color-coded map in figure 5.7c. The increasing intensity of the red color, when going clock-wise around the poloidal circumference, indicates that the time delays $\tau_{\max}$ continuously increase. Overall, this indicates a propagation into clock-wise direction, which is for the chosen configuration the ion-diamagnetic direction.

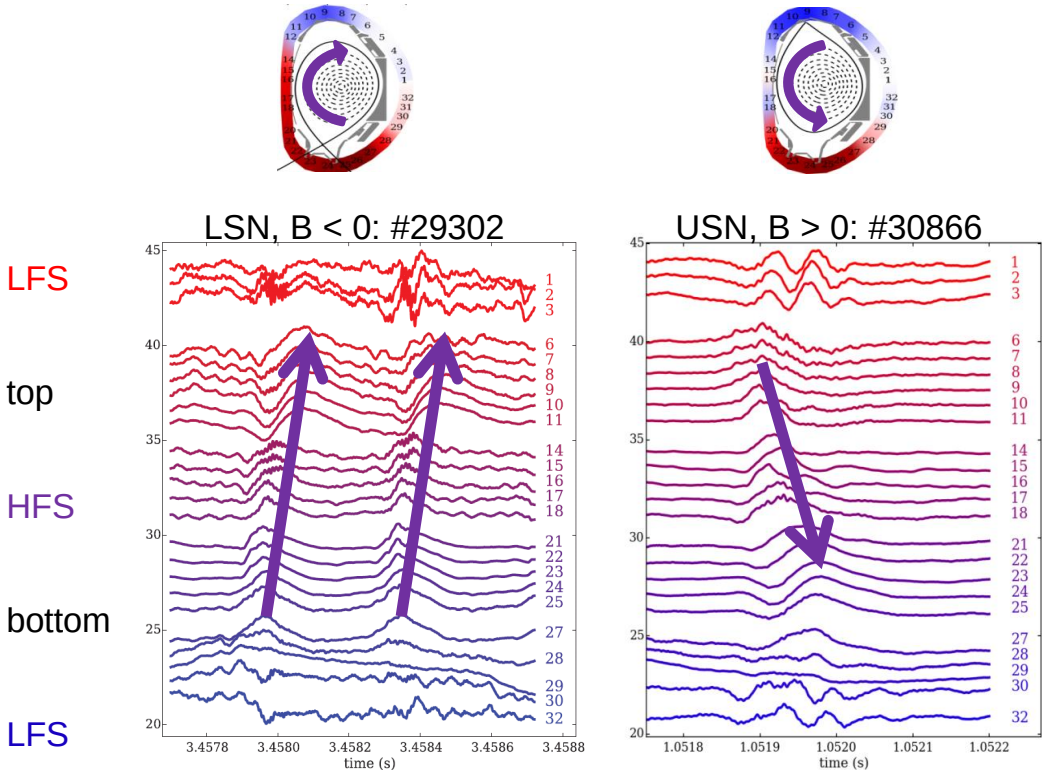

Figure 5.8: *Normalized signals of magnetic pick-up coils. In an LSN discharge with magnetic field vector pointing out of the poloidal plane, the propagation of the bursts is from bottom to top (left). In USN with magnetic field vector pointing into the poloidal plane (right), the propagation is from top to bottom. In both cases a propagation in ion diamagnetic direction and an up-down asymmetry is found.*

The propagation of the same plasma pulse is shown in figure 5.8a. This shows the same data as depicted in figure 5.6a, but here each signal is divided by its maximum value separately in order to obtain a normalized signal amplitude. It is clearly visible that the time delay of the maxima of a single burst moves from the bottom to the top along the HFS, i.e. in diamagnetic direction (the toroidal field vector points out of the plane in this case). For

an upper single null configuration and reversed magnetic field direction i.e. again with ion ∇B-drift pointing towards the active X-point (favorable configuration), the propagation of the burst reverses as shown in figure 5.8b. It starts again at the X-point and propagates along the HFS. This is now a clockwise propagation direction, but since the magnetic field is reversed, it is again in ion diamagnetic direction. The case of unfavorable configuration is difficult to be studied, since normally the I-phase cannot be observed and the I-mode regime appears. But in the rare cases of I-phase-like bursts (as e.g. in pulse #27944) in unfavorable configuration, the bursts seem to start again in the active X-point region and then propagation along the HFS. In this case, the propagation direction is in electron diamagnetic direction.

The time delays of polodoial propagation together with the connection length $L_{||}$ from bottom to top of the plasma assuming that the LCOs are located close the LCFS results in a propagation velocity of about $v_\theta = 90$ km/s. This value agrees very well with the sound speed c_s for the conditions typically obtained at this plasma conditions. Thus, the bursts propagate probably with sound speed along a magnetic field line from bottom to top along the HFS in the standard case (lower single null, magnetic field vector out of the plane). The same shapes of bursts and propagation directions are found in EAST [225] and in JET [219].

5.1.4 Frequency Scaling

As shown in figure 5.2 the frequency of the LCOs decreases after the L-H transition. Since the pedestal develops during this time, and, consequently, the density and temperature rise, it suggests that the frequency might scale inversely with density and temperature. This is confirmed in figure 5.9, which shows the LCO frequency against the density measured by an edge channel of the laser interferometry, the electron temperature measured with ECE at $\rho_\mathrm{pol} = 0.95$ and the resulting electron pressure estimate. As qualitatively argued above, the density is lower in I-phases at the L-H transition (blue symbols) than in I-phases at the H-L transition (figure 5.9a). For the temperatue the opposite is the case, but both density and temperature increase with decreasing frequency. If both quantities are multiplied with each other, a proxy for the edge pressure $\bar{n}_\mathrm{e} T_\mathrm{e,edge}$ is obtained. Pressure data of I-phases at the L-H transition perfectly overlaps with the pressure data of I-phases at the H-L transition. This indicates, that a universal scaling for the LCO frequency might exist and that it inversely depends on the edge pressure.

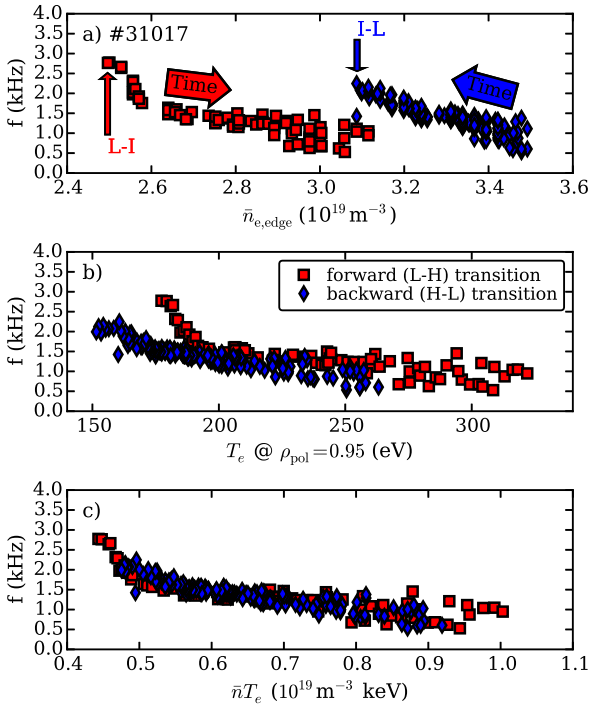

Figure 5.9: *LCO frequency dependence on density (a), temperature (b) and pressure (c) for the discharge shown in figure 4. The density is lower in the LCO state at the L-H transition (squares) and the temperature higher. For the I-phase at the H-L transition (diamonds) the opposite is the case (reproduced from [159]).*

Apart from this basic frequency scaling with pressure, a direct comparison of the measured frequencies with quantities from different LCOs models can be employed. This is an important step of validation of theoretical models. For this purpose, LCO frequencies were measured in plasmas with a range of different magnetic fields between $B = 1.4$ T and $B = 3.2$ T and plasma currents between $I_p = 0.47$ MA and $I_p = 1.07$ MA in order to vary as most as possible the global parameters in the plasmas. More details about this data set are given in reference [159].

By means of this set of discharges, we study the dependence of the LCO frequency during the first 60 LCO cycles on the edge density (approximated by the line-averaged edge density $\bar{n}_{e,edge}$), electron temperature T_e measured with Thomson scattering [287] at $\rho_{pol} = 0.95$, toroidal magnetic field B_t, toroidal plasma current I_p, and edge safety factor q_{95}.

First, we compare the measured LCO frequency with a prediction of the LCO frequency derived from a model based on mean field momentum transport equations [383]. In this model, the frequency of the LCO increases

approximately linearly with the neoclassical poloidal damping rate $\nu_{\mathrm{neo,damp}}$ if all model parameters (except for the density entering $\nu_{\mathrm{neo,damp}}$) are kept fix. Since the edge parameters of the considered discharges are in the transition region between banana and plateau regime, the multi-regime approximation of the damping rate [384]

$$\nu_{\mathrm{neo,damp}} = \frac{g\hat{\mu}_{00}^{B}\nu_{\mathrm{ii}}}{(1+2.92\nu^{*}\hat{\mu}_{00}^{B}/\hat{\mu}_{00}^{PS})\,[1+\hat{\mu}_{00}^{P}\nu_{\mathrm{ii}}/(6\omega_t\hat{\mu}^{PS})]} \tag{5.2}$$

is used. It depends on tabulated dimensionless viscosities $\hat{\mu}_{00}$ in the banana (B), plateau (P) and Pfirsch-Schlüter (PS) regime [384], on the ion-ion collision frequency ν_{ii}, on the ion transit frequency $\omega_{\mathrm{t}} = \sqrt{T_{\mathrm{i}}/m_{\mathrm{i}}}/(Rq_{95})$, and on the normalized ion collisionality [97]

$$\nu^{*} = 4.9\cdot 10^{-18}\frac{q_{95}Rn_i\ln\Lambda_{\mathrm{ii}}}{T_{\mathrm{i}}^{2}\epsilon^{3/2}}. \tag{5.3}$$

ϵ is the local inverse aspect ratio, R the major plasma radius, and $\ln\Lambda_{\mathrm{ii}} = 30-\ln\left(\sqrt{n_{\mathrm{i}}}/T_{\mathrm{i}}^{3/2}\right)$ [97] the Coulomb logarithm of deuterium ions. The factor g can be approximated with high accuracy [384] by

$$g = \frac{1}{1-1.46\sqrt{\epsilon}+0.46\epsilon\sqrt{\epsilon}} - 1. \tag{5.4}$$

As shown in figure 5.10a, the absolute values of the neoclassical poloidal damping rate $\nu_{\mathrm{neo,damp}}$ are in the same order of magnitude as the measured LCO frequency which is an important prerequisite to play a role in the dynamics of a LCO. In addition, the LCO frequencies of some individual discharges (one color corresponds to the covered LCO frequency range of one discharge) seem to increase with $\nu_{\mathrm{neo,damp}}$ (e.g. #29303, #29306, #29307) as expected. However, other discharges do only weakly depend on the estimated poloidal damping rate and the overall picture does not confirm a linear frequency dependence on $\nu_{\mathrm{neo,damp}}$. For the evaluation of $\nu_{\mathrm{neo,damp}}$, we used $T_{\mathrm{i}} = T_{\mathrm{e}}$ due to the lack of accurate ion temperature measurements in the edge plasma. This could be a source of errors, and, in addition, we neglected any dependence of the flux surface geometry, q_{95} or inertia which could affect the frequency of the LCO model presented in reference [383]. For a quantitative comparison a full kinetic calculation of $\nu_{\mathrm{neo,damp}}$ including geometric effects and a more elaborate comparison with the equation system of the model has to be done instead, which is out of the scope of this thesis.

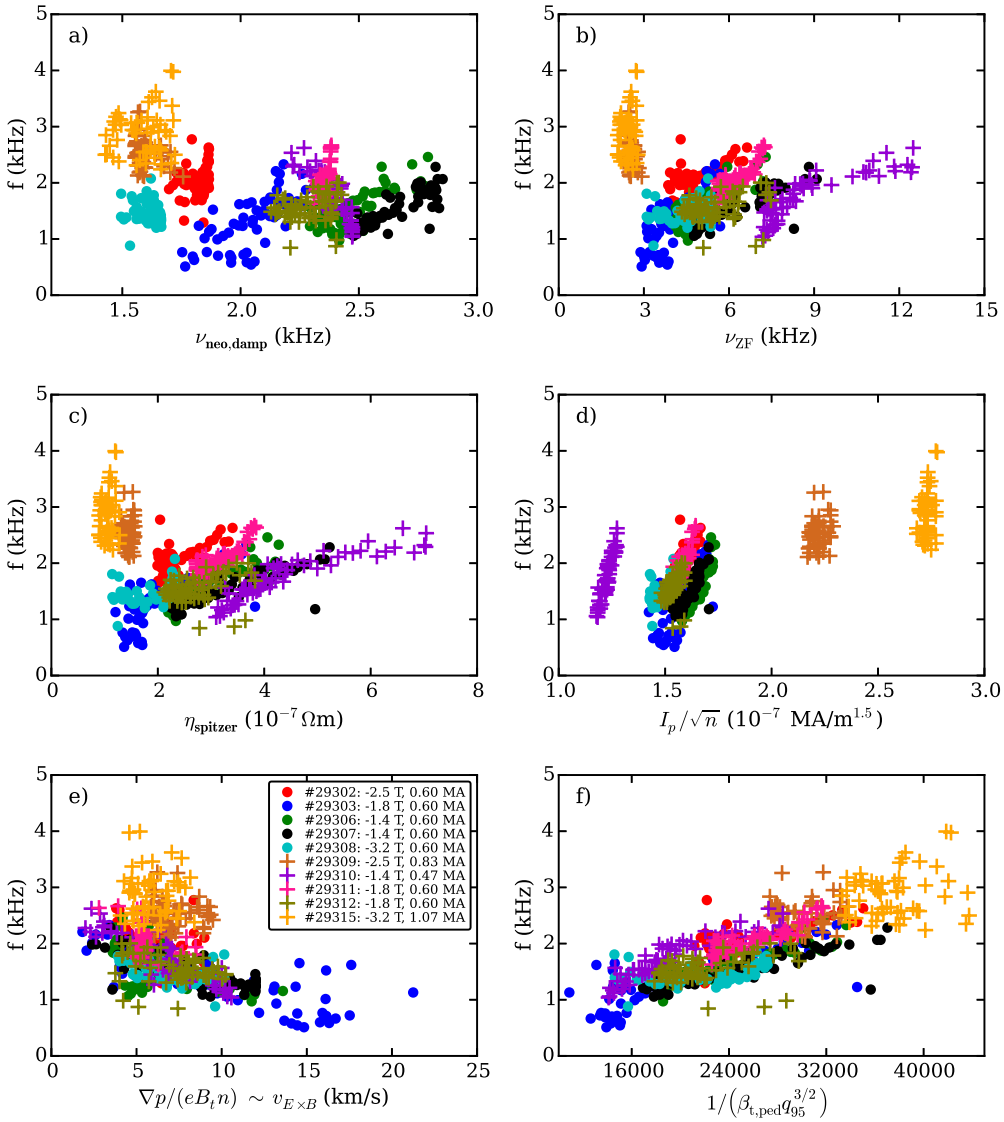

Figure 5.10: *Dependence of the LCO frequency f on the neoclassical poloidal damping rate (a), zonal flow damping rate (b), Spitzer resistivity (c), the JET M-mode scaling formula (d), estimated $E \times B$ flow velocity (e), and a fit formula based on a linear regression (f) for a set of discharges. Frequencies from individual discharges are depicted in the same color (reproduced from [159]).*

Following the LCO model based on a zonal flow-turbulence interaction [209, 385], the LCO frequency should depend on the collisional damping of the zonal flow if turbulent self-damping by non-linear saturation is weak [67] as can be expected for the I-phase which is a regime of reduced turbulence intensity. As described in reference [38], zonal flows can be damped in several ways. Despite the different damping processes, the dominant collisional damping rate of the zonal flow can be estimated as

$$\nu_{\mathrm{ZF}} = \nu_{\mathrm{ii}}/(1.5\epsilon) \tag{5.5}$$

with the inverse aspect ratio ϵ and the ion-ion collision frequency ν_{ii}. A large damping rate ν_{ZF} would correspond to a large zonal flow damping and would increase the frequency of the LCOs. As illustrated in figure 5.10b, some discharges (e.g. #29310, purple) exhibit larger LCO frequencies with increasing ν_{ZF} as expected. All discharges together, however, do not scale with ν_{ZF} and especially discharges #29309 (brown) and #29315 (yellow) do not follow the trend of the other discharges.

The existence of magnetic precursors as visible as high frequency oscillations in figure 5.6 and, as it will be discussed below in more detail, indicates that the LCOs could be of the same nature as type-III ELMs. As discussed in reference [115], the type-III ELM frequency could be attributed to resistive MHD effects due to its dependence on temperature. Therefore, we compare the LCO frequency with the Spitzer resistivity η_{Spitzer} [5] as shown in figure 5.10c. The LCO frequency in single discharges predominantly increases with η_{Spitzer} suggesting a positive scaling of the LCO frequency with resistivity. This is in agreement with the property of type-III ELMs, which decrease in frequency when the heating power (and therefore temperature) is increased. The frequency scaling of the complete set of discharges, however, is not coherent and, thus, disagrees with a simple dependence of the LCO frequency on resistivity only.

In the so-called M-mode at JET, which shares the higher harmonics in the spectrograms, the $m = 1$ magnetic structure, the high frequency band and the appearance close to the L-H power threshold with the AUG LCOs [226], a dependence of the frequency on the poloidal Alfvén speed $v_A = B_\theta/\sqrt{\mu_0 m_i n}$ was found [219, 386]. We approximate the poloidal Alfvén speed by the quantity $I_{\mathrm{p}}/\sqrt{n}$ and scale it against the measured LCO frequency as shown in figure 5.10d. Due to its density dependence, individual discharges clearly scale with $I_{\mathrm{p}}/\sqrt{n}$, and at a fixed plasma current of $I_{\mathrm{p}} = 0.6$ MA, which was chosen for most of the discharges in the considered data set, the data points lie on top of each other. For discharges with higher plasma current, the frequencies have a clear tendency to be higher. This is in agreement

with the proposed M-mode scaling. However, the frequency dependence of individual discharges does not fit to the overall scaling of different discharges with different I_p indicating a dependence on further quantities.

The pressure dependence of the LCO frequency as suggested by figure 5.9c could also be related to a perpendicular $E \times B$-flow $v_{E\times B} \sim E_\mathrm{r}/B \sim \nabla p_\mathrm{i}/(e n_\mathrm{i} B)$, depending on the radial electric field E_r which is dominantly determined by the diamagnetic term $\nabla p_\mathrm{i}/(e n_\mathrm{i} B)$ if set by neoclassical processes [49]. A direct comparison of the perpendicular flow velocity with the measured LCO frequency is, however, not possible for the considered data set due to the lack of direct velocity measurements or sufficiently accurate determination of the ion temperatures. Therefore, the density and temperature of the electrons are used instead of n_i and T_i for the estimation of the pressure gradient terms $\nabla p/n = \nabla T + T\nabla n/n$. While the inverse density gradient length $\nabla n/n$ is evaluated directly from the IDA electron density profiles [282, 387], the temperature gradient is approximated by the finite difference $(T_\mathrm{e}(\rho_\mathrm{pol} = 0.95) - T_\mathrm{e}(\rho_\mathrm{pol} = 1.0))/dr$ with constant $T_\mathrm{e}(\rho_\mathrm{pol} = 1.0) = 100$ eV and $dr = 3$ cm. It is conceivable that the LCOs have a constant frequency in the plasma frame, and that they appear at a higher frequency in the lab frame due to the perpendicular motion set by the E_r suggesting a scaling $f \sim v_{E\times B} \sim \nabla p_\mathrm{i}/(e n_\mathrm{i} B)$. This scaling, however, cannot be confirmed as shown in figure 5.10e since higher frequencies are found at lower velocities $v_{E\times B}$. In general, the data points from different discharges cluster in a narrow region between $v_{E\times B} = 5 - 10$ km/s, and exhibit no clear trend.

As shown in figure 5.10a-e, most of the proposed scalings do not fit to the considered data from different discharges. Therefore, we perform a multivariate linear regression in order to find a best fit of the LCO frequency on its dependent variables. We choose as input $\bar{n}_\mathrm{e,edge}$ in units of $10^{19}\mathrm{m}^{-3}$, T_e in eV, B_t in T and q_{95}. I_p is not used since it is connected to B_t and q_{95} via $q_{95} \sim B_\mathrm{t}/I_\mathrm{p}$. The regression yields a frequency dependence

$$f_\mathrm{fit} = 976.031 \bar{n}_\mathrm{e,edge}^{-1.10\pm0.16} T_\mathrm{e}^{-0.91\pm0.07} B_\mathrm{t}^{1.93\pm0.08} q_{95}^{-1.36\pm0.08}. \tag{5.6}$$

The root mean square error of the fit is 18.99. This scaling can be expressed in terms of $\beta_\mathrm{t,ped}$ and q_{95} with $\beta_\mathrm{t,ped} = 2\mu_0 e T_\mathrm{e} \bar{n}_\mathrm{e,edge}/B_\mathrm{t}^2$. It results in an approximate scaling

$$f_\mathrm{fit} = \frac{0.007}{\beta_\mathrm{t,ped} q_{95}^{3/2}}. \tag{5.7}$$

As illustrated in figure 5.10f, the total data set agrees very well with this approximate scaling and data from very different discharges overlap. Likewise, single discharges mainly follow this scaling and the pressure dependence as

discussed in figure 5.9c is covered by the proposed scaling. Due to the limitation of measurement accuracy and the small number of data points, the results of the fitting procedure could suggest a misleading trend. Within this limitations, however, our data set exhibits a clear dependence of the LCO frequency on the parameters $\beta_{\mathrm{t,ped}}$ and q_{95}. The fact that these parameters are dimensionless could possibly explain why the LCO frequency is typically found in a narrow range of a few kilohertz in many fusion experiments with very different densities, temperatures and magnetic fields.

5.1.5 Isotope Dependence

The characterization of LCOs in this chapter up to now was restricted to results from plasmas in D. But I-phases were likewise studied in H and He plasmas at AUG. The hydrogen plasmas behave very similarly to D plasmas, but just exhibit a different frequency scaling. The frequency of LCOs in H plasmas is about a factor of two higher than in D plasmas for otherwise constant parameters.

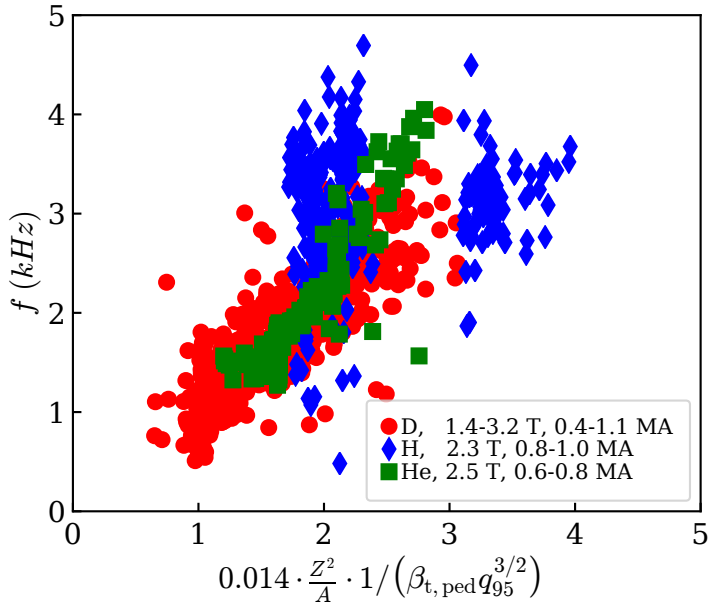

Figure 5.11: *Isotope dependence of the LCO frequency against the scaling formula 5.8 for a set of D, H and He plasmas (adapted from [388]).*

LCOs in He plasmas likewise exihibit about a factor of two higher LCO frequencies for otherwise constant parameters. Therefore, equation 5.7 must be extended by an isotope dependent factor. A regression of an LCO frequency data set consisting of the D data shown above and additional data of four H plasmas and three He plasmas provided the following isotope dependent scaling

$$f_{\mathrm{fit}} = \frac{0.014 \dfrac{Z_{\mathrm{i}}^2}{A_{\mathrm{i}}}}{\beta_{\mathrm{t,ped}} q_{95}^{3/2}}. \tag{5.8}$$

The measured LCO frequency against this data set is shown in figure 5.11. The data set of He plasmas (green) aligns relatively well to the D data (red). But the H plasmas included in this data set are split in two clouds of data points, so that it is difficult to find a common scaling formula for both of the H subsets. Nevertheless, the scaling formula 5.8 is a relatively reasonable approximation for this different isotopes in consideration of the fact that the measured frequencies between D and the other isotopes are a factor of two different, if the isotope factor is not taken into account.

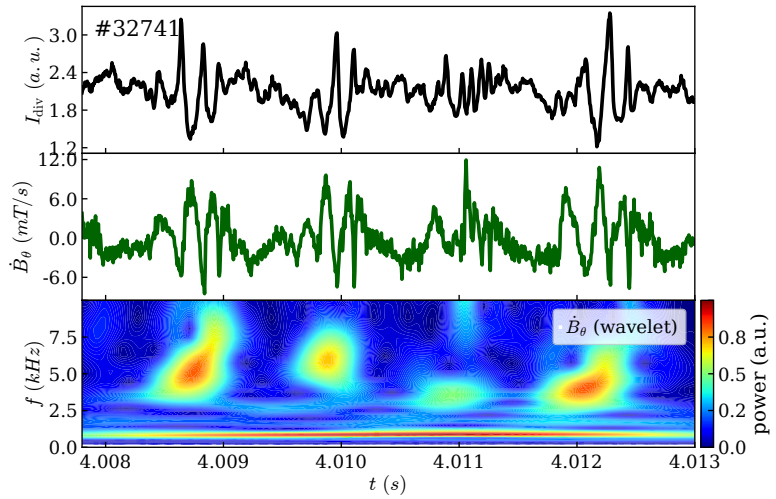

Figure 5.12: *The I-phase in He plasmas sometimes transitioned into a "breathing" state (reproduced from [388]). In this state, the amplitude of the LCO bursts as visible in the inner divertor shunt current (top) or the magnetic pick-up coil below the divertor (middle) is modulated with a frequency of about 1 kHz. The frequency of the LCO bursts itself is about 5 kHz as visible in the wavelet spectrum of the magnetic signal (bottom).*

Apart from the differences in frequency scaling, the H and He plasmas show the same phenomenology as D plasmas, i.e. the same magnetic structure, radial propagation, transitions from regular to irregular LCOs etc. There is only one observation in He plasmas, which was not found to date in D or H plasmas. It is a "breathing" I-phase as depicted in figure 5.12. In this regime, the LCO amplitude is modulated with a frequency of about 1 kHz, while the LCO itself exhibits a frequency between 5 kHz and 7 kHz, as visible in signals of the inner divertor shunt current or the magnetic pick-up coil below the divertor. The wavelet spectrogram as shown in the bottom panel of figure 5.12 was made by means of Morlet wavelets [389]. This breathing of the I-phase in He might be related to the amplitude modulation found for GAMs [72]. Due to the higher mass in He, the GAM frequency approaches the I-phase frequency, thus, LCOs and GAM possibly interacting probably more strongly than known for D or H plasmas.

5.2 On the Nature of LCOs

Based on the basic experimental features of LCOs, it is discussed in the following, what could be the nature of the LCOs. In other words, we try to compare the experimental findings with LCO models or other phenomena in order to connect it to a physical mechanism most likely at play during the I-phase.

5.2.1 Are the LCOs Driven by Zonal Flows?

Historically, a model was developed by Diamond et al. [162] aiming at a description of the bifurcation character of the L-H transition in order to find an explanation how a state of high turbulence and weak flows (L-mode) can spontaneously transition into a state of low turblence and strong flows (H-mode). Only a certain time later, it was recognized that this model contains oscillating solutions [209], so that this set of equations was considered as one possible explanation for the LCOs around the L-H transition. An essential part of this model is flow shear generation involving zonal flows (ZFs) driven by turbulence via the Reynolds stress (RS) force as introduced in section 2.1.3. This model is very elegant and was refined over the years in many aspects [390, 391, 392, 224, 377]. In addition, several experimental investigations were aiming at measuring the relevant quantities by means of Langmuir probes [372, 232, 393, 74, 394, 225] or gas puff imaging (GPI) [374, 373, 395]. All these studies found a significant contribution of ZFs or the Reynolds stress force, which were in general modulated during the LCO

phase or were triggering directly the L-H transition. According to the ZF-turbulence interaction scheme, first the turbulence rises (prey) and with a certain time delay, i.e. phase shift, the ZFs (predators) emerge after an energy transfer from turbulence to ZFs took place. However, there are other studies [222, 212], which found limit-cycles rotating into the opposite direction than predicted by the predator-prey scheme of the ZF-turbulence interaction. In addition, experimental investigations measuring the ZF activitiy and the RS drive found that these play only a minor role [221, 233, 396] indicating that the suggested predator-prey models do not apply in general.

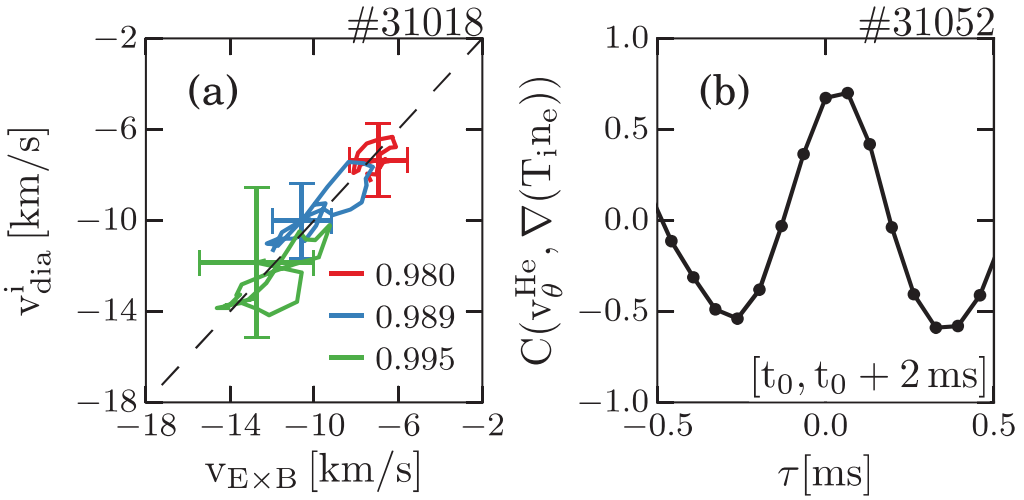

Figure 5.13: *(a) Lissajous diagrams between $E \times B$ velocity and ion diamagnetic velocity at three different radial positions, (b) Cross-correlation between poloidal velocity of He ions and the ion pressure gradient calculated in the first 2 ms after the L-I transition, i.e. during the first four LCOs (reproduced from [51]).*

At AUG, the RS drive was never measured, since no probe data or sufficiently resolved GPI data was available. But the effect of ZFs can be indirectly evaluated. First, the frequency scaling of the LCOs as shown in figure 5.10b involving the ZF damping did not show a consistent dependence on the ZF damping. This does not rule out an essential role of ZFs during LCOs, since the frequency can be determined in addition by other parameters than only the ZF damping. But it is already a first hint, that the ZF-turbulence

interaction might not be at play. Second, the strong magnetic signature of LCOs, which is one of the most prominent features of the I-phase, as well as the high frequency oscillations correlated with the bursts are not predicted by the ZF models, since they are typically of electrostatic nature. From a logical point of view, the presence of magnetic signatures in the experiment does not exclude the ZF-turbulence models per se, but it indicates that the existing ZF-turbulence models have to be extended in order to be able to describe the magnetic up-down asymmetry and high frequency modes. Third, the $E \times B$ flows measured with CXRS [51] during the I-phase were proportional to the ion diagmagnetic velocity within errors (figure 5.13, left) and the poloidal velocity of the He flow (serving as a proxy for the main ion flow) was in-phase with the ion pressure (serving as a proxy for the diamagnetic term of the radial electric field, see equation 2.9). If ZF components would have been present in these experiments, they would have had introduced a deviation of the measured flows from the pressure gradient driven flows, which was not found. The turbulence amplitude measured with Doppler reflectometry during I-phase was in phase with the velocities measured with CXRS. This is in contrast to the classical ZF-turbulence model, which predicts a phase delay between these two quantities.

All in all, the recent studies at AUG on LCO dynamics could not confirm the main features of the ZF-turbulence interaction model as originally proposed [209] within measurement errors and within the given time resolution of about 100 microseconds. But with new diagnostic capabilities of measurements with ball-pen probes [397], an imaging heavy ion beam probe (see chapter 6) or an improved GPI system further investigations at higher time-resolution and actually measuring the relevant quantities of the ZF-turbulence model are intended to clarify the role of ZFs during the L-H transition at AUG.

5.2.2 Are LCOs Driven by Poloidally Asymmetric Transport?

Based on equations of a drift-Alfvén model [68], oscillatory solutions for an in-out asymmetric transport, a so called ballooned transport, and its resulting flows can be derived [398]. This process is a very general property of magnetically confinement plasmas in toroidal geometry and does not depend on the nature of the ballooned transport, i.e. each kind of poloidally asymmetric transport with an in-out asymmetry can induce this oscillation. The in-out asymmetric transport couples to an up-down asymmetric flow, called the Stringer spin-up [399, 400], and can be described by a modified predator-

prey model including root terms with the in-out asymmetric pressure as prey and the up-down asymmetric flow perturbation as predator. This system is independent from its drive or damping, and just depends on the interaction between prey and predator. The predicted frequency of the Stringer-spin-up model is

$$\omega_{\mathrm{SSU}} = \frac{c_{\mathrm{s,i}}}{2\pi q_{\mathrm{s}} R} \tag{5.9}$$

with ion sound velocity $c_{\mathrm{s,i}}$.

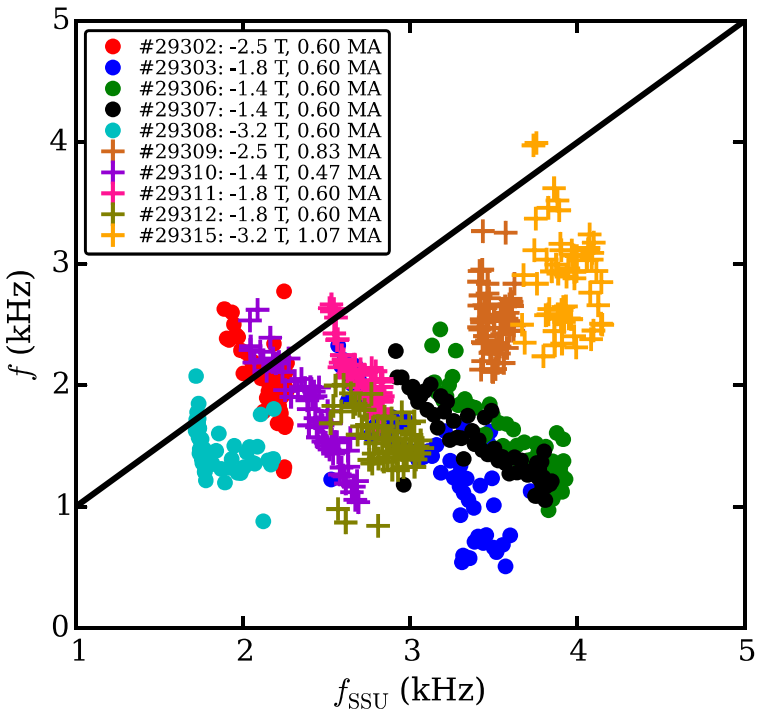

Figure 5.14: *Measured LCO frequencies against the scaling according to the Stringer-spin up mechanism (equation 5.9). The same data as shown in figure 5.10 is used (reproduced from [398]).*

Figure 5.14 shows a comparison of this formula with the experimental data discussed above in section 5.1.4. The absolute numbers between data and formula are approximately the same, indicating that the Stringer spin-up participates in the process of generating LCOs. However, the experimental data is slightly lower than the prediction given by equation 5.9. In addition, the data of a single discharge (one color) does not follow the scaling formula.

An extension of this model including a coupling to Alfvénic waves [401] was compared to LCO data of four different tokamaks and showed a reasonable quantitative agreement. Thus, a coupling of ballooned transport to the

Stringer spin-up and Alfvénic activity can explain the frequency behavior of the LCOs. However, it does not address the nature of the LCOs, i.e. the driving terms or underlying instability of a single LCO burst.

5.2.3 Are LCOs the Same as Type-III ELMs?

As presented in section 2.4.2, type-III ELMs have two characteristics according to their definition: First, the ELM frequency decreases with heating power, and second, a precursor mode is visible in magnetic pick-up coils prior to each ELM burst. As shown above in section 5.1.4, the frequency of LCOs decreases with increasing plasma pressure. Since the temperature, and hence pressure, increases with heating power, this frequency dependence is equivalent to a scaling resulting in a lower frequency for increasing heating power. Thus, the LCOs fulfill the first condition of the definition of a type-III ELM.

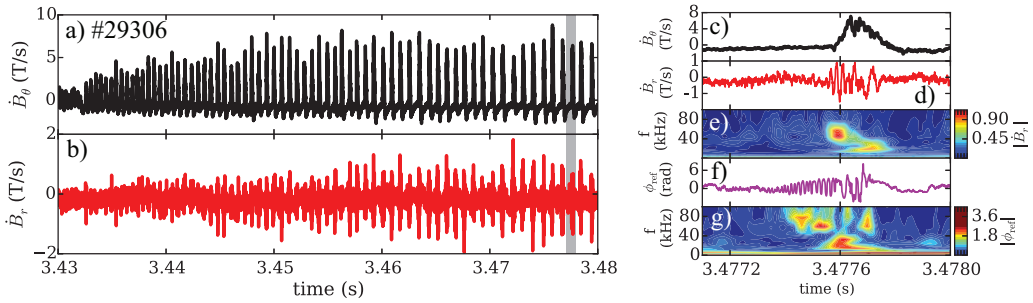

Figure 5.15: *Poloidal (a) and radial (b) magnetic field signals from pick-up coils during a neutral beam heated I-phase (#29306) reproduced from [159]. The late I-phase (shaded area in (a)) is shown more detailed in (c) to (g). Prior to the poloidal magnetic field perturbation (c), precursor activity is found in the raw signal (d) and wavelet spectrum (e) of the $\dot{B}_\mathrm{r}$-signal. This precursor is found even earlier in the phase signal of the hopping reflectometer (f) and shows activity in the frequency range 50 kHz to 100 kHz as seen in its wavelet spectrum (g).*

As shown in figure 5.15d, a precursor activity is visible in magnetic coils measuring the radial component $\dot{B}_\mathrm{r}$ prior to each LCO burst in the late phase of the I-phase (around $t = 3.46$ s and later) at AUG. The frequency of the precursor of about 50 kHz to 80 kHz and the fact that the precursors are only visible in the radial component of the magnetic signal $\dot{B}_\mathrm{r}$ perfectly fulfill the properties of type-III ELM precursors [115]. Due to these observations (frequency scaling and precursor activity), the late I-phase unambiguously agrees with the full definition of type-III ELMs.

The amplitude of the precursor modes are visible as spikes in figure 5.15b. They are very pronounced in the late I-phase and clearly correlated with the $\dot{B}_\theta$-signal in figure 5.15a, which is the monitor signal for LCO bursts similar as shown in figure 5.1. However, in the early I-phase, i.e. shortly after the L-I transition at about $t = 3.432$, the precursor amplitude is much smaller and hardly exceeds the noise level of the $\dot{B}_\mathrm{r}$-signal. Therefore, just considering the early phase of LCOs, where precursors in the magnetic signals are practically undetectable, makes it difficult to judge, whether these LCOs fulfill the definition of type-III ELMs.

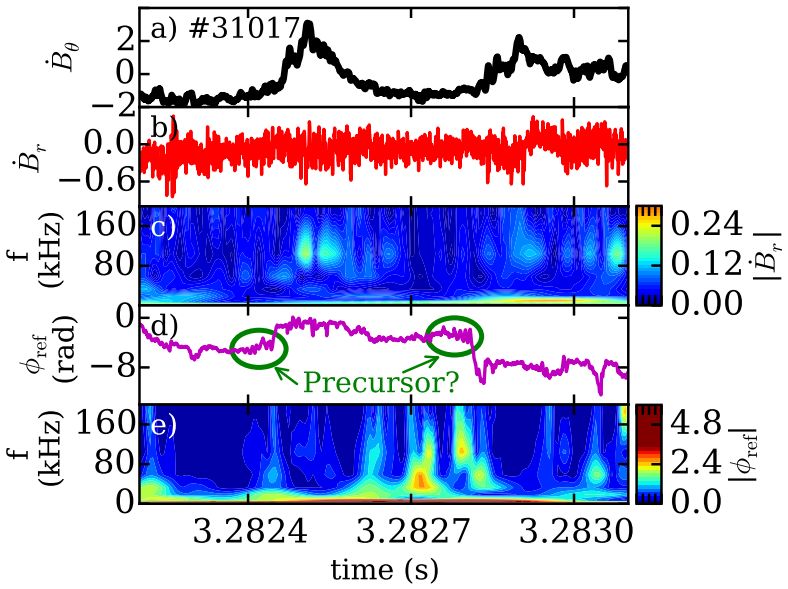

Figure 5.16: *The very first two LCO pulses after the L-I transition (early LCO) from discharge #31017: poloidal (a) and radial (b) magnetic field signals from pick-up coils, and wavelet spectrum of the $\dot{B}_\mathrm{r}$-signal (c). The phase signal of the hopping reflectometer (d) and its wavelet spectrum (e) indicate a weak precursor activity (reproduced from [159]).*

A precursor mode similar to the magnetic precursor is likewise visible in the phase signal of the normal incidence reflectometer (so called LFS hopping reflectometer [402]) as shown in figure 5.15f. Its signal is proportional to the density fluctuation at a radial position of $\rho_{\mathrm{pol}} = 1.0 \pm 0.01$, i.e. around the LCFS. This precursor is very pronounced in the late I-phase, but can also be observed in the early I-phase as shown in figure 5.16d, although the precursor is invisible in the magnetic signal (see figure 5.16b). Thus, the reflectometer

signal suggests, that the precursor is always present in I-phase, even in the early phase. The signal levels of precursors in the magnetic signals might be too low to be detected during the early I-phase, but this does not mean that the magnetic precursors do not exist *per se*. The continuous and smooth transition from the early I-phase with small precursors to the late I-phase, which clearly fulfills the definition of type-III ELMs, indicates, that all LCO bursts share the same properties, and they only differ in size, especially in terms of the amplitude of the precursors. Overall, these results suggest that the LCOs are the same phenomenon as type-III ELMs. More details about the precursors at AUG can be found in reference [159].

The strong precursors of LCO bursts appearing close to the H-L transitions were called Modulating Pedestal Mode (MPM) at DIII-D and are envisaged to be used as indicator, that the operational point of the plasma is close to the H-L transition, so that measures for a soft backtransition to L-mode can be applied [403]. They are likewise visible as density fluctuations measured with beam emission spectroscopy at the heating beams, and have the same frequency and wavenumber as in AUG [159]. Precursors of LCOs are also present in plasmas at EAST [225] and the data there shows likewise a continuous and smooth transition from LCOs to type-III ELMs confirming the results at AUG.

In summary, the presented results indicate, that LCOs at the L-H transitions are the same as type-III ELMs. But although many models for type-III ELMs have been proposed [404, 405, 406], there is no consent in the scientific community, how to quantitatively described type-III ELMs, and of what nature they are.

Chapter 6

A New Diagnostic Concept to Study Structure Formation at the Plasma Edge

6.1 The Imaging Heavy Ion Beam Probe

6.1.1 The Need for Improved Edge Diagnostics

As indicated by the light blue fields in table 2.1, certain fluctuation amplitudes of many phenomena and structures at the plasma edge were not determined yet. It is obvious, that measurements of the electrostatic potential perturbation are the most desirable, since these are missing for almost all of the phenomena. The electrostatic potential is one of the most important quantities due to the fact that the value of the cross phase between electrostatic potential and density fluctuations allows for a (sometimes unambiguous) characterization of the underlying instability of the structure of interest. Unfortunately, this quantity is very difficult to access experimentally.

In addition to the capability of measuring the electrostatic potential, an ideal edge plasma diagnostic needs good time resolution to resolve the fast processes on the time scales of the respective structures. This requires a time resolution of at least 1 ms or ideally 10 µs to capture the temporal characteristics of the structures given in table 2.1.

A third requirement is a good radial resolution. Most of the pheonomena presented in chapter 2 appear in the very narrow region slightly inside the LCFS, where the strongest gradients are present. This region is typically only a few centimeter wide, thus, a spatial resolution in the range of millimeters (or even below) are desirable. If possible, this good resolution should be available

for a wide radial range covering the steep gradient region, the LCFS and a large part of the SOL.

Ideally, the diagnostic would be non-invasive i.e. the measurement setup or its involved elements interact so weakly with the plasma that its dynamics is not modified.

Last but not least, a two-dimensional acquisition of the measurement quantities e.g. in the radial-poloidal plane, would be desirable in order to measure radial and poloidal structure sizes, the tilt of structures, and its poloidal and radial velocities. This would allow for a very comprehensive comparison of measured quantities with predictions from theory, which is typically not possible nowadays.

6.1.2 The Imaging Heavy Ion Beam Probe at AUG

A diagnostic concept, which promises to fulfill all the above mentioned conditions to a certain extend, is the imaging heavy ion beam probe (i-HIBP) [407, 408, 409]. It is an active diagnostics injecting a neutral beam of heavy alkali atoms into the plasma, where it is ionized in the region around the LCFS creating a secondary ion beam. The pattern of the secondary ion beam detected with a scintillator detector inside the vacuum vessel allows to deduce information on density perturbations, electrostatic potential perturbations and magnetic field perturbations at the points of ionization. Therefore, the measurement quantities provided by the i-HIBP seem to be well suited to fill the missing data in table 2.1.

The theoretical concept of the i-HIBP was developed in collaboration with the University of Seville, Spain, and the hardware was manufactured, designed and commissioned at AUG together with the University of Seville and the Centre for Energy Research, Budapest, Hungary. The diagnostic principle of the i-HIBP is very similar to the atomic beam probe (ABP) concept developed at the COMPASS tokamak [410, 411]. But instead of a Faraday-cup array as used for the ABP, the i-HIBP makes use of a scintillator and a camera for the beam detection, which allows a much higher spatial resolution. The i-HIBP is also related to the classical heavy ion beam probes [412, 413, 414, 415, 416, 417]. In contrast to these, the i-HIBP employs a neutral beam as primary beam instead of an ion beam, and instead of the electrostatic energy analyzer, which is usually placed outside the torus to measure the secondary beam of classical heavy ion beam probes, the i-HIBP uses an in-vessel detector based on a scintillator. The scintillator detector enables a more compact system and the possibility to measure in two dimensions with very high spatial resolution. On the other hand, due to the use of a camera and an indirect determination of the electrostatic

potential as opposed to a direct measurement in a classical heavy ion beam probe, the accuracy and time resolution of a classical heavy ion beam probe is higher than of the i-HIBP. Since a classical heavy ion beam probe is not feasible to be built for AUG due to its magnetic field helicity, the i-HIBP is the best realistic choice of a diagnostic enabling electrostatic potential measurements.

6.1.3 Measurement Principle

The i-HIBP makes use of a neutral heavy atom beam as a primary beam, which is injected radially inward from the midplane LFS into the plasma. As shown in figure 6.1, left, the neutral primary beam (blue) gets ionized due to the interaction with particles of the plasma. The ionization takes place at several (radial) positions along the primary beam creating a fan of ion beams (red). Due to the high mass of the heavy ions, m_i, these secondary beams of charge q perform such a large Larmor radius

$$\rho_\mathrm{L,i} = \frac{\sqrt{2 m_\mathrm{i} E_\mathrm{beam}}}{|q| B} \tag{6.1}$$

for a given beam energy E_beam and magnetic field B of the tokamak, that they leave the plasma. This way, they can be detected outside the plasma by means of a scintillator detector placed in the limiter shadow inside the vacuum vessel of the tokamak. The scintillation light pattern generated by the secondary beams is detected with a high speed camera and contains information of plasma quantities at the point of ionization and along the primary and secondary beam.

The fan of secondary beams gives rise to a strip-type pattern (red) referred to as scintillator strikeline as shown in figure 6.1, right. The upper part of the strikeline is created by ion beams starting from radial positions far inside the plasma, and ion beams starting from radial positions further outside give rise to scintillation at the bottom of the strikeline. Hence, the strikeline contains information of different radial positions. The resolution is given by the grain size of the scintillator (typically in the range of hundreds of micrometers) and the resolution of the optical system, which provides in total typically a resolution in the sub-millimeter range, when mapped back to the points of ionization.

A change of the poloidal magnetic field, typically induced by the (edge) plasma current, deflects the fan of secondary beams into toroidal direction due to the Lorentz force (see equation 1.4). Therefore, a magnetic field perturbation δB deflects the whole strikeline (purple) on the scintillator horizontally as shown in figure 6.1, right. This way, the magnitude and direction

of the magnetic field perturbation δB can be estimated from the deflection of the strikeline on the scintillator.

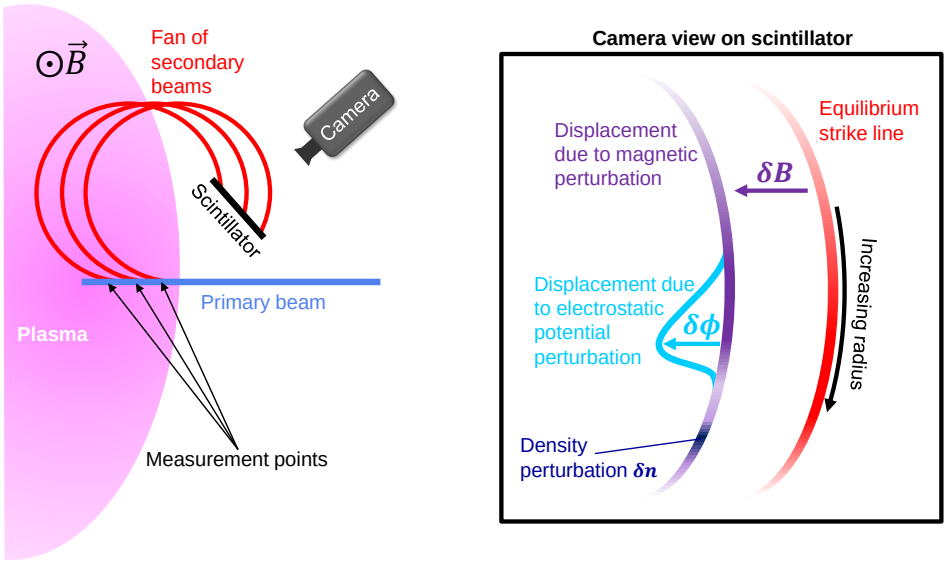

Figure 6.1: *Left: Schematic setup of the i-HIBP. Along the primary beam (blue) injected from the right, a fan of secondary beams (red) is created by ionization in the plasma. The secondary beams are detected by means of a scintillator and a camera. Right: Schematic camera view onto the scintillator. The scintillator strikeline (red) is globally deflected by a magnetic field perturbation δB (purple) and locally deformed by electrostatic potential perturbations $\delta\phi$ (light blue). Density fluctuations along the primary beam manifest as intensity perturbations of the strikeline intensity (reproduced from [408]).*

Due to the ionization processes of the primary beam and the attenuation of the secondary beams due to collisions, the intensity of the ion current reaching the scintillator, and, thus, the intensity of the scintillation light, is a strong function of the density and temperature in the plasma as will be shown in section 6.2.2 below. The intensity of the strikeline increases from the bottom of the strikeline towards the center due to the increase of the density profile in the plasma giving rise for more and more ionization processes of the primary beam during its propagation inside the plasma. At a certain point, however, the primary beam is fully ionized, so that no further secondary beams are created far inside the plasma, and the intensity on the strikeline decreases towards the top of the scintillator. Therefore, the maxi-

mum of the strikeline intensity is reached, where the primary beam can still provide sufficient neutrals for ionization and the density profile is sufficiently high to provide the plasmas density necessary for the ionization collisions. The whole strikeline intensity is additionally affected by the secondary beam attenuation, which is stronger for secondary beams further inside the plasma, where the beam trajectories have to pass regions of higher densities. A density perturbation δn in outer regions of the plasma, where the primary beam still consists of the majority of its particle content, leads to a local increase of ionization, and, thus, creates a local excess of ion beams, which is visible as an intensity perturbation on the scintillator strikeline (see figure 6.1, right). This way, density perturbations δn can be estimated from an intensity perturbation on the strikeline.

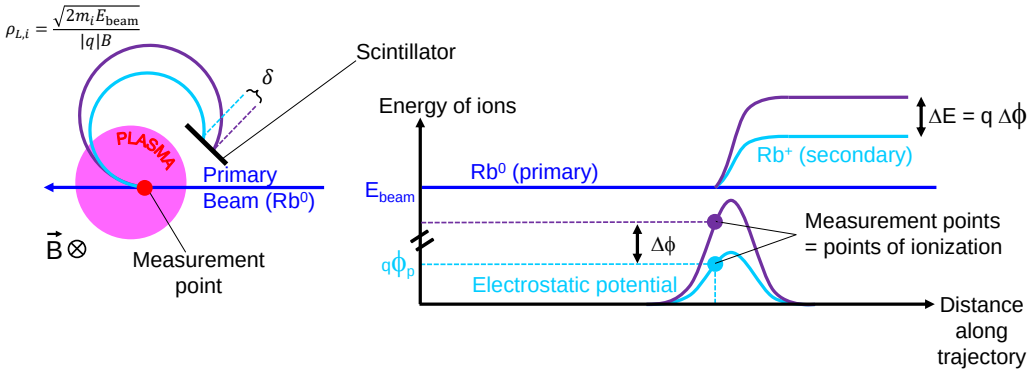

Figure 6.2: *Origin of the deflection δ of the scintillator pattern of secondary beams due to a potential perturbation $\delta\phi$ in the plasma. Compared to the energy of the primary beam, the secondary beam (light blue) gains energy in case that a positive electrostatic potential is present at the point of ionization. A larger potential perturbation (purple) leads to an even stronger raise of the kinetic energy of the ions, so that the electrostatic potential difference between the two cases causes a deflection δ on the scintillator due to the energy dependence of the Larmor radius $\rho_{L,i}$.*

A perturbation of the electrostatic potential in the plasma, $\delta\phi$, is estimated from a local deflection δ of the scintillator strikeline (see figure 6.1). The local deflection on the strikeline originates from a change in kinetic energy of the secondary beams due to an electrostatic potential perturbation inside the plasma. As shown in figure 6.2, the neutral primary beam has a certain energy E_{beam}, which stays constant along its path into the plasma. An ion, which is generated by ionization from the primary beam, has initially the same energy as the primary beam. However, if a positive potential

perturbation is present at the point of ionization, the positively charged ion (light blue) gains energy during its path towards the outside of the plasma, i.e. it is repelled from the positive potential. For higher values of the electrostatic potential at the point of ionization, the energy gain is even higher (purple). Due to the energy dependence of the Larmor radius (see equation 6.1) as well as the toroidal deflection of the secondary beams, an increase of the electrostatic potential by $\Delta\phi$ leads to an increase of the kinetic energy of the secondary beams of $q\Delta\phi$ and consequently to a correspondingly larger deflection.

In summary, a local and global deflection of the scintillator strikeline contains information on δB and $\delta\phi$, respectively, while the intensity of the strikeline is determined mainly by the density and its perturbations δn. The correct interpretation of the strikeline pattern and the quantitative determination of the actual measurement quantities is only possible by means of a numerical modeling of the beam trajectories and its collisional processes on the way to the scintillator.

6.2 Numerical Modeling for the Development of the i-HIBP

The numerical modeling of the i-HIBP signals is mainly done with the code package *i-HIBPsim* [418]. It consists of two main parts: one part handles the particle tracing of the beam particles in the three-dimensional tokamak field taking into account the deflection due to a given electric field, and the second part calculates the ionization and attenuation processes of the beam particles along the calculated trajectories. It can handle finite beam widths, divergent beams, arbitrary beam energies and is a flexible tool enabling studies of beam plasma interactions in three-dimensional geometry, i.e. including error fields, local perturbations of plasma quantities or field vectors and arbitrary geometries for the scintillator detector.

6.2.1 Particle Tracing

The particle tracing part of *i-HIBPsim* solves the equation of motion of a charged ion with charge q and mass m_i for a given magnetic field $\mathbf{B}$ and electric field $\mathbf{E}$

$$m_\mathrm{i}\frac{d\mathbf{v}}{dt} = q\left(\mathbf{E} + \mathbf{v}\times\mathbf{B}\right). \tag{6.2}$$

For this purpose, the three-dimensional vector fields $\mathbf{B}$ and $\mathbf{E}$ have to be constructed first. The magnetic field $\mathbf{B}$ is read from the result of the equilibrium reconstruction of AUG and mapped in three dimensions. The electric field is a manual input and typically constructed from a measured or experimentally inspired radial electrostatic potential profile, which is first mapped to the magnetic flux surfaces, and a three-dimensional field is created via $\mathbf{E} = -\nabla\phi$.

The injection of the primary beam is given by the beam energy E_beam delivering the initial beam velocity, the mass and charge of the particle, the point of origin, e.g. the center of the i-HIBP flange in AUG, and a toroidal and a poloidal injection angle with respect to the radial coordinate vector. The starting points of the secondary beams requires the input of a radial range, in which the trajectories are initialized, and the number of trajectories. The trajectories are then calculated until they reach a predefined plane of the scintillator.

An example of the primary beam geometry and the resulting secondary beam trajectories is shown in figure 6.3 for a toroidal injection of 5 degree calculated with an early version of i-HIBPsim [419]. It is obvious in the top view of the trajectories (figure 6.3, upper right), that the trajectories are toroidally displaced due to the poloidal magnetic field component and due to the fact, that the beam is injected with a finite toroidal angle. Figure 6.3, lower right) shows the energy of the particles during its propagation from the ionization points towards the scintillator. During the last 2 µs, the energy does not change, since the particles propagate through the very far SOL, where no significant electrostatic potential is present. The different energies of the particles in this phase and when they arrive at the scintillator is exclusively given by the electrostatic potential at the point of ionization, similar as sketched in figure 6.2.

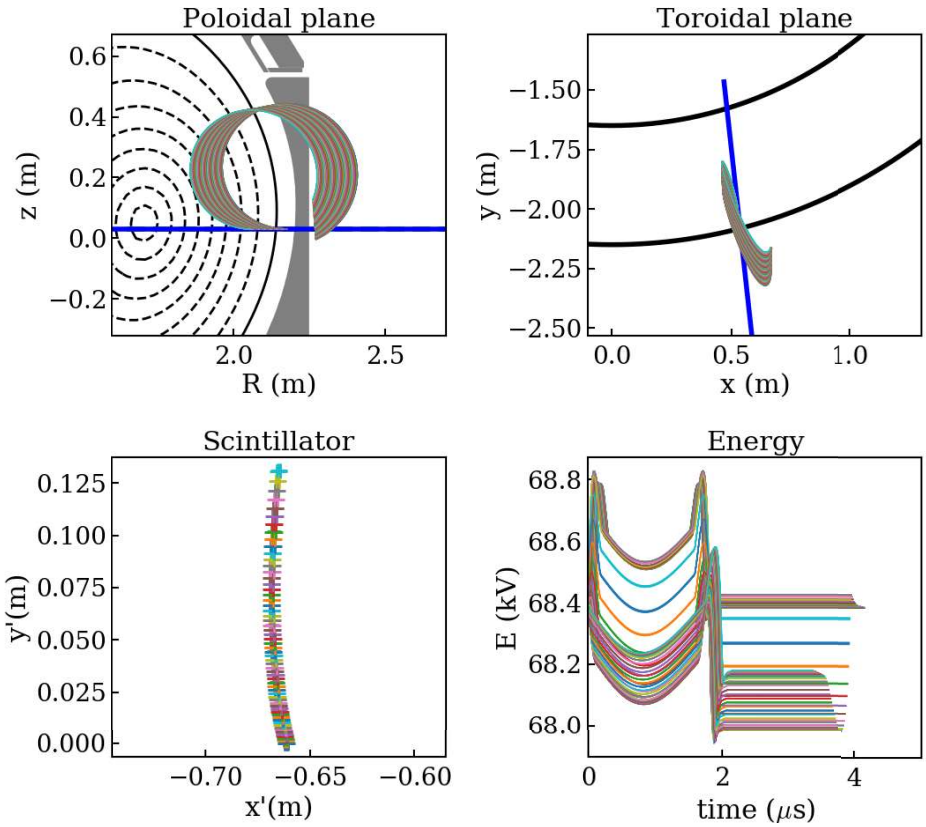

Figure 6.3: *Result of the output of a particle tracing code for the i-HIBP (reproduced from [419]). The upper plots show the primary beam (blue) and the fan of secondaries for a cesium (Cs) beam with $E_{\mathrm{beam}} = 68.4$ kV in the poloidal (left) and toroidal plane (right). The intersection of the secondaries with the scintillator plate given in scintillator coordinates x' and y' are shown on the lower left. This is the scintillator strikeline. Due to the presence of an electrostatic potential in the plasma, the kinetic energy (lower right) varies in time while the particle propagates through the plasma to the scintillator ($t = 0$ corresponds to the point of ionization, where the secondaries start).*

6.2.2 Collisional Model

After the trajectory calculation has been done, the ionization processes of the primary beam and the attenuation processes of the secondary beams are handled. For this purpose, the provided radial profiles of electron density and temperature are mapped onto the flux surfaces, so that local values of n_e, n_i, T_e and T_i are available in three-dimensions for further processing. The description of the collisional model, which uses these local values as shown in the following, reproduces results of reference [408].

A primary beam injected from the outside with a current density $j_p(l = 0)$ and a velocity v_{beam} along the beam coordinate l is attenuated due to collisions in a plasma with electron density n_e, ion density n_i, electron temperature T_e and ion temperature T_i at the position l_0 according to

$$j_p(l_0) = j_p(0) \exp\left\{-\frac{1}{v_{beam}} \int_0^{l_0} \left(n_e \langle\sigma v\rangle_{ei} + n_i \langle\sigma v\rangle_{CX}\right) dl\right\}. \tag{6.3}$$

For the rate coefficient of the electron impact ionization

$$\langle\sigma v\rangle_{ei} \approx 4\pi \int_0^{\infty} \sigma_{ei}(v_e) f_M(T_e) v_e^3 dv_e \tag{6.4}$$

the Lotz formula [420] is used for the cross section σ_{ei} and an isotropic Maxwell-Boltzmann distribution $f_M(T_e)$ is assumed for the electrons with velocity v_e. These rate coefficients depend on the plasma temperature and are shown for Cs and Rb in figure 6.4, left.

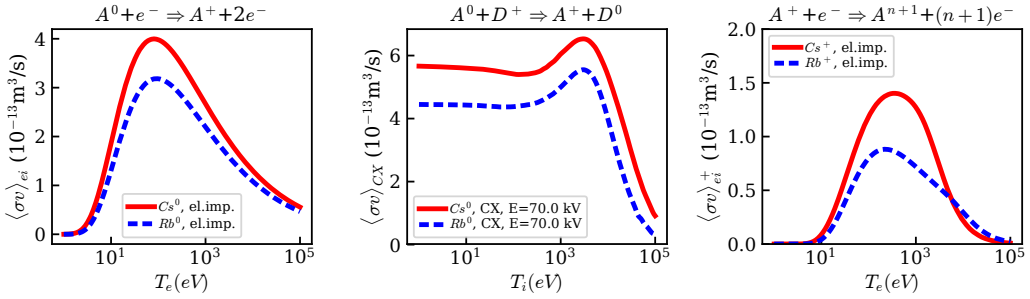

Figure 6.4: *Rate coefficients for the atomic species A = Cs and A = Rb. Left: electron impact ionization of neutral atoms. Middle: charge-exchange collisions with deuterium. Right: electron impact ionization of singly ionized ions (reproduced from [408]).*

For Cs and Rb, the charge-exchange collision rates with deuterium (figure 6.4, middle) are in the same order of magnitude as the electron impact ionization. Since the beam velocity v_{beam} is of the same order as the most probable deuteron velocities v_{i}, the three-dimensional integral

$$\langle \sigma v \rangle_{\mathrm{CX}} = \int_{-\infty}^{\infty} \int_{-\infty}^{\infty} \int_{-\infty}^{\infty} |\mathbf{v}_{\mathrm{beam}} - \mathbf{v}_{\mathrm{i}}| \sigma_{\mathrm{CX}}(|\mathbf{v}_{\mathrm{beam}} - \mathbf{v}_{\mathrm{i}}|) f_{\mathrm{M}}^{3D}(T_{\mathrm{i}}) d\mathbf{v}_{\mathrm{i}} \quad (6.5)$$

with the three-dimensional Maxwell-Boltzmann distribution for the deuterons $f^{3D}(T_{\mathrm{i}})$ has to be solved. For Cs a combination of the cross sections for low [421] and high energy [422] is used, in order to cover a wide energy range. For Rb a combination of data from references [423] and [424] are taken.

This data is also needed for the birth profile of the secondary beams along the primary beam coordinate l, which can be described as the current density

$$\Delta j_{\mathrm{b}}(l_0) = j_{\mathrm{p}}(l_0) \left(n_{\mathrm{e}} \langle \sigma v \rangle_{\mathrm{ei}} + n_{\mathrm{i}} \langle \sigma v \rangle_{\mathrm{CX}} \right) \Delta l \frac{1}{v_{\mathrm{beam}}} \quad (6.6)$$

generated in a small volume of the primary beam with length Δl.

The current density $j_{\mathrm{s}}(s)$ along the secondary trajectory coordinate s is determined by the attenuation of the curved secondary beam due to ionization collisions into higher charge states of the ion beam on the way out of the plasma. At the scintillator position s_0 we find

$$j_{\mathrm{s}}(s_0) = \Delta j_{\mathrm{b}}(l_0) \exp \left\{ -\frac{1}{v_{\mathrm{beam}}} \int_0^{s_0} n_{\mathrm{e}} \langle \sigma v \rangle_{\mathrm{ei}}^{+} \, ds \right\}. \quad (6.7)$$

The rate coefficient $\langle \sigma v \rangle_{\mathrm{ei}}^{+}$ is calculated according to formula 6.4, but with the data of the cross sections for secondary ionization as described in reference [425] for Cs (ionization into all higher states up to Cs^{5+} are taken into account) and reference [426] for Rb. The rate coefficients for the secondary ionization are shown in figure 6.4, right.

6.2.3 Density Dependence of Scintillator Signal

The ionization and attenuation processes expressed in equations 6.3, 6.6 and 6.7 strongly (i.e. exponentially) depend on the plasma density and the respective rate coefficients. The temperature dependent rate coefficients do not vary much in different plasma scenarios at the edge, so that the main impact originates from the density as shown in the following.

A typical output of the i-HIBPsim simulation is shown in figure 6.5. It shows the strikeline on the scintillator for the AUG discharge #34570 with $B_t = 2.5$ T, $I_p = 0.6$ MA and a density of $\bar{n}_e = 3.8{\cdot}10^{-19}$ m^{-3} at the time $t = 3.53$ s for a ^{87}Rb beam [418].

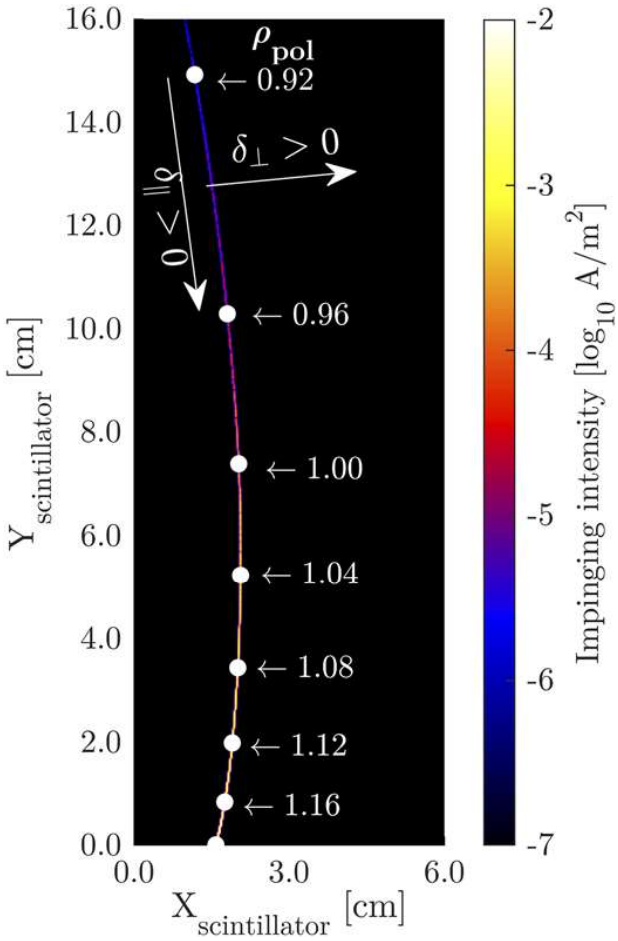

Figure 6.5: *Example of the output of an i-HIBPsim calculation for a ^{87}Rb beam injected into an AUG plasma at $B_t = 2.5$ T and, $I_p = 0.6$ MA (reproduced from [418]). The position of the strikeline is given in terms of the horizontal and vertical coordinate of the scintillator. The intensity of the strikeline is color-coded and displays the secondary beam current impinging on the scintillator. Different points along the strikeline (white circles) are connected via the respective secondary trajectory to different ionization points along the primary beam in the plasma, so that a certain ρ_{pol}-position of the point of ionization can be assigned to each corresponding point on the scintillator strikeline. The directions of vertical and parallel secondary beam displacements are indicated by large arrows.*

The simulation was done for an infinitely thin primary beam, i.e. the beam width was assumed to be arbitrarily small. The strikeline is slightly curved and the color-coded intensity of the strikeline given in terms of the current density $j_s(s_0)$ of the secondary beams (see equation 6.7) is increasing towards the bottom of the scintillator. The white markers on the strikeline indicate a few selected end points of secondary beam orbits, which can be assigned to the radial position of the corresponding starting points given in terms of the ρ_{pol}-position. In other words, the points of ionization along the primary beam at a certain ρ_{pol}-position in the plasma map to the respective end points of the secondary beams on the scintillator. Therefore, the strikeline shown in figure 6.5 contains information of a radial range between ρ_{pol} = 0.92 to ρ_{pol} = 1.16 and the LCFS (ρ_{pol} = 1.00) is roughly in the center of the scintilator. Due to the specific geometry of the trajectories, which depends on the magnetic field topology of the given plasma equilibrium, an equidistant radial grid of ionization points maps onto a non-equidistant grid of orbit end points on the scintillator.

The intensity of the strikeline depicted color-coded in figure 6.5 can equivalently be represented as an intensity curve along the strikeline. This is shown in figure 6.6, bottom row. Here, the intensity in terms of a secondary beam current density is drawn against the radial position of the ionization point of the respective secondary beam given in terms of ρ_{pol}. This is possible due to an unambiguous assignment of the ionization point in the plasma and the end point on the scintillator for each trajectory as indicated for some selected points in figure 6.5. As shown in the lower left panel of figure 6.6 for a high density edge plasma, a Rb secondary beam ionized at the LCFS (ρ_{pol} = 1.0) is associated with a secondary beam current density of about 10^{-4} A/m^2 reaching the scintillator. This is more than 1000 times higher than the secondary beam current produced by a Cs beam on the scintillator under the same plasma conditions. The main reason for this difference between Rb and Cs is the different beam velocity v_{beam} due to the different masses of the two isotopes, which strongly impact the secondary beam attenuation. Outside the LFCS, there is almost no difference between the calculations taking charge-exchange (CX) processes into account (solid) and simulations without CX collisions (dashed lines).

For lower densities (figure 6.6, right panels), the overall signal intensities are several orders of magnitude higher, and the differences between Rb and Cs is lower due to a general lower impact of the secondary attenuation. These calculations clearly show, that a low density operation in AUG is necessary to produce high signal levels on the scintillator.

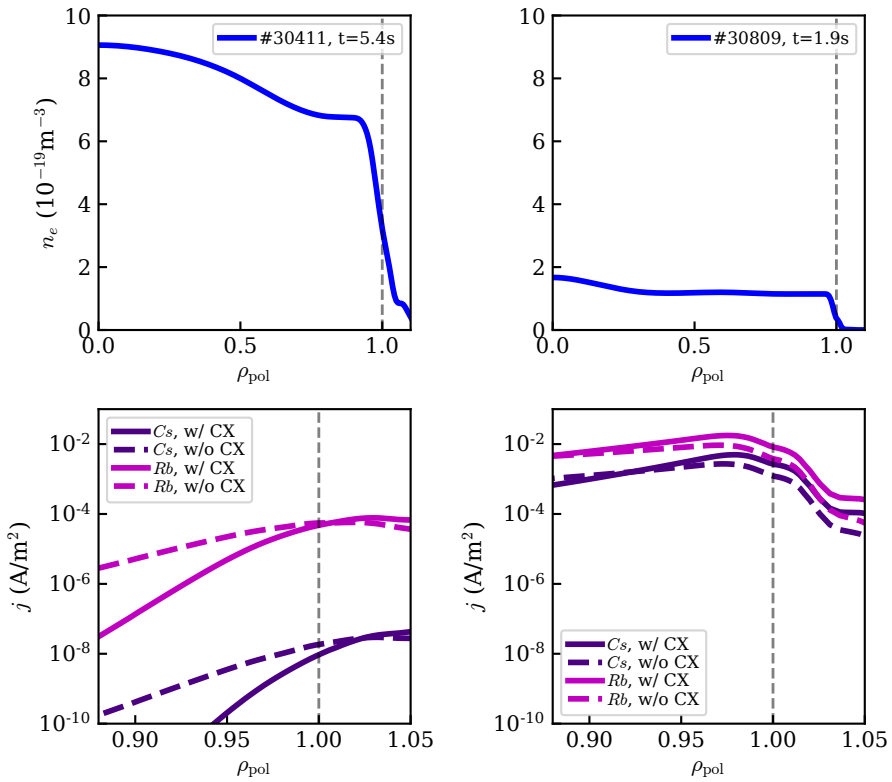

Figure 6.6: *Strikeline intensities (lower row) for a high density case (lower left) and a low density case (lower right). The corresponding radial electron density profiles used as input for the simulations are shown in the top row. Charge-exchange processes (CX) calculated assuming $n_i = n_e$ play in general a minor role, but can be significant at high densities.*

6.3 Sensitivity to Structures at the Edge

By means of numerical simulations as presented above, the impact of different plasma structures on the displacement and the intensity of the scintillator strikeline can be calculated for all edge plasma phenomena as presented in chapter 2. Due to the different amplitudes of the magnetic field perturbation δB, electrostatic potential perturbations $\delta\phi$, density perturbations δn and its location in the plasma, a more or less strong signal response associated to each plasma edge structure manifests on the scintillator detector. By means of the numerical modeling, the signal strengths on the i-HIBP detector for the different phenomena can be assessed and compared to the expected resolution of the i-HIBP system. A few selected examples are detailed in the following.

6.3.1 Determination of Edge Current density

During the type-I ELM cycle (see section 2.4.2), the gradients at the edge and the edge current density (see section 2.2.1) is temporally modulated. The strongest variation of these quantities is expected to take place between the time point shortly prior to the ELM onset (Pre-ELM), and shortly after the ELM crash (Post-ELM). Therefore, a simulation at the Pre-ELM and a second one at the Post-ELM time point is done, in order to assess the changes of the strikeline for these two time points. The magnetic field data at these time points is taken from a high-resolution equilibrium reconstruction of an AUG plasma at $B_t = 2.5$ T and, $I_p = 1.0$ MA (#27963) [103]. The electrostatic potential profile was estimated from the typical change of the radial electric field during an ELM cycle [427] and the radial density and temperature profiles as determined with the integrated data analysis [387]. This input data is shown in figure 6.7.

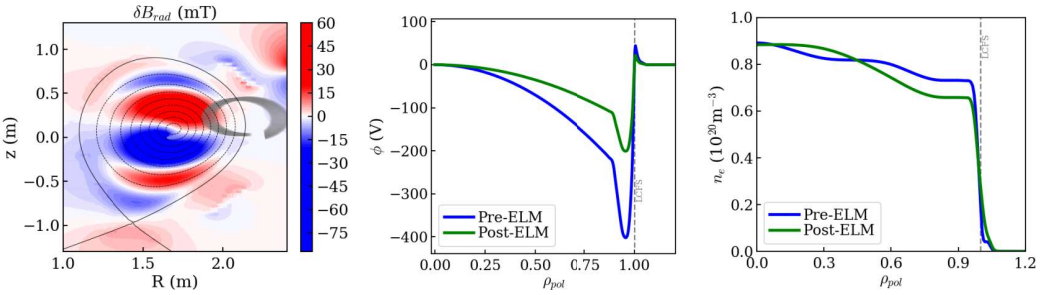

Figure 6.7: *Input data for the numerical modeling of i-HIBP signals during an ELM cycle (reproduced from [419]). Left: Difference between the radial magnetic field component of the plasma equilibria in the Pre-ELM and Post-ELM phase. The trajectories of the secondary beams is indicated in grey. Center: Input profile of the electrostatic potential for Pre-ELM (blue) and Post-ELM (green) time points. Right: Input profile of the electron density for Pre-ELM (blue) and Post-ELM (green) time points.*

The position of the scintillator strikeline for this input data is shown in figure 6.8. The beam is deflected up to 3 mm due to changes in the magnetic field, which is mainly caused by a change of the edge current density. This is a very clear effect and much larger than the expected spatial resolution of the i-HIBP setup in the order of 0.1 mm. Simulations with and without a change of the electrostatic potential reveal that the effect of the electrostatic potential (maximum displacement of 0.3 mm) is negligible compared to the dominant deflection due to the magnetic field perturbation δB.

The change of the strikeline intensity due to the change of the density profile during the ELM cycle is relatively strong. Although the density at the pedestal top is only changed by 10 %, the strikeline intensity on the scintillator is changed by a factor of three. This demonstrates again, that the strikeline intensity is a strong function of the edge density in the plasma.

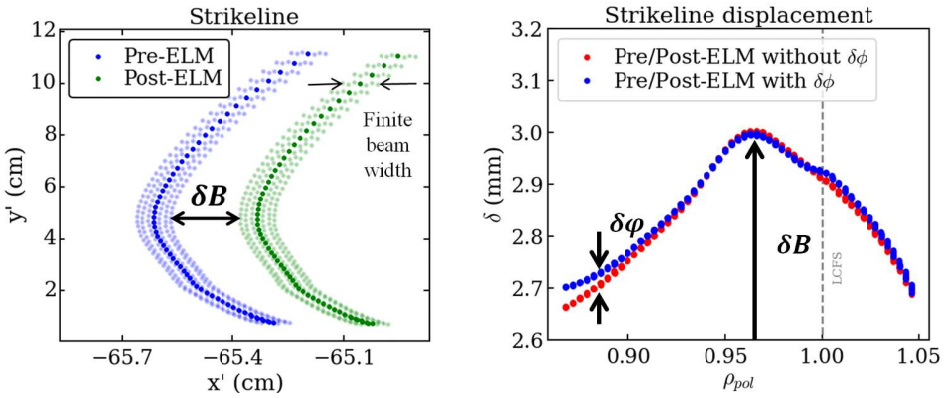

Figure 6.8: *Left: Scintillator strikeline for the Pre-ELM phase (blue) and Post-ELM phase (green) for a beam of a finite width. Right: For each point of ionization, a deflection δ between the Pre-ELM and Post-ELM strikeline as shown in the left panel can be obtained. The deflection due to the magnetic field perturbation is in the range of a few millimeters if the change of the electrostatic potential is neglected (red). Taking into account the additional deflection due to electrostatic potential (blue) demonstrates that its effect is small compared to the pure effect of δB in this radial region (reproduced from [419]).*

Overall, the i-HIBP is expected to react very sensitively to changes of the density and the magnetic field during the ELM cycle, so that it is well suited to quantitatively study the change of gradients and the edge current density in H-mode as these numerical investigations suggest.

6.3.2 Identification of Flow Structures

As introduced above, equilibrium flows (see section 2.1.1) and turbulence driven zonal flows (see sections 2.1.3, 2.1.4 and 2.1.5) are associated with electrostatic potential structures or their perturbations. Numerical modeling of the scintillator strikeline is used to estimate the deflections associated to such potential structures. For this purpose, the strikeline is calculated for a reference potential shown in blue in figure 6.9, right, and compared with the strikeline resulting from a more complex potential structure with four potential perturbations $\delta\phi$ located at different radial positions as shown in green. This resembles an extreme case of the staircases as described in section 2.1.5.

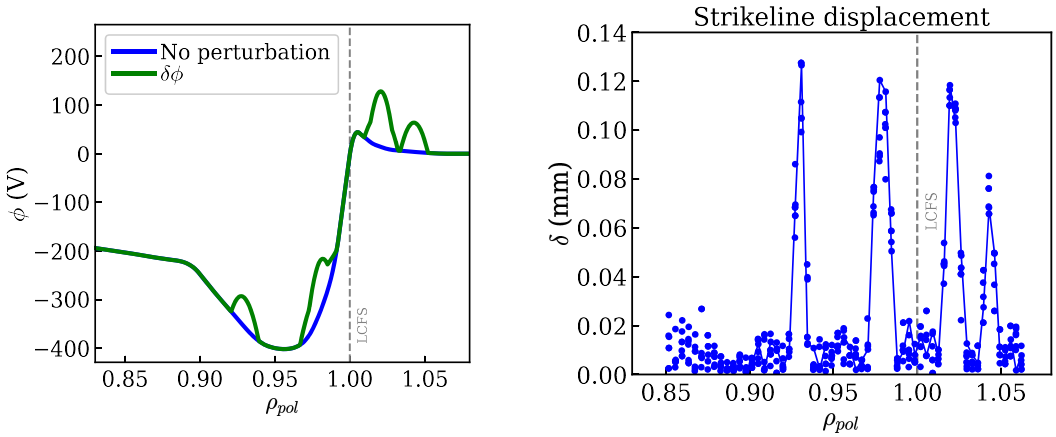

Figure 6.9: *Left: Input profiles of electrostatic potential for a reference case (blue) and a staircase (green). Right: The resulting diplacement δ between reference case and staircase (reproduced from [419]).*

The deflections between the staircase and the reference potential is shown in figure 6.9, right. The deflection is only about a tenth of a millimeter in this case and therefore only marginally above the expected spatial resolution of the i-HIBP detector of 0.1 mm. However, these simulations reveal that the location of the spikes of the deflections as mapped back to the points of ionization given in terms of ρ_{pol} (see 6.9, right) exactly agree with the locations of the electrostatic potential perturbations as given in figure 6.9, left. This demonstrates that the electrostatic potential determination of the i-HIBP is indeed a local measurement of electrostatic potential perturbations. For higher potential perturbations as they appear e.g. in LCOs or in blobs and further inside the pedestal during the ELM cycle (see figure 6.8), a larger displacement clearly above the spatial resolution of the i-HIBP detector is expected.

6.3.3 Characterization of Blob Filaments

Blob filaments are monopolar pressure perturbations traveling through the SOL as introduced in sections 2.4.1 and 3. Consequently, the simulations use likewise monopole density perturbations as input as shown in top row of figure 6.10. Since the blob is assumed to propagate radially outwards over time, three different radial positions corresponding to three different instances of time are investigated. Compared to a case without the density perturbation δn, i.e. a reference case with only monotonic background profiles (blue line in bottom row of figure 6.10), the intensity (green) changes quite significantly

for the three blob positions. A blob comparably far inside the LCFS (left column) produces a reduced intensity compared to the reference. This is due to the fact, that the blob is further inside than the region of ionization, so that only the secondary beams are in contact with the blob. This way, the blob only contributes to the secondary beam attenuation (see equation 6.7) and weakens the strikeline intensity.

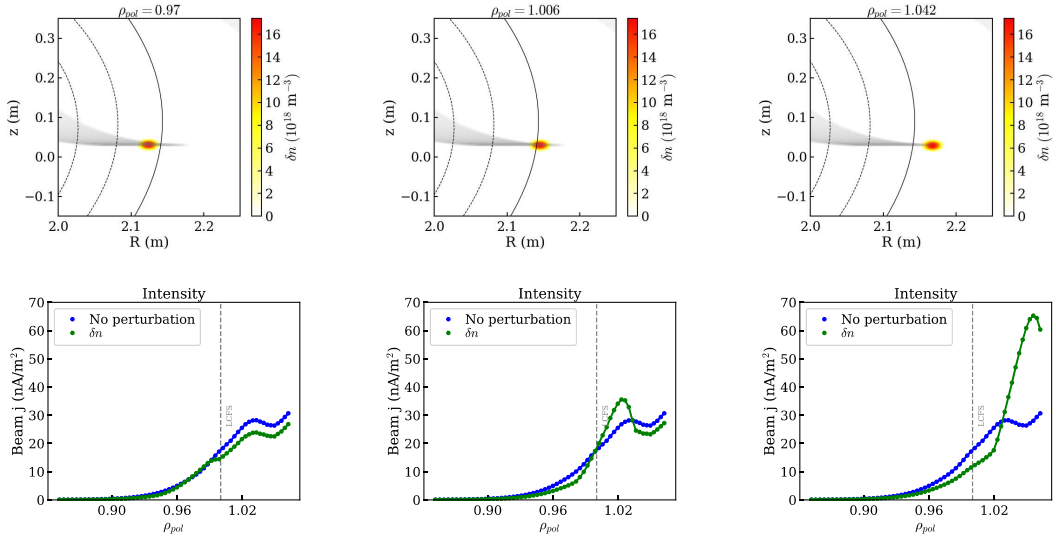

Figure 6.10: *Top row: Location of the density perturbation δn associated with filaments in the poloidal plane for three different radial filament positions as used as input for the numerical modeling. The fan of secondary beams is indicated in grey. Bottom row: the corresponding intensity (green) of the scintillator strikeline compared to a reference case without the filament (blue). The intensity of the strikeline is mapped to the ρ_{pol}-position of the point of ionization of the secondary beam (reproduced from [419]).*

A blob far outside of the SOL (right column in figure 6.10) only interacts with the primary beam, thus, leading to an increased ionization according to equation 6.6 and leads therefore to a higher birth rate resulting in a higher strikeline intensity relative to the reference case outside $\rho_{\mathrm{pol}} = 1.02$. Since more secondaries are born further outside, less neutrals of the primary beam can contribute to the ionization further inside. This is the reason, why the intensity inside $\rho_{\mathrm{pol}} = 1.02$ is lower than the reference case. A blob located at the LCFS (middle column of figure 6.10) is effected by both increased birth rate due to blob interaction with the primary beam and increased attenuation due to interaction of the blob with the secondary beams. In any case, these simulations suggest, that a blob filament propagating radially outward along

the primary beam, causes a strong response of the strikeline intensity allowing for size and velocity studies of blobs by means of the i-HIBP.

In addition to filament detection by means of the strikeline intensity as shown in figure 6.10, the dipolar electrostatic potential of filaments give rise to a measurable deflection, so that additional information about filaments dynamics is expected to be provided by the i-HIBP as simulations suggest [419].

6.3.4 Expected Measurement Capabilities

The expected spatial resolution of the i-HIBP detector is 0.1 mm (see also 6.4) and the dynamic range of the camera is sufficiently large to resolve changes of the strikeline intensity of 1 % assuming that the light intensity provided by the scintillation is above the noise level of the camera. Therefore, plasma edge structures giving rise to a deflection of $\delta > 0.1$ mm and a relative intensity perturbation $\delta I/I > 1$ % are considered to be detectable. A few more plasma edge phenomena than presented above have been assessed by means of the numerical modeling, and the above mentioned sensitivity criteria have been applied. Table 6.1 summarizes the perturbations associated with different plasma edge phenomena, which can be resolved (purple), marginally be resolved (magenta), and not resolved (red) by the i-HIBP.

Type	Name	Plasma regime	Time scale	δn → δI/I (%)	δϕ → δ (mm)	δB → δ (mm)
Filaments	Blobs	All	10-100 μs	30 – 200	0.7	-
	ELM cycle	H-mode	1-5 ms	70	0.4	3
Flows	Staircases / ZFs	L-mode	1 ms	18	0.14	-
	GAMs	L-mode	100 μs	11	0.14	0
Temporal structures	LCOs	After L-H transition	0.1-1 ms	20	0.4	0.3
	Inter-ELM modes	H-mode	2 μs	10	n/a	n/a
Equilibrium structures	External error fields	All	10 ms-∞	-	-	0.8-2.2

Table 6.1: *Sensitivity of the i-HIBP to certain edge phenomena according to the numerical modeling. Density perturbations δn give rise to a relative intensity perturbation on the scintillator $\delta I/I$, and the perturbations of the electrostatic potential $\delta\phi$ and the magnetic field δB are associated with a deflection δ on the scintillator. Perturbations, which can be resolved are marked in purple. Magenta fields indicate marginal sensitivity and the red field indicates, that the magnetic perturbations of the GAM are not resolvable.*

The two phenomena, which are certainly detectable with the i-HIBP due to their strong intensity change, are blob filaments in the SOL and the changes during an ELM cycle. The largest response in terms of the strikeline deflection δ is expected due to externally applied error fields as it is the case for ELM suppression techniques (see section 2.3.1) and due to the change of the edge current density during an ELM cycle. Thus, the numerical modeling suggests, that blobs, ELM cycles and effects of external magnetic perturbations can be studied with the i-HIBP. Depending on the actual resolution of the realized i-HIBP system, the signal-to-noise and signal-to-background ratio, the other quantities marked in purple in table 6.1 might be detectable as well. As a unique feature, the i-HIBP might be allowing for direct measurements of the electrostatic potential of blobs in two dimensions, during the ELM cycle and during LCOs, and under favorable conditions, even in staircases, ZFs and GAMs, depending on the actual performance of the realized hardware.

There are many other phenomena listed in table 2.1, which do not appear in table 6.1. This is owing to the fact, that there is no data of the perturbation amplitudes available (even not from theory) for many phenomena, so that it is not clear what to choose as input for the simulations.

6.4 Hardware Setup at ASDEX Upgrade

The numerical modeling as shown in section 6.2 indicated that a few very interesting plasma edge structures can be studied with the i-HIBP. Its excellent radial resolution including measurements in two dimensions and potentially enabling a measurement of the electrostatic potential perturbations $\delta\phi$ was considered to justify the costs and effort to develop this new type of diagnostics at AUG. The main components of the i-HIBP are an alkali beam injector, an in-vessel scintillator detector head including a custom-made powerful lens system, a heatable image guide and an ex-vessel camera. A CAD drawing of the full i-HIBP system including its main elements and its installation at the AUG vacuum vessel is shown in figure 6.11.

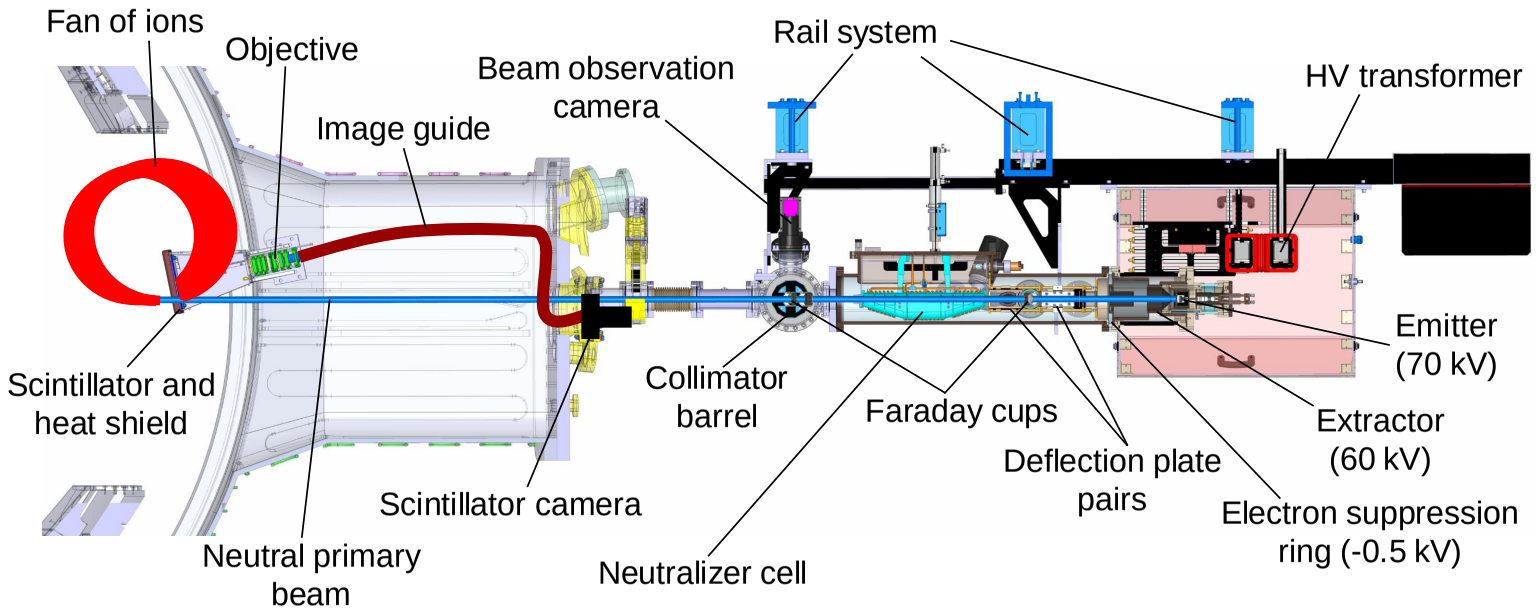

Figure 6.11: *CAD drawing of the i-HIBP system at AUG (adapted from [408]). The alkali ion beam (blue) is extracted by thermionic extraction from the emitter and accelerated towards the plasma on the left. It passes first two pairs of deflection plates for horizontal and vertical steering of the beam. Afterwards it is neutralized in a neutralizer cell and its diameter reduced by a collimator plate on the barrel. In the plasma (not shown) the neutral beam is ionized giving rise to a fan of secondary beams (red) intersected by a scintillator. The scintillation light is collected by a lens system and transferred in a heatable image guide to the vacuum window, where a camera is placed. The beam line is equipped with two Faraday-cups and three beam observation cameras. The i-HIBP injector is mounted on a rail system from the top.*

6.4.1 Alkali Beam Injector and Collimator

The alkali beam injector of the i-HIBP at AUG including its control system was provided by the companies Entimel Kft. and Fusion Instruments Kft. and developed and commissioned in collaboration with the Hungarian Centre for Energy Research, Budapest. The injector system is very similar to the injection system realized at K-STAR, EAST and W7-X for beam emission spectroscopy (BES) purposes [428, 429], but it differs in two main aspects: instead of the usual maximum 60 kV high voltage power supplies for BES, the i-HIBP requires higher voltages up to 80 kV and instead of Li or Na, the i-HIBP makes use of heavier elements like Rb and Cs as beam species.

The alkali beam injector contains a β-eucryptite-type of emitter as ion source consisting typically of an $Alk_2O{\cdot}Al_2O_3{\cdot}4SiO_2$ disk with Alk indicating an arbitrary alkali atom to be placed inside this matrix. Heating the source up to 1350° C increases the diffusion of the alkali ions in the emitter material to such high level, that they can be extracted by thermionic emission from the surface of the source. This type of beam source allows to extract currents in the range of a few mA [430].

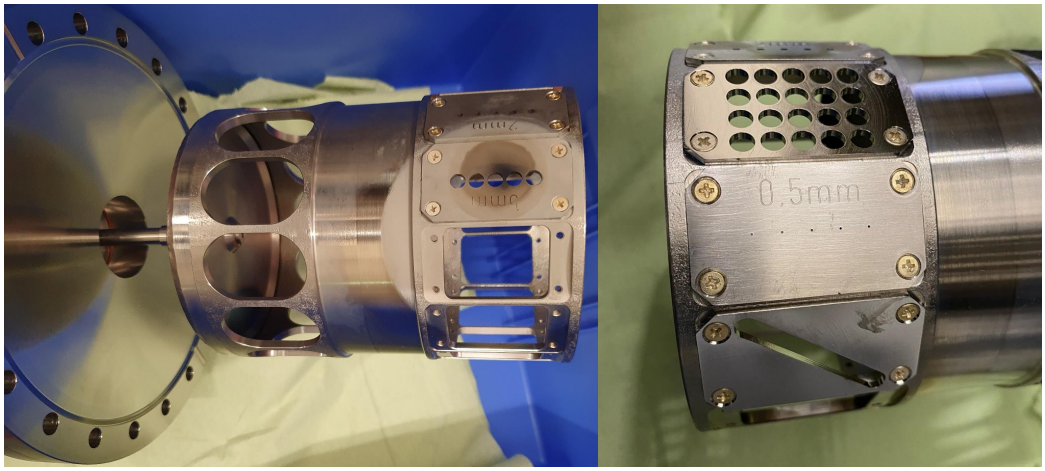

Figure 6.12: *Photograph of the collimator barrel removed from the beam line. Left: Most of the experiments were done using the plates with five holes of 5 mm diameter. The black circle on this plate indicates the typical location, where the Rb beam hit the collimator (the white circular shade is NaOH contamination originating from the neutralizer cell). Right: Alternative collimator plates with different hole diameters and geometries.*

The ion beam extracted by an extractor electrode from the emitter in a Pierce electrode setup propagates towards the plasma passing first two pairs of deflection plates, which can deflect the beam in horizontal and vertical direction. Afterwards, the ion beam is neutralized in a cloud of sodium vapor inside the neutralizer cell, which is optimized for minimum sodium losses during long time beam extraction [428]. After the beam is neutralized, it passes a beam diagnostic chamber, where two cameras (one from the top, one from the side) are employed to quantify the beam quality, focus properties and horizontal and vertical deflection by the detection of beam emission due to collisions with the rest gas or gas from the torus. At this place, a Faraday cup can be inserted by a manipulator to measure the beam current or the neutralization efficiency of the neutralizer.

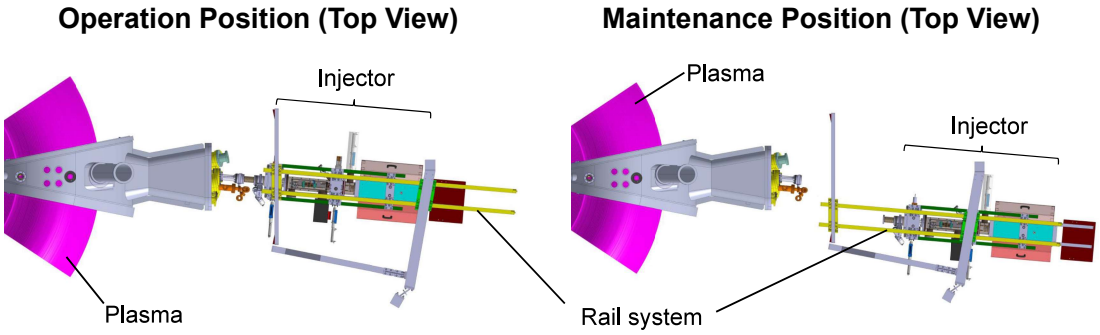

Figure 6.13: *Operation position of the i-HIBP (left) in toroidal sector 13 of AUG. During maintenance phases (right) the i-HIBP injector system can be moved into a parking position by means of the rails at the top in order to release a large volume in this sector of AUG to facilitate maintenance work (reproduced from [408]).*

The beam diagnostic chamber hosts also the collimator barrel, where the beam diameter is reduced to an appropriate size (typically 5 mm). This enables more precise deflection measurements on the scintillator, since a too wide beam would lead to an overlap of secondary beams on the scintillator, which were created at poloidally and toroidally displaced locations on the primary beam. A photograph of the collimator barrel including its various collimator plates with different hole geometries is shown in figure 6.12.

Depending on the collimator plate introduced into the beam line, holes of different sizes determine the beam diameter. The diagonal slit in one of the collimator plates (see figure 6.12, right) would allow for a well defined cross section of the neutral beam providing a 2D imaging of the ionization region.

In general, all plates were equipped with several holes in order to provide several beamlets allowing for measurements of several strikelines corresponding to more than one poloidal or toroidal position in the plasma.

The whole injector system including beam diagnostic chamber, manipulators and the metal-cased high-voltage setup around the source region consisting of a high-voltage transformer, load resistors and a cooling system by pressurized air for the emitter flange is mounted on a rail system from the top. Due to space restriction a support of the i-HIBP system from the bottom was not possible to be realized. The rail system enables to move the injector horizontally, vertically and radially towards the torus axis of AUG. As shown in figure 6.13, when the i-HIBP system is out of operation, it can be moved into a parking position establishing a free volume between the i-HIBP injector and the vacuum vessel of AUG for maintenance of the i-HIBP and other diagnostics in this sector of the tokamak experiment.

Apart from the components shown in figure 6.11, which are all placed inside the AUG torus hall, the main part of the i-HIBP control system and the high voltage power supplies providing voltages up to 100 kV are placed in two cabinets outside the torus hall, so that access of the control system and power supplies is always possible, even in the case that the torus hall is closed during plasma operation. The components outside the torus hall are connected to the injector and its related systems inside the torus hall via cables of a length of 40 m requiring tailor-made solutions of electrical devices and circuits in order to avoid unfavorable effects due to inductivities and capacities of the cables.

6.4.2 Detector Head and Image Guide

The detection of the secondary beams of the i-HIBP inside the vacuum vessel involves a scintillator screen placed as close as possible to the plasma, an optical lens system collecting the light from the scintillator, an image guide transferring the light to the vacuum window, and a camera outside the vacuum, which records the scintillator images at the other end of the image guide (see figure 6.11).

The scintillator screen has a size of 16 cm in vertical direction and 6 cm in horizontal direction. It is made of TG-Green powder consisting of a composition of $SrGa_2S_4$ doped with Eu^{2+} and was manufactured by the Plasma Science and Fusion Technology (PSFT) Group at the University of Seville. As shown in figure 6.14, the scintillator is encased in a metallic housing with an aperture at the top, where the secondary ions can enter the detector head in order to reach the scintillator. The plasma-facing side of the housing is made of a tungsten-coated graphite tile capable of dealing with the higher

heat loads at this side of the head. As monitoring signals, the temperature at the scintillator is measured with a thermocouple. In addition, the current on the scintillator plate as well as a reference current on a plate below the scintillator is determined in order to provide an electrical measurement of possible ion currents on the scintillator in addition to its light response.

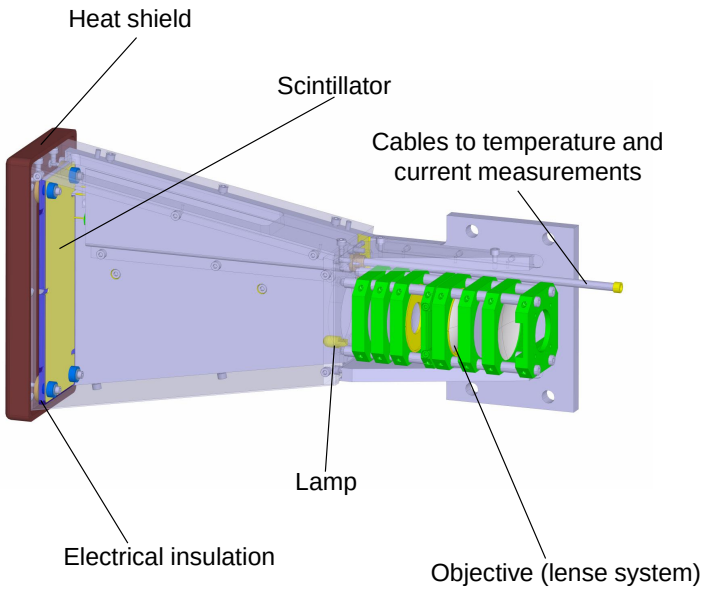

Figure 6.14: *Detector head of the i-HIBP. The scintillator screen and the lens system is cased in a metallic housing (front plates not shown) with only one large aperture at the top to allow the secondary ions to enter the head (reproduced from [408]). The heat shield consisting of a tungsten-coated graphite tile is facing the hot plasma. The image guide (not shown) is connected to the lens system from the right. The cables to lamp, current sensors and thermo couples enter the optical head from the right in a separate tube.*

The detector head contains a lens system on the opposite site of the scintillator to map the light from the comparably large scintillator screen onto the entrance of the image guide, which is only 17 mm high and 7 mm wide. The lens system enables a resolution of structures on the scintillator plane slightly smaller than 0.1 mm and has a high light throughput as well es a low distortion. For calibration purposes, a small halogen lamp is integrated on the side of the lens system illuminating the scintillator e.g. for light throughput measurements.

The image guide between the lens system and the vacuum window is 1.829 m long and consists of 1700×700 glass fibers with a diameter of 10 µm each. Since the lens system inside the detector head provides a resolution bet-

ter than 0.1 mm, the size of the fibers with an effective resolution of 0.1 mm given by the fiber diameter constitutes the resolution limit of the optical system. Due to neutron bombardment during plasma operation (mainly neutrons created in D-D fusion reactions), the transmission of the image guide is strongly reduced in the course of the experimental campaign, typically from about 50 % to below 1 %. This transmission loss induced by neutron damage can be compensated by means of heating of the image guide at about 200° C for several hours [431]. Since the image guide is located inside the AUG vacuum vessel, which is opened only once a year between two measurement campaigns, the image guide heating has to be applied in-situ, i.e. inside the AUG vacuum vessel. A technical solution for the i-HIBP image guide heating has been developed and the concept was submitted to the European Patent Office in October 2022.

The aperture at the top of the detector head can be closed by a shutter plate, which is driven by a pressurized air cylinder [409]. This is necessary in order to avoid damage and contamination of the scintillator screen during glow discharges inside the AUG vacuum vessel, which is used for wall conditioning and wall cleaning purposes on a regular basis.

6.4.3 Injector Characterization

Before the i-HIBP injector was used inside the torus hall of AUG, a few tests were done in the laboratory to characterize the quality and the properties of the alkali beam. Since the use of Rb and Cs as beam species was new even for the manufacturer of the ion sources, the beam properties and especially the beam current dependence on the applied heating and extraction voltage had to be characterized.

Alkali beams at such high extracted currents of a few mA are space charge limited and, therefore, follow the Child-Langmuir law [428]

$$I_\mathrm{b} = \frac{4\epsilon_0}{9}\sqrt{\frac{2q}{m_\mathrm{i}}}\frac{U_\mathrm{ex}^{2/3}}{d^2} \tag{6.8}$$

with U_ex, i.e. the voltage difference between the emitter and the extractor electrode, and the electrode distance d. Due to the thermionic extraction, alkali beams do not necessarily follow the Child-Langmuir law, since the ion diffusion inside the source material might further limit the extracted current, so that increasing voltages do not lead to higher extracted currents. In this diffusion-limited regime, the extracted current can only be increased by higher source heating.

The measured relation between applied voltage U_ex and the extracted current I_b for the i-HIBP system using a Cs beam is shown in figure 6.15. For

low voltages, the measurement points follow roughly the Child-Langmuir law 6.8. However, for $U_{ex} > 3$ kV all data points are below the Child-Langmuir curve. This indicates that the beam extraction is limited by the ion diffusivity in the source and the measured points do not increase anymore with applied voltage, i.e. I_b saturates. Increasing the heating power of the ion source indicated by the heating current I_s in figure 6.15 can increase the saturation level as obvious from the data taken at 18th July 2019. But conditioning effects of the source likewise play a role, as indicated by the measurement at the 31st of July 2019, which is almost on the same level as the data series of $I_b = 36$ A at 18th July 2019 despite the heating current was only $I_b = 30$ in this data series. Consecutive heating and beam extraction obviously help to increase the diffusion-limited beam extraction as long as a sufficient alkali inventory is available in the source material.

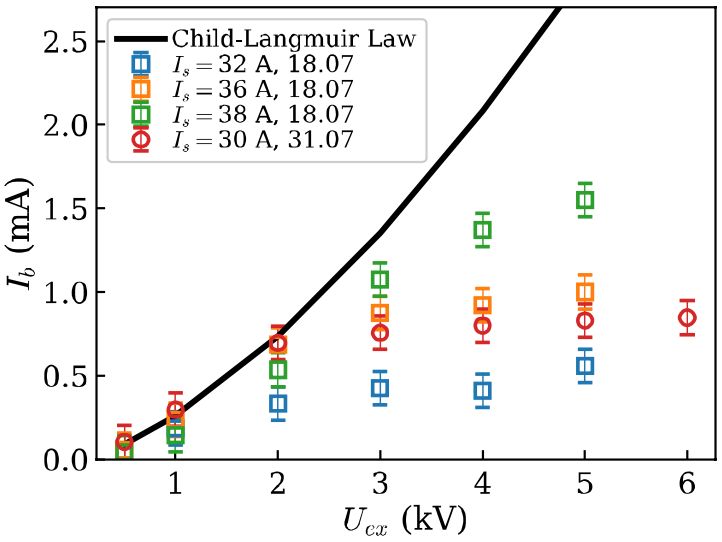

Figure 6.15: *Measured extracted beam current I_b depending on extraction voltage U_{ex} between emitter and extractor electrode (reproduced from [408]). For lower voltages, the data taken at two different days (18th July 2019 and 31st July 2019) follows approximately the Child-Langmuir curve (black line) according to equation 6.8. For higher voltages saturation takes place due to ion diffusion limits inside the source. This depends partially on the source heating current I_s, but also conditioning effects play a role as data from different days indicate.*

In general, beam currents of up to $I_b = 1.5$ mA were regularly obtained for Rb and Cs beams at about 70 kV. Higher currents were not possible without overheating the ion source. Nevertheless, the achieved extracted currents are higher than $I_b = 1.0$ mA assumed for the numerical modeling.

In this sense, the beam properties provided by the alkali beam injector was overachieving the specifications.

Apart from the characterization of the extracted beam current, several technical components had to be tested in laboratory tests to make sure that they work for the remote operation in the AUG torus hall. This includes tests of the beam steering by the deflection plates. By means of a camera viewing the surface of a Faraday cup in the beam line, the vertical and horizontal beam position was determined. The heavy ion beam gives rise to light emission due to recombination of beam ions on metallic surfaces, so that the beam shape and position can be measured as shown in figure 6.16. The beam intensity maximum is slightly off-axes with respect to the center of the Faraday cup. Applying a deflection voltage of 200 V on both plate pairs with opposing polarity, i.e. -200 V on one plate if the opposite plate is on 200 V, moves the beam towards the center of the Faraday cup. For 400 V, the beam moves fully into the center of the Faraday cup. This demonstrates that the deflection plates, which can be operated up to 500 V, can steer the beam by about ±1 cm at the Faraday cup location, which translates to about 2 cm at the ionization region in the plasma. This might be an important control tool to compensate beam deflection by magnetic stray fields of the tokamak or dedicated beam steering as an additional control tool to make sure that the secondary beams hit the scintillator in exotic plasma configurations.

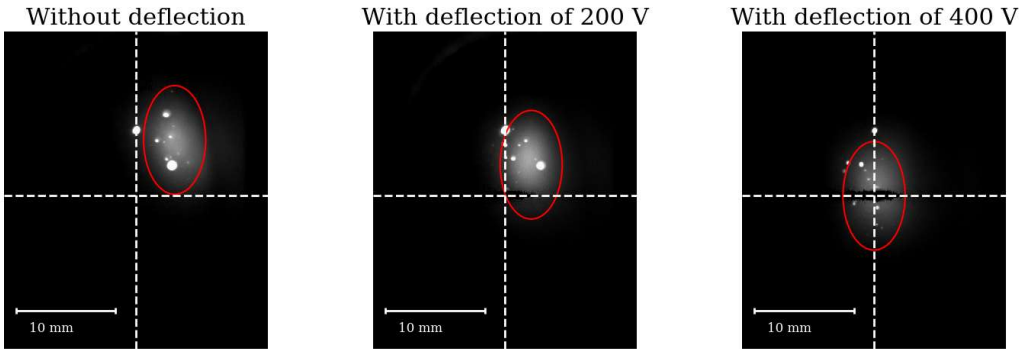

Figure 6.16: *Camera pictures on the Faraday cup (background subtracted) for a Cs beam at 55 kV (reproduced from [419]). The beam is moved towards the center of the Faraday cup (crossing point of white lines) by applying deflection voltages in steps of 0 V (left), 200 V (middle) and 400 V (right) on both plate pairs. The white bright spots are luminescent impurities on the metal surface of the Faraday cup.*

6.4.4 Scintillator Characterization

Several TG-Green-type of scintillators are successfully used since more than 10 years at AUG in fast ion loss detectors measuring fast hydrogen or deuterium ions [432], and the relevant data of the scintillator yield under irradiation with protons and deuterons was available [433, 434]. However, there was no data available about the scintillation properties of TG-Green under irradiation with heavy alkali atoms. Therefore, dedicated laboratory tests to determine the scintillator yield of TG-Green and a few other scintillator materials under Cs irradiation in the beam energy range from 5 kV to 70 kV were undertaken [435].

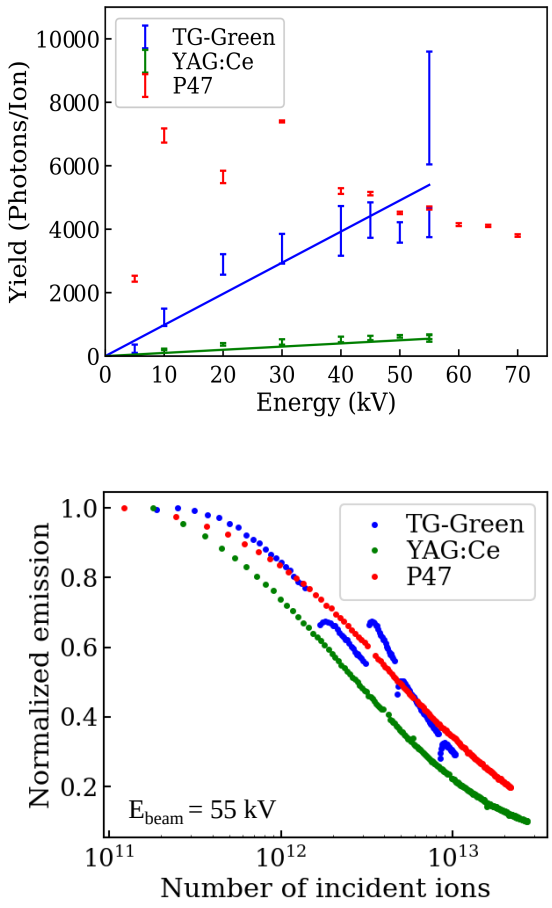

Figure 6.17: *Top: Scintillator yield i.e. number of emitted photons per incident ion. Bottom: Degradation of the scintillator yield normalized to its initial value versus ion fluence (reproduced from [419]).*

The main result of this study is shown in figure 6.17, top. It shows the scintillator yield, i.e. the number of emitted photons isotropically emitted into all directions of space per incident beam ion for three different scintillators. As expected, the yield increases with energy for TG-Green and YAG:Ce ($Y_3Al_5O_{12}$:Ce). The scintillator P47 ($Y_{24}Si_5O_{12}$:Ce), however, does not show a systematic dependence on energy [419]. The yield is highest for TG-Green and P47 in the relevant energy range of the i-HIBP between 40 kV and 70 kV.

During this study it was discovered, that the scintillator yield decreases over time, when the same spot on the scintillator screen was irradiated for longer times corresponding to high fluences (see figure 6.17, bottom). This ion-flux-induced degradation was then studied in more detail and it turned out [435], that the irradiation with heavy elements leads to a much stronger degradation of the scintillator material than irradiation with light ions. The reason is that the ion energy is deposited in a much thinner layer of the scintillator due to the higher mass of the heavy elements damaging the scintillating layer much more effective than light elements for the same fluence and energy.

Due to its high yield, the favorable energy dependence of the yield, comparably low degradation and the good temporal response (i.e. afterglow time lower than 1 µs) the TG-Green scintillator material was selected for the i-HIBP detector head.

6.5 First i-HIBP Measurements at AUG

The laboratory tests of the i-HIBP injector and other hardware components demonstrated that the design specifications were met. Operation of the same i-HIBP setup inside the AUG torus hall during plasma operation, however, gave rise to several challenges attributed to the long cables between control system and injector, to the stray magnetic field of the tokamak, to the electromagnetic interference with other devices, to programming errors in the control system and to hydrogen safety issues. Step by step each challenge, which seemed to make i-HIBP operation impossible, was overcome and after a commissioning phase of one year, the i-HIBP system was in full operation and successfully remote controlled on a regular basis during the experimental campaign starting in autumn 2021.

6.5.1 First Signals on the Scintillator

The very first clear signal of secondary beams on the scintillator was measured on 26th November 2021 in one of the first discharges after the restart of AUG for the 2021/2022 experimental campaign. The magnetic field of this discharge #39800 was $B_t = -2.5$ T and the plasma current was ramped up to $I_p = 0.6$ MA. An uncollimated Rb beam was injected with an energy of $E_{beam} = 67$ kV and an extracted beam current of $I_b = 0.67$ mA. The resulting scintillator pattern recorded with the camera (JAI CM-030PMCL-RH) is shown in figure 6.18.

Figure 6.18: *One of the first camera frames with a clear signal on the i-HIBP scintillator generated by the secondary beams of an injected Rb beam into an AUG discharge. The bright pattern with a maximum on the bottom is the actual beam signal and qualitatively agrees with the expected intensity dependence (see figure 6.5). Stray light illuminates also the bottom and side edges of the scintillator. The two black spots at the bottom left and right are the screws fixing the scintillator. The black spot at the bottom center is a damaged part of the scintillator. The tiny black dots all around the image are broken fibers of the image guide.*

A clear and strong scintillation pattern in form of a broad vertical stripe almost illuminating the whole scintillator area with a clear maximum of intensity at the bottom is found. The breadth is owing to the fact, that the focusing of the primary beam was not sufficiently small at this early trial of beam injection into AUG. The vertical intensity dependence indicating an increasing ion flux from top to bottom of the scintillator qualitatively agrees with the numerical modeling for plasmas of similar density as shown in figure 6.5. This result demonstrates that the basic concept of the intensity measurement of the i-HIBP works, and that the realized i-HIBP system behaves similarly as predicted by the numerical modeling as presented in section 6.2.

Apart from this very encouraging result, a few further observations were made during these early measurements. First, the stray light from the plasma entering the detector head through the large aperture at the top, was found to be significant and can even exceed the actual secondary beam signal. The higher the heating power injected into the plasma, the more background light was detected. The application of beam chopping allowed for background subtraction to some extend, but failed at high heating powers and due to the presence of ELMs and other plasma fluctuations, so that the chopped beam signal was difficult to be identified. Therefore, the more successful strategy to avoid high background light was to focus the i-HIBP analysis on low power discharges.

Second, the scintillator as shown in figure 6.18 exhibits signs of damage. The black spot at the bottom center does not produce scintillation, and as turned out after the campaign, the scintillating layer was brittle and several flakes of scintillator material were found distributed inside the detector head probably detached from the substrate due to thermal and mechanical stress. The two black spots at the very bottom left and bottom right in figure 6.18 are the screws, which fix the scintillator in the detector head. The tiny black spots randomly distributed over the image are broken fibers of the image guide probably arising due to mechanical manipulation of the image guide during the cleaning and installation process. Although clearly visible, their relative area is below 1 %, so that they fortunately do not hamper the measurement.

At the early stage of the AUG campaign, the transmission of the light system was excellent, so that high signal levels of scintillator light could be measured with the exisiting setup as long as the density in the plasma edge was below $2 \cdot 10^{19}$ m^{-3} and the stray light not too high. This upper density limit is about a factor of two lower than expected from the numerical modeling, which indicated that a measurement up to $4 \cdot 10^{19}$ m^{-3} should be possible. Nevertheless, reasonable signal levels on the scintillator could be achieved for whole plasma discharges, when the operational scenario was optimized for

the i-HIBP, i.e. choosing low density and low heating power. In later phases of the campaign, the transmission of the optical system was decreasing, so that regular application of the in-situ image guide heating was necessary to increase the transmission back to levels allowing for measurements. In addition, a more sensitive CMOS camera (Omron STC-RBS43PCL-UM12) was used at the end of the campaign to increase the signal level.

6.5.2 Beam Collimation

The predicted strength and uniqueness of the i-HIBP system is due to the ability of measuring the electrostatic potential and magnetic field perturbations by the secondary beam deflection. This is not possible with broad beams as shown in figure 6.18, since local deflections are difficult to be measured at such large structures with soft edges and due to the overlap of secondary beams from different toroidal and ploidal locations on the scintillator in this case. Thus, the beam collimation by means of the collimator barrel is essential for the measurement of the strikeline deflection δ.

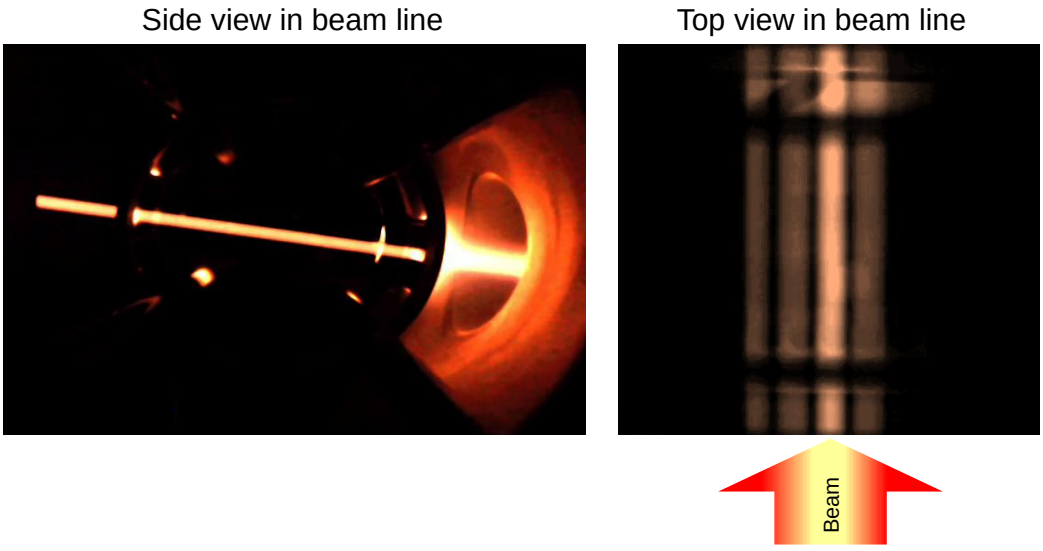

Figure 6.19: *Left: Horizontal side view into the beam line. The beam coming from the right is clearly reduced in diameter after it has passed the collimator plate with five holes of 5 mm diameter. Right: Top view into the beam line at approximately the same time point after the beam has passed the collimator plate. The broad initial beam gives rise to an array of four beamlets injected towards the plasma (located at the top of this image).*

Figure 6.19, left, shows a camera frame recorded with the side camera observing the beam line horizontally inside the collimator barrell and perpendicular to the beam axis during a high gas puff phase *after* the plasma discharge. The relatively broad beam is injected from the right of the image and passes the collimator plate with five holes of 5 mm diameter. The beam exhibits clearly a smaller diameter after it has passed the collimator (about 5 mm diameter) compared to the diameter prior to the collimator (about 2.5 cm diameter). This clearly demonstrates, that the collimator works and that the beam is injected into the plasma (located on the left in this view) with the desired smaller diameter given by the collimator plate.

A top view of approximately the same time point recorded with the camera viewing the beam line from the top after the beam has passed the collimator plate (see figure 6.19, right) reveals, that it is actually not only one but an array of four beamlets, which is created by the collimator plate. One beamlet exceeds the adjacent beamlets in terms of intensity due to the fact that the maximum of the initial beam intensity was present at this respective hole (second hole from the right), and the adjacent holes were only penetrated by the halo of the initial beam.

Measurements with the beam observation cameras in the beam line as shown in figure 6.19 demonstrated that the basic principle of collimating the (neutral) alkali beam works as expected. However, the primary beam collimated this way did usually not lead to a measurable signal on the scintillator during plasma operation. As a matter of fact, whenever a collimator plate was introduced into the beam line, the signal on the scintillator was gone. One possible explanation for this unfavorable behavior are stray magnetic fields produced by the tokamak, which deflected the primary beam a few millimeters into horizontal or vertical direction, so that the initial beam did not hit the collimator plates centrally anymore. Consequently, no or only very weak beamlets are created at the relevant positions, which produced a secondary beam signal below the detection level on the scintillator. Indeed, a dedicated study on the effect of stray magnetic fields on beam deflection demonstrated a correlation of beam deflection of a few millimeters with the activation of certain poloidal magnetic field coils of the tokamak. Despite the installation of additional shielding by ferromagnetic material, this undesired beam deflection could not be minimized to an acceptable level during the campaign. In other words, the collimation of the beam was not possible to be reliably used during plasma operation, so that the determination of the deflection due to small magnetic field or electrostatic potential perturbations could not be directly tested in this first phase of operation of the i-HIBP due to a too broad primary beam.

6.5.3 Filamentary Structures

As already shown in figure 6.18, the scintillator pattern due to secondary beams has often a single maximum of intensity along the vertical direction as it was also found in the numerical modeling (see figures 6.5 and 6.6). This is the expected intensity pattern due to the interplay between the monotonic increase of the plasma density and the ionization of the primary beam. However, in practically all plasmas, for which the i-HIBP signal intensity was sufficiently high, also different intensity patterns with one ore several local maxima at different places along the vertical scintillator axis were measured. A few examples are shown in figure 6.20.

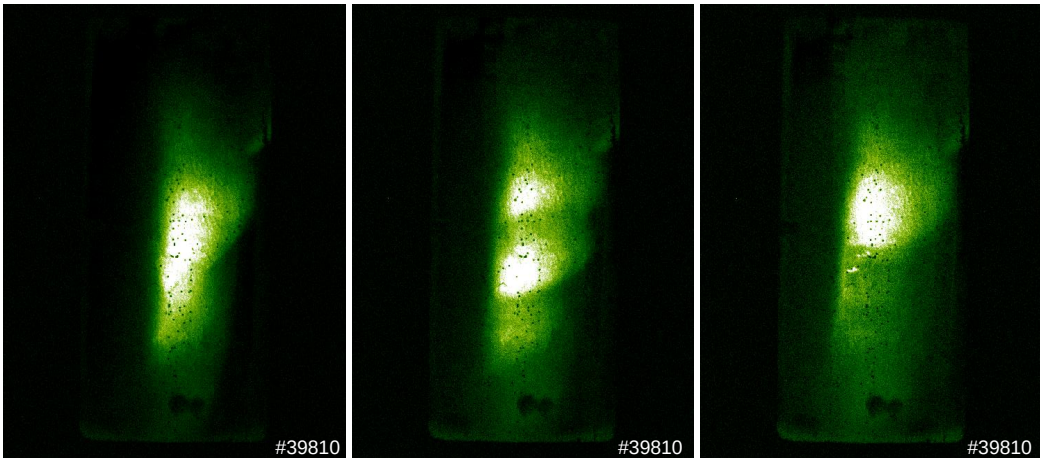

Figure 6.20: *Apart from the typical vertical intensity dependence (left) as seen likewise in simulations of monotonically rising background density profiles (see figure 6.5), many measured i-HIBP camera frames (exposure time: 8.3 ms) exhibit several (center) or single local maxima (right) resembling intensity perturbations due to blob filaments in the SOL as found predicted in 6.10.*

These local maxima were moving vertically in consecutive camera frames indicating that the plasma structures, which induce the local maxima, propagate into radial direction. As beam tracing calculations have shown, the local maxima measured on the scintillator are placed around the LCFS or even outside. All these findings suggest, that the local maxima are blob filaments in the SOL (see chapter 3 and section 2.4.1). Similar as found in the simulations shown in figure 6.10, the intensity on the strikeline moves along the long side (i.e. vertically in figure 6.20) of the scintillator, when the blob-associated density perturbation moves radially outward. This opens the

possibility to study blob filaments with the present setup of the i-HIBP, and a comparison with numerical modeling, as it is planned for the future, could enable quantitative estimations of poloidal and radial propagation velocities and the density content of blobs.

6.6 Prospects of the i-HIBP Diagnostics at AUG

The first campaign with measurements of the i-HIBP has shown that the basic idea of imaging a fan of secondary beams by means of a scintillator detector is possible to be realized at medium size tokamaks. The measured signal intensities are high in low density plasmas and correspond approximately to the predicted signal levels by the numerical modeling. A further clear confirmation of modeling predictions is the measured vertical scintillator intensity pattern, which typically increases towards the bottom of the scintillator up to a local maximum in the lower half of the scintillator. Most impressively, the measurement of radially propagating filamentary structures were very similar to the results of the numerical modeling.

However, the collimation of the beam was not possible to be reliably applied during plasma operation most probably due to deflection of the primary beam by the stray magnetic field of the tokamak. This made a quantitative comparison with the modeling of small strikeline deflections δ as presented in section 6.2 impossible, since the scintillator pattern is too broad to resolve small movements. Nevertheless, plenty of camera images of the scintillator pattern are available in a variety of plasmas with current and magnetic field scans, which have shown interesting movements and shape dynamics of the macroscopic scintillator pattern indicating an impact of magnetic field or electrostatic potential perturbations on the strikeline pattern. Therefore, an extension of the i-HIBPsim code package is under development to produce realistic scintillator patterns including finite beam width, finite divergence and a three-dimensional description of the detector head, so that a direct and quantitative comparison of the numerical output with the measured camera frames is possible. This modeling tool likewise enables to evaluate the impact and compensation of the stray magnetic field in order to investigate possible solutions to realize useful measurements of electrostatic potential and magnetic field perturbations. In other words, the i-HIBP did not reach all goals in the first campaign, but the tools are available to evaluate possible improvements for achieving the predicted performance of the i-HIBP in the next experimental campaign at AUG.

Chapter 7

Summary and Conclusion

The edge plasma of a tokamak is a complex physical object involving strong gradients and a complicated magnetic topology including the transition from closed flux surfaces to open magnetic field lines. Different types of particles like hydrogenic ions, impurity ions, electrons and neutral atoms are present there in various concentrations. These conditions give rise to a large variety of spatial and temporal structures due to non-linear effects, collisions, radiation and the complex interplay between particles and electromagnetic fields. It is the task of experimental physicists to describe these structures, to try to categorize them and to identify the underlying physical mechanisms, which give rise to certain properties of the respective structure. This work tried to contribute to this task in a number of ways.

In chapter 2, a comprehensive overview of experimentally observed edge structures was given. Five categories of structures have been introduced:

a) self-generated flows,

b) self-generated electric currents,

c) spontaneous phase transitions into improved confinement states,

d) filaments,

e) temporal structures.

Edge structures commonly observed at tokamak experiments were briefly introduced and assigned to one of the four categories.

The flow structures (category a) presented in section 2.1 represent the second largest group of structures. They are driven either by (normalized) pressure gradients (equilibrium flows) and additionally by ion temperature gradients (neoclassical flows) or by turbulence due to the Reynolds stress

(RS) force as in the case of low frequency zonal flows, GAMs or staircases. RS-driven flows share a small radial extend of about $10\rho_s$, and appear as annular structures with alternating amplitudes in the poloidal plane as shown in figure 2.3, right. The gradient driven flows exhibit in general a broader radial width and can persist over a longer period of time compared to RS-driven flows. All types of flows and their associated shear are considered to be extremely important to regulate the saturated level of turbulence: the higher the flow shear, the lower the turbulence level. Therefore, the control of these flows, ideally by an actuator driving such flows on purpose as suggested in reference [436], might contribute to reduce turbulent transport in fusion plasmas. By means of such a method, the confinement time could be increased facilitating to achieve fusion conditions in future tokamaks.

The two examples of self-generated electric currents (category b) as presented in section 2.2 are driven by gradients. In contrast to many other structures, they are quantitatively described by theoretical models (see table 2.1) and are considered to be well characterized by indirect measurements employing MHD-equilibrium reconstruction techniques. However, a local and direct measurement of the edge current density has never been convincingly shown for a broad range of plasma parameters and for relevant plasma scenarios, although the edge current density plays such a central role for the pedestal stability and the appearance of ELMs. For this purpose better diagnostics enabling electric current measurements are needed as the i-HIBP (chapter 6) might provide. In addition, the local magnetic shear contribution to the turbulence suppression as discussed in reference [107] has not been studied in detail, although the local magnetic shear driven by the edge current density might provide a convenient control tool to raise the total shearing rate, i.e. $E \times B$ plus magnetic shear, by plasma shaping, collisionality or external current drive. Control of the local magnetic shear might open a route to lower the L-H transition power threshold and reducing edge transport in general.

Spontaneous phase transitions (category c) are fascinating manifestations of self-organization, and the two most important transitions, the transition to I-mode (section 2.3.3) and the L-H transition (section 2.3.2), will probably play an important role for future fusion reactors, since I-mode [172] as well as H-mode [7] are envisaged as reactor-relevant plasma scenarios due to good energy confinement. Although discovered 40 years ago [108], the transition from L-mode to H-mode is still not fully understood and cannot be satisfactorily reproduced with modern turbulence simulations or other first principle models. However, many measured parameter dependencies of the threshold power to achieve H-mode, P_{LH}, and experimental observations around the L-H transition were documented over the last decades including rare and

recent experimental L-H transition studies of tritium plasmas as detailed in chapter 4. Key findings are a critical edge temperature, a critical edge ion heat flux and a critical edge $E \times B$ velocity at the L-H transition. It was shown in section 4.3.2 that a critical edge $E \times B$ velocity can qualitatively explain practically all further parameter dependencies of P_{LH} (see equation 4.29) and gives an explanation, why a critical edge ion heat flow (equation 4.10) is connected with the L-H transition. Furthermore, it was shown, that most of the manifold parameter dependencies of P_{LH} can be reproduced with an analytical formula (equation 4.19) based on the assumption that the critical edge ion heat flux has to be achieved to enter the H-mode. For plasmas with low torque input, as it will be the case in future tokamak reactors [7, 172], the formula predicts a U-shaped curve for P_{LH} as a consequence of the electron-to-ion energy exchange. The density, isotope and magnetic field dependence is mainly introduced due to the heuristic condition of the Ryter-Schmidtmayr scaling (equation 4.10) and the current dependence of P_{LH} enters via the L-mode confinement time scaling (equation 4.11). Despite the success of this formula (equation 4.19), it fails to predict the torque dependence, the plasma shape dependence and the magnetic configuration dependence of P_{LH}. Thus, better models are needed to predict P_{LH} in future devices, since the operational point and the size of a tokamak reactor depends very sensitively on P_{LH} [166]. Two essential ingredients are required for a successful prediction of P_{LH} as the discussion in chapter 4 has revealed: the prediction of L-mode transport and the prediction or explanation of the critical velocity (shear) as observed in the experiments. In principle, edge turbulence codes should be able to provide this information, but failed in the past to reproduce the turbulence suppression in the relevant parameter range or the models were lacking realistic geometry, gradients and fluctuation levels. Recent developments of turbulence codes (XGC [378], GRILLIX [371] and GENE-X [55], however, raise hope, that a comprehensive understanding of the L-H transition might be available in the near future.

Filamentary structures (category d) in the SOL as described in section 2.4 originate either from (peeling-)ballooning instabilities or other MHD instabilities as in the case of ELMs or are result of turbulent processes as for PREs and blobs. The high transient heat fluxes on PFCs associated with type-I ELMs and their unfavorable scaling to larger machines require to mitigate them in a tokamak reactor [116]. Therefore, the development of ELM-free plasma scenarios is an important and strong research activity at tokamaks worldwide to support scenario developments for DEMO [437]. Although PREs are typically smaller than type-I ELMs, they might still transfer too much energy to PFCs in a reactor, similar to ELMs [120]. While ELMs and PREs most probably must be mitigated in a reactor, the role of blobs,

which appear in all plasma regimes, is still open. As described in chapter 3, the observed blob sizes and radial blob velocities are well understood at low densities. It was found that the ion temperature in the SOL is a key ingredient to achieve reasonable agreement with analytical blob scaling laws. Above a certain threshold of density, the blob associated transport suddenly increases. This increase of the perpendicular convective particle transport is accompanied by a shoulder formation in time-averaged density profiles in the SOL. This process is qualitatively understood and might be related to high collisionality along the magnetic field line, but the blob dynamics and especially the blob transport levels cannot be predicted yet. Since a reactor must be operated at relatively high edge density in order to keep the divertor detached, a density shoulder accompanied by continuous ejection of blob filaments might be a very likely feature of reactor plasmas. This regime is favorable to minimize the heat loads onto PFCs in the divertor due to its strong perpendicular transport and high densities facilitating divertor detachment. On the other hand, the increased blob transport in this regime induces higher particle and heat fluxes to first wall material in the main chamber. The heat fluxes are probably not a concern, since blobs are relatively cold until they reach the wall. But the blob-induced erosion levels on PFCs outside the divertor are a potential concern. Based on measured data in AUG, the extrapolated erosion levels in a reactor might be substantial, if finite impurity concentrations are present in the SOL as it is likely the case due to application of impurity seeding for divertor detachment purposes. In this case, the background plasma likewise contributes to large erosion levels and the role of blobs is subdominant. But in case that the sheath potential at PFCs is reduced e.g. due to secondary emission of electrons, blobs are the dominant erosion process. This indicates that the interplay of blobs with the effects of low-Z impurities and secondary electron emission have to be taken into account for a quantitative prediction of wall erosion and the assessment of the role of blobs in a future fusion reactor.

The temporal structures (category e), i.e. regular oscillations or wobbling of edge parameters between two (or more) states are outnumbering the types of structures of other categories by far. Some of them appear on smallest time scales of about 1 µs (HFOs), and other oscillations involve time scales of the order of seconds (e.g. dithering transitions). The remaining oscillations appear on time scales between them. The waveforms of measured plasma quantities during the appearance of temporal structures can be almost perfect sinusoids as in the case of the QCM, square waves as e.g. the D_α signal of the inner divertor during divertor oscillations, non-sinusoidal but regular oscillations as during LCOs or mixtures of all of them as in dithering transitions. The understanding of these temporal structures could potentially

support the operation of a burning fusion plasma in at least two ways. First, temporal structures might play a role due to their potential ability to keep the edge plasma below the peeling-ballooning stability boundary in order to avoid harmful ELMs by providing additional transport at the right place at the edge. Only a thorough understanding and control of edge oscillations like WCMs, QCMs or EHOs will allow to develop a suitable ELM-free regime in a tokamak fusion reactor. Second, the presence of some of the structures can help to identify certain states of the plasma. As an example, the fluctuation state in the divertor indicates closeness to divertor detachment and represents a reliable indicator serving the control system to initiate countermeasures to push the SOL plasma back into deeper detachment states. Similarly, the characteristic frequency, harmonics in the spectrogram of fast signals and the magnetic structure of LCOs as presented in chapter 5 allow to judge how close the operational point of the plasma is to the L-H power threshold. This might help to keep the operational point in H-mode and to avoid an uncontrolled back transition to L-mode. Furthermore, the precursor activity of LCO bursts, which are considered to be identical to type-III ELM precursors as argued in chapter 5, are an additional unique feature indicating that the H-mode plasma is close to the H-L back transition allowing for countermeasures against an uncontrolled back transition to L-mode [403].

Overall, the experimental characterization is well advanced for some of the structures presented at the plasma edge. But as indicated in table 2.1, the perturbation amplitudes of some structures, in particular the electrostatic potential perturbations, are not satisfactorily determined yet. In addition, a few further properties like the radial localization, the cross-phase between different measurement quantities and the perpendicular wavenumber are missing for most of the edge structures. This hampers a profound comparison with theoretical models as well as a unique identification of the underlying physical mechanism, which gives rise to the respective structure. Therefore, better plasma edge diagnostics are required to measure the missing quantities. A new diagnostic concept, the imaging heavy ion beam probe (i-HIBP), enabling measurements of perturbations of density and magnetic field with desirable good spatial and temporal resolution in two dimensions, and exhibiting the unique feature of measuring the electrostatic potential in the confined region was presented in chapter 6. The measurement of first signals on the scintillator detector of this diagnostic at AUG proved that the basic principle of the concept works. The signal levels are in the same order of magnitude as predicted by numerical modeling of the involved ionization and attenuation processes. Furthermore, the vertical intensity pattern on the scintillator corresponds to the simulation results, so that a reconstruction of edge density profiles based on the scintillator pattern might be possible. The

clear signatures of filaments propagating radially outward and generating a vertical movement of local intensity maxima on the scintillator pattern demonstrates that the i-HIBP can be used for detection and characterization of blobs or other filamentary structures. Although first indications of a strikeline displacement have been found at the boundaries of the scintillator pattern during a plasma current ramp and related to filament activity, the envisaged strikeline displacements due to magnetic field or electrostatic potential perturbations have not been measured yet. This was due to unsuccessful collimation of the neutral primary beam during the relevant plasma phases most probably caused by the stray magnetic fields of the tokamak, so that a small beam diameter could not be achieved, which is needed to resolve small beam displacements on the scintillator. These obstacles are of technical nature and can be solved in principle. Therefore, strategies to overcome these obstacles are initiated and plans for an upgrade of the i-HIBP diagnostic guided by comprehensive numerical modeling with i-HIBPsim are developed in order to enable magnetic field and electrostatic potential perturbations in future experimental campaigns at AUG.

As indicated in the last column of table 2.1, some of the plasma edge structures lacking a quantitative theoretical description. For some of the structures as it is the case for HFOs or the fluctuation state in the divertor it does not even exist an idea, what type of physical model has to be used to describe the observations. In other words, also on the theoretical side a lot of work is required to understand the underlying physical mechanisms of the presented plasma edge structures. Urgently needed is a theoretical model describing correctly the turbulence at the plasma edge. Availability of such a model would enable the correct prediction of transport levels at the edge, which are important to predict the overall performance of a fusion plasma. Furthermore, it is needed to predict the L-H transition power P_{LH}, and could potentially give an explanation under what conditions the turbulence is suppressed to achieve H-mode. A good turbulence model would most likely be able to produce many of the temporal structures like QCMs, WCMs, SAOs, LCOs, dithering transitions, but also blobs and PREs, since all of them are believed to result from turbulent processes. The fact that the existing turbulence models are not fully successful yet in delivering quantitative predictions, indicates that the models were not sufficiently comprehensive due to a lack of realistic plasma shapes, neoclassical effects, unsatisfactory plasma sheath models and neutral particle physics, or they did not appropriately deal with steep gradients and large fluctuation amplitudes. Hopefully, this thesis can contribute to help guiding further developments of theoretical models and indicate where the most urgent needs exist from the perspective of experimental physicists.

The self-organized formation of structures at the edge of high temperature plasmas involve fascinating and multifaceted physical processes and are worth to be studied on its own. But at the same time, the understanding of these structures and the prediction of their properties in a future tokamak reactor might be crucial to realize controlled fusion energy sources on earth.

Appendix A

Drift Motion in Magnetized Plasmas

Electric fields, gravitation or inhomogeneities of the magnetic field strength or pressure can lead to drift motions [6] of particles with charge q and mass m.

A.1 Particle Drifts

Drifts relevant for single particles in a magnetic field:

A.1.1 Gravitational Drift

A gravitional force represented by a vector $\mathbf{g}$ leads to the gravitational drift

$$\mathbf{v}_{\mathrm{g}} = \frac{m\mathbf{g} \times \mathbf{B}}{qB^2}. \tag{A.1}$$

In laboratory experiments on earth this drift is usually negligibly small.

A.1.2 $E \times B$ Drift

An electric field $\mathbf{E}$ leads to the $E \times B$ drift

$$\mathbf{v}_{\mathrm{E}} = \frac{\mathbf{E} \times \mathbf{B}}{B^2}. \tag{A.2}$$

This is the only drift, which does not depend on the charge q and does therefore not giving rise to an electric current.

A.1.3 Curvature Drift

A curved magnetic field with curvature vector $\boldsymbol{\kappa} = -\mathbf{R}_k/R_k^2$ and curvature radius $\mathbf{R}_k$ leads to the curvature drift

$$\mathbf{v}_\kappa = \frac{2W_{||}}{qR_k^2}\frac{\mathbf{R}_k \times \mathbf{B}}{B^2}. \tag{A.3}$$

This drift depends on the parallel energy of the particle $W_{||}$.

A.1.4 ∇B Drift

A magnetic field with inhomogeneous magnetic field strength perpendicular to the magnetic field direction represented by a gradient $\nabla_\perp B$ leads to the ∇B drift

$$\mathbf{v}_{\nabla \mathrm{B}} = -\frac{W_\perp}{q}\frac{\nabla_\perp B \times \mathbf{B}}{B^3}. \tag{A.4}$$

This drift depends on the perpendicular energy of the particle $W_\perp$.

A.1.5 Generalized Magnetic Field Drift

Due to the relation $\mathbf{R}_k/R_k^2 = -\nabla_\perp B/B$ we can unify the curvature and ∇B drift to one expression

$$\mathbf{v}_\mathrm{D} = \mathbf{v}_\kappa + \mathbf{v}_{\nabla \mathrm{B}} = -\left(W_\perp + 2W_{||}\right)\frac{\nabla_\perp B \times \mathbf{B}}{qB^3} \tag{A.5}$$

$$= \left(W_\perp + 2W_{||}\right)\frac{\mathbf{R}_k \times \mathbf{B}}{qR_k^2 B^2}. \tag{A.6}$$

This expression is only valid if there is no current involved in the magnetic field generation.

A.1.6 Polarization Drift

A time varying electric field $\dot{\mathbf{E}}$ leads to the polarization drift

$$\mathbf{v}_\mathrm{pol} = \frac{m}{qB^2}\dot{\mathbf{E}}. \tag{A.7}$$

A.2 Fluid drifts

It can be shown by means of the fluid description of the plasma, that the gravitational drift, the $E \times B$ drift and the polarization drift likewise act on fluid elements. However, the curvature and the ∇B drift do not exist in fluids. Instead, the diamagnetic drift describes the dynamics in inhomogeneous field configurations.

A.2.1 Diamagnetic Drift

A pressure gradient perpendicular to the magnetic field, $\nabla_\perp p$ gives rise to the diamagnetic drift

$$\mathbf{v}_{\mathrm{dia}} = -\frac{\nabla_\perp p \times \mathbf{B}}{\rho B^2} \tag{A.8}$$

acting on a fluid element with charge density $\rho = qn$. The diamagnetic drift leads to diamagnetic currents, which reads in hydrogen plasmas with $n = n_{\mathrm{i}} = n_{\mathrm{e}}$

$$\mathbf{j}_{\mathrm{dia}} = +en_{\mathrm{i}}\mathbf{v}_{\mathrm{dia,i}} - en_{\mathrm{e}}\mathbf{v}_{\mathrm{dia,e}} = -\frac{\nabla_\perp p \times \mathbf{B}}{B^2}. \tag{A.9}$$

Bibliography

[1] C. S. Mattick, E. Williams, and B. R. Allenby, 2009 IEEE International Symposium on Sustainable Systems and Technology, ISSST '09 in Cooperation with 2009 IEEE International Symposium on Technology and Society, ISTAS doi:10.1109/ISSST.2009.5156766 1.1

[2] C. McGlade and P. Ekins, Nature 2015 517:7533 **517** (2015) 187–190, ISSN 1476-4687, doi:10.1038/nature14016, URL `https://www.nature.com/articles/nature14016` 1.1

[3] H. Poertner, D. Roberts, M. Tignor *et al.*, *IPCC, 2022: Climate Change 2022: Impacts, Adaptation and Vulnerability. Contribution of Working Group II to the Sixth Assessment Report of the Intergovernmental Panel on Climate Change* (2022), URL `https://www.ipcc.ch/report/ar6/wg2/` 1.1

[4] A. J. H. Donné, Philosophical Transactions of the Royal Society A: Mathematical, Physical and Engineering Sciences **377** (2019) 20170432, ISSN 1364-503X, doi:10.1098/rsta.2017.0432, URL `https://royalsocietypublishing.org/doi/10.1098/rsta.2017.0432` 1.1

[5] J. Wesson, *Tokamaks*, Oxford University Press, 4th edition (2011), ISBN 0199592233 1.1, 1.1, 1.1, 1.2, 1.3, 2.2.2, 4.3.4, 5.1.4

[6] F. F. Chen, *Introduction to Plasma Physics and Controlled Fusion*, Springer, 3rd edition (2015), ISBN 9783319223087 1.1, 1.1, 1.3, 2.1.1, 2, 3.2.3, 4.3.4, A

[7] M. Shimada, D. Campbell, V. Mukhovatov *et al.*, Nuclear Fusion **47** (2007) S1–S17, ISSN 0029-5515, doi:10.1088/0029-5515/47/6/S01, URL `https://iopscience.iop.org/article/10.1088/0029-5515/47/6/S01` 1.1, 1.2, 3.7.3, 4.1.1, 7

[8] H. Abu-Shawareb, R. Acree, P. Adams *et al.*, Physical Review Letters **129** (2022) 075001, ISSN 0031-9007,

doi:10.1103/PhysRevLett.129.075001, URL https://link.aps.org/doi/10.1103/PhysRevLett.129.075001 1.1

[9] D. Clery, Science **375** (2022) 600–600, ISSN 0036-8075, doi:10.1126/science.ada1089, URL https://www.science.org/doi/10.1126/science.ada1089 1.1

[10] EUROfusion, *European researchers achieve fusion energy record* (2022), URL https://www.euro-fusion.org/news/2022/european-researchers-achieve-fusion-energy-record/ 1.1

[11] C. Braams and P. Stott, *Nuclear Fusion: Half a Century of Magnetic Confinement Fusion Research*, Taylor and Francis Ltd (2002), ISBN 9780750307055 1.2, 1.2

[12] M. Wakatani, *Stellarator and Heliotron Devices*, Oxford University Press (1998), ISBN 0195078314 1.2

[13] A. H. Boozer, Nuclear Fusion **61** (2021) 096024, ISSN 0029-5515, doi:10.1088/1741-4326/ac170f, URL https://iopscience.iop.org/article/10.1088/1741-4326/ac170f 1.2

[14] D. Gates, A. Boozer, T. Brown *et al.*, Nuclear Fusion **57** (2017) 126064, ISSN 0029-5515, doi:10.1088/1741-4326/aa8ba0, URL https://iopscience.iop.org/article/10.1088/1741-4326/aa8ba0 1.2

[15] A. H. Boozer, Nuclear Fusion **60** (2020) 065001, ISSN 0029-5515, doi:10.1088/1741-4326/ab87af, URL https://iopscience.iop.org/article/10.1088/1741-4326/ab87af 1.2

[16] T. S. Pedersen, I. Abramovic, P. Agostinetti *et al.*, Nuclear Fusion **62** (2022) 042022, ISSN 0029-5515, doi:10.1088/1741-4326/ac2cf5, URL https://iopscience.iop.org/article/10.1088/1741-4326/ac2cf5 1.2

[17] B. N. Breizman, P. Aleynikov, E. M. Hollmann *et al.*, Nuclear Fusion **59** (2019) 083001, ISSN 0029-5515, doi:10.1088/1741-4326/ab1822, URL https://iopscience.iop.org/article/10.1088/1741-4326/ab1822 1.2

[18] N. W. Eidietis, Fusion Science and Technology **77** (2021) 738–744, doi:10.1080/15361055.2021.1889919, URL https://www.tandfonline.com/action/journalInformation?journalCode=ufst20 1.2

[19] S.-H. Hong, AAPPS Bulletin **32** (2022) 10, ISSN 2309-4710, doi:10.1007/s43673-022-00040-9, URL https://link.springer.com/10.1007/s43673-022-00040-9 1.2, 2.3.1, 2.3.2, 2.3.3

[20] P. C. Stangeby, *The Plasma Boundary of Magnetic Fusion Devices*, Institute of Physics, 1st edition (2002), ISBN 978-0750305594 1.3, 2, 3.2.2, 3.2.3, 3.2.3, 3.7, 3.7

[21] P. C. Stangeby, Plasma Physics and Controlled Fusion **42** (2000) B271–B291, ISSN 0741-3335, doi:10.1088/0741-3335/42/12B/321, URL https://iopscience.iop.org/article/10.1088/0741-3335/42/12B/321 1.3

[22] H. Zohm, *Magnetohydrodynamic Stability of Tokamaks*, Wiley-VCH, 1st edition (2014), ISBN 978-3527412327 1.3, 1.4, 2.2.1, 3.1, 4.4.3

[23] P. Mantica, C. Angioni, N. Bonanomi *et al.*, Plasma Physics and Controlled Fusion **62** (2020) 014021, ISSN 0741-3335, doi:10.1088/1361-6587/ab5ae1, URL https://iopscience.iop.org/article/10.1088/1361-6587/ab5ae1 1.3, 1.4

[24] A. W. Leonard, Physics of Plasmas **21** (2014) 090501, ISSN 1070-664X, doi:10.1063/1.4894742, URL https://aip.scitation.org/doi/abs/10.1063/1.4894742 1.3, 2.2.1, 2.3.1, 2.4.2, 2.4.2

[25] H. Meyer, T. Eich, M. Beurskens *et al.*, Nuclear Fusion **57** (2017) 102014, ISSN 0029-5515, doi:10.1088/1741-4326/aa6084, URL https://iopscience.iop.org/article/10.1088/1741-4326/aa6084 1.3, 1.4

[26] M. C. Cross and P. C. Hohenberg, Reviews of Modern Physics **65** (1993) 851, ISSN 00346861, doi:10.1103/RevModPhys.65.851, URL https://journals.aps.org/rmp/abstract/10.1103/RevModPhys.65.851 1.4

[27] P. A. Milewski and J. B. Keller, Studies in Applied Mathematics **97** (1996) 149–166, ISSN 00222526, doi:10.1002/sapm1996972149, URL https://onlinelibrary.wiley.com/doi/10.1002/sapm1996972149 1.4

[28] P. Davidson, *Turbulence: An Introduction for Scientists and Engineers*, Oxford University Press, 2nd edition (2015), ISBN 978-0198722595 1.4, 2.1.3

[29] S. S. Chen, J. F. Price, W. Zhao *et al.*, Bulletin of the American Meteorological Society pages 311–317, URL https://www.jstor.org/stable/26217257 1.4, 2.1.3

[30] L. Kulowski, H. Cao, R. K. Yadav *et al.*, Journal of Geophysical Research: Planets **126** (2021) e2020JE006795, ISSN 2169-9100, doi:10.1029/2020JE006795, URL https://onlinelibrary.wiley.com/doi/full/10.1029/2020JE006795https://onlinelibrary.wiley.com/doi/abs/10.1029/2020JE006795https://agupubs.onlinelibrary.wiley.com/doi/10.1029/2020JE006795 1.4, 2.1.3

[31] K. J. Richards, N. A. Maximenko, F. O. Bryan *et al.*, Geophysical Research Letters **33** (2006) 3605, ISSN 1944-8007, doi:10.1029/2005GL024645, URL https://onlinelibrary.wiley.com/doi/full/10.1029/2005GL024645https://onlinelibrary.wiley.com/doi/abs/10.1029/2005GL024645https://agupubs.onlinelibrary.wiley.com/doi/10.1029/2005GL024645 1.4, 2.1.3

[32] C. Domb and J. Lebowitz, *Phase Transitions and Critical Phenomena*, Academic Press, 1st edition (2000), ISBN 9780080538754 1.4, 2.3

[33] A. Erbach, F. Lutscher, and G. Seo, Ecological Complexity **14** (2013) 48–55, ISSN 1476945X, doi:10.1016/j.ecocom.2013.02.005, URL https://linkinghub.elsevier.com/retrieve/pii/S1476945X13000287 1.4

[34] G. Feichtinger, Annals of Operations Research 1992 37:1 **37** (1992) 313–344, ISSN 1572-9338, doi:10.1007/BF02071063, URL https://link.springer.com/article/10.1007/BF02071063 1.4

[35] X. Garbet, P. Mantica, C. Angioni *et al.*, Plasma Physics and Controlled Fusion **46** (2004) B557, ISSN 0741-3335, doi:10.1088/0741-3335/46/12B/045, URL https://iopscience.iop.org/article/10.1088/0741-3335/46/12B/045https://iopscience.iop.org/article/10.1088/0741-3335/46/12B/045/meta 1.4

[36] F. L. Hinton and R. D. Hazeltine, Reviews of Modern Physics **48** (1976) 239, ISSN 00346861, doi:10.1103/RevModPhys.48.239, URL https://journals.aps.org/rmp/abstract/10.1103/RevModPhys.48.239 1.4, 2.1.2, 2.1.2, 2.2

[37] U. Stroth, P. Manz, and M. Ramisch, Plasma Physics and Controlled Fusion **53** (2011) 024006, ISSN 0741-3335, doi:10.1088/0741-

3335/53/2/024006, URL https://iopscience.iop.org/article/10.1088/0741-3335/53/2/024006 1.4, 2.1.1, 2.1.2, 2.1.3

[38] P. H. Diamond, S.-I. Itoh, K. Itoh *et al.*, Plasma Physics and Controlled Fusion **47** (2005) R35–R161, ISSN 0741-3335, doi:10.1088/0741-3335/47/5/R01, URL https://iopscience.iop.org/article/10.1088/0741-3335/47/5/R01 1.4, 2.1.3, 2.1.3, 5.1.4

[39] D. A. D'Ippolito, J. R. Myra, and S. J. Zweben, Physics of Plasmas **18** (2011) 060501, ISSN 1070-664X, doi:10.1063/1.3594609, URL http://aip.scitation.org/doi/10.1063/1.3594609 1.4, 2.4.1, 4, 3.2, 3.5.2

[40] T. Pütterich, R. Dux, M. Janzer *et al.*, Journal of Nuclear Materials **415** (2011) S334–S339, ISSN 00223115, doi:10.1016/j.jnucmat.2010.09.052, URL https://linkinghub.elsevier.com/retrieve/pii/S0022311510005623 1.4

[41] R. Goldston, *Introduction to Plasma Physics*, Taylor and Francis (1995), ISBN 978-0750301831 2.1.1, 4.3.1

[42] P. Helander and D. J. Sigmar, *Collisional Transport in Magnetized Plasmas*, Cambridge University Press (2011), ISBN 9780521807982 2.1.2

[43] A. G. Peeters, Physics of Plasmas **7** (2000) 268–275, ISSN 1070-664X, doi:10.1063/1.873812, URL http://aip.scitation.org/doi/10.1063/1.873812 2.1.2, 2.2

[44] E. A. Belli and J. Candy, Plasma Physics and Controlled Fusion **50** (2008) 095010, ISSN 0741-3335, doi:10.1088/0741-3335/50/9/095010, URL https://iopscience.iop.org/article/10.1088/0741-3335/50/9/095010 2.1.2

[45] L. M. Shao, E. Wolfrum, F. Ryter *et al.*, Plasma Physics and Controlled Fusion **58** (2016) 025004, ISSN 0741-3335, doi:10.1088/0741-3335/58/2/025004, URL https://iopscience.iop.org/article/10.1088/0741-3335/58/2/025004 2.1.2, 4.1.1, 4.1.4, 4.3.2, 4.3.3

[46] P. Sauter, T. Pütterich, F. Ryter *et al.*, Nuclear Fusion **52** (2012) 012001, ISSN 0029-5515, doi:10.1088/0029-5515/52/1/012001, URL https://iopscience.iop.org/article/10.1088/0029-5515/52/1/012001 2.1.2, 4.2.4, 4.3.3

[47] F. Ryter, S. Rathgeber, L. B. Orte *et al.*, Nuclear Fusion **53** (2013) 113003, ISSN 0029-5515, doi:10.1088/0029-5515/53/11/113003, URL https://iopscience.iop.org/article/10.1088/0029-5515/53/11/113003 2.1.2, 2.14, 4.1.1, 4.1, 4.1.1, 4.5, 4.1.4, 4.7, 4.9, 4.2.4, 4.2.4, 5.4, 5.1.1

[48] E. Viezzer, T. Pütterich, G. Conway *et al.*, Nuclear Fusion **53** (2013) 053005, ISSN 0029-5515, doi:10.1088/0029-5515/53/5/053005, URL https://iopscience.iop.org/article/10.1088/0029-5515/53/5/053005 2.1.2, 2.3.1, 2.3.3

[49] E. Viezzer, T. Pütterich, C. Angioni *et al.*, Nuclear Fusion **54** (2014) 012003, ISSN 0029-5515, doi:10.1088/0029-5515/54/1/012003, URL https://iopscience.iop.org/article/10.1088/0029-5515/54/1/012003 2.1.2, 2.2, 4.2.4, 5.1.4

[50] E. Viezzer, T. Pütterich, R. M. McDermott *et al.*, Plasma Physics and Controlled Fusion **56** (2014) 075018, ISSN 0741-3335, doi:10.1088/0741-3335/56/7/075018, URL https://iopscience.iop.org/article/10.1088/0741-3335/56/7/075018 2.1.2

[51] M. Cavedon, T. Pütterich, E. Viezzer *et al.*, Nuclear Fusion **57** (2017) 014002, ISSN 0029-5515, doi:10.1088/0029-5515/57/1/014002, URL https://iopscience.iop.org/article/10.1088/0029-5515/57/1/014002 2.1.2, 2.5.4, 4.2.4, 4.4.1, 5.13, 5.2.1

[52] R. M. McDermott, B. Lipschultz, J. W. Hughes *et al.*, Physics of Plasmas **16** (2009) 056103, ISSN 1070-664X, doi:10.1063/1.3080721, URL https://aip.scitation.org/doi/abs/10.1063/1.3080721 2.1.2

[53] P. Gohil, K. Burrell, and T. Carlstrom, Nuclear Fusion **38** (1998) 93–102, ISSN 0029-5515, doi:10.1088/0029-5515/38/1/308, URL https://iopscience.iop.org/article/10.1088/0029-5515/38/1/308 2.1.2

[54] K. Kamiya, M. Honda, N. Miyato *et al.*, Nuclear Fusion **52** (2012) 114010, ISSN 0029-5515, doi:10.1088/0029-5515/52/11/114010, URL https://iopscience.iop.org/article/10.1088/0029-5515/52/11/114010 2.1.2

[55] D. Michels, P. Ulbl, W. Zholobenko *et al.*, Physics of Plasmas **29** (2022) 032307, ISSN 1070-664X, doi:10.1063/5.0082413, URL https://aip.scitation.org/doi/10.1063/5.0082413 2.1.3, 2.3, 4.3.4, 4.5, 7

[56] V. Grandgirard, Y. Sarazin, X. Garbet *et al.*, Communications in Nonlinear Science and Numerical Simulation **13** (2008) 81–87, ISSN 10075704, doi:10.1016/j.cnsns.2007.05.016, URL https://linkinghub.elsevier.com/retrieve/pii/S1007570407001220 2.1.3

[57] A. G. Peeters, F. Rath, R. Buchholz *et al.*, Physics of Plasmas **23** (2016) 082517, ISSN 1070-664X, doi:10.1063/1.4961231, URL http://aip.scitation.org/doi/10.1063/1.4961231 2.1.3

[58] L. Villard, S. Allfrey, A. Bottino *et al.*, Nuclear Fusion **44** (2004) 172–180, ISSN 0029-5515, doi:10.1088/0029-5515/44/1/019, URL https://iopscience.iop.org/article/10.1088/0029-5515/44/1/019 2.1.3

[59] N. Howard, C. Holland, A. White *et al.*, Nuclear Fusion **56** (2016) 014004, ISSN 0029-5515, doi:10.1088/0029-5515/56/1/014004, URL https://iopscience.iop.org/article/10.1088/0029-5515/56/1/014004 2.1.3

[60] R. H. Kraichnan, Physics of Fluids **10** (1967) 1417, ISSN 00319171, doi:10.1063/1.1762301, URL https://aip.scitation.org/doi/10.1063/1.1762301 2.1.3

[61] R. H. Kraichnan and D. Montgomery, Reports on Progress in Physics **43** (1980) 547–619, ISSN 0034-4885, doi:10.1088/0034-4885/43/5/001, URL https://iopscience.iop.org/article/10.1088/0034-4885/43/5/001 2.1.3

[62] P. Manz, M. Ramisch, and U. Stroth, Plasma Physics and Controlled Fusion **51** (2009) 035008, ISSN 0741-3335, doi:10.1088/0741-3335/51/3/035008, URL https://iopscience.iop.org/article/10.1088/0741-3335/51/3/035008 2.1.3, 2.1.3

[63] P. Manz, M. Ramisch, and U. Stroth, Physical Review Letters **103** (2009) 165004, ISSN 00319007, doi:10.1103/PHYSREVLETT.103.165004/FIGURES/3/MEDIUM, URL https://journals.aps.org/prl/abstract/10.1103/PhysRevLett.103.165004 2.1.3, 2.1.3, 4.16, 4.3.4

[64] P. Manz, M. Xu, N. Fedorczak *et al.*, Physics of Plasmas **19** (2012) 012309, ISSN 1070-664X, doi:10.1063/1.3676634, URL http://aip.scitation.org/doi/10.1063/1.3676634 2.1.3

[65] O. D. Gürcan, P. H. Diamond, P. Hennequin *et al.*, Physics of Plasmas **17** (2010) 112309, ISSN 1070-664X, doi:10.1063/1.3503624, URL `http://aip.scitation.org/doi/10.1063/1.3503624` 2.1.3

[66] E. jin Kim and P. H. Diamond, Physics of Plasmas **9** (2002) 4530–4539, ISSN 1070-664X, doi:10.1063/1.1514641, URL `http://aip.scitation.org/doi/10.1063/1.1514641` 2.1.3

[67] Z. Lin, T. S. Hahm, W. W. Lee *et al.*, Physical Review Letters **83** (1999) 3645–3648, ISSN 0031-9007, doi:10.1103/PhysRevLett.83.3645, URL `https://link.aps.org/doi/10.1103/PhysRevLett.83.3645` 2.1.3, 5.1.4

[68] B. D. Scott, New Journal of Physics **7** (2005) 92–92, ISSN 1367-2630, doi:10.1088/1367-2630/7/1/092, URL `https://iopscience.iop.org/article/10.1088/1367-2630/7/1/092` 2.1.3, 5.2.2

[69] V. Naulin, A. Kendl, O. E. Garcia *et al.*, Physics of Plasmas **12** (2005) 052515, ISSN 1070-664X, doi:10.1063/1.1905603, URL `http://aip.scitation.org/doi/10.1063/1.1905603` 2.1.3

[70] A. Kendl and B. D. Scott, Physics of Plasmas **12** (2005) 064506, ISSN 1070-664X, doi:10.1063/1.1938147, URL `http://aip.scitation.org/doi/10.1063/1.1938147` 2.1.3

[71] J. B. Parker and J. A. Krommes, Physics of Plasmas **20** (2013) 100703, ISSN 1070-664X, doi:10.1063/1.4828717, URL `http://aip.scitation.org/doi/10.1063/1.4828717` 2.1.3

[72] G. D. Conway, B. Scott, J. Schirmer *et al.*, Plasma Physics and Controlled Fusion **47** (2005) 1165–1185, ISSN 0741-3335, doi:10.1088/0741-3335/47/8/003, URL `https://iopscience.iop.org/article/10.1088/0741-3335/47/8/003` 2.1.3, 5.1.1, 5.1.5

[73] A. Fujisawa, Nuclear Fusion **49** (2009) 013001, ISSN 0029-5515, doi:10.1088/0029-5515/49/1/013001, URL `https://iopscience.iop.org/article/10.1088/0029-5515/49/1/013001` 2.1.3

[74] P. Manz, G. S. Xu, B. N. Wan *et al.*, Physics of Plasmas **19** (2012) 072311, ISSN 1070-664X, doi:10.1063/1.4737612, URL `http://aip.scitation.org/doi/10.1063/1.4737612` 2.1.3, 4.4.1, 5.2.1

[75] G. Birkenmeier, M. Ramisch, B. Schmid *et al.*, Physical Review Letters **110** (2013) 145004, ISSN 0031-9007,

doi:10.1103/PhysRevLett.110.145004, URL https://link.aps.org/doi/10.1103/PhysRevLett.110.145004 2.1.3

[76] P. Manz, M. Ramisch, and U. Stroth, Physical Review E - Statistical, Nonlinear, and Soft Matter Physics **82** (2010) 056403, ISSN 15393755, doi:10.1103/PHYSREVE.82.056403/FIGURES/6/MEDIUM, URL https://journals.aps.org/pre/abstract/10.1103/PhysRevE.82.056403 2.1.3

[77] A. Schmid, A. Herrmann, and H. W. Müller, Plasma Physics and Controlled Fusion **50** (2008) 045007, ISSN 0741-3335, doi:10.1088/0741-3335/50/4/045007, URL https://iopscience.iop.org/article/10.1088/0741-3335/50/4/045007 2.1.3

[78] C. Hidalgo, M. A. Pedrosa, C. Silva *et al.*, EPL (Europhysics Letters) **87** (2009) 55002, ISSN 0295-5075, doi:10.1209/0295-5075/87/55002, URL https://iopscience.iop.org/article/10.1209/0295-5075/87/55002 2.1.3

[79] B. Schmid, P. Manz, M. Ramisch *et al.*, Physical review letters **118** (2017) 055001, ISSN 1079-7114, doi:10.1103/PhysRevLett.118.055001, URL http://www.ncbi.nlm.nih.gov/pubmed/28211703 2.1.3

[80] T. Ullmann, B. Schmid, P. Manz *et al.*, Physics of Plasmas **28** (2021) 052502, ISSN 1070-664X, doi:10.1063/5.0039959, URL https://aip.scitation.org/doi/10.1063/5.0039959 2.1.3

[81] J. Hillesheim, E. Delabie, H. Meyer *et al.*, Physical Review Letters **116** (2016) 065002, ISSN 0031-9007, doi:10.1103/PhysRevLett.116.065002, URL https://link.aps.org/doi/10.1103/PhysRevLett.116.065002 2.1.3, 4.3.2

[82] N. Francois, H. Xia, H. Punzmann *et al.*, Physical Review Letters **110** (2013) 194501, ISSN 0031-9007, doi:10.1103/PhysRevLett.110.194501, URL https://link.aps.org/doi/10.1103/PhysRevLett.110.194501 2.1.3

[83] G. Conway, A. Smolyakov, and T. Ido, Nuclear Fusion **62** (2022) 013001, ISSN 0029-5515, doi:10.1088/1741-4326/ac0dd1, URL https://iopscience.iop.org/article/10.1088/1741-4326/ac0dd1 2.1.4, 2.1.4

[84] N. Winsor, Physics of Fluids **11** (1968) 2448, ISSN 00319171, doi:10.1063/1.1691835, URL https://aip.scitation.org/doi/10.1063/1.1691835 2.1.4

[85] G. Birkenmeier doi:http://dx.doi.org/10.18419/opus-1994, URL http://elib.uni-stuttgart.de/handle/11682/2011 2.1.4

[86] P. Simon, G. D. Conway, U. Stroth *et al.*, Plasma Physics and Controlled Fusion **58** (2016) 045029, ISSN 0741-3335, doi:10.1088/0741-3335/58/4/045029, URL https://iopscience.iop.org/article/10.1088/0741-3335/58/4/045029 2.1.4

[87] F. Palermo, E. Poli, A. Bottino *et al.*, Physics of Plasmas **24** (2017) 072503, ISSN 1070-664X, doi:10.1063/1.4990074, URL http://aip.scitation.org/doi/10.1063/1.4990074 2.1.4

[88] A. Kendl, Physics of Plasmas **18** (2011) 072303, ISSN 1070-664X, doi:10.1063/1.3603838, URL http://aip.scitation.org/doi/10.1063/1.3603838 2.1.4

[89] P. Simon URL http://elib.uni-stuttgart.de/handle/11682/9229 2.1.4

[90] Z. Qiu and L. Chen, Plasma Science and Technology **13** (2011) 257–266, ISSN 1009-0630, doi:10.1088/1009-0630/13/3/01, URL https://iopscience.iop.org/article/10.1088/1009-0630/13/3/01 2.1.4

[91] R. Nazikian, G. Y. Fu, M. E. Austin *et al.*, Physical Review Letters **101** (2008) 185001, ISSN 00319007, doi:10.1103/PHYSREVLETT.101.185001/FIGURES/4/MEDIUM, URL https://journals.aps.org/prl/abstract/10.1103/PhysRevLett.101.185001 2.1.4

[92] G. Dif-Pradalier, G. Hornung, P. Ghendrih *et al.*, Physical Review Letters **114** (2015) 085004, ISSN 0031-9007, doi:10.1103/PhysRevLett.114.085004, URL https://link.aps.org/doi/10.1103/PhysRevLett.114.085004 2.1.5

[93] G. Dif-Pradalier, G. Hornung, X. Garbet *et al.*, Nuclear Fusion **57** (2017) 066026, ISSN 0029-5515, doi:10.1088/1741-4326/aa6873, URL https://iopscience.iop.org/article/10.1088/1741-4326/aa6873 2.1.5, 2.7

[94] G. Hornung, G. Dif-Pradalier, F. Clairet *et al.*, Nuclear Fusion **57** (2017) 014006, ISSN 0029-5515, doi:10.1088/0029-5515/57/1/014006, URL https://iopscience.iop.org/article/10.1088/0029-5515/57/1/014006 2.1.5

[95] L. Qi, J.-M. Kwon, T. Hahm *et al.*, Nuclear Fusion **59** (2019) 026013, ISSN 0029-5515, doi:10.1088/1741-4326/aaf5fd, URL https://iopscience.iop.org/article/10.1088/1741-4326/aaf5fd 2.1.5

[96] L. Qi, M. Choi, J.-M. Kwon *et al.*, Nuclear Fusion **61** (2021) 026010, ISSN 0029-5515, doi:10.1088/1741-4326/abc976, URL https://iopscience.iop.org/article/10.1088/1741-4326/abc976 2.1.5

[97] O. Sauter, C. Angioni, and Y. R. Lin-Liu, Physics of Plasmas **6** (1999) 2834–2839, ISSN 1070-664X, doi:10.1063/1.873240, URL http://aip.scitation.org/doi/10.1063/1.873240 2.2.1, 2.2.1, 5.1.4, 5.1.4

[98] O. Sauter, C. Angioni, and Y. R. Lin-Liu, Physics of Plasmas **9** (2002) 5140–5140, ISSN 1070-664X, doi:10.1063/1.1517052, URL http://aip.scitation.org/doi/10.1063/1.1517052 2.2.1, 2.2.1

[99] R. Hager and C. S. Chang, Physics of Plasmas **23** (2016) 042503, ISSN 1070-664X, doi:10.1063/1.4945615, URL http://aip.scitation.org/doi/10.1063/1.4945615 2.2.1

[100] A. Redl, C. Angioni, E. Belli *et al.*, Physics of Plasmas **28** (2021) 022502, ISSN 1070-664X, doi:10.1063/5.0012664, URL https://aip.scitation.org/doi/10.1063/5.0012664 2.2.1

[101] A. G. Peeters, Plasma Physics and Controlled Fusion **42** (2000) B231–B242, ISSN 0741-3335, doi:10.1088/0741-3335/42/12B/318, URL https://iopscience.iop.org/article/10.1088/0741-3335/42/12B/318 2.2.1

[102] M. Reisner, E. Fable, J. Stober *et al.*, Nuclear Fusion **60** (2020) 082005, ISSN 0029-5515, doi:10.1088/1741-4326/ab8b32, URL https://iopscience.iop.org/article/10.1088/1741-4326/ab8b32 2.2.1

[103] M. Dunne, P. McCarthy, E. Wolfrum *et al.*, Nuclear Fusion **52** (2012) 123014, ISSN 0029-5515, doi:10.1088/0029-5515/52/12/123014, URL https://iopscience.iop.org/article/10.1088/0029-5515/52/12/123014 2.2.1, 6.3.1

[104] G. Harrer, M. Faitsch, L. Radovanovic *et al.*, Physical Review Letters **129** (2022) 165001, doi:10.1103/PhysRevLett.129.165001, URL https://journals.aps.org/prl/abstract/10.1103/PhysRevLett.129.165001?utm_source=email&utm_medium=email&utm_campaign=prl-alert 2.2.1, 2.3.1, 2.4.2, 2.5.6

[105] A. Kendl and B. D. Scott, Physical Review Letters **90** (2003) 035006, ISSN 0031-9007, doi:10.1103/PhysRevLett.90.035006, URL https://link.aps.org/doi/10.1103/PhysRevLett.90.035006 2.2.1

[106] P. Snyder, K. Burrell, H. Wilson *et al.*, Nuclear Fusion **47** (2007) 961–968, ISSN 0029-5515, doi:10.1088/0029-5515/47/8/030, URL https://iopscience.iop.org/article/10.1088/0029-5515/47/8/030 2.2.1, 2.3.1, 2.5.8

[107] T. Hahm, D. Na, J. Lee *et al.*, Nuclear Fusion **53** (2013) 093005, ISSN 0029-5515, doi:10.1088/0029-5515/53/9/093005, URL https://iopscience.iop.org/article/10.1088/0029-5515/53/9/093005 2.2.1, 4.3.4, 7

[108] F. Wagner, G. Becker, K. Behringer *et al.*, Physical Review Letters **49** (1982) 1408, ISSN 00319007, doi:10.1103/PhysRevLett.49.1408, URL https://journals.aps.org/prl/abstract/10.1103/PhysRevLett.49.1408 2.3.1, 4.5, 7

[109] F. Wagner, The European Physical Journal H **43** (2018) 523–549, ISSN 2102-6459, doi:10.1140/epjh/e2016-70064-9, URL http://link.springer.com/10.1140/epjh/e2016-70064-9 2.3.1

[110] F. Wagner and S. Benkadda, AIP Conference Proceedings **1013** (2008) 143–165, ISSN 0094243X, doi:10.1063/1.2939028, URL http://aip.scitation.org/doi/abs/10.1063/1.2939028 2.3.1

[111] P. Schneider doi:10.5282/edoc.14723, URL https://edoc.ub.uni-muenchen.de/14723/1/Schneider_Philip.pdf 2.10

[112] J. Schirmer, G. Conway, H. Zohm *et al.*, Nuclear Fusion **46** (2006) S780–S791, ISSN 0029-5515, doi:10.1088/0029-5515/46/9/S13, URL https://iopscience.iop.org/article/10.1088/0029-5515/46/9/S13 2.10

[113] K. H. Burrell, Physics of Plasmas **6** (1999) 4418–4435, ISSN 1070-664X, doi:10.1063/1.873728, URL http://aip.scitation.org/doi/10.1063/1.873728 2.3.1

[114] T. S. Hahm, Plasma Physics and Controlled Fusion **44** (2002) 305, ISSN 07413335, doi:10.1088/0741-3335/44/5A/305, URL https://iopscience.iop.org/article/10.1088/0741-3335/44/5A/305 2.3.1

[115] H. Zohm, Plasma Physics and Controlled Fusion **38** (1996) 105–128, ISSN 0741-3335, doi:10.1088/0741-3335/38/2/001, URL https://iopscience.iop.org/article/10.1088/0741-3335/38/2/001 2.3.1, 2.3.1, 2.4.2, 5.1.4, 5.2.3

[116] R. Wenninger, R. Albanese, R. Ambrosino *et al.*, Nuclear Fusion **57** (2017) 046002, ISSN 0029-5515, doi:10.1088/1741-4326/aa4fb4, URL https://iopscience.iop.org/article/10.1088/1741-4326/aa4fb4 2.3.1, 2.4.1, 2.4.2, 7

[117] F. Ryter, W. Suttrop, B. Brüsehaber *et al.*, Plasma Physics and Controlled Fusion **40** (1998) 725–729, ISSN 0741-3335, doi:10.1088/0741-3335/40/5/032, URL https://iopscience.iop.org/article/10.1088/0741-3335/40/5/032 2.3.1

[118] F. Ryter, R. Fischer, J. Fuchs *et al.*, Nuclear Fusion **57** (2017) 016004, ISSN 0029-5515, doi:10.1088/0029-5515/57/1/016004, URL https://iopscience.iop.org/article/10.1088/0029-5515/57/1/016004 2.3.1, 2.5.7, 4.1.3

[119] A. E. Hubbard, D. G. Whyte, R. M. Churchill *et al.*, Physics of Plasmas **18** (2011) 056115, ISSN 1070-664X, doi:10.1063/1.3582135, URL http://aip.scitation.org/doi/10.1063/1.3582135 2.11, 2.3.1, 2.5.7

[120] D. Silvagni, J. Terry, W. McCarthy *et al.*, Nuclear Fusion **62** (2022) 036004, ISSN 0029-5515, doi:10.1088/1741-4326/AC4296, URL https://iopscience.iop.org/article/10.1088/1741-4326/ac4296https://iopscience.iop.org/article/10.1088/1741-4326/ac4296/meta 2.3.1, 2.4.3, 2.4.3, 7

[121] M. Greenwald, R. Boivin, P. Bonoli *et al.*, Physics of Plasmas **6** (1999) 1943–1949, ISSN 1070-664X, doi:10.1063/1.873451, URL http://aip.scitation.org/doi/10.1063/1.873451 2.3.1, 2.3.3, 2.5.6

[122] L. Gil, C. Silva, T. Happel *et al.*, Nuclear Fusion **60** (2020) 054003, ISSN 0029-5515, doi:10.1088/1741-4326/ab7d1b, URL https://iopscience.iop.org/article/10.1088/1741-4326/ab7d1b 2.3.1, 2.5.6

[123] C. Theiler, J. L. Terry, E. Edlund *et al.*, Plasma Physics and Controlled Fusion **59** (2017) 025016, ISSN 0741-3335, doi:10.1088/1361-6587/aa52e5, URL https://iopscience.iop.org/article/10.1088/1361-6587/aa52e5 2.3.1, 2.5.6

[124] B. LaBombard, T. Golfinopoulos, J. L. Terry *et al.*, Physics of Plasmas **21** (2014) 056108, ISSN 1070-664X, doi:10.1063/1.4873918, URL http://aip.scitation.org/doi/10.1063/1.4873918 2.3.1, 2.5.6, 2.5.6

[125] D. A. Mossessian, P. B. Snyder, M. Greenwald *et al.*, Plasma Physics and Controlled Fusion **44** (2002) 423–437, ISSN 0741-3335, doi:10.1088/0741-3335/44/4/303, URL https://iopscience.iop.org/article/10.1088/0741-3335/44/4/303 2.3.1

[126] P. B. Snyder, H. R. Wilson, J. R. Ferron *et al.*, Physics of Plasmas **9** (2002) 2037–2043, ISSN 1070-664X, doi:10.1063/1.1449463, URL http://aip.scitation.org/doi/10.1063/1.1449463 2.3.1, 2.4.2

[127] M. Griener, E. Wolfrum, G. Birkenmeier *et al.*, Nuclear Materials and Energy **25** (2020) 100854, ISSN 23521791, doi:10.1016/j.nme.2020.100854, URL https://linkinghub.elsevier.com/retrieve/pii/S2352179120301204 2.3.1, 2.4.1, 2.4.2, 2.5.6, 2.29, 2.5.6

[128] L. Radovanovic, M. Dunne, E. Wolfrum *et al.*, Nuclear Fusion **62** (2022) 086004, ISSN 0029-5515, doi:10.1088/1741-4326/ac6d6a, URL https://iopscience.iop.org/article/10.1088/1741-4326/ac6d6a 2.3.1

[129] J. Stober, P. Lomas, G. Saibene *et al.*, Nuclear Fusion **45** (2005) 1213–1223, ISSN 0029-5515, doi:10.1088/0029-5515/45/11/001, URL https://iopscience.iop.org/article/10.1088/0029-5515/45/11/001 2.3.1, 2.4.2

[130] A. Kirk, H. W. Muller, E. Wolfrum *et al.*, Plasma Physics and Controlled Fusion **53** (2011) 095008, ISSN 0741-3335, doi:10.1088/0741-3335/53/9/095008, URL https://iopscience.iop.org/article/10.1088/0741-3335/53/9/095008 2.3.1

[131] E. Wolfrum, M. Bernert, J. E. Boom *et al.*, Plasma Physics and Controlled Fusion **53** (2011) 085026, ISSN 0741-3335, doi:10.1088/0741-3335/53/8/085026, URL https://iopscience.iop.org/article/10.1088/0741-3335/53/8/085026 2.3.1

[132] G. Xu, Q. Yang, N. Yan *et al.*, Physical Review Letters **122** (2019) 255001, ISSN 0031-9007, doi:10.1103/PhysRevLett.122.255001, URL https://link.aps.org/doi/10.1103/PhysRevLett.122.255001 2.3.1

[133] Q. Yang, G. Xu, N. Yan *et al.*, Nuclear Fusion **60** (2020) 076012, ISSN 0029-5515, doi:10.1088/1741-4326/ab8e0f, URL https://iopscience.iop.org/article/10.1088/1741-4326/ab8e0f 2.3.1, 2.4.2

[134] Y. Kamada, T. Oikawa, L. Lao *et al.*, Plasma Physics and Controlled Fusion **42** (2000) A247–A253, ISSN 0741-3335, doi:10.1088/0741-3335/42/5A/329, URL https://iopscience.iop.org/article/10.1088/0741-3335/42/5A/329 2.3.1, 2.4.2

[135] M. Faitsch, T. Eich, G. Harrer *et al.*, Nuclear Materials and Energy **26** (2021) 100890, ISSN 23521791, doi:10.1016/j.nme.2020.100890, URL https://linkinghub.elsevier.com/retrieve/pii/S2352179120301526 2.3.1

[136] K. H. Burrell, W. P. West, E. J. Doyle *et al.*, Physics of Plasmas **12** (2005) 056121, ISSN 1070-664X, doi:10.1063/1.1894745, URL http://aip.scitation.org/doi/10.1063/1.1894745 2.3.1

[137] W. Suttrop, V. Hynönen, T. Kurki-Suonio *et al.*, Nuclear Fusion **45** (2005) 721–730, ISSN 0029-5515, doi:10.1088/0029-5515/45/7/021, URL https://iopscience.iop.org/article/10.1088/0029-5515/45/7/021 2.3.1, 2.5.8, 2.32

[138] K. H. Burrell, T. H. Osborne, P. B. Snyder *et al.*, Physical Review Letters **102** (2009) 155003, ISSN 0031-9007, doi:10.1103/PhysRevLett.102.155003, URL https://link.aps.org/doi/10.1103/PhysRevLett.102.155003 2.3.1, 2.5.8

[139] K. H. Burrell, W. P. West, E. J. Doyle *et al.*, Plasma Physics and Controlled Fusion **46** (2004) A165–A178, ISSN 0741-3335, doi:10.1088/0741-3335/46/5A/018, URL https://iopscience.iop.org/article/10.1088/0741-3335/46/5A/018 2.3.1

[140] K. H. Burrell, M. E. Austin, D. P. Brennan *et al.*, Physics of Plasmas **8** (2001) 2153–2162, ISSN 1070-664X, doi:10.1063/1.1355981, URL http://aip.scitation.org/doi/10.1063/1.1355981 2.3.1, 2.5.8, 2.5.8

[141] W. Suttrop, M. Maraschek, G. D. Conway *et al.*, Plasma Physics and Controlled Fusion **45** (2003) 1399–1416, ISSN 0741-3335, doi:10.1088/0741-3335/45/8/302, URL https://iopscience.iop.org/article/10.1088/0741-3335/45/8/302 2.3.1, 2.5.8, 2.5.8, 2.32

[142] X. Chen, K. Burrell, T. Osborne *et al.*, Nuclear Fusion **57** (2017) 086008, ISSN 0029-5515, doi:10.1088/1741-4326/aa7531, URL https://iopscience.iop.org/article/10.1088/1741-4326/aa7531 2.3.1, 2.5.8

[143] K. Burrell, X. Chen, C. Chrystal *et al.*, Nuclear Fusion **60** (2020) 086005, ISSN 0029-5515, doi:10.1088/1741-4326/ab940d, URL https://iopscience.iop.org/article/10.1088/1741-4326/ab940d 2.3.1, 2.5.8

[144] T. E. Evans, Plasma Physics and Controlled Fusion **57** (2015) 123001, ISSN 0741-3335, doi:10.1088/0741-3335/57/12/123001, URL https://iopscience.iop.org/article/10.1088/0741-3335/57/12/123001 2.3.1

[145] W. Suttrop, T. Eich, J. C. Fuchs *et al.*, Physical Review Letters **106** (2011) 225004, ISSN 0031-9007, doi:10.1103/PhysRevLett.106.225004, URL https://link.aps.org/doi/10.1103/PhysRevLett.106.225004 2.3.1

[146] A. Kirk, I. T. Chapman, T. E. Evans *et al.*, Plasma Physics and Controlled Fusion **55** (2013) 124003, ISSN 0741-3335, doi:10.1088/0741-3335/55/12/124003, URL https://iopscience.iop.org/article/10.1088/0741-3335/55/12/124003 2.3.1

[147] Y. M. Jeon, J.-K. Park, S. W. Yoon *et al.*, Physical Review Letters **109** (2012) 035004, ISSN 0031-9007, doi:10.1103/PhysRevLett.109.035004, URL https://link.aps.org/doi/10.1103/PhysRevLett.109.035004 2.3.1

[148] M. Wade, R. Nazikian, J. deGrassie *et al.*, Nuclear Fusion **55** (2015) 023002, ISSN 0029-5515, doi:10.1088/0029-5515/55/2/023002, URL https://iopscience.iop.org/article/10.1088/0029-5515/55/2/023002 2.3.1

[149] N. Leuthold, W. Suttrop, R. Fischer *et al.*, Plasma Physics and Controlled Fusion **59** (2017) 055004, ISSN 0741-3335,

doi:10.1088/1361-6587/aa5f70, URL https://iopscience.iop.org/article/10.1088/1361-6587/aa5f70 2.3.1, 2.4.3

[150] Y. Liu, C. Paz-Soldan, L. Li *et al.*, Nuclear Fusion **60** (2020) 036018, ISSN 0029-5515, doi:10.1088/1741-4326/ab6c35, URL https://iopscience.iop.org/article/10.1088/1741-4326/ab6c35 2.3.1

[151] S. Wang, H. Liu, Y. Jie *et al.*, Nuclear Fusion **58** (2018) 112013, ISSN 0029-5515, doi:10.1088/1741-4326/aae15a, URL https://iopscience.iop.org/article/10.1088/1741-4326/aae15a 2.3.1

[152] M. Willensdorfer, T. Cote, C. Hegna *et al.*, Physical Review Letters **119** (2017) 085002, ISSN 0031-9007, doi:10.1103/PhysRevLett.119.085002, URL https://link.aps.org/doi/10.1103/PhysRevLett.119.085002 2.3.1

[153] N. Leuthold, W. Suttrop, M. Willensdorfer *et al.*, Nuclear Fusion **63** (2023) 046014, ISSN 0029-5515, doi:10.1088/1741-4326/acb1c5, URL https://iopscience.iop.org/article/10.1088/1741-4326/acb1c5 2.3.1

[154] F. Reimold, M. Wischmeier, M. Bernert *et al.*, Nuclear Fusion **55** (2015) 033004, ISSN 0029-5515, doi:10.1088/0029-5515/55/3/033004, URL https://iopscience.iop.org/article/10.1088/0029-5515/55/3/033004 2.3.1

[155] M. Bernert, F. Janky, B. Sieglin *et al.*, Nuclear Fusion **61** (2021) 024001, ISSN 0029-5515, doi:10.1088/1741-4326/abc936, URL https://iopscience.iop.org/article/10.1088/1741-4326/abc936 2.3.1

[156] O. Pan, in *48th EPS Conference on Plasma Physics*, Proceedings of the 48th EPS Conference on Plasma Physics, Maastricht (2022), URL http://ocs.ciemat.es/EPS2022PAP/pdf/O3.106.pdf 2.3.1

[157] U. Stroth, M. Bernert, D. Brida *et al.*, Nuclear Fusion **62** (2022) 076008, ISSN 0029-5515, doi:10.1088/1741-4326/ac613a, URL https://iopscience.iop.org/article/10.1088/1741-4326/ac613a 2.3.1

[158] K. H. Burrell, T. N. Carlstrom, E. J. Doyle *et al.*, Plasma Physics and Controlled Fusion **34** (1992) 1859–1869, ISSN 0741-3335, doi:10.1088/0741-3335/34/13/014, URL https://iopscience.iop.org/article/10.1088/0741-3335/34/13/014 2.3.2

[159] G. Birkenmeier, M. Cavedon, G. Conway *et al.*, Nuclear Fusion **56** (2016) 086009, ISSN 0029-5515, doi:10.1088/0029-5515/56/8/086009, URL https://iopscience.iop.org/article/10.1088/0029-5515/56/8/086009 2.3.2, 2.4.2, 5, 5.1, 5.2, 5.3, 5.4, 5.5, 5.6, 5.7, 5.9, 5.1.4, 5.10, 5.15, 5.16, 5.2.3

[160] S.-I. Itoh and K. Itoh, Nuclear Fusion **29** (1989) 1031–1045, ISSN 0029-5515, doi:10.1088/0029-5515/29/6/013, URL https://iopscience.iop.org/article/10.1088/0029-5515/29/6/013 2.3.2

[161] H. Zohm, W. Suttrop, K. Buchl *et al.*, Plasma Physics and Controlled Fusion **37** (1995) 437–446, ISSN 0741-3335, doi:10.1088/0741-3335/37/4/005, URL https://iopscience.iop.org/article/10.1088/0741-3335/37/4/005 2.3.2, 2.5.3, 3

[162] P. H. Diamond, Y.-M. Liang, B. A. Carreras *et al.*, Physical Review Letters **72** (1994) 2565–2568, ISSN 0031-9007, doi:10.1103/PhysRevLett.72.2565, URL https://link.aps.org/doi/10.1103/PhysRevLett.72.2565 2.3.2, 4.3.4, 4.4.1, 5.2.1

[163] S.-I. Itoh and K. Itoh, Nuclear Fusion **54** (2014) 114017, ISSN 0029-5515, doi:10.1088/0029-5515/54/11/114017, URL https://iopscience.iop.org/article/10.1088/0029-5515/54/11/114017 2.3.2

[164] S.-I. Itoh, K. Itoh, and S. Inagaki, Nuclear Fusion **57** (2017) 022003, ISSN 0029-5515, doi:10.1088/0029-5515/57/2/022003, URL https://iopscience.iop.org/article/10.1088/0029-5515/57/2/022003 2.3.2

[165] F. Ryter, L. B. Orte, B. Kurzan *et al.*, Nuclear Fusion **54** (2014) 083003, ISSN 0029-5515, doi:10.1088/0029-5515/54/8/083003, URL https://iopscience.iop.org/article/10.1088/0029-5515/54/8/083003 2.3.2, 4.1.5, 4.2.3, 4.13, 4.14, 4.2.3, 4.3.1, 4.3.1, 4.3.2

[166] R. Wenninger, R. Kembleton, C. Bachmann *et al.*, Nuclear Fusion **57** (2017) 016011, ISSN 0029-5515, doi:10.1088/0029-5515/57/1/016011, URL https://iopscience.iop.org/article/10.1088/0029-5515/57/1/016011 2.3.2, 4.5, 7

[167] ITER-organization, *ITER Research Plan within Staged Approach, ITR-Report 18-003, https://www.iter.org/technical-reports?id=9* (2018), URL https://www.iter.org/technical-reports?id=9 2.3.2, 4.3.1

[168] Y. R. Martin, T. Takizuka, and the ITPA CDBM H-mode Threshold Data Group, Journal of Physics: Conference Series **123** (2008) 012033, ISSN 1742-6596, doi:10.1088/1742-6596/123/1/012033, URL https://iopscience.iop.org/article/10.1088/1742-6596/123/1/012033 2.3.2, 4.1.1

[169] T. Happel, M. Griener, D. Silvagni *et al.*, Nuclear Materials and Energy **18** (2019) 159–165, ISSN 23521791, doi:10.1016/j.nme.2018.12.022, URL https://linkinghub.elsevier.com/retrieve/pii/S2352179118301017 2.15, 2.4.3, 2.5.7

[170] A. Hubbard, S.-G. Baek, D. Brunner *et al.*, Nuclear Fusion **57** (2017) 126039, ISSN 0029-5515, doi:10.1088/1741-4326/aa8570, URL https://iopscience.iop.org/article/10.1088/1741-4326/aa8570 2.16, 2.3.3

[171] Y. Liu, Z. Liu, A. Liu *et al.*, Nuclear Fusion **60** (2020) 082003, ISSN 0029-5515, doi:10.1088/1741-4326/ab88e0, URL https://iopscience.iop.org/article/10.1088/1741-4326/ab88e0 2.3.3

[172] B. Sorbom, J. Ball, T. Palmer *et al.*, Fusion Engineering and Design **100** (2015) 378–405, ISSN 09203796, doi:10.1016/j.fusengdes.2015.07.008, URL https://linkinghub.elsevier.com/retrieve/pii/S0920379615302337 2.3.3, 7

[173] S. J. Zweben, J. A. Boedo, O. Grulke *et al.*, Plasma Physics and Controlled Fusion **49** (2007) S1–S23, ISSN 0741-3335, doi:10.1088/0741-3335/49/7/S01, URL https://iopscience.iop.org/article/10.1088/0741-3335/49/7/S01 2.4.1

[174] O. E. Garcia, R. Kube, A. Theodorsen *et al.*, Physics of Plasmas **25** (2018) 056103, ISSN 1070-664X, doi:10.1063/1.5018709, URL http://aip.scitation.org/doi/10.1063/1.5018709 2.4.1

[175] A. Theodorsen, O. E. Garcia, J. Horacek *et al.*, Plasma Physics and Controlled Fusion **58** (2016) 044006, ISSN 0741-3335, doi:10.1088/0741-3335/58/4/044006, URL https://iopscience.iop.org/article/10.1088/0741-3335/58/4/044006 2.4.1

[176] G. Fuchert, G. Birkenmeier, D. Carralero *et al.*, Plasma Physics and Controlled Fusion **56** (2014) 125001, ISSN 0741-3335, doi:10.1088/0741-3335/56/12/125001, URL https://iopscience.iop.org/article/10.1088/0741-3335/56/12/125001 2.4.1, 3.5.3

[177] N. B. Ayed, A. Kirk, B. Dudson *et al.*, Plasma Physics and Controlled Fusion **51** (2009) 035016, ISSN 0741-3335, doi:10.1088/0741-3335/51/3/035016, URL https://iopscience.iop.org/article/10.1088/0741-3335/51/3/035016 2.4.1

[178] M. Spolaore, N. Vianello, M. Agostini *et al.*, Physical Review Letters **102** (2009) 165001, ISSN 0031-9007, doi:10.1103/PhysRevLett.102.165001, URL https://link.aps.org/doi/10.1103/PhysRevLett.102.165001 2.4.1

[179] R. Maqueda, D. Stotler, and S. Zweben, Journal of Nuclear Materials **415** (2011) S459–S462, ISSN 00223115, doi:10.1016/j.jnucmat.2010.11.002, URL https://linkinghub.elsevier.com/retrieve/pii/S0022311510006707 2.18

[180] D. Carralero, G. Birkenmeier, H. Müller *et al.*, Nuclear Fusion **54** (2014) 123005, ISSN 0029-5515, doi:10.1088/0029-5515/54/12/123005, URL https://iopscience.iop.org/article/10.1088/0029-5515/54/12/123005 2.4.1, 3.2.3, 3.6, 3.6, 3.6

[181] D. Carralero, J. Madsen, S. Artene *et al.*, Nuclear Materials and Energy **12** (2017) 1189–1193, ISSN 23521791, doi:10.1016/j.nme.2016.11.016, URL https://linkinghub.elsevier.com/retrieve/pii/S2352179116301715 2.4.1, 3.6

[182] G. Birkenmeier, P. Manz, D. Carralero *et al.*, Nuclear Fusion **55** (2015) 033018, ISSN 0029-5515, doi:10.1088/0029-5515/55/3/033018, URL https://iopscience.iop.org/article/10.1088/0029-5515/55/3/033018 2.4.1, 3, 3.9, 3.10, 3.7, 3.12, 3.13, 3.14

[183] F. Maviglia, M. Siccinio, C. Bachmann *et al.*, Nuclear Materials and Energy **26** (2021) 100897, ISSN 23521791, doi:10.1016/j.nme.2020.100897, URL https://linkinghub.elsevier.com/retrieve/pii/S2352179120301587 2.4.1

[184] E. J. Doyle, R. J. Groebner, K. H. Burrell *et al.*, Physics of Fluids B: Plasma Physics **3** (1991) 2300–2307, ISSN 0899-8221, doi:10.1063/1.859597, URL http://aip.scitation.org/doi/10.1063/1.859597 2.4.2

[185] J. Schweinzer, M. Beurskens, L. Frassinetti *et al.*, Nuclear Fusion **56** (2016) 106007, ISSN 0029-5515, doi:10.1088/0029-5515/56/10/106007, URL https://iopscience.iop.org/article/10.1088/0029-5515/56/10/106007 2.4.2

[186] A. Diallo, J. Hughes, S.-G. Baek *et al.*, Nuclear Fusion **55** (2015) 053003, ISSN 0029-5515, doi:10.1088/0029-5515/55/5/053003, URL https://iopscience.iop.org/article/10.1088/0029-5515/55/5/053003 2.4.2, 2.5.10, 2.33

[187] F. M. Laggner, E. Wolfrum, M. Cavedon *et al.*, Plasma Physics and Controlled Fusion **58** (2016) 065005, ISSN 0741-3335, doi:10.1088/0741-3335/58/6/065005, URL https://iopscience.iop.org/article/10.1088/0741-3335/58/6/065005 2.4.2, 2.5.10

[188] A. Hassanein and V. Sizyuk, Scientific Reports **11** (2021) 2069, ISSN 2045-2322, doi:10.1038/s41598-021-81510-2, URL http://www.nature.com/articles/s41598-021-81510-2 2.4.2

[189] M. Hoelzl, G. Huijsmans, F. Orain *et al.*, Contributions to Plasma Physics **58** (2018) 518–528, ISSN 08631042, doi:10.1002/ctpp.201700142, URL https://onlinelibrary.wiley.com/doi/10.1002/ctpp.201700142 2.20

[190] A. Kallenbach, R. Dux, M. Mayer *et al.*, Nuclear Fusion **49** (2009) 045007, ISSN 0029-5515, doi:10.1088/0029-5515/49/4/045007, URL https://iopscience.iop.org/article/10.1088/0029-5515/49/4/045007 2.4.2

[191] P. T. Lang, H. Meyer, G. Birkenmeier *et al.*, Plasma Physics and Controlled Fusion **57** (2015) 045011, ISSN 0741-3335, doi:10.1088/0741-3335/57/4/045011, URL https://iopscience.iop.org/article/10.1088/0741-3335/57/4/045011 2.4.2

[192] E. de la Luna, I. Chapman, F. Rimini *et al.*, Nuclear Fusion **56** (2016) 026001, ISSN 0029-5515, doi:10.1088/0029-5515/56/2/026001, URL https://iopscience.iop.org/article/10.1088/0029-5515/56/2/026001 2.4.2

[193] T. Happel, P. Manz, F. Ryter *et al.*, Nuclear Fusion **56** (2016) 064004, ISSN 0029-5515, doi:10.1088/0029-5515/56/6/064004, URL https://iopscience.iop.org/article/10.1088/0029-5515/56/6/064004 2.4.3

[194] D. Silvagni, T. Eich, T. Happel *et al.*, Nuclear Fusion **60** (2020) 126028, ISSN 0029-5515, doi:10.1088/1741-4326/abb423, URL https://iopscience.iop.org/article/10.1088/1741-4326/abb423 2.4.3, 2.4.3, 2.21

[195] P. Manz, D. Silvagni, O. Grover *et al.*, Physics of Plasmas **28** (2021) 102502, ISSN 1070-664X, doi:10.1063/5.0059295, URL https://aip.scitation.org/doi/10.1063/5.0059295 2.22, 2.4.3

[196] P. Manz, T. Happel, U. Stroth *et al.*, Nuclear Fusion **60** (2020) 096011, ISSN 0029-5515, doi:10.1088/1741-4326/ab9e17, URL https://iopscience.iop.org/article/10.1088/1741-4326/ab9e17 2.4.3, 2.5.7

[197] S. Potzel, M. Wischmeier, M. Bernert *et al.*, Journal of Nuclear Materials **438** (2013) S285–S290, ISSN 00223115, doi:10.1016/j.jnucmat.2013.01.048, URL https://linkinghub.elsevier.com/retrieve/pii/S0022311513000561 2.5.1, 2.23, 2.5.2

[198] S. Potzel, M. Wischmeier, M. Bernert *et al.*, Nuclear Fusion **54** (2014) 013001, ISSN 0029-5515, doi:10.1088/0029-5515/54/1/013001, URL https://iopscience.iop.org/article/10.1088/0029-5515/54/1/013001 2.5.1

[199] A. Loarte, R. D. Monk, A. S. Kukushkin *et al.*, Physical Review Letters **83** (1999) 3657–3660, ISSN 0031-9007, doi:10.1103/PhysRevLett.83.3657, URL https://link.aps.org/doi/10.1103/PhysRevLett.83.3657 2.5.1, 2.5.2

[200] A. Matsubara, T. Watanabe, T. Sugimoto *et al.*, Journal of Nuclear Materials **337-339** (2005) 181–185, ISSN 00223115, doi:10.1016/j.jnucmat.2004.09.028, URL https://linkinghub.elsevier.com/retrieve/pii/S0022311504008670 2.5.1

[201] P. Heinrich, P. Manz, M. Bernert *et al.*, Nuclear Fusion **60** (2020) 076013, ISSN 0029-5515, doi:10.1088/1741-4326/ab8a05, URL https://iopscience.iop.org/article/10.1088/1741-4326/ab8a05 2.5.1, 2.5.2, 2.5.2, 2.24

[202] A. R. Field, I. Balboa, P. Drewelow *et al.*, Plasma Physics and Controlled Fusion **59** (2017) 095003, ISSN 0741-3335, doi:10.1088/1361-6587/aa764c, URL https://iopscience.iop.org/article/10.1088/1361-6587/aa764c 2.5.2

[203] S. Krasheninnikov, A. Kukushkin, V. Pistunovich *et al.*, Nuclear Fusion **27** (1987) 1805–1816, ISSN 0029-5515, doi:10.1088/0029-5515/27/11/006, URL https://iopscience.iop.org/article/10.1088/0029-5515/27/11/006 2.5.2

[204] S. I. Krasheninnikov, A. S. Kukushkin, and A. A. Pshenov, Physics of Plasmas **23** (2016) 055602, ISSN 1070-664X, doi:10.1063/1.4948273, URL http://aip.scitation.org/doi/10.1063/1.4948273 2.5.2

[205] A. S. Kukushkin and S. I. Krasheninnikov, Plasma Physics and Controlled Fusion **61** (2019) 074001, ISSN 0741-3335, doi:10.1088/1361-6587/ab1bba, URL https://iopscience.iop.org/article/10.1088/1361-6587/ab1bba 2.5.2

[206] K. Itoh, S.-I. Itoh, and A. Fujisawa, Plasma and Fusion Research **8** (2013) 1102168–1102168, ISSN 1880-6821, doi:10.1585/pfr.8.1102168, URL https://www.jstage.jst.go.jp/article/pfr/8/0/8_1102168/_article 2.5.3, 2.5.3

[207] L. Schmitz, L. Zeng, T. L. Rhodes *et al.*, Physical Review Letters **108** (2012) 155002, ISSN 0031-9007, doi:10.1103/PhysRevLett.108.155002, URL https://link.aps.org/doi/10.1103/PhysRevLett.108.155002 2.5.3

[208] T. Estrada, C. Hidalgo, T. Happel *et al.*, Physical Review Letters **107** (2011) 245004, ISSN 0031-9007, doi:10.1103/PhysRevLett.107.245004, URL https://link.aps.org/doi/10.1103/PhysRevLett.107.245004 2.5.3

[209] E. jin Kim and P. H. Diamond, Physical Review Letters **90** (2003) 185006, ISSN 0031-9007, doi:10.1103/PhysRevLett.90.185006, URL https://link.aps.org/doi/10.1103/PhysRevLett.90.185006 2.5.3, 2.5.5, 5.1.4, 5.2.1, 5.2.1

[210] Z. B. Guo, P. H. Diamond, Y. Kosuga *et al.*, Physics of Plasmas **21** (2014) 090702, ISSN 1070-664X, doi:10.1063/1.4894695, URL http://aip.scitation.org/doi/10.1063/1.4894695 2.5.3

[211] X. Wu, G. Xu, B. Wan *et al.*, Nuclear Fusion **55** (2015) 053029, ISSN 0029-5515, doi:10.1088/0029-5515/55/5/053029, URL https://iopscience.iop.org/article/10.1088/0029-5515/55/5/053029 2.5.3

[212] J. J. Rasmussen, A. H. Nielsen, J. Madsen *et al.*, Plasma Physics and Controlled Fusion **58** (2016) 014031, ISSN 0741-3335, doi:10.1088/0741-3335/58/1/014031, URL https://iopscience.iop.org/article/10.1088/0741-3335/58/1/014031 2.5.3, 4.1.1, 5.2.1

[213] H. Zohm, Physical Review Letters **72** (1994) 222–225, ISSN 0031-9007, doi:10.1103/PhysRevLett.72.222, URL https://link.aps.org/doi/10.1103/PhysRevLett.72.222 2.5.3, 3

[214] S.-I. Itoh, K. Itoh, A. Fukuyama *et al.*, Physical Review Letters **67** (1991) 2485–2488, ISSN 0031-9007, doi:10.1103/PhysRevLett.67.2485, URL https://link.aps.org/doi/10.1103/PhysRevLett.67.2485 2.5.3

[215] B. Chatthong and T. Onjun, Contributions to Plasma Physics **56** (2016) 528–533, ISSN 08631042, doi:10.1002/ctpp.201610034, URL https://onlinelibrary.wiley.com/doi/10.1002/ctpp.201610034 2.5.3

[216] G. D. Conway, C. Angioni, F. Ryter *et al.*, Physical Review Letters **106** (2011) 065001, ISSN 0031-9007, doi:10.1103/PhysRevLett.106.065001, URL https://link.aps.org/doi/10.1103/PhysRevLett.106.065001 2.5.3, 4.4.1

[217] R. J. Colchin, M. J. Schaffer, B. A. Carreras *et al.*, Physical Review Letters **88** (2002) 255002, ISSN 0031-9007, doi:10.1103/PhysRevLett.88.255002, URL https://link.aps.org/doi/10.1103/PhysRevLett.88.255002 2.5.3

[218] R. Colchin, B. Carreras, R. Maingi *et al.*, Nuclear Fusion **42** (2002) 312, ISSN 00295515, doi:10.1088/0029-5515/42/9/312, URL https://iopscience.iop.org/article/10.1088/0029-5515/42/9/312 2.5.3

[219] E. R. Solano, N. Vianello, E. Delabie *et al.*, Nuclear Fusion **57** (2017) 022021, ISSN 0029-5515, doi:10.1088/0029-5515/57/2/022021, URL https://iopscience.iop.org/article/10.1088/0029-5515/57/2/022021 2.5.3, 5.1.3, 5.1.4

[220] L. Schmitz, Nuclear Fusion **57** (2017) 025003, ISSN 0029-5515, doi:10.1088/1741-4326/57/2/025003, URL https://iopscience.iop.org/article/10.1088/1741-4326/57/2/025003 2.5.3

[221] T. Kobayashi, K. Itoh, T. Ido *et al.*, Physical Review Letters **111** (2013) 035002, ISSN 0031-9007, doi:10.1103/PhysRevLett.111.035002, URL https://link.aps.org/doi/10.1103/PhysRevLett.111.035002 2.5.3, 4.4.1, 5.2.1

[222] J. Cheng, J. Q. Dong, K. Itoh *et al.*, Physical Review Letters **110** (2013) 265002, ISSN 0031-9007, doi:10.1103/PhysRevLett.110.265002, URL

https://link.aps.org/doi/10.1103/PhysRevLett.110.265002 2.5.3, 5.2.1

[223] J. Cheng, J. Dong, K. Itoh *et al.*, Nuclear Fusion **54** (2014) 114004, ISSN 0029-5515, doi:10.1088/0029-5515/54/11/114004, URL https://iopscience.iop.org/article/10.1088/0029-5515/54/11/114004 2.5.3, 2.25

[224] G. Xu, L. Shao, S. Liu *et al.*, Nuclear Fusion **54** (2014) 013007, ISSN 0029-5515, doi:10.1088/0029-5515/54/1/013007, URL https://iopscience.iop.org/article/10.1088/0029-5515/54/1/013007 2.5.3, 5.2.1

[225] G. Xu, H. Wang, M. Xu *et al.*, Nuclear Fusion **54** (2014) 103002, ISSN 0029-5515, doi:10.1088/0029-5515/54/10/103002, URL https://iopscience.iop.org/article/10.1088/0029-5515/54/10/103002 2.5.3, 2.5.4, 2.5.5, 5.1.3, 5.2.1, 5.2.3

[226] D. Refy, E. Solano, N. Vianello *et al.*, Nuclear Fusion **60** (2020) 056004, ISSN 0029-5515, doi:10.1088/1741-4326/ab7594, URL https://iopscience.iop.org/article/10.1088/1741-4326/ab7594 2.5.3, 5.1.3, 5.1.4

[227] S. Glöggler, M. Wischmeier, E. Fable *et al.*, Nuclear Fusion **59** (2019) 126031, ISSN 0029-5515, doi:10.1088/1741-4326/ab3f7a, URL https://iopscience.iop.org/article/10.1088/1741-4326/ab3f7a 2.5.3, 4.1.6

[228] P. Liu, G. Xu, H. Wang *et al.*, Plasma Science and Technology **15** (2013) 619–622, ISSN 1009-0630, doi:10.1088/1009-0630/15/7/03, URL https://iopscience.iop.org/article/10.1088/1009-0630/15/7/03 2.5.4

[229] M. Cavedon, G. Birkenmeier, T. Pütterich *et al.*, Nuclear Fusion **60** (2020) 066026, ISSN 0029-5515, doi:10.1088/1741-4326/ab8777, URL https://iopscience.iop.org/article/10.1088/1741-4326/ab8777 2.5.4, 4.2.4, 4.15, 4.3.2, 4.3.2, 4.3.3

[230] L. M. Shao, G. S. Xu, R. Chen *et al.*, Plasma Physics and Controlled Fusion **60** (2018) 035012, ISSN 0741-3335, doi:10.1088/1361-6587/aaa57a, URL https://iopscience.iop.org/article/10.1088/1361-6587/aaa57a 2.5.5, 2.28

[231] L. Shao, *Oscillating plasma states around the L-H transition at ASDEX Upgrade (IPP Report 17/51)* (2016), doi:doi:10.17617/2.2327600, URL http://hdl.handle.net/11858/00-001M-0000-002B-1BFD-E 2.5.5

[232] G. S. Xu, B. N. Wan, H. Q. Wang *et al.*, Physical Review Letters **107** (2011) 125001, ISSN 0031-9007, doi:10.1103/PhysRevLett.107.125001, URL https://link.aps.org/doi/10.1103/PhysRevLett.107.125001 2.5.5, 5.2.1

[233] T. Kobayashi, K. Itoh, T. Ido *et al.*, Nuclear Fusion **55** (2015) 063009, ISSN 0029-5515, doi:10.1088/0029-5515/55/6/063009, URL https://iopscience.iop.org/article/10.1088/0029-5515/55/6/063009 2.5.5, 5.2.1

[234] S. H. Müller, G. D. Conway, G. Birkenmeier *et al.*, Physics of Plasmas **21** (2014) 042301, ISSN 1070-664X, doi:10.1063/1.4870012, URL http://aip.scitation.org/doi/10.1063/1.4870012 2.5.5

[235] A. Medvedeva, C. Bottereau, F. Clairet *et al.*, Plasma Physics and Controlled Fusion **61** (2019) 085011, ISSN 0741-3335, doi:10.1088/1361-6587/ab2575, URL https://iopscience.iop.org/article/10.1088/1361-6587/ab2575 2.5.6

[236] H. Wang, G. Xu, B. Wan *et al.*, Physical Review Letters **112** (2014) 185004, ISSN 0031-9007, doi:10.1103/PhysRevLett.112.185004, URL https://link.aps.org/doi/10.1103/PhysRevLett.112.185004 2.5.6, 2.5.6

[237] A. Mazurenko, M. Porkolab, D. Mossessian *et al.*, Physical Review Letters **89** (2002) 225004, ISSN 0031-9007, doi:10.1103/PhysRevLett.89.225004, URL https://link.aps.org/doi/10.1103/PhysRevLett.89.225004 2.5.6

[238] B. N. Rogers and J. F. Drake, Physics of Plasmas **6** (1999) 2797–2801, ISSN 1070-664X, doi:10.1063/1.873237, URL http://aip.scitation.org/doi/10.1063/1.873237 2.5.6

[239] D. A. Russell, D. A. D'Ippolito, J. R. Myra *et al.*, Physics of Plasmas **19** (2012) 082311, ISSN 1070-664X, doi:10.1063/1.4747503, URL http://aip.scitation.org/doi/10.1063/1.4747503 2.5.6

[240] I. Cziegler, P. H. Diamond, N. Fedorczak *et al.*, Physics of Plasmas **20** (2013) 055904, ISSN 1070-664X, doi:10.1063/1.4803914, URL http://aip.scitation.org/doi/10.1063/1.4803914 2.5.7, 2.30

[241] P. Manz, G. Birkenmeier, D. Carralero *et al.*, Plasma Physics and Controlled Fusion **57** (2015) 014012, ISSN 0741-3335, doi:10.1088/0741-3335/57/1/014012, URL https://iopscience.iop.org/article/10.1088/0741-3335/57/1/014012 2.5.7, 5

[242] Z. X. Liu, X. Q. Xu, X. Gao *et al.*, Physics of Plasmas **23** (2016) 120703, ISSN 1070-664X, doi:10.1063/1.4972088, URL http://aip.scitation.org/doi/10.1063/1.4972088 2.5.7

[243] Z. Liu, Y. Liu, J. Xiao *et al.*, Nuclear Fusion **62** (2022) 086029, ISSN 0029-5515, doi:10.1088/1741-4326/ac7537, URL https://iopscience.iop.org/article/10.1088/1741-4326/ac7537 2.5.7

[244] Y. Lang, X. Xu, Z. Guo *et al.*, Nuclear Fusion **62** (2022) 086018, ISSN 0029-5515, doi:10.1088/1741-4326/ac7245, URL https://iopscience.iop.org/article/10.1088/1741-4326/ac7245 2.5.7

[245] G. Huysmans, T. Hender, and B. Alper, Nuclear Fusion **38** (1998) 179–187, ISSN 0029-5515, doi:10.1088/0029-5515/38/2/303, URL https://iopscience.iop.org/article/10.1088/0029-5515/38/2/303 2.5.8

[246] E. R. Solano, P. J. Lomas, B. Alper *et al.*, Physical Review Letters **104** (2010) 185003, ISSN 0031-9007, doi:10.1103/PhysRevLett.104.185003, URL https://link.aps.org/doi/10.1103/PhysRevLett.104.185003 2.5.8, 2.5.8

[247] T. Wilks, A. Garofalo, P. Diamond *et al.*, Nuclear Fusion **58** (2018) 112002, ISSN 0029-5515, doi:10.1088/1741-4326/aad143, URL https://iopscience.iop.org/article/10.1088/1741-4326/aad143 2.31

[248] J. C. Rost, M. Porkolab, J. Dorris *et al.*, Physics of Plasmas **21** (2014) 062306, ISSN 1070-664X, doi:10.1063/1.4883135, URL http://aip.scitation.org/doi/10.1063/1.4883135 2.5.8

[249] W. Suttrop, G. D. Conway, L. Fattorini *et al.*, Plasma Physics and Controlled Fusion **46** (2004) A151–A156, ISSN 0741-3335, doi:10.1088/0741-3335/46/5A/016, URL https://iopscience.iop.org/article/10.1088/0741-3335/46/5A/016 2.5.8

[250] N. Aiba, X. Chen, K. Kamiya *et al.*, Nuclear Fusion **61** (2021) 126044, ISSN 0029-5515, doi:10.1088/1741-4326/ac318e, URL https://iopscience.iop.org/article/10.1088/1741-4326/ac318e 2.5.8

[251] F. Liu, G. T. A. Huijsmans, A. Loarte *et al.*, Plasma Physics and Controlled Fusion **60** (2018) 014039, ISSN 0741-3335, doi:10.1088/1361-6587/aa934f, URL https://iopscience.iop.org/article/10.1088/1361-6587/aa934f 2.5.8

[252] Z. Yan, G. R. McKee, R. J. Groebner *et al.*, Physical Review Letters **107** (2011) 055004, ISSN 0031-9007, doi:10.1103/PhysRevLett.107.055004, URL https://link.aps.org/doi/10.1103/PhysRevLett.107.055004 2.5.9

[253] F. Laggner, A. Diallo, M. Cavedon *et al.*, Nuclear Materials and Energy **19** (2019) 479–486, ISSN 23521791, doi:10.1016/j.nme.2019.02.030, URL https://linkinghub.elsevier.com/retrieve/pii/S2352179118301911 2.5.10, 2.5.10

[254] F. M. Laggner, E. Wolfrum, M. Cavedon *et al.*, Physics of Plasmas **24** (2017) 056105, ISSN 1070-664X, doi:10.1063/1.4977461, URL http://aip.scitation.org/doi/10.1063/1.4977461 2.5.10

[255] B. Vanovac, E. Wolfrum, M. Hoelzl *et al.*, Nuclear Fusion **58** (2018) 112011, ISSN 0029-5515, doi:10.1088/1741-4326/aada20, URL https://iopscience.iop.org/article/10.1088/1741-4326/aada20 2.5.10

[256] G. Birkenmeier, F. M. Laggner, M. Willensdorfer *et al.*, Plasma Physics and Controlled Fusion **56** (2014) 075019, ISSN 0741-3335, doi:10.1088/0741-3335/56/7/075019, URL https://iopscience.iop.org/article/10.1088/0741-3335/56/7/075019 3, 3.5, 3.5.2, 3.5, 3.6, 3.7, 3.5.2, 3.8, 3.5.2

[257] B. D. Scott, Physics of Plasmas **12** (2005) 062314, ISSN 1070-664X, doi:10.1063/1.1917866, URL http://aip.scitation.org/doi/10.1063/1.1917866 3.1

[258] S. I. Krasheninnikov and A. I. Smolyakov, Physics of Plasmas **10** (2003) 3020–3021, ISSN 1070-664X, doi:10.1063/1.1579692, URL http://aip.scitation.org/doi/10.1063/1.1579692 3.1, 3.1

[259] H.-L. Berk, R. Cohen, D. Ryutov *et al.*, Nuclear Fusion **33** (1993) 263–282, ISSN 0029-5515, doi:10.1088/0029-5515/33/2/I07, URL https://iopscience.iop.org/article/10.1088/0029-5515/33/2/I07 3.1, 3.1

[260] S. I. Krasheninnikov, D. A. D'Ippolito, and J. R. Myra, Journal of Plasma Physics **74** (2008) 679–717, ISSN 0022-3778, doi:10.1017/S0022377807006940, URL https://www.cambridge.org/core/product/identifier/S0022377807006940/type/journal_article 3.1, 4, 3.2, 3.2, 3.4

[261] O. E. Garcia, N. H. Bian, and W. Fundamenski, Physics of Plasmas **13** (2006) 082309, ISSN 1070-664X, doi:10.1063/1.2336422, URL http://aip.scitation.org/doi/10.1063/1.2336422 1, 5, 3.2, 3.2.1, 3.4

[262] S. Krasheninnikov, Physics Letters A **283** (2001) 368–370, ISSN 03759601, doi:10.1016/S0375-9601(01)00252-3, URL https://linkinghub.elsevier.com/retrieve/pii/S0375960101002523 2, 5, 3.2.2

[263] J. R. Myra, D. A. Russell, and D. A. D'Ippolito, Physics of Plasmas **13** (2006) 112502, ISSN 1070-664X, doi:10.1063/1.2364858, URL http://aip.scitation.org/doi/10.1063/1.2364858 3, 3.1, 3.2.3

[264] D. A. Russell, J. R. Myra, and D. A. D'Ippolito, Physics of Plasmas **14** (2007) 102307, ISSN 1070-664X, doi:10.1063/1.2780137, URL http://aip.scitation.org/doi/10.1063/1.2780137 3, 3.1

[265] G. S. Xu, V. Naulin, W. Fundamenski *et al.*, Physics of Plasmas **17** (2010) 022501, ISSN 1070-664X, doi:10.1063/1.3302535, URL http://aip.scitation.org/doi/10.1063/1.3302535 4

[266] M. Kocan, F. P. Gennrich, A. Kendl *et al.*, Plasma Physics and Controlled Fusion **54** (2012) 085009, ISSN 0741-3335, doi:10.1088/0741-3335/54/8/085009, URL https://iopscience.iop.org/article/10.1088/0741-3335/54/8/085009 5, 3.5.2, 3.5.3, 3.7, 3.7.1

[267] S. Elmore, S. Y. Allan, A. Kirk *et al.*, Plasma Physics and Controlled Fusion **54** (2012) 065001, ISSN 0741-3335, doi:10.1088/0741-3335/54/6/065001, URL https://iopscience.iop.org/article/10.1088/0741-3335/54/6/065001 5

[268] P. Manz, D. Carralero, G. Birkenmeier *et al.*, Physics of Plasmas **20** (2013) 102307, ISSN 1070-664X, doi:10.1063/1.4824799, URL http://aip.scitation.org/doi/10.1063/1.4824799 5, 3.2, 3.2, 3.2.1, 3.2.1, 3.2.2, 3.2.3, 3.4

[269] D. Jovanovic, P. K. Shukla, and F. Pegoraro, Physics of Plasmas **15** (2008) 112305, ISSN 1070-664X, doi:10.1063/1.3008050, URL http://aip.scitation.org/doi/10.1063/1.3008050 5

[270] B. Shanahan, B. Dudson, and P. Hill, Plasma Physics and Controlled Fusion **61** (2019) 025007, ISSN 0741-3335, doi:10.1088/1361-6587/aaed7d, URL https://iopscience.iop.org/article/10.1088/1361-6587/aaed7d 3.1, 3.2, 3.2

[271] B. D. Scott, Plasma Physics and Controlled Fusion **49** (2007) S25–S41, ISSN 0741-3335, doi:10.1088/0741-3335/49/7/S02, URL https://iopscience.iop.org/article/10.1088/0741-3335/49/7/S02 3.2

[272] R. Hazeltine and J. Meiss, Physics Reports **121** (1985) 1–164, ISSN 03701573, doi:10.1016/0370-1573(85)90083-3, URL https://linkinghub.elsevier.com/retrieve/pii/0370157385900833 3.2

[273] M. Nadeem, T. Rafiq, and M. Persson, Physics of Plasmas **8** (2001) 4375–4385, ISSN 1070-664X, doi:10.1063/1.1396842, URL http://aip.scitation.org/doi/10.1063/1.1396842 3.2

[274] M. H. Nasim, T. Rafiq, and M. Persson, Plasma Physics and Controlled Fusion **46** (2004) 193–209, ISSN 0741-3335, doi:10.1088/0741-3335/46/1/012, URL https://iopscience.iop.org/article/10.1088/0741-3335/46/1/012 3.2

[275] J. R. Myra and D. A. D'Ippolito, Physics of Plasmas **12** (2005) 092511, ISSN 1070-664X, doi:10.1063/1.2048847, URL http://aip.scitation.org/doi/10.1063/1.2048847 3.2

[276] A. Y. Aydemir, Physics of Plasmas **12** (2005) 062503, ISSN 1070-664X, doi:10.1063/1.1927539, URL http://aip.scitation.org/doi/10.1063/1.1927539 3.3, 3.4, 3.4, 3.5.3

[277] C. Tomkins, K. Prestridge, P. Rightley *et al.*, Physics of Fluids **15** (2003) 986–1004, ISSN 1070-6631, doi:10.1063/1.1555802, URL http://aip.scitation.org/doi/10.1063/1.1555802 3.4

[278] E. Wolfrum, F. Aumayr, D. Wutte *et al.*, Review of Scientific Instruments **64** (1993) 2285–2292, ISSN 0034-6748, doi:10.1063/1.1144460, URL http://aip.scitation.org/doi/10.1063/1.1144460 3.5.1

[279] E. Wolfrum, J. Schweinzer, M. Reich *et al.*, Review of Scientific Instruments **77** (2006) 033507, ISSN 0034-6748, doi:10.1063/1.2179887, URL http://aip.scitation.org/doi/10.1063/1.2179887 3.5.1

[280] M. Willensdorfer, E. Wolfrum, R. Fischer *et al.*, Review of Scientific Instruments **83** (2012) 023501, ISSN 0034-6748, doi:10.1063/1.3682003, URL http://aip.scitation.org/doi/10.1063/1.3682003 3.5.1, 3.4

[281] M. Willensdorfer, G. Birkenmeier, R. Fischer *et al.*, Plasma Physics and Controlled Fusion **56** (2014) 025008, ISSN 0741-3335, doi:10.1088/0741-3335/56/2/025008, URL https://iopscience.iop.org/article/10.1088/0741-3335/56/2/025008 3.5.1, 3.5.1, 3.5.2, 3.5.2, 5.1.1, 5.1.2

[282] R. Fischer, E. Wolfrum, and J. Schweinzer, Plasma Physics and Controlled Fusion **50** (2008) 085009, ISSN 0741-3335, doi:10.1088/0741-3335/50/8/085009, URL https://iopscience.iop.org/article/10.1088/0741-3335/50/8/085009 3.5.1, 5.1.4

[283] A. Mlynek, G. Schramm, H. Eixenberger *et al.*, Review of Scientific Instruments **81** (2010) 033507, ISSN 0034-6748, doi:10.1063/1.3340944, URL http://aip.scitation.org/doi/10.1063/1.3340944 3.5.2

[284] M. Greenwald, Plasma Physics and Controlled Fusion **44** (2002) 201, ISSN 07413335, doi:10.1088/0741-3335/44/8/201, URL https://iopscience.iop.org/article/10.1088/0741-3335/44/8/201 3.5.2, 4.1.2

[285] H. Johnsen, H. L. Pecseli, and J. Trulsen, Plasma Physics and Controlled Fusion **28** (1986) 1519–1523, ISSN 0741-3335, doi:10.1088/0741-3335/28/9B/008, URL https://iopscience.iop.org/article/10.1088/0741-3335/28/9B/008 3.5.2, 5.1.2

[286] H. Johnsen, H. L. Pécseli, and J. Trulsen, Physics of Fluids **30** (1987) 2239, ISSN 00319171, doi:10.1063/1.866158, URL https://aip.scitation.org/doi/10.1063/1.866158 3.5.2, 5.1.2

[287] B. Kurzan and H. D. Murmann, Review of Scientific Instruments **82** (2011) 103501, ISSN 0034-6748, doi:10.1063/1.3643771, URL http://aip.scitation.org/doi/10.1063/1.3643771 3.5.3, 5.1.4

[288] C. Theiler, I. Furno, P. Ricci *et al.*, Physical Review Letters **103** (2009) 065001, ISSN 0031-9007, doi:10.1103/PhysRevLett.103.065001, URL https://link.aps.org/doi/10.1103/PhysRevLett.103.065001 3.5.3

[289] D. Carralero, P. Manz, L. Aho-Mantila *et al.*, Physical Review Letters **115** (2015) 215002, ISSN 0031-9007,

doi:10.1103/PhysRevLett.115.215002, URL https://link.aps.org/doi/10.1103/PhysRevLett.115.215002 3.6, 3.6

[290] B. LaBombard, R. L. Boivin, M. Greenwald *et al.*, Physics of Plasmas **8** (2001) 2107–2117, ISSN 1070-664X, doi:10.1063/1.1352596, URL http://aip.scitation.org/doi/10.1063/1.1352596 3.6

[291] M. V. Umansky, S. I. Krasheninnikov, B. LaBombard *et al.*, Physics of Plasmas **5** (1998) 3373–3376, ISSN 1070-664X, doi:10.1063/1.873051, URL http://aip.scitation.org/doi/10.1063/1.873051 3.6

[292] D. A. D'Ippolito, J. R. Myra, and S. I. Krasheninnikov, Physics of Plasmas **9** (2002) 222–233, ISSN 1070-664X, doi:10.1063/1.1426394, URL http://aip.scitation.org/doi/10.1063/1.1426394 3.6

[293] D. Carralero, H. Müller, M. Groth *et al.*, Journal of Nuclear Materials **463** (2015) 123–127, ISSN 00223115, doi:10.1016/j.jnucmat.2014.10.019, URL https://linkinghub.elsevier.com/retrieve/pii/S002231151400703X 3.6, 3.11

[294] N. Vianello, D. Carralero, C. Tsui *et al.*, Nuclear Fusion **60** (2020) 016001, ISSN 0029-5515, doi:10.1088/1741-4326/ab423e, URL https://iopscience.iop.org/article/10.1088/1741-4326/ab423e 3.6

[295] D. Carralero, S. Artene, M. Bernert *et al.*, Nuclear Fusion **58** (2018) 096015, ISSN 0029-5515, doi:10.1088/1741-4326/aacb04, URL https://iopscience.iop.org/article/10.1088/1741-4326/aacb04 3.6, 3.7

[296] D. Carralero, M. Siccinio, M. Komm *et al.*, Nuclear Fusion **57** (2017) 056044, ISSN 0029-5515, doi:10.1088/1741-4326/aa64b3, URL https://iopscience.iop.org/article/10.1088/1741-4326/aa64b3 3.6

[297] H. Bolt, V. Barabash, G. Federici *et al.*, Journal of Nuclear Materials **307-311** (2002) 43–52, ISSN 00223115, doi:10.1016/S0022-3115(02)01175-3, URL https://linkinghub.elsevier.com/retrieve/pii/S0022311502011753 3.7

[298] D. Naujoks, K. Asmussen, M. Bessenrodt-Weberpals *et al.*, Nuclear Fusion **36** (1996) 671–687, ISSN 0029-5515, doi:10.1088/0029-5515/36/6/I01, URL https://iopscience.iop.org/article/10.1088/0029-5515/36/6/I01 3.7, 3.7.2

[299] K. Schmid, M. Mayer, C. Adelhelm *et al.*, Nuclear Fusion **50** (2010) 105004, ISSN 0029-5515, doi:10.1088/0029-5515/50/10/105004, URL https://iopscience.iop.org/article/10.1088/0029-5515/50/10/105004 3.7

[300] C. García-Rosales, W. Eckstein, and J. Roth, Journal of Nuclear Materials **218** (1995) 8–17, ISSN 00223115, doi:10.1016/0022-3115(94)00376-9, URL https://linkinghub.elsevier.com/retrieve/pii/0022311594003769 3.7

[301] W. Eckstein, C. Garcia-Rosales, J. Roth *et al.*, *Sputtering Data* (1993), URL https://hdl.handle.net/11858/00-001M-0000-0027-6324-6 3.7

[302] W. Eckstein, *Calculated Sputtering, Reflection and Range Values* (2002), URL https://hdl.handle.net/11858/00-001M-0000-0027-4522-5 3.7

[303] A. Thoma, K. Asmussen, R. Dux *et al.*, Plasma Physics and Controlled Fusion **39** (1997) 1487–1499, ISSN 0741-3335, doi:10.1088/0741-3335/39/9/014, URL https://iopscience.iop.org/article/10.1088/0741-3335/39/9/014 3.7.2

[304] R. Dux, V. Bobkov, A. Herrmann *et al.*, Journal of Nuclear Materials **390-391** (2009) 858–863, ISSN 00223115, doi:10.1016/j.jnucmat.2009.01.225, URL https://linkinghub.elsevier.com/retrieve/pii/S0022311509002529 3.7.2

[305] G. Matthews, G. McCracken, P. Sewell *et al.*, Journal of Nuclear Materials **145-147** (1987) 225–230, ISSN 00223115, doi:10.1016/0022-3115(87)90332-1, URL https://linkinghub.elsevier.com/retrieve/pii/0022311587903321 3.7.3

[306] M. Kocan, J. Gunn, V. Fuchs *et al.*, Journal of Nuclear Materials **438** (2013) S501–S504, ISSN 00223115, doi:10.1016/j.jnucmat.2013.01.103, URL https://linkinghub.elsevier.com/retrieve/pii/S0022311513001116 3.7.3

[307] J. P. Gunn, Plasma Physics and Controlled Fusion **54** (2012) 085007, ISSN 0741-3335, doi:10.1088/0741-3335/54/8/085007, URL https://iopscience.iop.org/article/10.1088/0741-3335/54/8/085007 3.7.3

[308] G. Matthews, R. Pitts, G. McCracken *et al.*, Nuclear Fusion **31** (1991) 1495–1509, ISSN 0029-5515, doi:10.1088/0029-5515/31/8/007, URL https://iopscience.iop.org/article/10.1088/0029-5515/31/8/007 3.7.3

[309] A. Herrmann, A. Kirk, A. Schmid *et al.*, Journal of Nuclear Materials **363-365** (2007) 528–533, ISSN 00223115, doi:10.1016/j.jnucmat.2006.12.041, URL https://linkinghub.elsevier.com/retrieve/pii/S0022311506006507 3.7.3

[310] H. Müller, J. Adamek, R. Cavazzana *et al.*, Nuclear Fusion **51** (2011) 073023, ISSN 0029-5515, doi:10.1088/0029-5515/51/7/073023, URL https://iopscience.iop.org/article/10.1088/0029-5515/51/7/073023 3.7.3

[311] H. Maier, Journal of Nuclear Materials **335** (2004) 515–519, ISSN 00223115, doi:10.1016/j.jnucmat.2004.09.002, URL https://linkinghub.elsevier.com/retrieve/pii/S0022311504006968 3.7.3

[312] F. Ryter, M. Cavedon, T. Happel *et al.*, Plasma Physics and Controlled Fusion **58** (2016) 014007, ISSN 0741-3335, doi:10.1088/0741-3335/58/1/014007, URL https://iopscience.iop.org/article/10.1088/0741-3335/58/1/014007 4.1.1, 4.2.1, 4.2.3, 4.2.3, 4.3.2

[313] P. Gohil, T. Evans, M. Fenstermacher *et al.*, Nuclear Fusion **51** (2011) 103020, ISSN 0029-5515, doi:10.1088/0029-5515/51/10/103020, URL https://iopscience.iop.org/article/10.1088/0029-5515/51/10/103020 4.1.1, 4.1.1, 4.1.3, 4.1.7

[314] R. Behn, B. Labit, B. P. Duval *et al.*, Plasma Physics and Controlled Fusion **57** (2015) 025007, ISSN 0741-3335, doi:10.1088/0741-3335/57/2/025007, URL https://iopscience.iop.org/article/10.1088/0741-3335/57/2/025007 4.1.1, 4.1.1

[315] L. Shao, G. Xu, Y. Yu *et al.*, Nuclear Fusion **61** (2021) 016010, ISSN 0029-5515, doi:10.1088/1741-4326/abbf34, URL https://iopscience.iop.org/article/10.1088/1741-4326/abbf34 4.1.1

[316] U. Plank, T. Pütterich, C. Angioni *et al.*, Nuclear Fusion **60** (2020) 074001, ISSN 0029-5515, doi:10.1088/1741-4326/ab8e11, URL https://iopscience.iop.org/article/10.1088/1741-4326/ab8e11 4.1.1

[317] E. Solano, G. Birkenmeier, E. Delabie *et al.*, Nuclear Fusion **61** (2021) 124001, ISSN 0029-5515, doi:10.1088/1741-4326/ac2b76, URL https://iopscience.iop.org/article/10.1088/1741-4326/ac2b76 4.1.1

[318] B. Zhang, X. Gong, J. Qian *et al.*, Nuclear Fusion **60** (2020) 092001, ISSN 0029-5515, doi:10.1088/1741-4326/ab9be6, URL https://iopscience.iop.org/article/10.1088/1741-4326/ab9be6 4.1.1

[319] E. Righi, D. Bartlett, J. Christiansen *et al.*, Nuclear Fusion **39** (1999) 309–319, ISSN 0029-5515, doi:10.1088/0029-5515/39/3/302, URL https://iopscience.iop.org/article/10.1088/0029-5515/39/3/302 4.1.1, 4.2

[320] G. F. Matthews, M. Beurskens, S. Brezinsek *et al.*, Physica Scripta **T145** (2011) 014001, ISSN 0031-8949, doi:10.1088/0031-8949/2011/T145/014001, URL https://iopscience.iop.org/article/10.1088/0031-8949/2011/T145/014001 4.1.1

[321] J. Roth, E. Tsitrone, A. Loarte *et al.*, Journal of Nuclear Materials **390-391** (2009) 1–9, ISSN 00223115, doi:10.1016/j.jnucmat.2009.01.037, URL https://linkinghub.elsevier.com/retrieve/pii/S0022311509000506 4.1.1

[322] J. Roth, E. Tsitrone, T. Loarer *et al.*, Plasma Physics and Controlled Fusion **50** (2008) 103001, ISSN 0741-3335, doi:10.1088/0741-3335/50/10/103001, URL https://iopscience.iop.org/article/10.1088/0741-3335/50/10/103001 4.1.1

[323] G. Birkenmeier, E. R. Solano, I. S. Carvalho *et al.*, Plasma Physics and Controlled Fusion **65** (2023) 054001, ISSN 0741-3335, doi:10.1088/1361-6587/acc423, URL https://iopscience.iop.org/article/10.1088/1361-6587/acc423 4.3, 4.1.1, 4.4, 4.1.1, 4.10, 4.11, 4.12, 4.3.2

[324] G. Birkenmeier, E. Solano, E. Lerche *et al.*, Nuclear Fusion **62** (2022) 086005, ISSN 0029-5515, doi:10.1088/1741-4326/ac6d6b, URL https://iopscience.iop.org/article/10.1088/1741-4326/ac6d6b 4.1.1, 4.2.3

[325] E. Lerche, M. Goniche, P. Jacquet *et al.*, Nuclear Fusion **56** (2016) 036022, ISSN 0029-5515, doi:10.1088/0029-5515/56/3/036022, URL https://iopscience.iop.org/article/10.1088/0029-5515/56/3/036022 4.1.1

[326] C. Guillemaut, A. Jardin, J. Horacek *et al.*, Physica Scripta **T167** (2016) 014005, ISSN 0031-8949, doi:10.1088/0031-8949/2015/T167/014005, URL https://iopscience.iop.org/article/10.1088/0031-8949/2015/T167/014005 4.1.1

[327] C. Maggi, E. Delabie, T. Biewer *et al.*, Nuclear Fusion **54** (2014) 023007, ISSN 0029-5515, doi:10.1088/0029-5515/54/2/023007, URL https://iopscience.iop.org/article/10.1088/0029-5515/54/2/023007 4.1.1, 4.1.2, 4.1.3, 4.1.4, 4.1.4, 4.1.6, 4.1.7, 4.2.1, 4.2.2, 4.2.4, 4.3.3

[328] A. Nielsen, G. Xu, J. Madsen *et al.*, Physics Letters A **379** (2015) 3097–3101, ISSN 03759601, doi:10.1016/j.physleta.2015.10.004, URL https://linkinghub.elsevier.com/retrieve/pii/S0375960115008592 4.1.1

[329] Y. Andrew, R. Sartori, E. Righi *et al.*, Plasma Physics and Controlled Fusion **48** (2006) 479–488, ISSN 0741-3335, doi:10.1088/0741-3335/48/4/001, URL https://iopscience.iop.org/article/10.1088/0741-3335/48/4/001 4.1.2, 4.1.4

[330] Z. Yan, G. R. Mckee, P. Gohil *et al.*, Physics of Plasmas **26** (2019) 062507, ISSN 1070-664X, doi:10.1063/1.5091701, URL http://aip.scitation.org/doi/10.1063/1.5091701 4.1.2

[331] Y. Andrew, T. M. Biewer, K. Crombe *et al.*, Plasma Physics and Controlled Fusion **50** (2008) 124053, ISSN 0741-3335, doi:10.1088/0741-3335/50/12/124053, URL https://iopscience.iop.org/article/10.1088/0741-3335/50/12/124053 4.1.3, 4.2.1, 4.2.2

[332] P. Gohil, T. Jernigan, T. Osborne *et al.*, Nuclear Fusion **50** (2010) 064011, ISSN 0029-5515, doi:10.1088/0029-5515/50/6/064011, URL https://iopscience.iop.org/article/10.1088/0029-5515/50/6/064011 4.1.3, 4.1.5, 4.8

[333] Y. Ma, J. W. Hughes, A. E. Hubbard *et al.*, Plasma Physics and Controlled Fusion **54**, ISSN 07413335, doi:10.1088/0741-3335/54/8/082002 4.1.3

[334] Y. Andrew, N. C. Hawkes, M. G. O'Mullane *et al.*, Plasma Physics and Controlled Fusion **46** (2004) A87–A93, ISSN 0741-3335, doi:10.1088/0741-3335/46/5A/009, URL https://iopscience.iop.org/article/10.1088/0741-3335/46/5A/009 4.1.3, 4.1.4, 4.2.1, 4.2.2

[335] L. D. Horton, Plasma Physics and Controlled Fusion **42** (2000) A37–A49, ISSN 0741-3335, doi:10.1088/0741-3335/42/5A/303, URL https://iopscience.iop.org/article/10.1088/0741-3335/42/5A/303 4.1.3, 4.2.2

[336] J. C. Hillesheim, E. Delabie, E. R. Solano *et al.*, in *2016 IAEA Fusion Energy Conference, Kyoto, EX/5-2*, 2016 IAEA Fusion Energy Conference, Kyoto (2016), URL https://nucleus.iaea.org/sites/fusionportal/Shared%20Documents/FEC%202018/fec2018-preprints/preprint0346.pdf 4.1.3, 4.1.5, 4.2.1, 4.3.2

[337] D. Moulton, G. Corrigan, J. Harrison *et al.*, Nuclear Fusion **58** (2018) 096029, ISSN 0029-5515, doi:10.1088/1741-4326/aacf0f, URL https://iopscience.iop.org/article/10.1088/1741-4326/aacf0f 4.1.3

[338] J. W. Hughes, A. E. Hubbard, D. A. Mossessian *et al.*, Fusion Science and Technology **51** (2007) 317–341, ISSN 1536-1055, doi:10.13182/FST07-A1425, URL https://www.tandfonline.com/doi/full/10.13182/FST07-A1425 4.1.3

[339] L. Chen, G. S. Xu, N. Yan *et al.*, Physics of Plasmas **25** (2018) 072504, ISSN 1070-664X, doi:10.1063/1.5033983, URL http://aip.scitation.org/doi/10.1063/1.5033983 4.1.3

[340] C. Bourdelle, C. Maggi, L. Chôné *et al.*, Nuclear Fusion **54** (2014) 022001, ISSN 0029-5515, doi:10.1088/0029-5515/54/2/022001, URL https://iopscience.iop.org/article/10.1088/0029-5515/54/2/022001 4.1.6

[341] T. Takizuka, Plasma Physics and Controlled Fusion **46** (2004) A227–A233, ISSN 0741-3335, doi:10.1088/0741-3335/46/5A/024, URL https://iopscience.iop.org/article/10.1088/0741-3335/46/5A/024 4.1.6

[342] M. Willensdorfer, U. Plank, D. Brida *et al.*, Physics of Plasmas **29** (2022) 032506, ISSN 1070-664X, doi:10.1063/5.0073841, URL https://aip.scitation.org/doi/10.1063/5.0073841 4.1.7

[343] A. Aydemir, Nuclear Fusion **52** (2012) 063026, ISSN 0029-5515, doi:10.1088/0029-5515/52/6/063026, URL https://iopscience.iop.org/article/10.1088/0029-5515/52/6/063026 4.1.7

[344] B. A. Carreras, L. W. Owen, R. Maingi *et al.*, Physics of Plasmas **5** (1998) 2623–2636, ISSN 1070-664X, doi:10.1063/1.872949, URL http://aip.scitation.org/doi/10.1063/1.872949 4.1.7

[345] A. R. Field, P. G. Carolan, N. J. Conway *et al.*, Plasma Physics and Controlled Fusion **46** (2004) 981–1007, ISSN 0741-3335, doi:10.1088/0741-3335/46/6/005, URL https://iopscience.iop.org/article/10.1088/0741-3335/46/6/005 4.1.7, 4.3.2

[346] L. Frassinetti, M. N. A. Beurskens, R. Scannell *et al.*, Review of Scientific Instruments **83** (2012) 013506, ISSN 0034-6748, doi:10.1063/1.3673467, URL http://aip.scitation.org/doi/10.1063/1.3673467 4.2.1

[347] C. F. Maggi, H. Weisen, J. C. Hillesheim *et al.*, Plasma Physics and Controlled Fusion **60** (2018) 014045, ISSN 0741-3335, doi:10.1088/1361-6587/aa9901, URL https://iopscience.iop.org/article/10.1088/1361-6587/aa9901 4.2.1, 4.2.2

[348] U. Plank, R. M. McDermott, G. Birkenmeier *et al.*, Plasma Physics and Controlled Fusion **65** (2022) 014001, ISSN 0741-3335, doi:10.1088/1361-6587/aca35b, URL https://iopscience.iop.org/article/10.1088/1361-6587/aca35b 4.2.1, 4.3.3

[349] E. de la Luna, J. Sánchez, V. Tribaldos *et al.*, Review of Scientific Instruments **75** (2004) 3831–3833, ISSN 0034-6748, doi:10.1063/1.1781376, URL http://aip.scitation.org/doi/10.1063/1.1781376 4.2.1

[350] H. Meyer, E. Delabie, C. F. Maggi *et al.*, in *41th EPS Conference on Plasma Physics*, Proceedings of the 41th EPS Conference on Plasma Physics, Berlin (2014), URL http://ocs.ciemat.es/EPS2014PAP/pdf/P1.013.pdf 4.2.1, 4.3.3

[351] E. Righi, Plasma Physics and Controlled Fusion **40** (1998) 857–861, ISSN 0741-3335, doi:10.1088/0741-3335/40/5/056, URL https://iopscience.iop.org/article/10.1088/0741-3335/40/5/056 4.2.1

[352] A. E. Hubbard, R. L. Boivin, J. F. Drake *et al.*, Plasma Physics and Controlled Fusion **40** (1998) 689–692, ISSN 0741-3335, doi:10.1088/0741-3335/40/5/024, URL https://iopscience.iop.org/article/10.1088/0741-3335/40/5/024 4.2.1, 4.4.2

[353] J. W. Connor and H. R. Wilson, Plasma Physics and Controlled Fusion **42** (2000) R1–R74, ISSN 0741-3335, doi:10.1088/0741-3335/42/1/201, URL https://iopscience.iop.org/article/10.1088/0741-3335/42/1/201 4.2.1, 4.4, 4.5

[354] N. Bonanomi, C. Angioni, P. Crandall *et al.*, Nuclear Fusion **59** (2019) 126025, ISSN 0029-5515, doi:10.1088/1741-4326/ab3ecc, URL https://iopscience.iop.org/article/10.1088/1741-4326/ab3ecc 4.2.2, 4.3.4

[355] P. Schneider, A. Bustos, P. Hennequin *et al.*, Nuclear Fusion **57** (2017) 066003, ISSN 0029-5515, doi:10.1088/1741-4326/aa65b3, URL https://iopscience.iop.org/article/10.1088/1741-4326/aa65b3 4.2.2

[356] W. Suttrop, M. Kaufmann, H. J. de Blank *et al.*, Plasma Physics and Controlled Fusion **39** (1997) 2051–2066, ISSN 0741-3335, doi:10.1088/0741-3335/39/12/008, URL https://iopscience.iop.org/article/10.1088/0741-3335/39/12/008 4.2.2

[357] M. Schmidtmayr, J. Hughes, F. Ryter *et al.*, Nuclear Fusion **58** (2018) 056003, ISSN 0029-5515, doi:10.1088/1741-4326/aaaed0, URL https://iopscience.iop.org/article/10.1088/1741-4326/aaaed0 4.2.3, 4.3.2

[358] R. Bilato, C. Angioni, G. Birkenmeier *et al.*, Nuclear Fusion **60** (2020) 124003, ISSN 0029-5515, doi:10.1088/1741-4326/abb540, URL https://iopscience.iop.org/article/10.1088/1741-4326/abb540 4.2.3, 4.3.1, 4.3.1, 3, 4.3.1, 4.3.3, 4.3.4

[359] M. Willensdorfer, E. Wolfrum, A. Scarabosio *et al.*, Nuclear Fusion **52** (2012) 114026, ISSN 0029-5515, doi:10.1088/0029-5515/52/11/114026, URL https://iopscience.iop.org/article/10.1088/0029-5515/52/11/114026 4.2.4

[360] S. Kaye, M. Greenwald, U. Stroth *et al.*, Nuclear Fusion **37** (1997) 1303–1328, ISSN 0029-5515, doi:10.1088/0029-5515/37/9/I10, URL https://iopscience.iop.org/article/10.1088/0029-5515/37/9/I10 4.3.1

[361] P. Vincenzi, E. R. Solano, E. Delabie *et al.*, Plasma Physics and Controlled Fusion **64** (2022) 124004, ISSN 0741-3335, doi:10.1088/1361-6587/ac97c0, URL https://iopscience.iop.org/article/10.1088/1361-6587/ac97c0 4.3.1, 4.3.2

[362] E. A. Belli, G. W. Hammett, and W. Dorland, Physics of Plasmas **15** (2008) 092303, ISSN 1070-664X, doi:10.1063/1.2972160, URL http://aip.scitation.org/doi/10.1063/1.2972160 4.3.2

[363] G. M. Staebler, J. Candy, E. A. Belli *et al.*, Plasma Physics and Controlled Fusion **63** (2021) 015013, ISSN 0741-3335, doi:10.1088/1361-6587/abc861, URL https://iopscience.iop.org/article/10.1088/1361-6587/abc861 4.3.2

[364] C. Silva, E. Solano, J. Hillesheim *et al.*, Nuclear Fusion **61** (2021) 126006, ISSN 0029-5515, doi:10.1088/1741-4326/ac2abb, URL https://iopscience.iop.org/article/10.1088/1741-4326/ac2abb 4.3.3

[365] C. Silva, E. Solano, J. Hillesheim *et al.*, Nuclear Fusion **62** (2022) 126057, ISSN 0029-5515, doi:10.1088/1741-4326/ac97f4, URL https://iopscience.iop.org/article/10.1088/1741-4326/ac97f4 4.3.3

[366] H. Biglari, P. H. Diamond, and P. W. Terry, Physics of Fluids B: Plasma Physics **2** (1990) 1–4, ISSN 0899-8221, doi:10.1063/1.859529, URL http://aip.scitation.org/doi/10.1063/1.859529 4.3.4

[367] P. W. Terry, Reviews of Modern Physics **72** (2000) 109–165, ISSN 0034-6861, doi:10.1103/RevModPhys.72.109, URL https://link.aps.org/doi/10.1103/RevModPhys.72.109 4.3.4

[368] T. Eich, P. Manz, and the ASDEX Upgrade team, Nuclear Fusion **61** (2021) 086017, ISSN 0029-5515, doi:10.1088/1741-4326/ac0412, URL https://iopscience.iop.org/article/10.1088/1741-4326/ac0412 4.3.4, 4.3.4, 4.4.2

[369] P. Schneider, E. Wolfrum, R. Groebner *et al.*, Nuclear Fusion **53** (2013) 073039, ISSN 0029-5515, doi:10.1088/0029-5515/53/7/073039, URL https://iopscience.iop.org/article/10.1088/0029-5515/53/7/073039 4.3.4

[370] J. Garcia, T. Görler, and F. Jenko, Physics of Plasmas **25** (2018) 055902, ISSN 1070-664X, doi:10.1063/1.5016331, URL http://aip.scitation.org/doi/10.1063/1.5016331 4.3.4

[371] W. Zholobenko, A. Stegmeir, T. Body *et al.*, Contributions to Plasma Physics **60**, ISSN 0863-1042, doi:10.1002/ctpp.201900131, URL https://onlinelibrary.wiley.com/doi/10.1002/ctpp.201900131 4.3.4, 4.5, 7

[372] Y. H. Xu, C. X. Yu, J. R. Luo *et al.*, Physical Review Letters **84** (2000) 3867–3870, ISSN 0031-9007, doi:10.1103/PhysRevLett.84.3867, URL https://link.aps.org/doi/10.1103/PhysRevLett.84.3867 4.4.1, 5.2.1

[373] I. Cziegler, G. Tynan, P. Diamond *et al.*, Nuclear Fusion **55** (2015) 083007, ISSN 0029-5515, doi:10.1088/0029-5515/55/8/083007, URL https://iopscience.iop.org/article/10.1088/0029-5515/55/8/083007 4.4.1, 5.2.1

[374] I. Cziegler, G. R. Tynan, P. H. Diamond *et al.*, Plasma Physics and Controlled Fusion **56** (2014) 075013, ISSN 0741-3335, doi:10.1088/0741-3335/56/7/075013, URL https://iopscience.iop.org/article/10.1088/0741-3335/56/7/075013 4.4.1, 5.2.1

[375] W. Fundamenski, F. Militello, D. Moulton *et al.*, Nuclear Fusion **52** (2012) 062003, ISSN 0029-5515, doi:10.1088/0029-5515/52/6/062003, URL https://iopscience.iop.org/article/10.1088/0029-5515/52/6/062003 4.4.1

[376] T. Kobayashi, Nuclear Fusion **60** (2020) 095001, ISSN 0029-5515, doi:10.1088/1741-4326/ab7a67, URL https://iopscience.iop.org/article/10.1088/1741-4326/ab7a67 4.4.1

[377] M. A. Malkov, P. H. Diamond, K. Miki *et al.*, Physics of Plasmas **22** (2015) 032506, ISSN 1070-664X, doi:10.1063/1.4914934, URL http://aip.scitation.org/doi/10.1063/1.4914934 4.4.1, 5.2.1

[378] C. Chang, S. Ku, G. Tynan *et al.*, Physical Review Letters **118** (2017) 175001, ISSN 0031-9007, doi:10.1103/PhysRevLett.118.175001, URL http://link.aps.org/doi/10.1103/PhysRevLett.118.175001 4.4.1, 4.5, 7

[379] B. LaBombard, J. Hughes, D. Mossessian *et al.*, Nuclear Fusion **45** (2005) 1658–1675, ISSN 0029-5515, doi:10.1088/0029-5515/45/12/022, URL https://iopscience.iop.org/article/10.1088/0029-5515/45/12/022 4.4.2

[380] B. N. Rogers, J. F. Drake, and A. Zeiler, Physical Review Letters **81** (1998) 4396–4399, ISSN 0031-9007, doi:10.1103/PhysRevLett.81.4396, URL https://link.aps.org/doi/10.1103/PhysRevLett.81.4396 4.4.2

[381] E. R. Solano and R. D. Hazeltine, Nuclear Fusion **52** (2012) 114017, ISSN 0029-5515, doi:10.1088/0029-5515/52/11/114017, URL https://iopscience.iop.org/article/10.1088/0029-5515/52/11/114017 4.4.3

[382] G. D. Conway, J. Schirmer, S. Klenge *et al.*, Plasma Physics and Controlled Fusion **46** (2004) 951–970, ISSN 0741-3335, doi:10.1088/0741-3335/46/6/003, URL https://iopscience.iop.org/article/10.1088/0741-3335/46/6/003 5.1.1

[383] G. M. Staebler and R. J. Groebner, Plasma Physics and Controlled Fusion **57** (2015) 014025, ISSN 0741-3335, doi:10.1088/0741-3335/57/1/014025, URL https://iopscience.iop.org/article/10.1088/0741-3335/57/1/014025 5.1.4, 5.1.4

[384] Y. B. Kim, P. H. Diamond, and R. J. Groebner, Physics of Fluids B: Plasma Physics **3** (1991) 2050–2060, ISSN 0899-8221, doi:10.1063/1.859671, URL http://aip.scitation.org/doi/10.1063/1.859671 5.1.4, 5.1.4, 5.1.4

[385] K. Miki, P. H. Diamond, O. D. Gürcan *et al.*, Physics of Plasmas **19** (2012) 092306, ISSN 1070-664X, doi:10.1063/1.4753931, URL http://aip.scitation.org/doi/10.1063/1.4753931 5.1.4

[386] N. Vianello, Proceedings of the 42nd EPS Conference on Plasma Physics, Lisbon (2015), URL http://ocs.ciemat.es/EPS2015PAP/pdf/P2.133.pdf 5.1.4

[387] R. Fischer, C. J. Fuchs, B. Kurzan *et al.*, Fusion Science and Technology **58** (2010) 675–684, ISSN 1536-1055, doi:10.13182/FST10-110, URL https://www.tandfonline.com/doi/full/10.13182/FST10-110 5.1.4, 6.3.1

[388] G. Birkenmeier, T. Happel, P. Hennequin *et al.*, in *44th Conference on Plasma Physics*, Proceedings of the 44th EPS Conference on Plasma Physics, Belfast (2017), URL http://ocs.ciemat.es/eps2017pap/pdf/P1.166.pdf 5.11, 5.12

[389] C. Torrence and G. P. Compo, Bulletin of the American Meteorological Society **79** (1998) 61–78, ISSN 0003-0007, doi:10.1175/1520-0477(1998)079<0061:APGTWA>2.0.CO;2, URL http://journals.ametsoc.org/doi/10.1175/1520-0477(1998)079<0061:APGTWA>2.0.CO;2 5.1.5

[390] K. Miki and P. Diamond, Nuclear Fusion **51** (2011) 103003, ISSN 0029-5515, doi:10.1088/0029-5515/51/10/103003, URL https://iopscience.iop.org/article/10.1088/0029-5515/51/10/103003 5.2.1

[391] M. Sasaki, K. Itoh, S.-I. Itoh *et al.*, Nuclear Fusion **52** (2012) 023009, ISSN 0029-5515, doi:10.1088/0029-5515/52/2/023009, URL https://iopscience.iop.org/article/10.1088/0029-5515/52/2/023009 5.2.1

[392] M. A. Malkov, P. H. Diamond, and M. N. Rosenbluth, Physics of Plasmas **8** (2001) 5073–5076, ISSN 1070-664X, doi:10.1063/1.1415424, URL http://aip.scitation.org/doi/10.1063/1.1415424 5.2.1

[393] M. Xu, G. R. Tynan, P. H. Diamond *et al.*, Physical Review Letters **108** (2012) 245001, ISSN 0031-9007, doi:10.1103/PhysRevLett.108.245001, URL https://link.aps.org/doi/10.1103/PhysRevLett.108.245001 5.2.1

[394] G. S. Xu, H. Q. Wang, B. N. Wan *et al.*, Physics of Plasmas **19** (2012) 122502, ISSN 1070-664X, doi:10.1063/1.4769852, URL http://aip.scitation.org/doi/10.1063/1.4769852 5.2.1

[395] I. Cziegler, A. Hubbard, J. Hughes *et al.*, Physical Review Letters **118** (2017) 105003, ISSN 0031-9007, doi:10.1103/PhysRevLett.118.105003, URL https://link.aps.org/doi/10.1103/PhysRevLett.118.105003 5.2.1

[396] T. Kobayashi, K. Itoh, T. Ido *et al.*, Nuclear Fusion **57** (2017) 072005, ISSN 0029-5515, doi:10.1088/1741-4326/aa5d03, URL https://iopscience.iop.org/article/10.1088/1741-4326/aa5d03 5.2.1

[397] G. Grenfell, J. Adamek, M. Komm *et al.*, Review of Scientific Instruments **93** (2022) 023507, ISSN 0034-6748, doi:10.1063/5.0075846, URL https://aip.scitation.org/doi/10.1063/5.0075846 5.2.1

[398] P. Manz, G. Birkenmeier, G. Fuchert *et al.*, Physics of Plasmas **23** (2016) 052302, ISSN 1070-664X, doi:10.1063/1.4948787, URL http://aip.scitation.org/doi/10.1063/1.4948787 5.2.2, 5.14

[399] T. E. Stringer, Physical Review Letters **22** (1969) 770–774, ISSN 0031-9007, doi:10.1103/PhysRevLett.22.770, URL https://link.aps.org/doi/10.1103/PhysRevLett.22.770 5.2.2

[400] A. B. Hassam and J. F. Drake, Physics of Fluids B: Plasma Physics **5** (1993) 4022–4029, ISSN 0899-8221, doi:10.1063/1.860622, URL `http://aip.scitation.org/doi/10.1063/1.860622` 5.2.2

[401] O. Grover, submitted to Nuclear Fusion 5.2.2

[402] L. Cupido, S. Graca, G. D. Conway *et al.*, Review of Scientific Instruments **77** (2006) 10E915, ISSN 0034-6748, doi:10.1063/1.2235206, URL `http://aip.scitation.org/doi/10.1063/1.2235206` 5.2.3

[403] D. Eldon, R. L. Boivin, C. Chrystal *et al.*, Physics of Plasmas **22** (2015) 112506, ISSN 1070-664X, doi:10.1063/1.4935919, URL `http://aip.scitation.org/doi/10.1063/1.4935919` 5.2.3, 7

[404] J. W. Connor, Plasma Physics and Controlled Fusion **40** (1998) 191–213, ISSN 0741-3335, doi:10.1088/0741-3335/40/2/003, URL `https://iopscience.iop.org/article/10.1088/0741-3335/40/2/003` 5.2.3

[405] J. Seol and K. C. Shaing, Physics of Plasmas **20** (2013) 042504, ISSN 1070-664X, doi:10.1063/1.4795731, URL `http://aip.scitation.org/doi/10.1063/1.4795731` 5.2.3

[406] V. Parail, G. Bateman, M. Becoulet *et al.*, Plasma Physics Reports **29** (2003) 539–544, ISSN 1063-780X, doi:10.1134/1.1592551, URL `http://link.springer.com/10.1134/1.1592551` 5.2.3

[407] J. Galdon-Quiroga, J. Rivero-Rodriguez, M. Garcia-Munoz *et al.*, Journal of Instrumentation **12** (2017) C08023–C08023, ISSN 1748-0221, doi:10.1088/1748-0221/12/08/C08023, URL `https://iopscience.iop.org/article/10.1088/1748-0221/12/08/C08023` 6.1.2

[408] G. Birkenmeier, J. Galdon-Quiroga, V. Olevskaia *et al.*, Journal of Instrumentation **14** (2019) C10030–C10030, ISSN 1748-0221, doi:10.1088/1748-0221/14/10/C10030, URL `https://iopscience.iop.org/article/10.1088/1748-0221/14/10/C10030` 6.1.2, 6.1, 6.2.2, 6.4, 6.11, 6.13, 6.14, 6.15

[409] G. Birkenmeier, J. Galdon-Quiroga, V. Olevskaia *et al.*, Fusion Engineering and Design **168** (2021) 112644, ISSN 09203796, doi:10.1016/j.fusengdes.2021.112644, URL `https://linkinghub.elsevier.com/retrieve/pii/S0920379621004208` 6.1.2, 6.4.2

[410] M. Berta, G. Anda, M. Aradi *et al.*, Fusion Engineering and Design **88** (2013) 2875–2880, ISSN 09203796, doi:10.1016/j.fusengdes.2013.05.064, URL https://linkinghub.elsevier.com/retrieve/pii/S0920379613005048 6.1.2

[411] P. Hacek, M. Berta, G. Anda *et al.*, Review of Scientific Instruments **89** (2018) 113506, ISSN 0034-6748, doi:10.1063/1.5044529, URL http://aip.scitation.org/doi/10.1063/1.5044529 6.1.2

[412] A. V. Melnikov, L. G. Zimeleva, L. I. Krupnik *et al.*, Review of Scientific Instruments **68** (1997) 316–319, ISSN 0034-6748, doi:10.1063/1.1147859, URL http://aip.scitation.org/doi/10.1063/1.1147859 6.1.2

[413] A. Melnikov, L. Krupnik, L. Eliseev *et al.*, Nuclear Fusion **57** (2017) 072004, ISSN 0029-5515, doi:10.1088/1741-4326/aa5382, URL https://iopscience.iop.org/article/10.1088/1741-4326/aa5382 6.1.2

[414] T. Crowley, IEEE Transactions on Plasma Science **22** (1994) 291–309, ISSN 00933813, doi:10.1109/27.310636, URL http://ieeexplore.ieee.org/document/310636/ 6.1.2

[415] P. M. Schoch, A. Carnevali, K. A. Conner *et al.*, Review of Scientific Instruments **59** (1988) 1646–1651, ISSN 0034-6748, doi:10.1063/1.1140270, URL http://aip.scitation.org/doi/10.1063/1.1140270 6.1.2

[416] D. R. Demers, P. M. Schoch, T. P. Crowley *et al.*, Physics of Plasmas **8** (2001) 1278, ISSN 1070664X, doi:10.1063/1.1355674, URL http://scitation.aip.org/content/aip/journal/pop/8/4/10.1063/1.1355674 6.1.2

[417] A. Fujisawa, H. Iguchi, A. Taniike *et al.*, IEEE Transactions on Plasma Science **22** (1994) 395–402, ISSN 00933813, doi:10.1109/27.310646, URL http://ieeexplore.ieee.org/document/310646/ 6.1.2

[418] P. Oyola, J. Gonzalez-Martin, M. Garcia-Munoz *et al.*, Review of Scientific Instruments **92** (2021) 043558, ISSN 0034-6748, doi:10.1063/5.0043757, URL https://aip.scitation.org/doi/10.1063/5.0043757 6.2, 6.2.3, 6.5

[419] V. Olevskaia 6.2.1, 6.3, 6.7, 6.8, 6.9, 6.10, 6.3.3, 6.16, 6.17, 6.4.4

[420] W. Lotz, The Astrophysical Journal Supplement Series **14** (1967) 207, ISSN 0067-0049, doi:10.1086/190154, URL http://adsabs.harvard.edu/doi/10.1086/190154 6.2.2

[421] F. W. Meyer, Journal of Physics B: Atomic and Molecular Physics **13** (1980) 3823–3828, ISSN 0022-3700, doi:10.1088/0022-3700/13/19/020, URL https://iopscience.iop.org/article/10.1088/0022-3700/13/19/020 6.2.2

[422] F. Meyer and L. Anderson, Physics Letters A **54** (1975) 333–334, ISSN 03759601, doi:10.1016/0375-9601(75)90282-0, URL https://linkinghub.elsevier.com/retrieve/pii/0375960175902820 6.2.2

[423] F. Ebel and E. Salzborn, Journal of Physics B: Atomic and Molecular Physics **20** (1987) 4531–4542, ISSN 0022-3700, doi:10.1088/0022-3700/20/17/029, URL https://iopscience.iop.org/article/10.1088/0022-3700/20/17/029 6.2.2

[424] R. Girnius, L. Anderson, and E. Staab, Nuclear Instruments and Methods **143** (1977) 505–511, ISSN 0029554X, doi:10.1016/0029-554X(77)90239-7, URL https://linkinghub.elsevier.com/retrieve/pii/0029554X77902397 6.2.2

[425] D. R. Hertling, R. K. Feeney, D. W. Hughes *et al.*, Journal of Applied Physics **53** (1982) 5427–5434, ISSN 0021-8979, doi:10.1063/1.331472, URL http://aip.scitation.org/doi/10.1063/1.331472 6.2.2

[426] M. Higgins, *Report CLM-R294* (1989), URL https://www-amdis.iaea.org/ALADDIN/collision.html 6.2.2

[427] M. Cavedon, T. Pütterich, E. Viezzer *et al.*, Plasma Physics and Controlled Fusion **59** (2017) 105007, ISSN 0741-3335, doi:10.1088/1361-6587/aa7ad0, URL https://iopscience.iop.org/article/10.1088/1361-6587/aa7ad0 6.3.1

[428] G. Anda, D. Dunai, M. Lampert *et al.*, Review of Scientific Instruments **89** (2018) 013503, ISSN 0034-6748, doi:10.1063/1.5004126, URL http://aip.scitation.org/doi/10.1063/1.5004126 6.4.1, 6.4.1, 6.4.3

[429] G. Anda, D. Dunai, T. Krizsanóczi *et al.*, Fusion Engineering and Design **146** (2019) 1814–1819, ISSN 09203796, doi:10.1016/j.fusengdes.2019.03.042, URL https://linkinghub.elsevier.com/retrieve/pii/S0920379619303631 6.4.1

[430] S. Zoletnik, G. Anda, M. Aradi *et al.*, Review of Scientific Instruments **89** (2018) 10D107, ISSN 0034-6748, doi:10.1063/1.5039309, URL http://aip.scitation.org/doi/10.1063/1.5039309 6.4.1

[431] C. P. Chrobak, M. A. V. Zeeland, R. A. Moyer *et al.*, Review of Scientific Instruments **83** (2012) 10E514, ISSN 0034-6748, doi:10.1063/1.4733544, URL http://aip.scitation.org/doi/10.1063/1.4733544 6.4.2

[432] M. García-Muñoz, H.-U. Fahrbach, and H. Zohm, Review of Scientific Instruments **80** (2009) 053503, ISSN 0034-6748, doi:10.1063/1.3121543, URL http://aip.scitation.org/doi/10.1063/1.3121543 6.4.4

[433] M. Jiménez-Ramos, J. G. López, M. García-Muñoz *et al.*, Nuclear Instruments and Methods in Physics Research Section B: Beam Interactions with Materials and Atoms **332** (2014) 216–219, ISSN 0168583X, doi:10.1016/j.nimb.2014.02.064, URL https://linkinghub.elsevier.com/retrieve/pii/S0168583X14003218 6.4.4

[434] M. Rodriguez-Ramos, M. Garcia-Munoz, M. C. Jimenez-Ramos *et al.*, Plasma Physics and Controlled Fusion **59** (2017) 105009, ISSN 0741-3335, doi:10.1088/1361-6587/aa7e5f, URL https://iopscience.iop.org/article/10.1088/1361-6587/aa7e5f 6.4.4

[435] J. Toledo-Garrido, J. Galdon-Quiroga, E. Viezzer *et al.*, Journal of Instrumentation **17** (2022) P02026, ISSN 1748-0221, doi:10.1088/1748-0221/17/02/P02026, URL https://iopscience.iop.org/article/10.1088/1748-0221/17/02/P02026 6.4.4, 6.4.4

[436] K. Hallatschek and G. R. McKee, Physical Review Letters **109** (2012) 245001, ISSN 0031-9007, doi:10.1103/PhysRevLett.109.245001, URL https://link.aps.org/doi/10.1103/PhysRevLett.109.245001 7

[437] M. Siccinio, W. Biel, M. Cavedon *et al.*, Fusion Engineering and Design **156** (2020) 111603, ISSN 09203796, doi:10.1016/j.fusengdes.2020.111603, URL https://linkinghub.elsevier.com/retrieve/pii/S0920379620301514 7

List of Symbols

α_{neo}	Neoclassical prefactor for poloidal flow (collisionality dependent)
$\bar{n}$	Line-averaged density
$\bar{n}_{\text{e,edge}}$	Line-averaged edge electron density
$\bar{n}_{\text{e}}$	Line-averaged electron density
β_{pol}	Poloidal plasma beta
β_{e}	Electron plasma beta
$\beta_{\text{t,ped}}$	Beta for pedestal electron parameters
$\mathbf{B}$	Magnetic field vector
$\mathbf{E}$	Electric field vector
$\mathbf{g}$	Gravitational force vector
$\mathbf{u}_{\text{e}}$	Electron fluid velocity
$\mathbf{u}_{\text{i}}$	Ion fluid velocity
$\mathbf{v}$	Velocity vector
$\boldsymbol{\kappa}$	Curvature vector
χ_{eff}	One fluid heat diffusivity
χ_{i}	Ion heat diffusivity
δB	Magnetic field perturbation
$\delta I/I$	Relative intensity perturbation
Δj_{b}	Birth profile of secondary beams

δn Density perturbation

δx Apparent radial blob width

δ Deflection of secondary beams on the i-HIBP scintillator

δ_* Most stable blob scale

δ_{se} Secondary electron coefficient

δ_{b} Vertical blob size or poloidal blob width

$\dot{B}_{\mathrm{r}}$ Time derivative of the radial magnetic field

$\dot{B}_\theta$ Time derivative of the poloidal magnetic field

ϵ_0 Vacuum permittivity

γ Adiabatic index

γ_{t} Growth rate of most unstable turbulent mode

κ_{e} Plasma elongation

κ_{g} Geodesic curvature

λ_{ei} Mean free path of electron unless colliding with ions

$\langle \sigma v \rangle_{\mathrm{ei}}^{+}$ secondary ionization

$\langle \sigma v \rangle_{\mathrm{CX}}$ Rate coefficient of charge-exchange collisions

$\langle \sigma v \rangle_{\mathrm{ei}}$ Rate coefficient of electron impact ionization

$\langle \tilde{u}_{\mathrm{r}} \tilde{u}_\theta \rangle$ Reynolds stress

$\ln \Lambda$ Coulomb logarithm

$\mathbf{F}_{\mathrm{L}}$ Lorentz force vector, see equation 1.4

$\mathbf{F}_{\mathrm{r}}$ Restoring force

$\mathbf{R}_\kappa$ Curvature radius vector

$\mathbf{u}_\perp$ Fluid velocity perpendicular to the magnetic field

$\mathbf{v}_\kappa$ Curvature drift

$\mathbf{v}_{\nabla \mathrm{B}}$ ∇B drift

$\mathbf{v}_{\mathrm{dia}}$ Diamagnetic drift

$\mathbf{v}_{\mathrm{D}}$ Generalized magnetic drift

$\mathbf{v}_{\mathrm{E}}$ $E \times B$ drift

$\mathbf{v}_{\mathrm{g}}$ Gravitational drift

$\mathbf{v}_{\mathrm{pol}}$ Polarization drift

μ Temporal average of time trace

μ_{V} Viscosity

ν Collision frequency

ν^* Normalized collisionality

ν_{ei} Electron-ion collision frequency

ν_{ii} ion-ion collision frequency

$\nu_{\mathrm{neo,damp}}$ Neoclassical poloidal damping rate

ω_{SW} Sound wave frequency

ω_{t} Ion transit frequency

$\omega_{E\times B}$ $E \times B$ shearing rate

$\overline{n}_0$ Volume-averaged plasma density

$\overline{n}_{\mathrm{i}}$ Volume-averaged ion density

$\overline{T}$ Volume-averaged plasma temperature

$\overline{T}_{\mathrm{i}}$ Volume-averaged ion temperature

ρ Charge density

ρ_{e} Electron charge density

ρ_{i} Ion charge density

$\rho_{\mathrm{L,i}}$ Ion Larmor radius

ρ_{m} Mass density

ρ_{pol} Normalized poloidal flux coordinate

ρ_s	Drift scale or drift parameter
σ	Standard deviation
σ_ei	Electron impact ionization cross section
τ_ei	Collisional energy transfer time between electrons and ions
τ_E	Energy confinement time
τ_t	Turbulence autocorrelation time or eddy turn-over time
$\tau_{E\times B}$	$E \times B$ shearing time
$\tilde{\Omega}$	Generalized vorticity
$\tilde{n}$	Density fluctuation amplitude
a	Minor radius of the plasma
A_i	Ion mass number
B	Magnetic field strength (modulus of $\mathbf{B}$)
B_ϕ	Toroidal magnetic field
B_t	Toroidal magnetic field
$B_\mathrm{z,PS}$	Vertical magnetic field components generated by Pfirsch-Schlüter currents
B_θ	Poloidal magnetic field
c_s	Ion sound speed
D_p	Particle diffusion coefficient
e	Elementary charge (prevailing meaning of this symbol in this thesis)
e	Euler's number, $e \approx$2.71828, as in exponential functions
$E_\mathrm{r,dia}$	Diamagnetic part of the radial electric field
$E_\mathrm{r,min}$	Radial electric field in the minimum of the E_r profile
E_r	Radial electric field
f^{3D}	three-dimensional Maxwell-Boltzmann distribution

f_{blob} Blob frequency

f_{GW} Greenwald fraction

f_{M} Isotropic Maxwell-Boltzmann distribution

I_{b} Extracted beam current

I_{div} Divertor shunt current

I_{s} Heating current of the ion source

j_{p} Current density of the primary beam

j_{s} Current density of secondary beams

j_θ Poloidal current density

$k_\perp$ Perpendicular wavenumber

k_θ Poloidal wavenumber

l Coordinate along primary beam

L_{t} Turbulent correlation lengths

$L_{E\times B}$ $E \times B$ shear length

m Mass of a particle

m_{e} Electron mass

m_{i} Ion mass

n Number density, i.e. number of particles per volume

n_0 Background density

n_{e} Electron number density

n_{GW} Greenwald density

n_{i} Ion number density

n_{PFC} Density of the material of the plasma facing component

p Plasma pressure

P_{eq} Collisional energy transfer from electrons to ions

p_e Electron pressure

$P_\mathrm{heat,i}$ Ion heating provided by external heating systems

P_heat Heating power

P_in Input heating power as used in scaling laws

p_i Ion pressure

P_LH Power threshold of the L-H transition

P_loss Loss power i.e. $P_\mathrm{ohm} + P_\mathrm{aux} - \frac{dW}{dt}$

P_net Net heating power (same as P_loss)

P_sep Power through separatrix i.e. $P_\mathrm{loss} - P_\mathrm{rad}$

q Charge of a particle

q_s Safety factor

q_{95} Edge safety factor taken at ρ_pol =0.95

$Q_\mathrm{i,edge}$ Edge ion heat flow

$q_\mathrm{i,edge}$ Edge ion heat flux

$Q^\mathrm{crit}_\mathrm{i,edge}$ Critical edge ion heat flow

R Major radius of the plasma

S Surface area of the LFCS

s Coordinate along secondary beam

S_n Density source term of the continuity equation

$T_\mathrm{e,edge}$ Edge electron temperature

T_e Electron temperature

T_i Ion temperature

U_ex Extraction voltage

u_ph Phase velocity of turbulent structures

v_beam Beam velocity

v_b Blob propagation velocity

v_e Electron velocity

$v_\mathrm{r,mean}$ Average radial blob velocity

V_s Drop of the sheath potential

v_turb Turbulent velocity

$v_\mathrm{r,max}$ Maximum radial blob velocity

W Energy content of the plasma, $W \approx 3\overline{n}_0\overline{T}$

x_s Radial coordinate indicating the distance to the LCFS

Y Effective sputtering yield

Y_blob Sputtering yield for blob parameters

Z_eff Effective charge number

Z_i Ion charge number

^{0}n Neutron

^{4}He Helium 4 or alpha particle

Cs Cesium

D Deuterium

d Distance between two electrodes

eV Electron Volts

H Hydrogen

K Kelvin (temperature unit)

m Poloidal mode number

n Toroidal mode number

Rb Rubidium

T Tritium

Index

Acknowledgment

I would like to thank all the great persons, who contributed directly or indirectly to this habilitation thesis and who gave me support during my working hours and beyond:

- **Prof. Dr. Ulrich Stroth** for supporting me since the beginning of my career as a scientist and giving me the opportunity to do the habilitation at the TUM. He taught me how to teach and to think as a scientist, and I appreciate also his permanent support to reach my scientific and personal goals.

- **Prof. Dr. Eric Sonnendrücker and Prof. Dr. Peter Fierlinger** for their willingness to contribute to my habilitation as Fachmentors and for their considerate evaluation of the habilitation project.

- **Prof. Dr. Elisabeth Wolfrum** for her continuous and friendly support, especially for her sensitive support in difficult situations of all kind.

- **Dr. Michael "Adlerauge" Griener and Daniel Wendler** for reading and correcting my manuscript and for their support during teaching and examining students at the TUM.

- **Dr. Joaquin Galdon, Dr. Balázs Tál, Joey Kalis, Karlheinz Kaunert, Manfred Sochor, Pablo Oyola, Viktoriia Olevskaia, and Hannah Lindl** for their sedulous effort to get the i-HIBP developed, improved, running, controlled and cleaned, so that it - yes! - finally delivered a signal.

- **The whole AUG Team**, especially the vacuum group, the AUG vessel team, the AUG operations team, the video diagnostics group, the electric and electronic workshops for their efforts to get the intractable hardware of the i-HIBP running, and the friendly atmosphere in daily life with my great colleagues.

- **Dr. Gábor Anda, Gábor Gárdonyi** and the whole team at the Centre for Energy Research in Budapest for the development of the i-HIBP injector and their quick and tremendous support to operate the i-HIBP injector.

- **Prof. Dr. Eleonora Viezzer, Prof. Dr. Manuel García Muñoz, José Rueda Rueda** and the whole team at the Universty of Seville for

the development of the i-HIBP measurement principle, the tremendous effort to develop and run the i-HIBPsim code and for the characterization and manufacturing of the scintillator detectors.

- **Dr. Emilia Solano** for her inspiring commitment to fight for our L-H transition experiments at JET and for introducing me into the culture and IT systems at the CCFE.
- **Prof. Dr. Peter Manz** for his help and advice as a peer and for his support of my PhD students.
- **My parents** for financing my studies and for their everlasting support and understanding that I live far away from them, in order to be able to do crazy science and espousing a probably unrealistic idea of realizing a burning fusion plasma on earth.
- **My wife and my lovely daugther** for bearing my moods and their changes, for tolerating that I had my mind still at work although I was at home, and for carrying me off my sorrows during the dark times of the last two and a half years.

In addition, I would like to thank the Helmholtz Association for funding my work and the work of Joaquin Galdon, Balás Tál, Joey Kalis and Daniel Wendler under grant No. VH-NG-1350.